ORNL/HTSPC-18

ORNL Superconducting Technology Program for Electric Power Systems

Annual Report for FY 2006

SUPERCONDUCTIVITY FOR ELECTRIC SYSTEMS

ORNL/HTSPC-18

ORNL SUPERCONDUCTING TECHNOLOGY PROGRAM FOR ELECTRIC POWER SYSTEMS

ANNUAL REPORT FOR FY 2006

Compiled by
D. F. Lee
A. W. Murphy

Edited by
W. S. Koncinski

Manuscript Completed: April 2007
Date Published: September 2007

Prepared for the
Office of Electricity Delivery and Energy Reliability
U.S. DEPARTMENT OF ENERGY
(TD 5001)

Prepared by the
OAK RIDGE NATIONAL LABORATORY
P. O. Box 2008
Oak Ridge, Tennessee 37831-6283
Managed by
UT-Battelle, LLC
for the
U. S. DEPARTMENT OF ENERGY
Under contract DE-AC05-00OR22725

Contributors

Left to right: M. Reeves, L. Heatherly, Jr., D. F. Lee, F. A. List, M. P. Paranthaman, D. R. James, M. J. Gouge, A. Goyal, I. Sauers, E. D. Specht, E. Tuncer, P. M. Martin, R. Feenstra, R. C. Duckworth, A. R. Ellis, S. Kang, J. Li, H. M. Christen, C. M. Rey, B. Demps, T. Aytug, D. K. Christen, S-H. Wee, J. A. Demko, S. W. Schwenterly, S. Sathyamurthy, Y. Zhang, D. M. Kroeger, and R. A. Hawsey

Not shown: D. B. Beach, S. Bhuiyan, C. Cantoni, S. W. Cook, K. Kim, B. W. McConnell, A. W. Murphy, and J. R. Thompson

Contents

List of Figures

List of Tables

NOMENCLATURE

$\Delta\phi$	in-plane texture
$\Delta\omega$	out-of-plane texture
ρ	normal-state resistivity
σ	standard deviation
B_{irr}	irreversibility field
c (2 × 2)	centered (2 × 2) superstructure
G_P	precursor growth rate
H	magnetic field
H_{max}	maximum magnetic field
I_c	critical current
I_p	peak current
I_{mp}	propagation current
I_{rms}	root mean square cable current
J_c	critical current density
J_c^{GB}	intergrain critical current density
J_c^{G}	intragrain critical current density
J_E	engineering critical current density
K_c	critical current per unit width of conductor
langmuir	10^{-6} Torr/s
ML	surface adsorbate atoms per surface substrate atoms
M_{sat}	saturation magnetization
Pa.s	pascal.second
P_{base}	base pressure
$P(CO_2)$	CO_2 partial pressure
P(CO)	CO partial pressure
$P(H_2O)$	water vapor partial pressure
$P(O_2)$	oxygen partial pressure
T	tesla
T_c	critical temperature/transition temperature
t	thickness
θ_{mis}	misorientation angle
C_p	heat capacity
P_{tot}	total pressure
R_a	root mean square roughness

ACRONYMS AND INITIALISMS

ac	alternating current
acac	acetylacetonate
ACT	Applied Cryogenics Technology
AEA	Applied Energy Analysis
AEP	American Electric Power
AFM	atomic force microscopy
AFRL	Air Force Research Laboratory

AMSC	American Superconductor Corporation
ANL	Argonne National Laboratory
APS	Advanced Photon Source
ASC	Applied Superconductivity Conference, Inc.
ASC	Applied Superconductivity Conference, Inc.
ASG	Applied Superconductivity Group
ASTM	American Society for Testing and Materials
BIL	basic impulse level
BSCCO	Bi-Sr-Ca-Cu-O
BZO	$BaZrO_3$
CCAS	Coalition for the Commercial Application of Superconductors
CCVD	combustion chemical vapor deposition
CEC	Cryogenic Engineering Conference
CEIDP	Conference on Electrical Insulation and Dielectric Phenomena
CGA	Compressed Gas Association
CRADA	cooperative research and development agreement
CSD	chemical solution deposition
CTAB	cetyl trimethyl ammonium bromide
CTFE	chlorotrifluoroethylene
CZO	$CaZrO_3$
dc	direct current
DEIS	Dielectrics and Electrical Insulation Society
DMF	dimethyl formamide
DMM	digital multimeter
DOE	U.S. Department of Energy
DOE-HQ	DOE Headquarters
DSM	diffraction space mapping
e-beam	electron beam
EBKP	electron backscattering Kikuchi pattern
EBSD	electron backscatter diffraction
EDS	energy-dispersive spectroscopy
EDX	energy-dispersive X-ray diffraction
fcc	face-centered cubic lattice
FFT	fast Fourier transform
FM	ferromagnetism
FRP	fiberglass-reinforced plastic
FWHM	full width at half maximum
GBMD	grain-boundary misorientation distribution
GE	General Electric
GE-CRD	General Electric Corporate R&D
GM	Gifford-McMahon
GZO	gadolinium zirconium oxide
HR-PLD	high-rate pulsed-laser deposition
HRTEM	high-resolution transmission electron microscope
HTS	high-temperature superconductivity/superconductor/superconducting
IBAD	ion-beam-assisted deposition
ICP-MS	inductively coupled plasma mass spectroscopy
IEA	International Energy Agency
IEEE	Institute of Electrical and Electronics Engineers, Inc.
ISD	inclined substrate deposition
ISTEC	International Superconductivity Technology Center

LANL	Los Alamos National Laboratory
LMO	$LaMnO_3$
LN	liquid nitrogen
LNO	$LaNiO_3$
LPE	liquid-phase epitaxy
LSMO	$La_{0.7}Sr_{0.3}MnO_3$
LTS	low-temperature superconductor
LZO	lanthanum zirconium oxide ($La_2Zr_2O_7$)
MCP	melt-cast processed
MFCL	matrix fault current limiter
MgO	magnesium oxide
MLI	multiple-layer insulation
MOCVD	metal-organic chemical vapor deposition
MOD	metal organic decomposition
MRCAT	Materials Research Collaborative Access Team
MRS	Materials Research Society
OIM	orientation image micrograph
OPIT	oxide powder-in-tube
ORNL	Oak Ridge National Laboratory
PD	partial discharge
PDIV	partial discharge inception voltage
PED	pulsed-electron deposition
PIT	powder-in-tube
PLD	pulsed-laser deposition
PSD	position-sensitive detector
PTFE	polytetrafluoroethylene
PVA	polyvinyl alcohol
PVC	polyvinyl chloride
PVD	physical vapor deposition
R&D	research and development
RABiTS™	Rolling-Assisted Biaxially Textured Substrate
RBCO	rare-earth element + $Ba_2Cu_3O_x$
RBS	Rutherford backscattering spectroscopy/spectrum
RE	rare earth
rf	radio frequency
RHEED	reflection high-energy electron diffraction
rms	root mean square
SAD	select area diffraction
SAED	selected-area electron diffraction
SCE	standard calomel electrode
SD	standard deviation
SEM	scanning electron microscopy
SIMS	secondary ion mass spectrometer
SPI	Superconductivity Partnership with Industry
SQUID	superconductivity quantum interference device
SRO	$SrRuO_3$
STEM	scanning transmission electron micoscope
STO	$SrTiO_3$
TBAP	tetrabutylammonium perchlorate
TEM	transmission electron microscopy

TFA	trifluoroacetate
TMAP	trimethyl acetate salts and proponic acid
VLF	very low frequency
WES	Waukesha Electric Systems
XPS	X-ray photoemission spectroscopy
XRD	X-ray diffraction
YBCO	yttrium barium copper oxide ($YBa_2Cu_3O_{7-d}$)
YNO	Y_3NbO_7
YSZ	yttria-stabilized zirconia
Z-STEM	Z-contrast scanning transmission electron microscopy

Executive Summary

This report presents the results of projects conducted at Oak Ridge National Laboratory (ORNL) and its industry and university partners working in the U.S. Department of Energy's (DOE's) Superconducting Technology Research Program for Electric Systems. Funded primarily by DOE's Office of Electricity Delivery and Energy Reliability, ORNL projects include research and development toward second-generation high-temperature superconducting (HTS) wires, the Superconductivity Partnerships with Industry (SPI), and strategic research in materials and process development. Many of the articles in this report are adapted from papers submitted for open-literature publications; presentations at the annual DOE Peer Review in August 2006; and presentations given at the Materials Research Society meetings, the American Ceramics Society meetings, and other conferences and workshops held during FY 2006.

Among the SPI projects included in this report is the HTS cable project with long-time partner Southwire Company. Progress is reported on the testing of a prototype 5-m-long, 3-kA triaxial cable. For this testing, all three phases of the cable are concentric with one another, and the outer shield layer can be made of nonsuperconducting metal such as copper. This design has the potential to revolutionize the development of distribution-voltage-level cables, as it is the most compact and uses half the superconducting wire used in competing technologies. Progresses on the SuperPower HTS matrix fault current limiter project, the Waukesha Electric Systems HTS transformer project, and the General Electric Company HTS generator project are also reported.

In the areas of second-generation HTS wire materials and process research, substantial progress has been achieved, as described in the many articles in this report. Significant flux-pinning enhancement has been achieved in short lab-scale samples with thick YBCO films. This improvement, achieved through nano-defect engineering using aligned nanorods, demonstrated that second-generation wires have the potential to satisfy the demanding performance requirements of most applications. Collaborative works with American Superconductor Corp. and the Wire Development Group in FY 2005 have also yielded essential insights in the means to control the angular dependence of critical current density in these second-generation HTS wires. This is of significance because the response of critical current to external magnetic fields may be tailored to specific applications. Important insights have also been obtained in the long-range percolative behavior of supercurrents in a textured material as well as in the relative influences of out-of-plane and in-plane textures. These studies are highly pertinent because they can reveal potential limitations and areas of opportunity for second-generation wires. In addition to critical-current performance research, high-voltage and ac-loss characterizations have also been conducted on second-generation wires. The results on high-voltage qualification showed that when a wire is surrounded by a copper subsidizer layer, the breakdown voltage is increased compared with the breakdown voltage of its as-slit counterpart. These and other results indicate that performance and properties of second-generation wires may be altered through conductor design and engineering.

1. Technical Progress in Application Development

1.1 Ultera/ORNL HTS Cable SPI

J. A. Demko, R. C. Duckworth, A. R. Ellis, P. W. Fisher, M. J. Gouge, D. R. James, C. R. Rey, I. Sauers

1.1.1 Ultera HTS Triaxial Cable at AEP Bixby Substation

The 200-m triaxial cable, manufactured by Ultera Co., a partnership between Southwire Co. and NKT Cables, has arrived from Europe at the Southwire Co. plant in Carrollton, Georgia. The cable was installed in late January–February 2006. Extra lengths of the cable will be cut off and sent to Oak Ridge National Laboratory (ORNL) for testing then.

A meeting was held among Ultera, American Electric Power (AEP), Praxair, and ORNL December 14–15, 2005, at the AEP Gahanna, Ohio, location. A brief tour of the high-temperature superconducting (HTS) cable site was conducted. The surveyor markers for locating the cable duct banks have been placed, and construction was imminent. We also visited PhpK, which is fabricating the cryogenic system, the termination housings, and much of the cryogenic piping. PhpK had fabricated the subcooler heat exchanger and other vessels internal to the cryogenic system and was beginning their installation into the main vacuum vessel.

The remainder of the meeting on December 15 covered cable and splice status, site construction status, cable installation schedule, and monitoring and control issues. One significant topic that was reviewed was the cable system status definitions needed to determine whether the cable should be taken on or off line. A set of definitions and actions was agreed upon by the participants.

ORNL completed the modifications of the cable termination design from the basic "T4" termination design tested at ORNL in the spring of 2005. The major change was use of vacuum-jacketed multiple-layer (MLI) instead of foam thermal insulation in the termination housings. By the end of the quarter, all of the new termination parts were out for bid and most orders had been placed with fabrication shops. Figure 1.1 shows an outline view of one of the three-phase terminations.

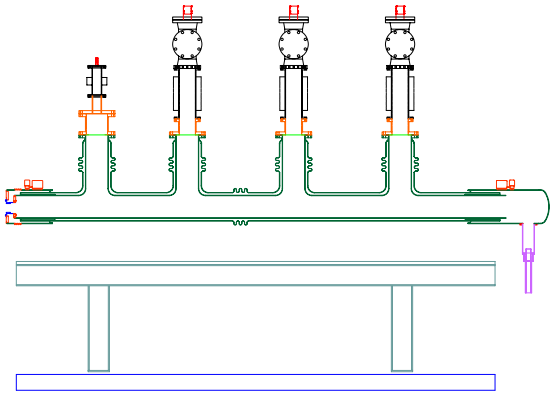

Fig. 1.1. Outline view of one of the three-phase triaxial cable terminations.

1.1.2 Tests on Samples from 50-m Test Cable and the Triaxial Splice Prototype

The 3-m splice cable was received at ORNL on December 1, 2005. Due to its length, the cable could not be tested in the existing liquid nitrogen (LN) cryostats under pressure, so tests were performed in an open bath of LN. To determine whether existing stress cones could be used for the open bath tests, some preliminary tests were done with the shorter (4 ft.) sample designated "10d" of the NKT triaxial cable used for pulling tests with the 50 m prototype cryostat.

1.1.2.1 NKT Cable Sample 10d Tests

To test each insulation layer of sample 10d individually, namely Phase 3 to shield, Phase 3 to Phase 2, and Phase 2 to Phase 1, a cryoflex stress cone was installed on each end using the outermost conductor as ground. The inner conductors were shorted together, and a corona ring was placed over each end (see Fig. 1.2). High voltage was applied at one end of the sample. The sample was placed in the open styrofoam dewar that was filled with LN. The sample was allowed to cool down for typically 3 or 4 h

Fig. 1.2. Corona ring over end of sample 10d with holes for LN.

before applying voltage. A large amount of bubbling occurred over the cable, usually from underneath or at the edges of tapes and the stress cones. Either no ice or only a small amount of ice was observed on the stress cones before the tests, but after voltage was applied, ice could be seen covering large portions of the stress cones, much like a tracking pattern. In one case, the sample was tested in ambient air and SF_6 at room temperature (Fig. 1.3). The voltage tests performed were

- partial discharge (PD) onset and extinction
- ac withstand at 39 kermes for 5 min
- 10+/10- impulse tests at 110 kV (1.2/50 μs)

The test results on cable sample 10d are summarized in Tables 1.1 and 1.2:

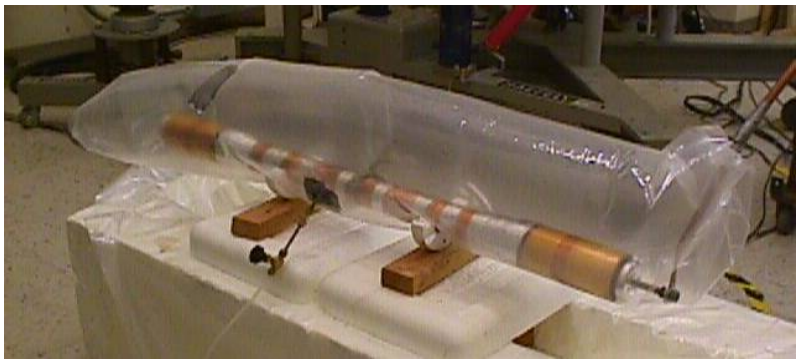

Fig. 1.3. Sample 10d bagged with SF_6 for ac withstand and PD onset tests.

Table 1.1. Impulse results on NKT sample 10d in open LN bath
WS = withstand; BD=breakdown

Date	Insulation	Impulse (kV peak) (scope)		No. shots		Comment
29 Nov 05	P3 to P2	Pos	112.4	10	WS	Passed
	P3 to P2	Neg	104.7	1	BD	Ice observed on stress cone
30 Nov 05	P3 to P2	Neg	107.0	1	WS	Withstand
	P3 to P2	Neg	111.5	1	BD	Breakdown; at rise (transition) part of stress cone
19 Dec 05	P2 to P1	Pos	110.6	10	WS	Passed
	P2 to P1	Neg	109.2	1	WS	
	P2 to P1	Neg	109.7	1	WS	
	P2 to P1	Neg	110.1	7	WS	
	P2 to P1	Neg	110.1	1	BD	Failed on last shot at voltage;6 μs after peak
21 Dec 05	P2 to P1	Neg	110.1	10	WS	Passed, even though it had previous breakdown; at rise of stress cone also

Table 1.2. PD onset and ac withstand for NKT sample 10d

Date	Insulation	Bath	PD onset (kVrms)	PD ext. (kVrms)	Withstand
8 Nov 05	P3 to P2	LN	15	14	
	P3 to P2	LN			39 kVrms/5 min
9 Nov 05	P3 to P2	air	3.8	3.5	
10 Nov 05	P3 to P2	SF_6	4.5	4.2	39 kVrms/5 min
19 Dec 05	P2 to P1	LN	14 -15		39 kVrms/5 min

The breakdowns occurring in 10d start at the rising part of the stress cone, where there is curvature of the ground plane—this is the highest field and thus the weakest point. Discharges occur in the butt gaps and across cryoflex layers working inward. The discharge then punctures straight through when it arrives at a thickness of about six or seven layers. (The actual direction of the discharge is not known, but it is easier to picture this way.)

1.1.2.2 Splice Cable Tests

A large styrofoam dewar was obtained with dimensions 11 × 1.5 × 2 ft with a 10 in. × 10 in. × 10 ft trough cut out for LN. The same stress cones used in the 10d tests were put on each end of the splice cable. One end of the cable was shortened to allow it to fit in the dewar (Fig. 1.4).

The ground lead is attached to the center of the ground shield. The inner phases are shorted together with tabs under the corona ring. Results of testing are shown in Tables 1.3 and 1.4.

Fig. 1.4. Completed stress cone and corona ring with splice cable in dewar.

Table 1.3. PD onset and ac withstand for 3-m splice cable in open LN bath

Date	Insulation	Bath	PD onset (kVrms)	PD ext. (kVrms)	Withstand
28 Dec 05	P3 to shield	LN2	15	14 – 14.5	39 kVrms/ 5 min

Table 1.4. Impulse results on 3-m splice cable in open LN bath
WS = withstand; BD=breakdown

Date	Insulation	Impulse (kV peak) (scope)		No. shots		Comment
28 Dec 05	P3 to shield	Pos	107.9	1	WS	Within 3% spec for 110 kV
	P3 to shield	Pos	109.2 to 110.6	9	WS	Passes 10+ BIL
	P3 to shield	Neg	94.4	1	BD	Possible flashover
	P3 to shield	Neg	85.9	1	WS	Start at 43 kV and go up
	P3 to shield	Neg	94.0	1	BD	Breakdown; bubble turbulence at high-voltage lead end near stress cone; moderate to heavy ice on cones
4 Jan 06	P3 to P2	Neg	43.2	1	WS	Neg polarity first; no ac tests
		Neg	80.9	1	WS	
		Neg	100.7	1	BD	Breakdown at peak
	P3 to P2	Pos	29.2	1	BD	
		Pos	31.9	1	BD	Does not hold off voltage

The breakdown on P3 to shield occurred several inches away from the shield splice on the high-voltage lead end. Phase 3 to shield insulation was removed, and stress cones were put on for the P2 to P3 insulation test. The cable was immersed in LN for 2 h and 20 min. Again, much bubbling of the LN occurred. Only a negative polarity impulse was run on P3 to P2 insulation to see whether it would improve negative basic insulation level (BIL) performance. It did not. There was a breakdown at 100.7 kV at the peak. The capacitance was the same before and after the breakdown. There was some ice on the stress cones. On December 5, 2006, a dc power supply voltage was applied to the cable in air after being warmed up overnight to try to locate the breakdown, similar to what was done on the 5-m cable. An audible breakdown could be heard at the splice near one end, and dissection revealed breakdown at the splice. There are no obvious field enhancements at the point of breakdown. There were considerable bubbles along the cable; this could be a point of bubble generation. The results for splice testing generally indicate that the ac (withstand, PD inception) high-voltage requirements and positive impulse test requirements can be met in the conservative (nonideal) test of an open LN bath. Given the scaling of impulse performance with LN pressure, the observed performance at negative impulse (~ 80 kV) is probably sufficient; however this will be confirmed in the next sequence of tests in a dewar with pressurized LN.

1.1.2.3 Future Tests

In the next sequence of tests, the splice section of the cable will be cut to fit in the large cryostat, which can be pressurized. Stress cones will be applied, and testing will be conducted at up to 5 to 6 bar pressure to remove bubbles and increase the dielectric strength of the LN.

1.1.3 Improved Tape Insulation for Superconducting Cables

Recent data taken by the cryogenic dielectrics staff were used to compare the breakdown field performance at room temperature (295 K) of the original Cryoflex gold dielectric tape and the new Cryoflex clear dielectric tape. (the color designation is for coding and does not reflect the nature of the material content.) The Cryoflex gold tape is used as insulation (it is immersed in LN) in all Southwire superconducting cables manufactured to date. The breakdown geometry was plane-plane electrodes: 15.87 mm diam; 4.70 mm thick. The thickness of both the clear and gold Cryoflex is nominally 102 µm (0.004 in.); the embossing pattern on the clear is different from that of the gold. All measurements for both types of samples were taken in the same way with Apiezon N grease applied to the electrodes. The grease fills the valleys in the embossing that prevents air from being trapped in the tape. The sample in a jig is then placed in an oil bath at room temperature. The plot (Fig. 1.5) is a Weibull (a common distribution function used in dielectric R&D probability of failure given in a percentage). The data have been normalized to the breakdown strength (with an assigned value of 1) of Cryoflex gold at 63.2% cumulative failure probability. The 1% probability of breakdown failure for Cryoflex clear is 60% higher than that of the original Cryoflex gold. The Cryoflex clear also has less

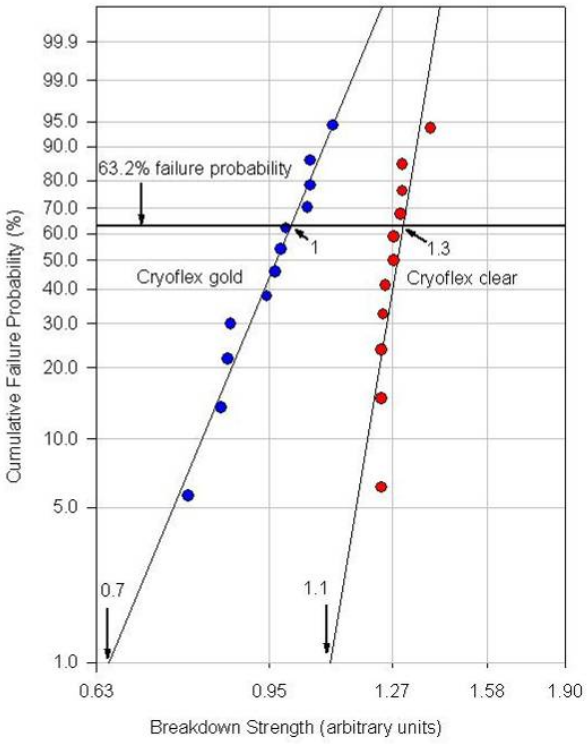

Fig. 1.5. Cumulative failure probability vs. relative breakdown electric field for Cryoflex.

spread over breakdown values (i.e., steeper slope) and therefore affords greater safety margins in the high-voltage design.

1.1.4 Thermal Hydraulic Response of Triaxial Cables to a Severe Fault

The triaxial HTS cable design will be placed in the AEP utility grid and will experience system faults as a part of normal operation. The thermal hydraulic response to a worst-case fault was determined from a simulation. The cable recovery time from a worst-case fault was estimated. Only the worst-case electrical fault possible in normal operation that is assumed recoverable is included in this report; it does not cover the case of loss of insulating vacuum in the cryostat.

The fault energy input into the triaxial HTS cable for the AEP Bixby installation has been estimated from AEP-specified current transients to be around 6.3 kJ/m and estimated from cable testing to be around 6.7 kJ/m. This is about 1.3 MJ of energy deposited in the 200-m length of the installed cable. The specified fault duration is 0.25 s.

The simulations presented in Figs. 1.6 through 1.9 are for the AEP Bixby triaxial cable operating parameters (inlet temperature, flow, and pressure). A very conservative severe fault condition was simulated that deposited 5 MJ of energy distributed uniformly over the length of the cable during a period of 0.2 s. Figure 1.6 shows the average temperature developed at the cable mid-point, at the 200-m point along the cable, and the far-end termination based on a lumped parameter approximation. The highest cable temperature reaches 88 K at the end of the fault application. Figure 1.7 shows the temperature profiles developed along the length of the cable. The extra thermal mass inside the terminations causes their temperatures to lag behind the rest of the cable. Figures 1.8 and 1.9 are the mass of nitrogen that must be relieved to a buffer, and the flow rate of the buffer flow for a period after the fault. As shown in Fig. 1.8, most of the liquid is sent to the buffer in the first 20 s after the fault. After about 2500 s, the overall state of the cable system has cooled down sufficiently so that it begins accepting liquid that was expelled during the fault. The triaxial cable appears to be capable of enduring the faults expected at the AEP Bixby substation with moderate impact to the cryogenic system. A severe fault (four times the expected energy deposition) would require more than an hour to cool down enough for full operation and the capability to withstand another similar fault.

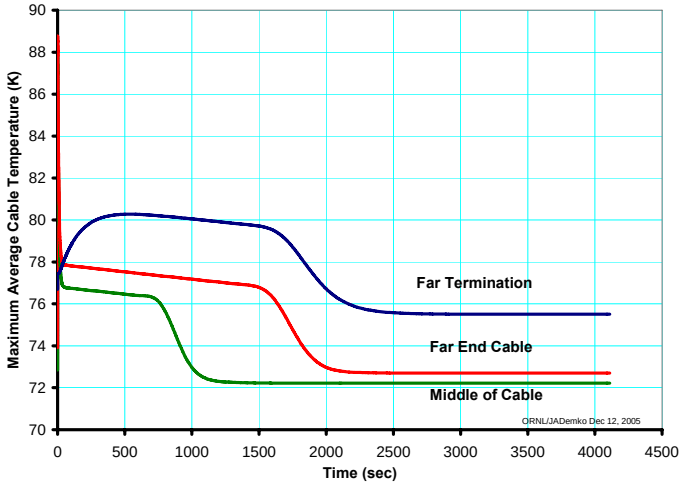

Fig. 1.6. Triaxial cable thermal response at three locations until recovery after the severe fault current pulse.

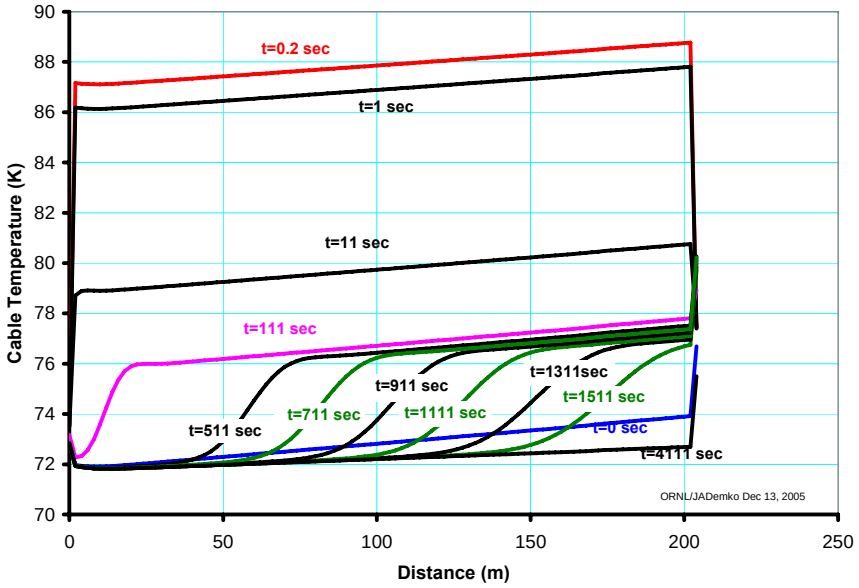

Fig. 1.7. Triaxial cable thermal response after application of the severe fault.

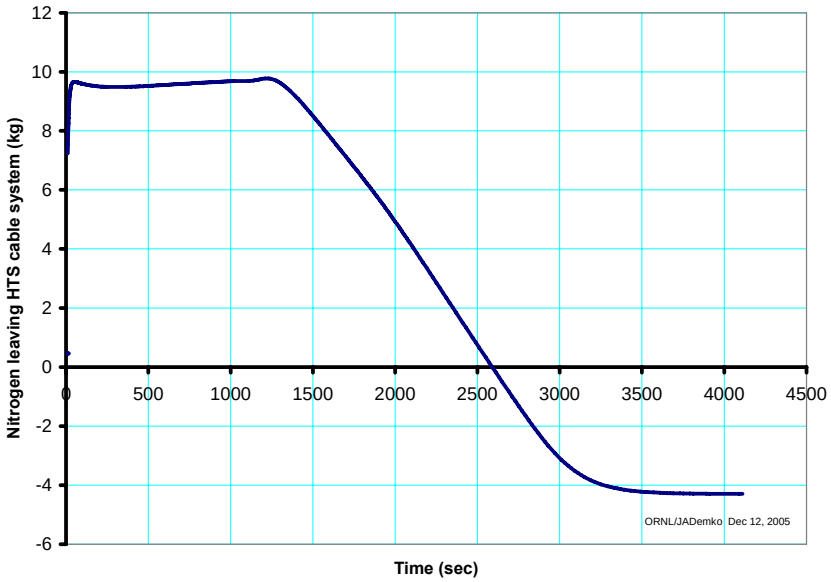

Fig. 1.8. Mass discharged from the 200-m triaxial cable into the buffer during a severe fault.

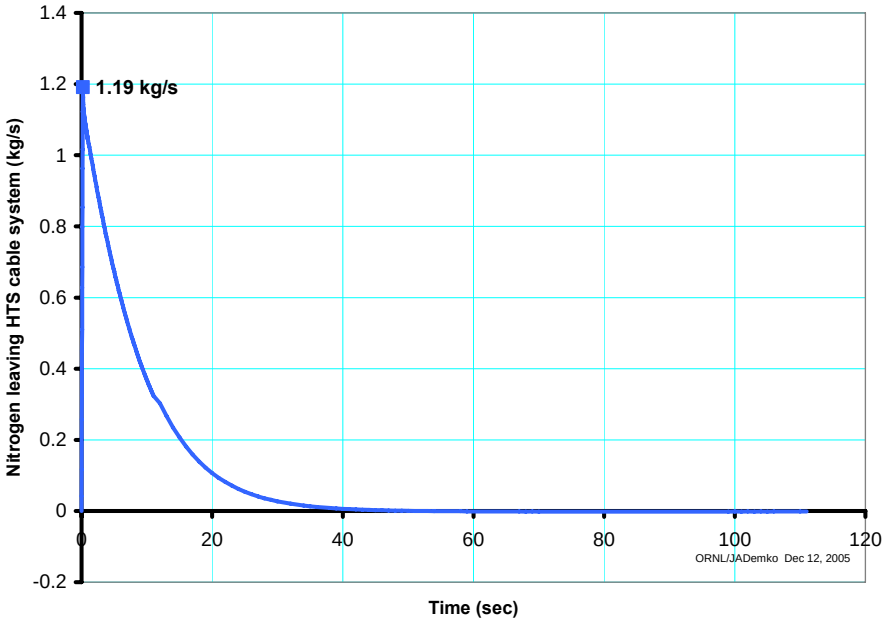

Fig. 1.9. Mass flow rate of nitrogen into the buffer from the 200-m triaxial cable.

1.1.5 HTS Cable Test Facility Move

The relocation of the cable test facility's equipment and the triaxial cable to Building 7625 at the ORNL facility was completed in the previous quarter. The craft completed electrical connections to the equipment (ac/dc power supplies, cryogenic skid, and related equipment). New casework has been installed. Piping has been installed from the LN tank to the facility. Piping connections to bring LN to the skid from the external tank, vent line connections, and cooling water connections have been completed. Remaining work includes installation of a safety fence and commissioning of the cryogenic skid and power supplies.

1.1.6 AEP Columbus Triaxial Cable and Cryogenic System Status

Significant progress has been made on the AEP Bixby substation triaxial HTS cable project. In January 2006 the 200-m-long HTS cable and the two 100-m-long vacuum-jacketed, flexible cryostats arrived on site. During the week of February 6, the two-cryostat sections were inserted into the underground duct near each of the termination locations (Fig. 1.10) and were pulled into the underground manhole at the middle of the cable run. A nylon pulling sock was attached to the end of the HTS cable (Fig. 1.11). The cable sections were then pulled into the cryostats by using a nylon rope and a small winch rigged on top of the manhole. With a pulling speed of 3 m/min (10 ft/min), the duration of the pull was about 33 min. The allowable pulling force was not exceeded.

After the cable was pulled, it was cut in two pieces in the manhole to demonstrate a 3-phase cable-splice procedure. The vacuum-jacketed cryostat sections have specially designed ends so that a vacuum-insulated cryostat splice can be used to join them in the manhole. The splice vacuum is separate from the

Fig. 1.10. Pulling the vacuum-jacketed flexible cryostat into the underground duct at AEP's Bixby substation.

Fig. 1.11. Pulling the superconducting cable into the cable cryostat.

100-m cryostat section vacuum spaces. Figure 1.12 shows the completed cable and cryostat splice that was made in the manhole. In addition to the splice, the HTS triaxial cable termination assembly work has begun. The connections have been made between the HTS triaxial cable and the current leads. The termination assembly is expected to be completed early in the next quarter.

The Praxair cryogenic system, built by PhpK, Inc., in Columbus, Ohio, has been delivered to the site. The major components have been installed (Fig. 1.13) and initial checkout of the system has begun.

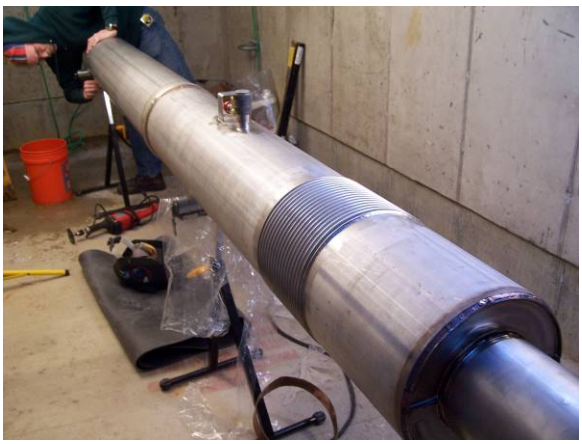

Fig. 1.12. Triaxial HTS cable splice outer cryostat after assembly.

Fig. 1.13. AEP cryogenic system has been delivered.

1.1.7 Thermal Hydraulic Response of the Triaxial Cable System to Fault Scenarios

The triaxial HTS cable design will be placed in the AEP utility grid and will experience system faults as a part of normal operation. This section shows the calculated LN system thermal hydraulic response to a few fault scenarios. The HTS cable system can experience electrical faults, some of which are high-energy events over very short durations. This excess energy must be removed by the LN coolant stream. The total energy that must be removed is finite, so the HTS cable system can recover from typical electrical faults. Predicted expansion of the LN in the cable system is shown in Fig. 1.14 based on the difference in mass of nitrogen in the cable system after the fault for specified electrical system faults of 10 kA_{rms} (for 600 ms) and 20 kA_{rms} (57 kA peak, for 250 ms). The expansion rate is shown in Fig. 1.15. The results assume the nitrogen is free to expand with no change in cable system volume. Figure 1.16 is the estimated pressure rise due to the overcurrent faults, assuming the quantity of nitrogen and the cable system volume stay the same throughout the event. The pressure relief valves are set to open at 10 barg, so if the system were operating around 5 barg, they would relieve,

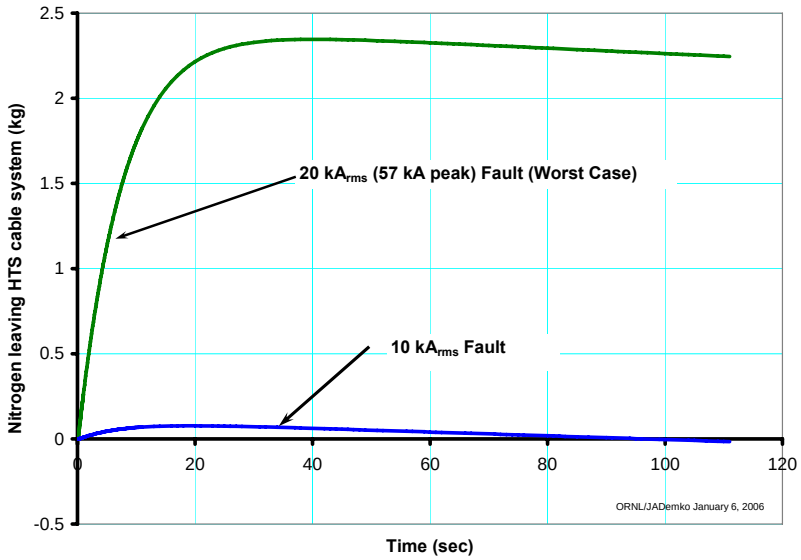

Fig. 1.14. Mass of nitrogen leaving the HTS cable system for an electrical fault.

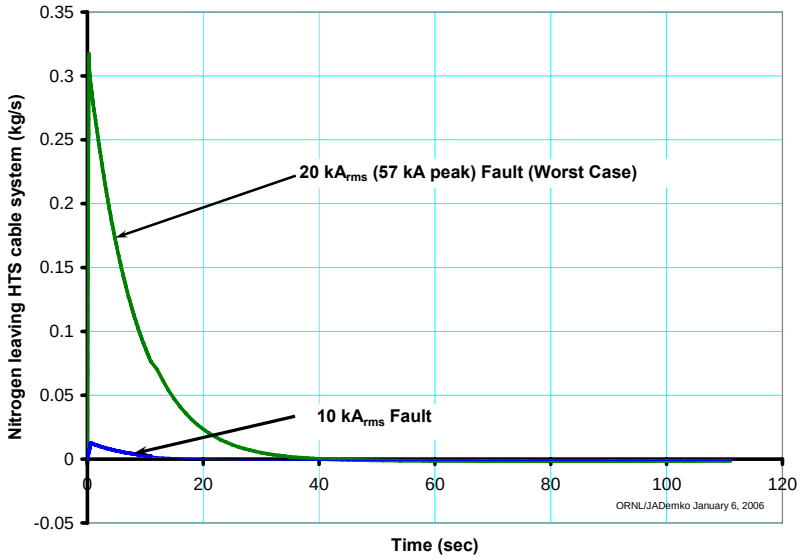

Fig. 1.15. Rate of nitrogen leaving the HTS cable system due to free expansion for electrical faults.

for the 20 kA$_{rms}$ fault, after about 7 s based on this calculation. The cable system should not experience any significant change for the 10 kA$_{rms}$ fault.

In reality, the fluid expansion is going to be taken up in three ways: (1) expansion into the LN storage tank, (2) expansion of the flexible cable inner cryostat, (3) venting through the pressure relief valves. Expansion into the storage tank is going to be limited by the flow resistance of the piping into the tank. The flexible cable cryostat will expand depending on its stiffness and could take up a majority of the fluid expansion, which is a relatively small volume compared to the total fluid volume. The remainder would be vented through the relief valves and burst disks.

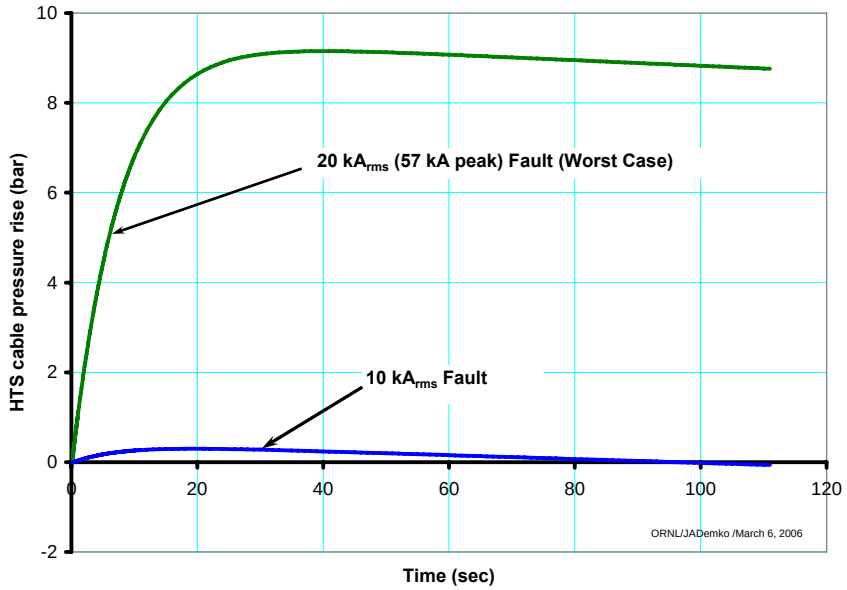

Fig. 1.16. Pressure rise of nitrogen in the HTS cable system for an electrical fault assuming the mass remains constant in the system.

The results for this case are not as easily defined. Two approaches have been taken; the first uses the measured effective thermal conductivity for a superinsulated section of corrugated line. This provides a 25-fold increase of the heat transfer to the cable on loss of vacuum. Results for this case are shown in Figs. 1.17, 1.18, and 1.19. Cases where either the first 100-m section or the second 100-m section lose vacuum are also compared. For the first 100 s after the event, there is little difference in the expansion of then LN or the potential pressure rise of the system. Since energy is continuously deposited into the cable system, potential pressure rise does not reach a maximum but continues to increase. The relief valves will vent and the burst disks will probably rupture for this situation.

The loss of insulating vacuum failure is a scenario that has a continuous and high heat-transfer rate to the LN coolant stream. The thermal energy transferred from the surroundings continuously accumulates in the coolant streams as long as the system is cold. This failure is not recoverable unless the vacuum leak is located and repaired.

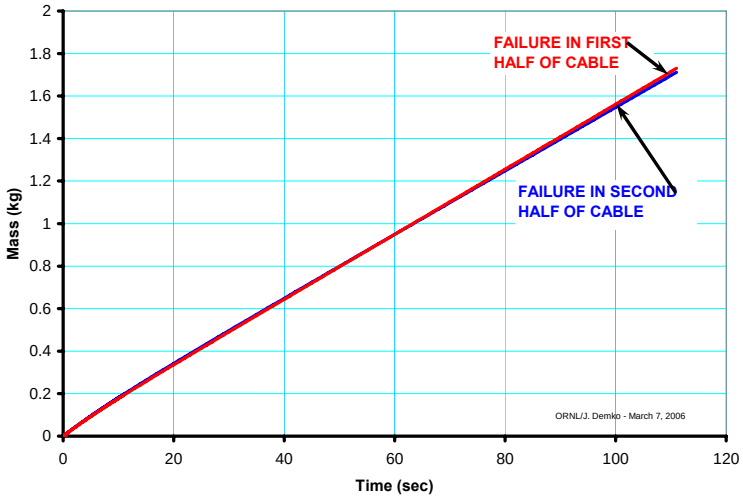

Fig. 1.17. Mass of nitrogen leaving the HTS cable system assuming free expansion for loss of insulating vacuum using a 25× multiplier based on NASA cryostat results.

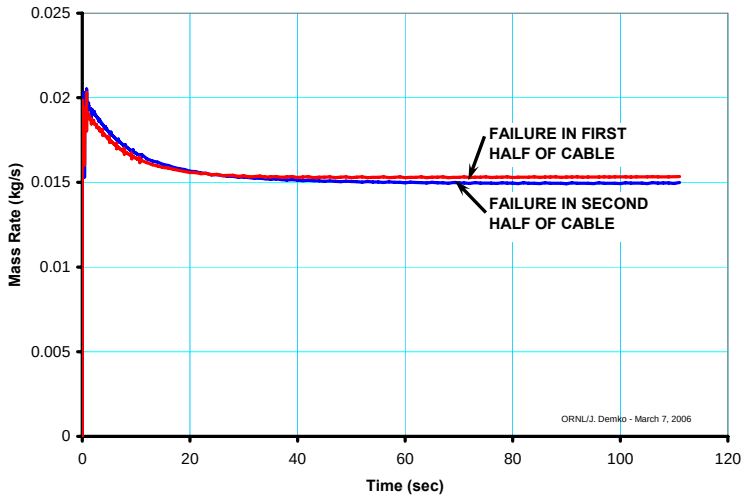

Fig. 1.18. Rate of nitrogen leaving the HTS cable system due to free expansion for loss of insulating vacuum using a 25× multiplier.

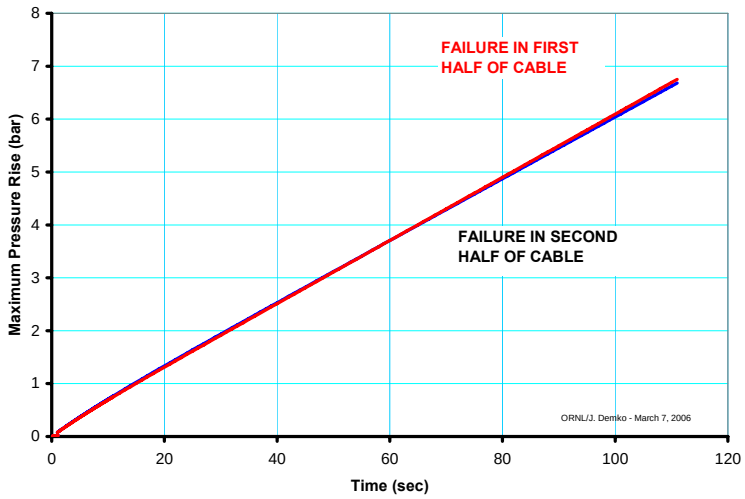

Fig. 1.19. Pressure rise of nitrogen in the HTS cable system for loss of insulating vacuum using a 25× multiplier assuming the mass remains constant in the system.

Figures 1.20, 1.21, and 1.22 show similar results except assuming a 165× multiplier on the heat load based on the Compressed Gas Association (CGA) standard S-1.3. This standard is for storage tanks (dewars) that have an ullage volume because they contain saturated liquid and would vent vapor, not liquid. Thus the large difference between the calculations (25× vs 165×). The CGA standard is well suited for storage dewars and is an accepted industry standard for sizing the pressure relief devices on tanks. Its applicability to this situation is considered conservative.

Well-documented studies have been conducted on loss of insulating vacuum in a helium dewar, which is probably a more severe case than a nitrogen dewar due to the larger temperature difference. The presence of superinsulation in the dewar vacuum had a profound effect on the heat loads. The cable system has a high aspect ratio (L/D) and flowing, sub-cooled LN so that the pressure relief

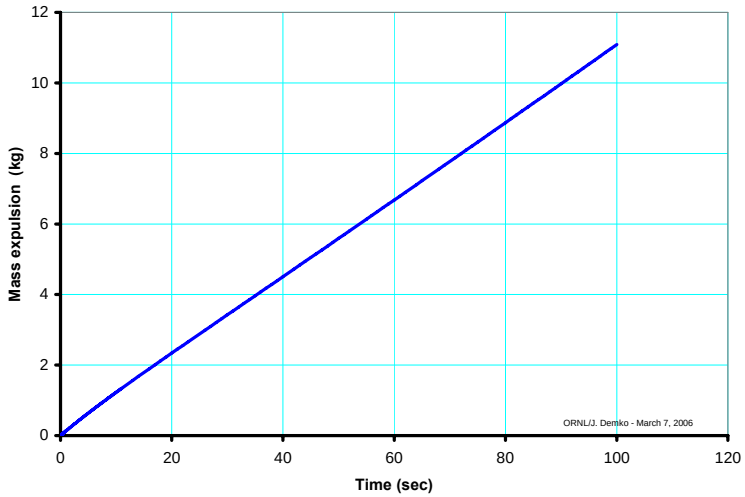

Fig. 1.20. Mass of nitrogen leaving the HTS cable system assuming free expansion for loss of insulating vacuum using multiplier based on the CGA code.

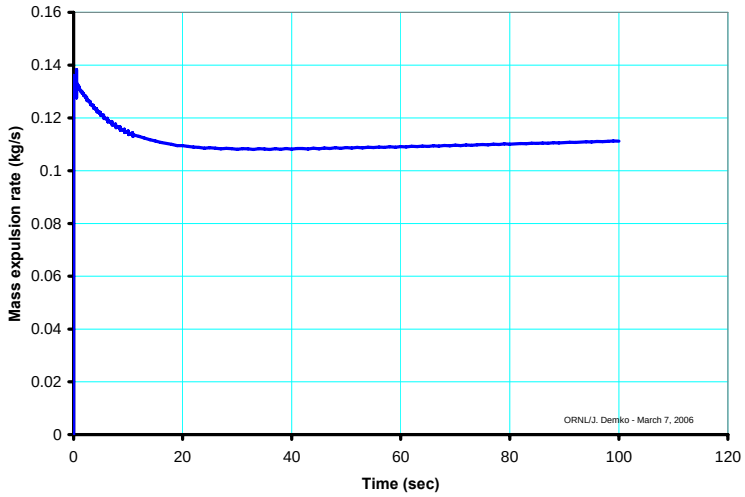

Fig.1.21. Rate of nitrogen leaving the HTS cable system due to free expansion for loss of insulating vacuum using the multiplier based on the CGA code.

system requirement is different from that for a storage dewar. The feasibility of testing a short flexible cryostat section with proper instrumentation to measure the response is being discussed. This would provide data (such as the proper heat load multiplier for loss of vacuum) useful for the design of the pressure relief systems for long superconducting cables.

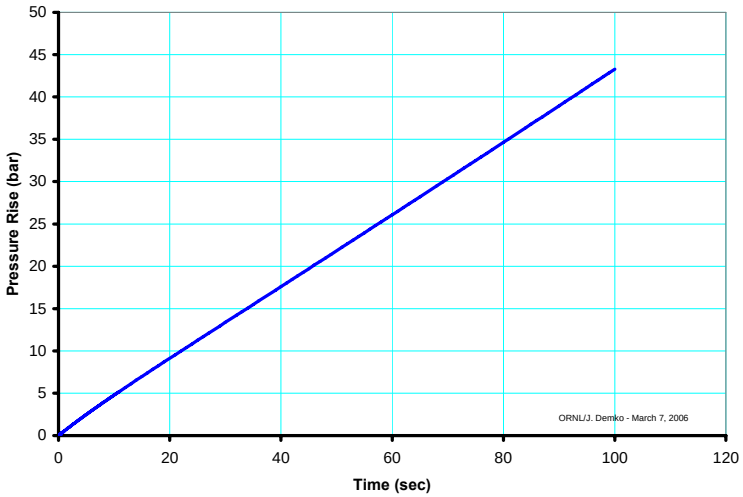

Fig. 1.22. Pressure rise of nitrogen for loss of insulating vacuum using a multiplier based on CGA code and assuming that the mass remains constant in the system.

1.1.8 HTS Cable Project High-Voltage Testing of Splice Joint

The spliced HTS cable was tested for ac withstand and impulse BIL withstand in an open bath of LN. Although the cable passed the ac withstand criteria at 39 kV_{rms} for 5 min, several external flashovers occurred during some of the impulse tests. These flashovers were thought to be due to ice formation on the stress cones and/or bubble formation in the LN at atmospheric pressure. To test the splice in conditions the cable will see in service (running with 5- to 6-bar pressure LN), the shield and outer electric phase 3 were removed from the splice sample. This reduction in diameter and length allowed the remaining two phases to fit inside the pressurized test dewar (Fig. 1.23).

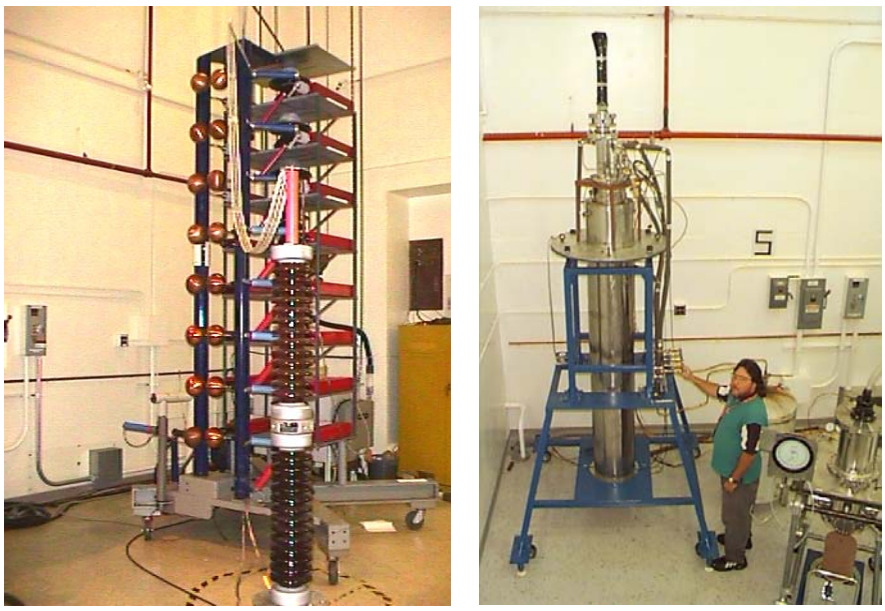

Fig. 1.23. 800-kV impulse generator (left) and pressure dewar (right) used to test the splice cable section.

The splice cable was put in the large cryostat on January 12, 2006, and was pumped down for four days. Next, the chamber was filled with LN to 6-bar pressure. Starting with negative polarity, the voltage was stepped up from 45.9 kV to 107.9 kV with no breakdowns. The splice section then passed ten successive withstands at 110 to 112 kV BIL. PD onset and ac withstand tests were performed at 6 bar pressure; PD onset was approximately 25 kV_{rms}, significantly higher than the 15-kV onset in boiling nitrogen. Changing back to impulse test configuration, the pressure was increased to 8 bar and the impulse voltage was applied. Starting with positive polarity, the voltage was stepped up from 44.5 kV to 145.2 kV without any breakdowns or flashovers. Polarity was switched to negative, and voltage was stepped up from 42.7 kV to 145.6 kV when a breakdown occurred (the sound suggested a flashover to the chamber wall). The voltage was stepped up again from that point to 158.2 kV, where a breakdown/flashover occurred. The cable would not hold voltage afterwards, indicating a probable puncture in the cable insulation (subsequent dissection showed it to be in the cable, not the splice area). This performance above the IEEE requirement (110 kV) is what is expected, given the radial build of tape insulation in the cable section. This positive result means the splice is qualified for service in the superconducting cable demonstration at the AEP Bixby substation in Columbus, Ohio. The 200-m superconducting cable was installed in March 2006 with a similar splice at the cable midpoint.

1.1.9 Spliced Former Cable Tests to Date

A section of the AEP cable, which has a splice in the former (not the phases), was received for high-voltage testing. Phase 3 (P3) to screen was tested at 6 and 8 bar in the large cryostat. A splice in the former is not expected to affect the P3 to screen or the P3 to P2, but possibly could affect the P2 to P1 insulation. The screen to P3 passed the BIL tests of 10+ and 10– withstands at 110 kV at 6 bar. It was not possible to break down the sample at higher voltages due to flashovers to the wall or along or under the stress cone. The maximum voltage was 129 kV. A pressure increase to 8 bar did not increase the voltage before flashover, which suggested the flashover was in the LN. Since the cable could not be broken down, successive impulse shots were done at nominal 110 kV, alternating 10+ and 10– with conditioning shots of the same polarity at lower voltage before each run. On February 14, 2006, about 100 shots at 8 bar were taken in this manner. About 5 to10% of the shots were flashovers, but the following shots were withstands, meaning that the insulation was not punctured. On March 15, 2006, the impulse shots were continued with the pressure at 6 bar. After another 100 withstand shots, the PD onset and ac withstand were tested. The PD onset was 17–18 kV_{rms} with very low counts, just above 5 pC, and large PD at 3 to 4 nC kicking on at 30 kV_{rms}. The test section withstood 39 kV_{rms} for 5 min. Extinction was approximately 28 kV_{rms} for the large PD and about 15–16 kV_{rms} for the very small PD. It is difficult to determine PD onset in this case. After the ac withstand, another 100 shots of impulse were applied with no breakdown of the cable. The total number of impulse withstands was 300 shots without a breakdown of the cable. The test system was warmed up to room temperature, and the cable was removed. There was evidence of dust/tracking at the end of one stress cone, which suggested a flashover site. Dissection of the stress cone will be performed, and the P3-P2 and P2-P1 phases will be tested.

1.1.10 AEP Columbus Triaxial Cable System Status

In 2006, AEP installed an HTS underground cable system in Columbus, Ohio. The system had been designed and built by Ultera (Southwire Company and NKT cables) and its technology partners (ORNL is responsible for cable and termination R&D). This installation will showcase a new triaxial cable design and advanced cryogenic cooling systems. In April 2006, the superconducting cable terminations on each end of the 200-m cable run) were completed with direct support from ORNL staff. The termination components are rated for cable voltage (13.2 kV) and current (3,000 A_{rms}) and make the difficult thermal transition from 77 K (LN) to 300 K (ambient temperature). Figures 1.24 and 1.25 show the assembled 3-phase south termination; the north termination is identical. The Applied Superconductivity Group (ASG) performed high-voltage and high-current testing and qualification of 3-phase, full-scale, prototype terminations at ORNL in 2005.

Fig. 1.24. South HTS cable termination at AEP's Bixby substation. The 3-phase bushings are shown and the smaller neutral bushing on the right side.

Fig. 1.25. The south HTS cable termination with cable entering underground duct. The control trailer for the cryogenic system is in the background.

A cryogenic system readiness review was held on May 24 with George Mulholland (Applied Cryogenics Technology [ACT]) leading the review; ORNL participated with Ultera and Praxair staff. On June 19–20, the cable system was cooled down from ambient conditions to about 70–72 K using a cryogenic system provided by Praxair, Inc. The cooldown proceeded smoothly at a rate to limit thermal gradients. Contractions in the cable and terminations were as expected. Pressure drops and heat loads were as predicted or lower. Off-grid testing of the cable superconductors to 5,000–6,000 A dc and of the cable high-voltage insulation to 20 kV_{rms} was successfully completed during the last week of June.

1.1.11 Test Results on Phase 2-Phase 3 AEP Cable Sample

The high-voltage field test for the on-site AEP cable will be done using a very low frequency (VLF) 0.1-Hz voltage, which requires much less charging current than 60 Hz. All ac tests on model cables done at ORNL so far have been at 60 Hz. Since the VLF power supply was unavailable for testing samples at ORNL, it was decided that a dc test of P2-P3 would be a "worst case" scenario. It is generally believed that dc high-potential testing can be harmful to extruded cables due to space charge buildup followed by application of ac [1].The test plan was to perform a baseline 60-Hz PD and ac withstand test first, followed by a dc withstand test. Then the PD test would be repeated to see if there were any changes that might indicate cable degradation. The PD test would be followed by impulse testing at 110 kV.

Phase 3 (the outermost phase) was stripped back and made the ground. Phases 2, 1, and the former were shorted together with copper tabs and were made the high-voltage electrode. Stress cones were prepared for each end of the cable on the lathe. A copper tube was inserted through the former, and an expandable plug was made to mount the cable rigidly on the lathe. This method allowed the stress cones to be wrapped considerably tighter than the previous ones, which were done by hand.

The cable was placed in the large cryostat on June 2, 2006, and the cryostat was pumped down by roughing pump for several days. On June 7th the chamber was filled with LN at 6-atm pressure and allowed to soak at pressure for 4 h. The PD system was set up and calibrated.

1.1.11.1 Initial PD tests

At 20.1 kVrms, there was a low level of 6 to 7 pC of PD. At 24.5 to 25.0 kVrms, PD kicked on at a high level of 1.4 to 1.6 nC. The PD dropped to 20 to 40 pC at 23 kVrms and was extinguished at 18 to 19 kVrms. The high-voltage supply was turned off.

1.1.11.2 Alternating-Current Withstand Test

PD onset repeated: 16 to 20 pC at 22.7 kVrms and 1.2 to 1.4 nC at 25 kVrms. The voltage was raised to 39 kVrms and held for 5 min. Consecutive 60 s PD scans were made and the level was 3.7 to 4.4 nC. The sample successfully passed the ac withstand.

1.1.11.3 Direct Current Tests

The dc breakdown voltage of conventional extruded cable was 1.5 times higher than the breakdown voltage at 0.1 Hz. AEP plans to test the real cable at 28-kV peak at 0.1 Hz. Hence, the dc voltage level selected was $1.5 \times 28 = 42$ kV dc to apply a comparable stress level to what will be done at AEP. However, these data are for extruded cables at room temperature and may not apply to a cable with lapped tapes of cryoflex impregnated with LN.

The ac power supply was removed, and a 50-kV dc Glassman power supply was connected to the sample with negative polarity. Direct current voltage was applied for 1 min at steps of 5, 10, 15, 20, 25, 30, 35, and 42 kV. No current was drawn at any voltage and voltage was returned to 0.

Negative dc voltage was then raised to 42 kV dc and was applied for 30 min. No current was drawn as indicated on the power supply meter. The sample successfully passed the dc withstand test. The voltage was returned to 0 slowly. The cable was grounded and remained in standby overnight.

The tests were repeated with positive polarity after allowing the cable to remain at pressure for 4 h. The voltage was raised in 5-kV increments and held for 1 min at each step as before. The sample successfully withstood 42 kV dc for 30 min with no current drawn on the power supply. There was some audible external corona heard, which most likely came from the top of the bushing.

1.1.11.4 Second PD/ac Withstand Test

PD onset was determined to be 23.7 kV at 65 to 75 pC. Large PD occurred at 24.5 to 25.5 kVrms at 1.8 to 2.2 nC, very similar to the measurements done before dc was applied. PD extinguished at 21.5 kV_{rms}. The voltage was raised to 39 kV_{rms} and held for 5 min. The PD level was 2.3 to 2.6 nC, lower than the previous measurement, but the difference may not be significant at such high levels. The PD extinction at 21.5 kV_{rms} is very close to the previous value. The dc tests did not appear to affect the PD onsets.

1.1.11.5 Impulse Tests

Positive impulse tests were conducted on the sample. Following a breakdown, several withstands were obtained at 117 kV, and the voltage was lowered to 111 kV where 10 consecutive withstands were achieved. The polarity was switched to negative. Following several breakdowns at 99.8 kV, the voltage was raised to 113.3 kV where 25 consecutive withstands were obtained. Polarity was switched back to positive, and 15 consecutive withstands were obtained at 111.9 kV. The voltage was then stepped up at positive polarity above the testing requirement of 110 kV. Breakdowns and withstands occurred at 132.6 kV followed by a withstand and a breakdown at 148.3 kV. Above this level only breakdowns occurred. This successfully completed the impulse testing.

1.1.11.6 Conclusion

The dc withstand tests do not appear to have significantly affected the PD onset voltages or ac withstand capability. The impulse withstands and breakdowns observed in the P3-P2 test following application of dc are similar to those obtained in tests without dc application. However, actual aging tests to failure have not been performed for dc aged cables, so we do not know whether there will be any long-term effects of dc application. If the 42 kV dc tests are indeed more severe than a 0.1 Hz VLF test, then these results suggest that the AEP cable should withstand the 30-min VLF test.

1.1.12 ORNL Superconducting Cable Test Facility Operational

The relocation of the Applied Superconductivity Group's cable test facility from a former location at NNSA's Y-12 plant to the new, multiprogram, high-bay Building 7625 at ORNL was completed in 2005. ORNL completed electrical and piping connections to the equipment (ac/dc power supplies, cryogenic skid and related equipment) in early 2006. New casework has been installed in the facility. High-current power supplies (3 kA ac and 25 kA dc) were commissioned. A safety fence was installed around the power supplies, and the external LN tank was filled. The research safety summary document was reviewed and updated, and ORNL management and staff conducted a safety review and physical inspection of the space. The facility was authorized for experiments in late April. Figure 1.26 below shows the facility control area outside the safety fence.

Fig. 1.26. Cable test facility control area with safety fence on the right side.

1.1.13 AEP Bixby Substation 200 m HTS Cable

Ultera has installed a 200-m-long HTS 3-phase triaxial cable at the AEP Bixby substation in Columbus, Ohio. The cable connects a 138-/13.2-kV transformer to the distribution switchgear serving seven outgoing circuits. It was designed to carry 3000 A_{rms}. Testing of 3- to 5-m prototype cables, including a 5 m prototype with full-scale terminations at ORNL, was conducted prior to the manufacture and installation of the AEP triaxial cable. The prototypes were used to demonstrate the crucial operating conditions, including steady-state operation at the 3000 A_{rms} design current, high-voltage operation, high-voltage ac withstand, 110 kV-impulse, and overcurrent fault capability. The three phases are concentric, as shown in Fig. 1.27. There is no net magnetic field when the three phase currents are balanced. The triaxial HTS cable offers an advantage over the coaxial HTS cable design in that it does not have a superconducting shield layer and thus, because it uses about half the HTS tapes, it is a lower-cost design. An additional savings is realized because the size of the triaxial cable is smaller than three coaxial cables and fits in a single, smaller cryostat, resulting in a lower heat load. The main operating parameters for the triaxial cable at the AEP Bixby substation are listed in Table 1.5. The cable was officially commissioned in a ceremony at the Bixby substation on September 18, 2006.

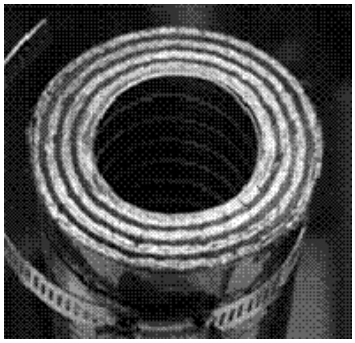

Fig. 1.27. Cross section of a triaxial HTS cable.

Table 1.5. Cable system description

Parameter	Value
Length, m	200
Current capacity, A_{rms}	3000
Voltage, kV	13.2
Power, MVA	69

The cable cooling is accomplished with LN supplied from a cooling system designed by Praxair. A schematic is shown in Fig. 1.28. It uses an open cycle vacuum subcooler approach that has been continuously improved over earlier systems. This Praxair unit has a separate storage tank that holds a backup supply of subcooled LN, which, in the event that the main system is lost due to a power outage, could keep the cable cold for up to 8 h. In addition, the Praxair system has provisions for including pulse tube cryocoolers to substantially reduce the thermal load on the vacuum subcooler.

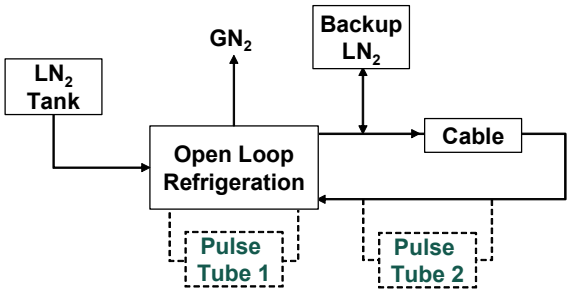

Fig. 1.28. Schematic of the LN cooling system for the triaxial HTS cable.

The cooling circuit begins with LN leaving the cooling system and being supplied to the first termination. The flow cools the termination and then flows down the cable former and annular space, thus cooling the cable. The nitrogen stream then cools the second termination and returns to the Praxair refrigeration system via a 120-m-long vacuum-insulated rigid pipe.

The 200-m-long triaxial HTS cable installed at the AEP Bixby substation underwent a series of rigorous tests prior to being energized. Figure 1.29 shows the completed termination and HTS cable (going underground) at the Bixby substation.

The critical current was above 5.5 kA for each phase, which was the maximum current that could be provided with the dc power supplies available. It was concluded that the operating current of 3000 A_{rms} was less than half the critical current, which is sufficient to maintain the peak current in an ac cycle below. Additional tests included a high-voltage VLF test at 0.1 Hz at 20 kV_{rms} and a line voltage soak at 13.2 kV_{rms} for 24 h prior to energizing. The cable has been in service at the substation since August 8, 2006, and has experienced phase currents of more than 2400 A_{rms}. Phase current and temperature data across the cable for a 24-h period (August 9, 2006) is shown in Fig. 1.30. There is a slight change in the cable outlet temperature as the load varies on the cable while the inlet temperature remains stable.

Fig. 1.29. Triaxial HTS cable and termination installed at the AEP Bixby substation.

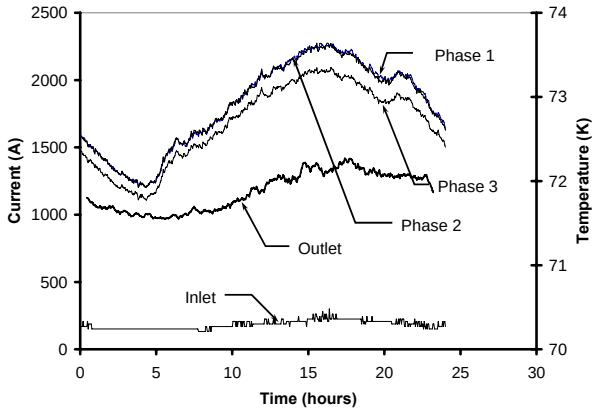

Fig. 1.30. Operation data taken from the triaxial HTS cable.

1.1.14 HTS Cable High Voltage Assessment

Work has been initiated on assessing the scale-up to higher voltages. This includes determination of the number of layers of dielectric, scaling up the stress cones for model cable testing, and the scaling up of solid insulation used in the terminations. The ORNL testing facilities permit ac withstand tests to 200 kV_{rms} and 800 kV impulse BIL.

1.1.15 Spliced Former Test of Phase 1 to Phase 2

A splice was made in the former of a section of the AEP cable. High-voltage tests were done to determine whether the splice affected the electrical insulation of phase 1 (P1) to phase 2 (P2). In summary, the P1 to P2 insulation passed the PD, ac withstand, and 10+/- BIL tests. The Phase 2 conductor and shields were stripped back in the usual way so that stress cones could be put on each end of the test piece with P2 as a ground. High-voltage connections were made to P1. On July 19, 2006,

following pump-out overnight in the cryostat, the system was filled with LN and was pressurized. After 4 h of stabilization at pressure, PD measurements were done. PD onset was 22.1 kV_{rms} at 30 to 40 pC. Extinction was 21.2 kV_{rms}. The voltage was increased to 38.8 kV_{rms} and held for 5 min; no breakdown occurred. The test constitutes the ac withstand. The PD level at that voltage was high, 2.5 to 2.6 nC, which is similar to the voltage in previous tests. The voltage was lowered, and the system was prepared for impulse testing.

Starting on positive polarity at 50 kV (1.2/50 μs), the voltage was increased in steps to 112 kV (peak value) where ten consecutive withstands were recorded. This test passes the + BIL part. Polarity was switched to negative, and impulses were made starting at 55 kV. Several "conditioning" withstands at lower voltage levels are required to reduce the effect of any space charge buildup from the previous test (polarity reversal effects). Several breakdowns/flashovers occurred below 110 kV on negative polarity such that it was not possible to get the ten consecutive withstands at 110 kV. The breakdowns or flashovers were suspected to be the same problem as before, where there was a discharge starting at the first step of the stress cone where it starts to rise (highest field region) and proceeding under the stress cone and working its way radially inward and down through the butt gaps. These types of discharges do not occur in the cable test region. A number of tests were tried at higher pressures, where, after more than 7 h of stabilization under pressure, it was possible to achieve ten consecutive positive and negative impulse withstands. The pressure was then lowered to the test pressure (6 bar), and ten negative impulses at 110.6 kV were withstood.

The cable was dissected, and the breakdowns/flashovers were verified to be under the stress cone and not in the cable insulation region. The breakdown starts at the highest electric field point where the ground semiconductor contacts the first step of the stress cone. There is also a longitudinal component of the electric field at this location. The discharge then runs under the first layer of the stress cone until it hits a butt gap in the cryoflex and then goes across the next cryoflex layer toward the end until it hits another butt gap. It proceeds radially inward until it punctures straight through. It is unknown whether the LN gets into the butt gaps and between the layers of the cryoflex insulation. If so, the time it takes for LN to fully impregnate the butt gaps under pressure would need to be determined. We will continue to look at this issue because it is important to resolve it, especially for progressing to higher voltages.

1.1.16 Stress Relief Material Tests in LN

A commercial stress relief tape was wrapped on a G-10 cylinder and was covered with standard commercial electrical tape to ensure that it stayed in place. The sample was immersed in LN, where it was allowed to stabilize, and was then removed. Significant cracking in both tapes occurred. The tests confirmed earlier similar tests on stress relief materials and emphasized that the materials are unsuitable for cryogenic conditions. Stress relief materials that will withstand LN temperatures would be very useful, especially for terminations.

1.2 Rockwell HTS Motor R&D Task CRADA

In August 2005 a cooperative research and development agreement (CRADA) was implemented between UT-Battelle (ORNL) and Reliance Electric Company (a unit of Rockwell Automation) to perform research related to commercial viability of industrial motors with HTS windings. Reliance Electric is conducting a Superconductivity Partnership with Industry (SPI) Project with focused research in eight areas related to their commercial viability. One of these R&D areas is the rotor coil quench protection system, and a CRADA task involves testing of the motor coils at ORNL.

1.2.1 1000 hp Motor Coils

1.2.1.1 Background

ORNL personnel in collaboration with Rockwell Automation's Advanced Motor Division, performed quench and stability testing on rotor coils rated at 1000 hp. The quench characteristics of two

of Rockwell's 200-hp-rated rotor coils were measured at the magnet test facility at ORNL. The 1000 hp motors consisted of Bi-2223 powder-in-tube (PIT) tape wound and potted in a racetrack-style winding. The Bi-2223 tape used to fabricate the 1000 hp motors was fabricated by American Superconductor Corp. (AMSC) and had dimensions of ~ 4.1 mm-wide and 0.31 mm thick. The HTS coils were previously tested in an open bath of LN at Rockwell Automation. The 77 K test results have been published elsewhere. The purpose of the HTS coil tests at ORNL was to investigate the quench characteristics of the HTS coils at lower temperatures (~ 25–45 K) and in a conduction-cooling environment. The quench data will be used for computer modeling to predict the quench behavior of future HTS rotor coils.

1.2.1.2 Experimental

To accommodate the heavy weight of the 1000 hp motor in the ORNL test cryostat, a specially designed mounting structure was jointly designed by ORNL and Rockwell personnel. The spring-supported mounting structure consisted of a two-piece split top flange mounted directly to both the AL-330 cryocooler and a large Al block that supports the HTS coil. The provided both structural support and acted as a thermal bus for conduction cooling of the HTS rotor coils. The spring supports were used to reduce the tensile load on the AL-330 cryocooler shaft caused by the hanging of the heavy HTS coil and the Al conduction block. When not supported by the spring tension, the total mass of both the Al thermal bus and the 1000 hp HTS coil was ~ 200 lb. With the spring supports in place, the total tensile load as seen by the AL-330 cryocooler shaft was < 5 lb. The remaining portion of the load was carried by the spring support structure, which mounted directly to the top plate of the cryostat.

Each of the two HTS rotor coils was instrumented with a pair of voltage taps across the terminals of the coils and six Cernox™ temperature sensors mounted at various locations along the vertical axis of the HTS coil. The entire vertical length of the rotor coil was wrapped with five layers of MLI to reduce the radiation heat load impinging on the coil. Temperature and voltage data were collected at the rate of one power-line-cycle, using a computer-controlled data acquisition system. Data were graphed and stored for off-line analysis.

The HTS rotor coils were lowered into the cryostat, sealed, and then initially evacuated to ~ 10^{-5} torr. LN was then introduced into the radiation-cooling shield to further reduce the radiation impinging on the HTS coil. To speed the cool down, a few cubic centimeters of He exchange gas was backfilled into the evacuated space to provide additional thermal conduction to the outside wall of the cryostat. The AL-330 cryocooler was then turned on to further speed cooling. Once the HTS coil had reached a temperature of ~ 100 K, the He exchange gas was evacuated, allowing only the cryocooler to reduce the temperature from ~ 100 K to ~ 25 K. Cooldown from room temperature to 25 K took approximately 48 h.

1.2.1.3 Quench Tests

Quench tests were performed on two 1000 hp rotor coils over the temperature range from 25 K to 45 K. Three types of tests were performed on the HTS coils: (a) transport dc critical current, (b) quench current characterization, and (c) loss of cryocooler. The first test performed on each of the two 1000 hp rotor coils upon cool down was the transport dc critical current test using the 1 μV/cm criteria. After the initial dc critical current tests, the quench current was measured by monitoring both the voltage and temperature vs time curve for several values of applied current. The quench current was defined as the value of current at which the HTS coil terminal voltage vs time became nonlinear with a positive curvature. Since in a conduction-cooled HTS coil operating under dc conditions, the quench current is determined by the competing factors of heating from the index loss (n-value) vs conduction cooling, it was important that each test run begin at the same initial starting temperature to accurately determine the quench current. This type of testing requires significant expenditure of time; it can often take hours for nonlinear conditions to appear across the HTS coil terminals. The final tests performed were the simulated loss of cryocooler. In these experiments, the HTS coils were ramped to various levels of applied current below known quench current values and held steady for several hours so that thermal equilibrium could be reached. Once thermal equilibrium had been reached for a given value of applied current (below the quench current), the cryocooler was then shut off so that there was no active cooling of

the HTS coil. Temperature vs time and voltage vs time measurements were recorded for a specified time, typically the time it took the HTS coils to increase their temperature by 5 K from their starting value. Data were recorded for subsequent analysis.

After the initial set of quench experiments were performed at ~ 25 K, the LN in the radiation shield of the test cryostat was removed and the temperature of the coil was allowed to rise to ~ 45 K. The series of quench tests was then repeated for the higher operational temperatures. Temperature-dependent characteristics of the quench current are important for more accurate computer simulation and prediction.

1.2.1.4 Results

Quench test results on the 1000 hp rotor coils were surprisingly consistent over the broad range of temperatures investigated. Results at 77 K and 25–45 K clearly indicate that in large HTS coils of this type fabricated with Bi-2223 tape, that a 1 μV/cm criterion is inadequate to characterize the operational current of these large-scale devices. Results also indicate that using a 1 μV/cm criterion would have led to damage to the HTS conductor. A more appropriate value of 0.1 μV/cm appears to be appropriate.

Another result of the quench tests clearly show the sharpness of the value of the quench current. Values just below the quench current (e.g., 1-2 A) would often take several hours before reaching final thermal equilibrium. Likewise, applied current values just above the quench current (1-2 A) typically would result in nonlinear voltage vs time behavior shortly after application. A goal of the project is to provide the HTS user more clear characteristics, which can be used to more accurately predict the quench values in large scale HTS coils.

1.2.2 200 hp Motor Coils

The quench characteristics of two of Rockwell's 200-hp-rated rotor coils were measured at the magnet test facility at ORNL (Fig. 1.31). The 200 hp coils consisted of older style Bi-2223 PIT tape wound and potted in a racetrack-style winding. The conductor, fabricated by AMSC, was composed of older style Bi-2223 tape with dimensions of 3 mm wide by 0.22 mm thick. HTS PIT tape with those dimensions is no longer commercially available. Two of the 200 hp motor coils were mounted in a vacuum cryostat and cooled via an Al-330 cryocooler to ~ 25–27 K for testing. The quench characteristics of the two 200 hp HTS coils were measured using two different test configurations: (a) individually energized and (b) both coils energized. Terminal voltage and temperature vs time measurements were also recorded for various values of applied current. Quench characteristics were determined for both test configurations. In addition, measurements of the temperature and terminal voltage vs time were collected under conditions simulating the loss of cryocooler to the system. Preliminary results showed strikingly similar characteristics to the earlier 1000 hp motor test results, also taken at ~ 25–27 K but fabricated from the newer 4.1-mm-wide HTS PIT tape fabricated by AMSC. Similar with the 1000 hp HTS motor coil quench tests, results clearly indicate that a more stringent electric-field criterion of 0.1 μV/cm is more appropriate for large HTS coil operation than the traditional 1 μV/cm criterion. With a 1 μV/cm criterion, all HTS coils tests experienced thermal runaway and an

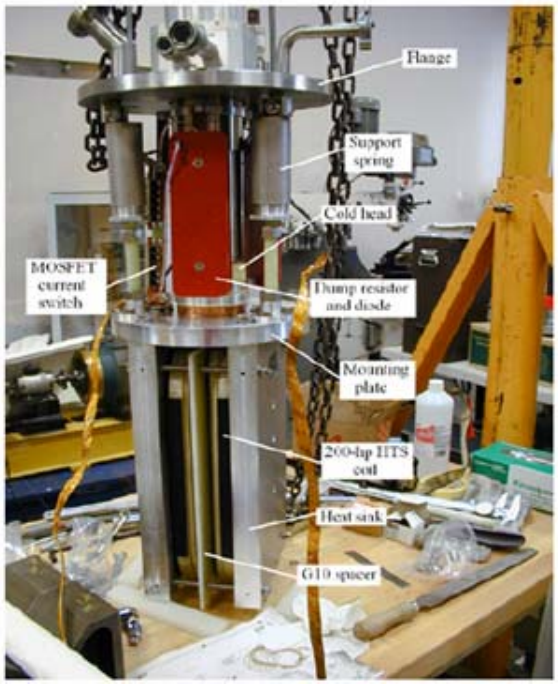

Fig. 1.31. Experimental test apparatus of 200 hp Rockwell motor. Note the two 200 hp coils mounted back-to-back.

eventual quench, which, if left unprotected, would result is catastrophic failure of the device. (The quench results were published in the proceedings of the Applied Superconductivity Conference, September 2006, Seattle, Washington.) Testing on the two remaining 200 hp Rockwell motors was concluded in February 2006. Direct current critical current and stability tests were performed at ~ 25–30 K.

Stability measurements made on the 200 hp coils were consistent with the 1000 hp coils (reported last quarter). Results clearly demonstrate that for conduction-cooled coils, there is a need for a more stringent operating criterion than the standard 1 uV/cm (see Fig. 1.32). Using the standard 1 uV/cm criterion, the resulting critical current of the 200 hp coils would be at about 200 mV, whereas the 200 hp coil is clearly beginning a thermal runaway at voltages less than ~ 10-12 mV. If the standard 1 uV/cm criterion were used in either the 200 or 1000 hp motor conduction-cooled test, the HTS coils would have certainly quenched. This is an important result and will be promulgated to the entire HTS community.

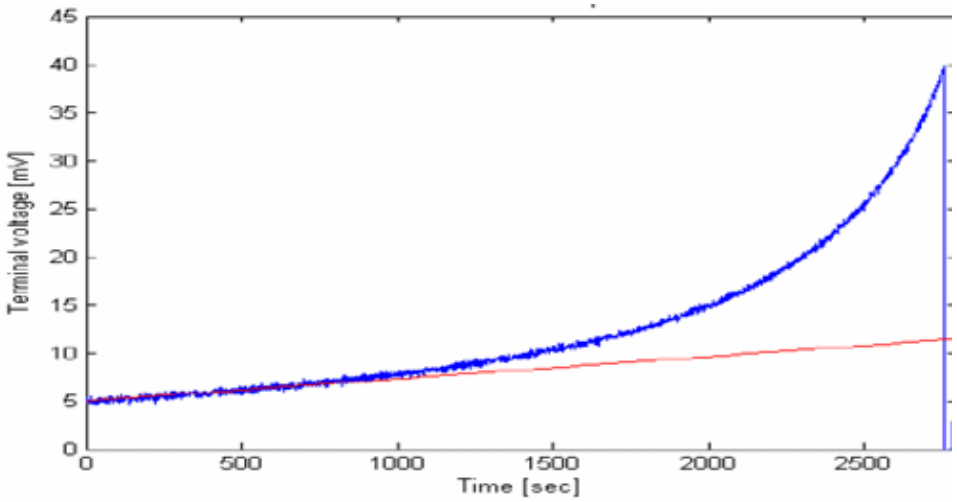

Fig. 1.32. Coil terminal voltage vs time for one of the Rockwell 200-hp motors. The terminal voltage deviation from linearity is observed at ~ 1000 s after reaching full field.

Rockwell and ORNL staff reviewed and analyzed the data from the quench and stability experiments conducted in the previous quarter on the cryocooled 200 hp and 1000 hp HTS motor coils.

Rockwell and ORNL presented a project overview at the 2006 DOE Peer Review in July. Steve Umans (Rockwell) presented an invited paper at the Applied Superconductivity Conference on the quench and stability experiments conducted in FY 2006 on the cryocooled 200 hp and 1000 hp HTS motor coils.

1.3 Waukesha Electric Systems HTS Transformer SPI

S.W. Schwenterly, A. E. Ellis, D. R. James, and I. Sauers

Work continued under the no-cost extension of the existing Pilot Center Agreement with Waukesha Electric Systems (WES) on HTS transformer development. Under the agreement, both parties will continue on interim transformer development activities using their own funds while an extension of the current HTS transformer SPI is being negotiated. A formal proposal for the extension was completed and was submitted to DOE in February. No decision on the proposal has yet been received from DOE-HQ.

S.W. Schwenterly visited WES for 3 days during October. During this visit he and E. F. Pleva carefully reviewed and documented WES's conventional transformer-manufacturing processes to determine whether their techniques could be modified for use with HTS conductors; they also continued to review HTS transformer conceptual designs. A transformer design spreadsheet developed at ORNL was benchmarked against WES's in-house design tools. The two sources yielded very similar results for a given transformer voltage and power rating. Figure 1.33 shows a rendering of the coil in its fiberglass dewar mounted on the 1-MVA core.

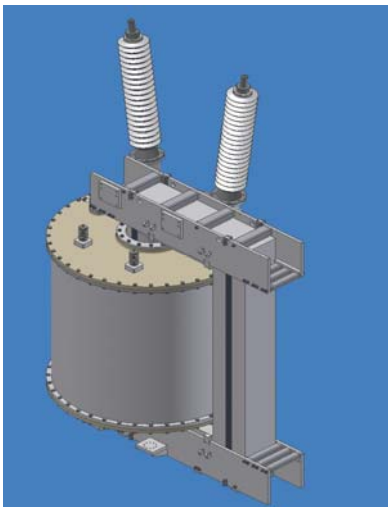

Fig. 1.33. 1-MVA core with 138-kV HTS test coil and fiberglass dewar installed.

E. F. Pleva visited ORNL for four days in December for work on a new proposal to DOE for a 2-year interim project to carry out further high-voltage dielectric studies and conceptual designs. The goal is to provide a foundation for a Phase III SPI on development of a 138-kV HTS transformer. T. Golner, a representative from WES attended the DOE Wire Workshop in January 2006 to present conductor requirements for commercial HTS transformers.

E. F. Pleva visited ORNL in February to work on completion of the interim proposal and a mechanical layout of a small test transformer. The latter activity continued through February and was completed during a visit by S.W. Schwenterly to WES. Further discussions on detailed design of the windings were held during a visit to ORNL by E. F. Pleva and WES transformer design expert R. Del Vecchio. An attractive option for the test transformer is to use the existing core from the original 1-MVA transformer with a new fiberglass dewar and HTS coils. To limit the cost for second-generation HTS tape, only the low-voltage winding would be superconducting, with only two or three tapes in parallel. The high-voltage winding would be made with normal dummy conductor that would simulate the second-generation tape, and would run open-circuit. This would validate the high-voltage insulation concept without the need for thousands of turns of HTS tape to reach 138 kV. To test the low-voltage HTS winding to its full current, a short-circuited tertiary winding at room temperature could be added. Alternatively, the first part of the high-voltage winding could also be made superconducting with a provision to short-circuit it.

E. F. Pleva visited ORNL in May to work on completion of the interim proposal and on mechanical layout of the small test transformer. An interim proposal for a one-year extension of the project was completed and submitted to DOE in May. It would cover some of the dielectric testing and design work but would not allow for construction of any hardware. WES and ORNL intend to submit another new proposal for further follow-on funding in the upcoming new solicitation.

1.3.1 General Design Activities

In August, S.W. Schwenterly and E. F. Pleva visited CK Composites in Mount Pleasant, Pennsylvania, to present drawings for the fiberglass dewar. CK thought that the design was feasible and indicated that they were interested in bidding on the job. Other cryogenic equipment manufacturers were contacted about the possibility of building this dewar in stainless steel with an insulating electrical break. S.W. Schwenterly visited WES later in August for discussions on ac losses, dielectric design, and details of the winding pack, and E. F. Pleva visited ORNL in September for continuation of those activities. Updates to the ORNL transformer design spreadsheets continued in order to add new conceptual design information.

1.3.2 Bushing Core Acquisition and Testing

In early February, E. F. Pleva negotiated with Trench, UK, to obtain a 126-kV resin/paper bushing core (a factory-reject obtained at no cost other than shipping). The bushing core was shipped to ORNL for thermal tests with the lower end immersed in LN to determine its heat load and survival at 77 K. The bushing had a PD of only 22 pC at 230 kV and may be usable for future high-voltage tests. If it survives

several cooldown cycles without any increased PD, a flange, center conductor, and terminals will be installed on it and it will be used for high voltage tests in the large 30-in. LN dewar that was purchased last year.

The dewar was moved into the high-voltage laboratory, and the bushing core is being prepared for testing. Figure 1.34 shows the test set up which includes a custom stand provided by WES. The core was then subjected to several cooldown cycles in LN without any mechanical damage or evidence of increased PD. The PD was 10 - 12 pC at 145 kV_{rms} in LN, showing no change despite some ice buildup above the open bath. The ice is not expected to occur in a closed high-voltage cryostat. A flange, center conductor, and terminals will now be installed on it, and it will be used for high-voltage tests in the large dewar. The setup will allow high-voltage testing of dielectric materials (including LN and G1) and small prototype assemblies.

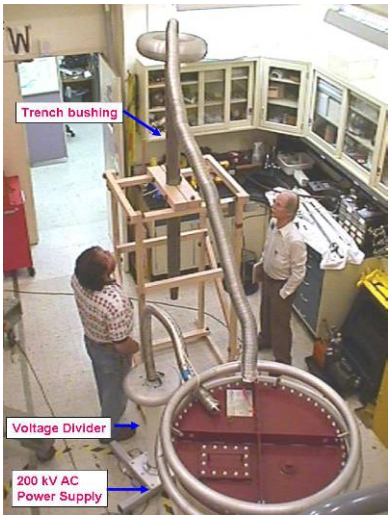

Fig. 1.34. 138-kV class bushing from Trench and WES-supplied test stand.

1.3.3 Cryostat Preparation

Progress is being made on completing the 30–in.-diam cryostat top plate assembly. Figures 1.35 and 1.36 show, respectively, a side and top view of the top plate and high-voltage bushing. Work is being completed on installing the LN level sensors, temperature sensors, LN fill system and electrode supports. The system should be operational in about 1 month.

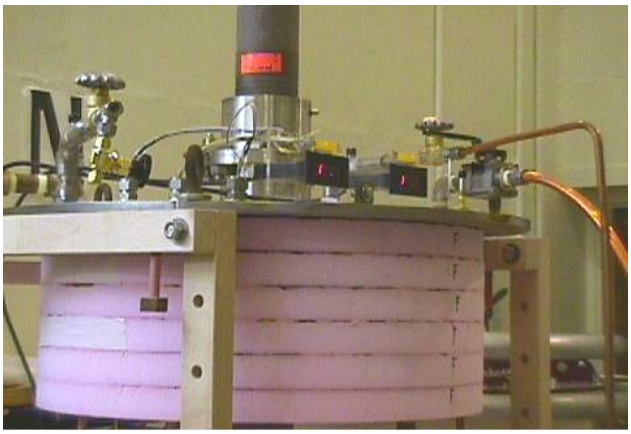

Fig. 1.35. Cryostat top plate and foam insulation.

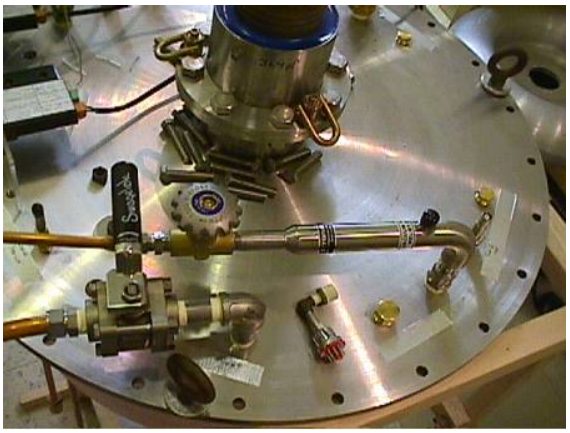

Fig. 1.36. Top view of cryostat top plate.

1.4 General Electric Co. HTS Generator SPI

R. C. Duckworth, A. R. Ellis, M. J. Gouge, D. R. James, I. Sauers and S. W. Schwenterly

GE informed ORNL late in the quarter that they had reached an agreement with DOE to discontinue work on this 100 MVA generator SPI project due to economic scaling issues with present superconducting tape and cryogenic technology.

GE made a public announcement in January 2006 that they had reached an agreement with DOE to discontinue work on this 100 MVA generator SPI project due to economic scaling issues with present superconducting tape and cryogenic technology. GE stated that they believe the economic breakpoint for an HTS base-load utility generator to be above 500 MVA.

1.5 Second-Generation Conductor Applications

R. C. Duckworth, J. A. Demko, C. M. Rey

1.5.1 Measurement of Losses due to ac Fields for Laminated and Nonlaminated Second-Generation Yttrium Barium Copper Oxide (YBCO) Conductors

Two separate YBCO conductors were examined to determine the influence of stabilization on ac loss as a function of perpendicular ac field. The two YBCO conductors were a nonlaminated 4.1-mm-wide YBCO conductor with a critical current of 83 A at 77 K and a copper-laminated 4.4-mm-wide YBCO conductor with a critical current of 74 A at 77 K. The copper laminated YBCO conductor consisted of a 4.1-mm-wide YBCO conductor soldered between two 50 μm, 4.4-mm-wide pieces of copper. It was assumed that the solder thickness was approximately 12 μm on each side.

The ac field losses were measured in a solenoid with the capability of producing a central field of 120 mT. This solenoid has inside diameter of 5 in. (12.5 cm) and a total height of 6 in. (15 cm). To reduce the variation in field across the sample, only short samples with lengths less than 5 cm were measured at the center of the magnet. Each sample was cut to length, and a heater and thermocouple were mounted on the side of the tape nearest to the YBCO to minimize any error that could occur with heat transfer through the Ni-5at%W substrate and associated buffer layers (more of an issue for the nonlaminated YBCO sample). Each sample was then completely enclosed within two pieces of styrofoam with Apiezon grease to isolate it from the LN and to improve the experiment sensitivity. Once the sample was placed in the LN bath, the heater served as a source of known heat load and the thermocouple was calibrated as a function of heat load. Then an ac field was applied to a sample, and the thermocouple response was used to determine the total ac loss.

Figure 1.37 shows the ac losses as a function of peak perpendicular field for each sample. Each sample more or less had a linear dependence with respect to field, consistent with the functional dependence of the hysteretic superconducting loss that is predicted by Brandt model for a superconducting film with a constant critical current and at high fields.

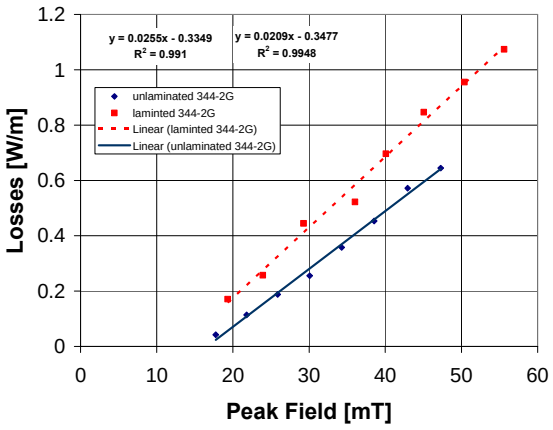

Fig. 1.37. Alternating current losses as a function of peak perpendicular ac field for a nonlaminated and laminated YBCO-coated conductor. The critical current density for the nonlaminated sample is 2.0 MA/cm^2 and for the laminated sample is 1.7 MA/cm^2.

High fields refer to those greater than $H_d = J_c d_{ybco}/\pi$. Since the nonlaminated tape has a higher critical current and the tape widths are the same, the slope of this curve should be higher, but as is shown in Fig. 1.37, this is not the case. According to the Brandt model at 50 mT, the nonlaminated tape sample should have a greater hysteretic loss of 1.17 W/m, while the laminated sample should be 1.04 W/m.

The difference between the two tapes is attributed to the possible nonuniformity of the critical current density because of two reasons. First, when the transport ac losses were measured in the two samples previously, the laminated tape was greater than the Norris elliptical model, while the nonlaminated tape was closer to the Norris thin-strip model at higher I_{peak}/I_c. Second, when the other ac loss contributions are taken into account, they do not add up to the observed difference of 0.25 W/m at 50 mT. At that field, the estimated eddy current loss for the laminated sample is 45 mW/m whereas the nonlaminated tape has an eddy current loss of 2.5 mW/m from the silver cap layer. The ferromagnetic contribution is not an issue because each tape has a 4.1-mm-wide Ni-5at%W substrate. The only possibility for the ferromagnetic term between the two samples would be if the lamination process caused some additional deformation of the substrate and the loss increased, as was observed by Ijaduola [2]. For

a vacuum-cast, annealed-cut sample, the maximum ferromagnetic loss was 275 erg/g-cycle in a parallel applied magnetic field, which translates to a value of 52 mW/m at 60 Hz. If we take into account the field direction and assume 4 half-cycles of deformation, the difference between the laminated and nonlaminated sample is at most 30 mW/m. To confirm this, measurements can be carried out in a superconductivity quantum interference device (SQUID) magnetometer to see whether the FM loss increased after the lamination occurred. With both the eddy current and ferromagnetic loss contribution, the total additional loss between the laminated and nonlaminated tape is approximately 0.08 W/m.

1.5.2 Low ac Loss Multifilament Inkjet YBCO Conductors

With narrow-width filaments, the hysteretic ac loss due to applied ac fields can be reduced significantly in YBCO-coated conductors. While there have been methods to physically alter the YBCO through cutting or laser scribing, inkjet technology allows for YBCO filaments to be created without any waste of solution components and offers a different option for patterning. Starting with an AMSC-fully buffered substrate, a modified trifluoroacetate (TFA) approach was used to create the ink that was deposited through the inkjet system shown in Fig. 1.38. The "ink" consists of a mixture of yttrium and barium TFAs and nonfluorine copper salts with methanol to prepare a solution suitable for printing through the 25-μm-diam stationary inkjet nozzle. The tape is placed on a 30-cm-long translation table, which is heated slightly to aid in the drying of the ink upon contact with the substrate. Through variations of the droplet actuation and pressure in the solution, the printed filament width can be varied between 50 and 150 μm. After the ink has been placed on the buffered substrate, the film is baked to decompose the methanol solution from the TFA mixture and is converted to the final stoichiometric YBCO form. The average thickness of the YBCO filaments is 0.9 μm with preliminary critical current densities of 0.3–1.3 MA/cm^2 at 77 K.

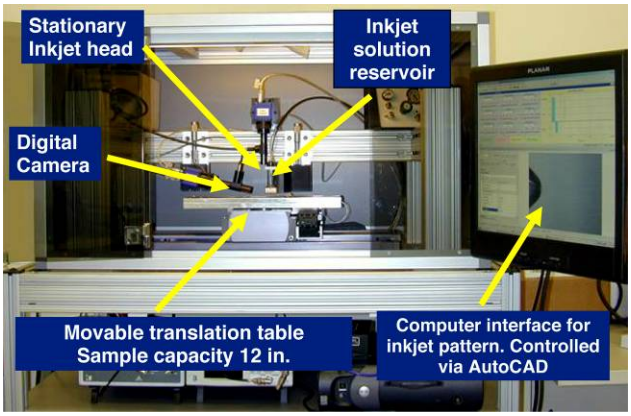

Fig. 1.38. Inkjet deposition device at ORNL.

Figure 1.39 shows a converted YBCO sample that has a filament width of 90 μm and a spacing of 150 μm. The overall dimensions of the sample are 6.5 × 1 cm. This sample was coated with aluminum oxide paint before it was instrumented with a thermometer and heater, and was insulated with two Styrofoam blocks. The ac losses were determined thermally by comparing the response of a thermocouple from a known heat input to the response when the ac field was applied for the same duration. The sample was placed in the center of a 100 mT solenoid that was submerged in LN, and the ac losses were measured in a perpendicular field orientation as a function of peak field and field frequency with a 6-kVA variable-frequency Behlman power supply. The ac losses as a function of field and frequency are shown in Fig. 1.40.

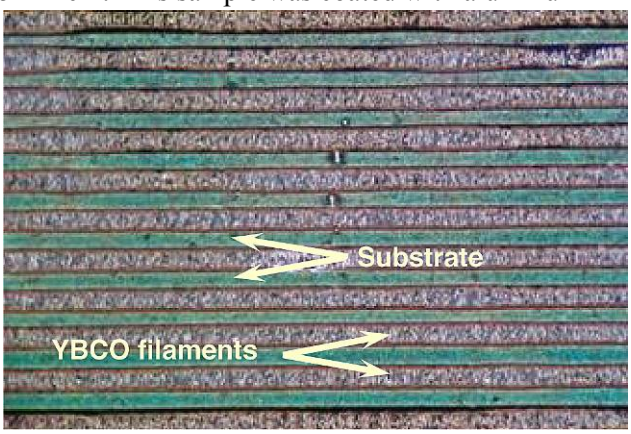

Fig. 1.39. Converted YBCO filaments with a filament width of 90 μm and a spacing of 150 μm.

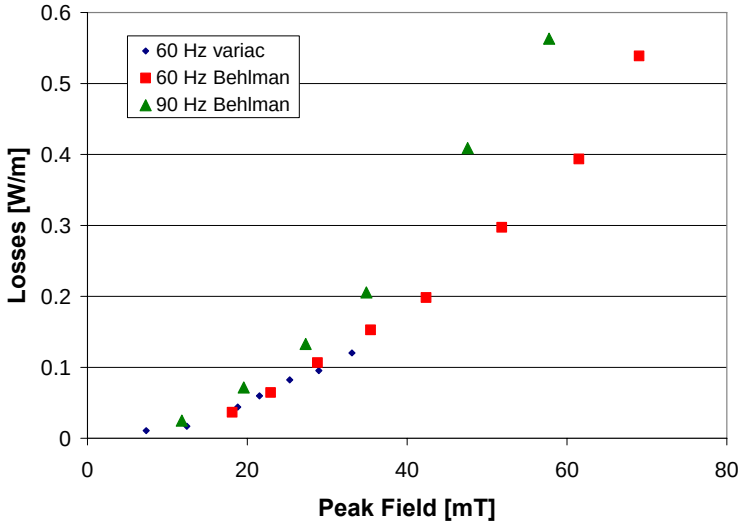

Fig. 1.40. Alternating current losses at 77 K for the multifilament inkjet conductor as a function of peak applied perpendicular magnetic field and field frequency.

The 60-Hz losses that were generated with a variable transformer were compared with those from the Behlman to determine the extent to which noise from the ac Behlman source was generating additional losses. There was no observable difference over similar applied fields. The total losses in this sample did not demonstrate a linear dependence on applied field as is typical of hysteretic losses from the superconductor. Dividing the losses by the frequency and plotting on a log-log plot as shown in Fig. 1.41, a quadratic dependence with respect to applied field was observed. While filament-coupling losses are proportional to the square of the applied field, coupling losses typically take the following form:

$$Q_{coupling}\left[\frac{J}{cycle-m}\right]=\frac{1}{4\rho_{eff}}f\left[L^2\left(\mu_o H\right)^2\right]$$

with the losses proportional to the frequency. Additional measurements on different filament widths and filament spacings are needed and will be conducted to determine the nature of this initial discrepancy. Alternating-current losses are going to be measured in a series of laser-patterned YBCO samples with similar filament patterns to determine whether the observed ac losses are affected by the substrate or by the manner in which the filaments are created.

1.5.3 Cryocooled Characterization of YBCO Tapes in Coil Geometries

To better understand how ac losses translate from single tapes to coils in second-generation YBCO tapes, an experimental test setup and method has been developed to examine the ac losses in small coils as a function of current, temperature, and geometry. Figure 1.42 shows the radial build for the first coils tested and relative positions of the instrumentation.

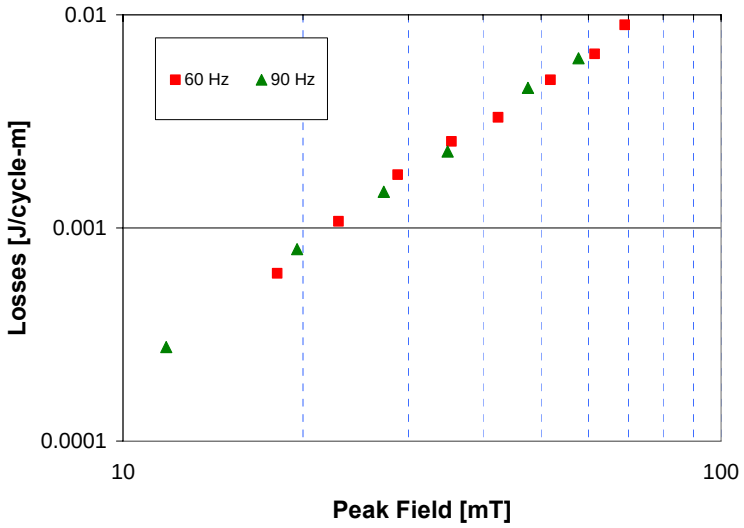

Fig. 1.41. Rationalized ac losses with respect to frequency at 77 K for the multifilament inkjet conductor as a function of peak applied perpendicular magnetic field.

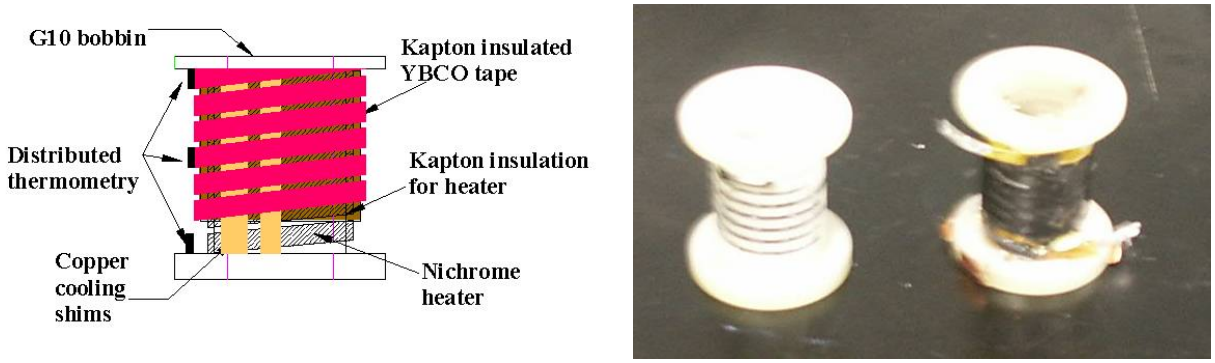

Fig. 1.42. Radial build for ac loss test setup for YBCO coils (left) and single-layer YBCO tape winding from bobbin to final fabrication (right).

On a G10 bobbin with a diameter of 31.75 mm, nichrome tape, which will function as a heater, is wrapped in a single layer and insulated with Kapton® tape. The nichrome tape is then attached through the G10 bobbin to allow for current and voltage lead connections without interfering with the profile YBCO tape and its current leads. After a thin layer of Kapton® is placed on top of the heater, copper strips that run down the axis of the bobbin are anchored with Apiezon® grease above the heater to achieve uniform coil temperature and to provide some measure of cooling as heat is applied to the coil. Then, Kapton®-insulated YBCO tape is wound on the bobbin, and instrumentation is added to the coil before the entire bobbin is epoxy-potted as shown in Fig. 1.42.

The coil is anchored to a Cryomech GB37 two-stage cryocooler, which provides a conduction-cooled interface with temperatures between 30 and 70 K. After the coil reaches equilibrium and the coil critical current is measured at the equilibrium temperature, the heater is energized at intervals of 5 s and the response of the thermometry to this known heat input is measured. Then an ac current is applied, and the change in temperature is used to determine the ac loss of the coil. A series of thermocouples, which were anchored to the second stage of the cryocooler to avoid drift, are placed along the coil to examine the ac loss distribution of the coil.

Figure 1.43 shows the total ac loss as a function of ratio of peak current to critical current at 60 K for a single-layer coil made with YBCO tape from AMSC. The critical current at 60 K was 130 A. The YBCO tape is designated 344-2G, which has a width of 4.4 mm, a thickness of 0.2 mm, and 50 μm of laminated copper stabilization. The inner diameter of the YBCO coil is 34.9 mm and consists of nine turns over a coil height of 44.4 mm. When compared to the Norris elliptical model for a single tape with a critical current of 130 A, the measured ac loss is higher. For a peak current ratio of 1, the maximum perpendicular field at the end turn is 17 mT and the peak parallel field at the middle of the coil is 25 mT. Based on these values, the ac loss that is generated by the ac field is considerably lower than the difference between data and the elliptical single tape model. The eddy current loss for the field that is generated at a peak current ratio of 1 is not significant.

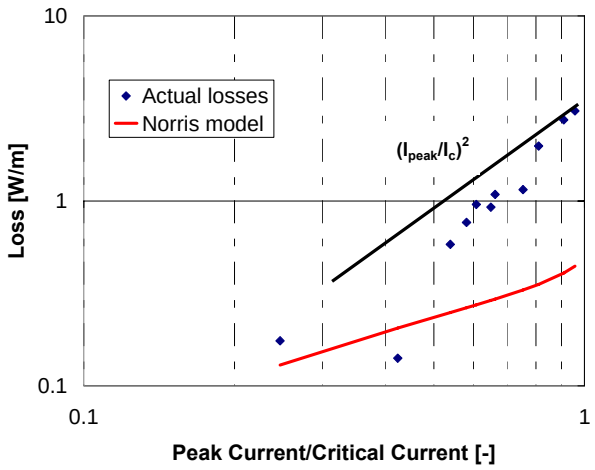

Fig. 1.43. Alternating current loss in single-layer YBCO coil at 60 K as a function of ratio of peak ac current to the coil critical current.

The deviation is likely caused from damage that was done during winding. Critical current was measured in the top half and bottom half of the coil, only the top half of coil showed a superconducting transition. This was verified by measuring the critical current as a function of temperature and at 77 K the critical current was 8 A in the top half of the coil. The distributed thermometry indicated that heating was only occurring in the top half of the coil. With a localized defect or area of low critical current, the difference can be explained by simple resistive heating of the stabilizer as the peak current ratio approaches one. Additional coils will be examined to determine the contribution of the stabilization to the ac loss as the number turns and the current uniformity of the coil is improved.

1.5.4 YBCO Coil Testing

Testing of the second-generation YBCO coil has continued. Thermal cycling tests continued to show slight degradations in critical current performance for each successive thermal cycle to 77 K, up to eight thermal cycles, the maximum number to date. An approximate 0.5 A/thermal cycle decrease in critical current has been observed during thermal cycle measurements, which had an original starting critical current value of 31 A at 77 K.

HTS coil stability tests at have also been performed at 77 K. Interestingly, results were quite similar to stability measurements performed on much larger Bi-2223 rotor coils fabricated by Rockwell. Results for the second-generation YBCO coil showed that slight deviations from quench currents (< 0.5 A), result in an immediate thermal runaway. Similar to the Bi-2223 coils, the quench current is different from (and always lower than) the critical current based solely upon the 1 uV/cm criterion. In addition, thermal runaway occurs on a much shorter time scale than in previous Bi-2223–based coils. This difference in time scale can be attributed to the significantly higher n-values in YBCO conductors. Plans include stability measurements at 30 K in a conduction-cooled environment.

1.5.5 Conductor Engineering: Low-Loss Splices

Design work on a splice-resistance test fixture started in February 2006. The final fabricated part was delivered on March 15. The test apparatus is designed to measure the splice resistance of up to eight splices over the temperature range from 77 K to ~ 30 K and in a background magnetic field from 0 to 6 T.

1.5.6 Stability of a Small YBCO Coil in a Cryocooled Environment

The conductor performance of YBCO is projected to put operation into the LN range (64–77 K) within the next few years; however, applications such as transformers and motors also rely on cryocoolers to provide either helium gas cooling or conduction cooling at temperatures between 30 and 40 K. To better understand the role of stability and the quench dynamics of a YBCO conductor in a cryocooled environment, a 0.3-T YBCO coil was mounted to an AL 330 cryocooler (Fig. 1.44). This coil consists of three sets of double pancakes and was made from 120 m of 4.4-mm-wide YBCO with copper stabilizer (344-2G) that was produced by AMSC in May 2005. The critical currents of this coil were 25 A at 77 K and ~100 A at 30 K.

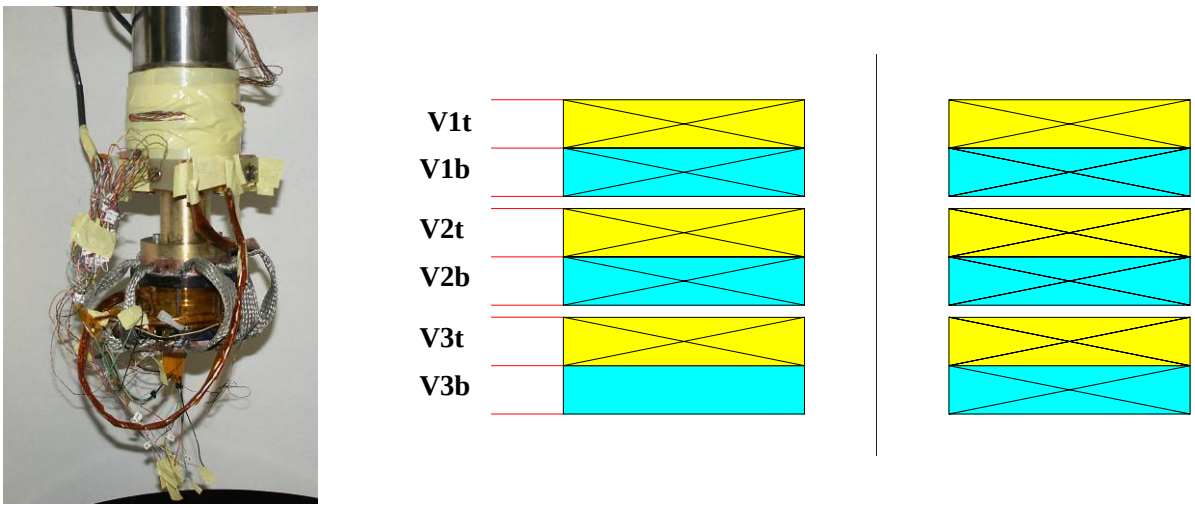

Fig. 1.44. Cryocooled mounting of YBCO coil to AL 330 cryocooler (left) and the distribution of the voltage taps within the YBCO coil (right).

This coil was cooled down to 36 K, and 40 K and a constant current was applied to the coil. The voltages were tracked as a function of time throughout the coil to determine where heating was occurring and to identify when a quench had occurred. Figure 1.44 also shows the distribution of voltage taps throughout the coil. Figure 1.45 shows the sensitivity of the quench dynamics with respect to operating current at 40 K. For the cases where the voltages went nonlinear, it only took seconds for the rate of voltage rise to change dramatically. For both temperatures, it was the top half of the first double pancake (V1t) that contributed to the runaway in voltage. Given that the voltages V1t and V3b were about the same, this indicates that the heating of the current leads was the reason for the instability.

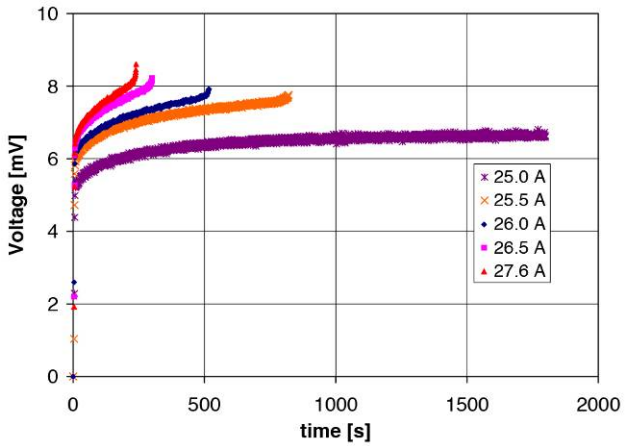

Fig. 1.45. End-to-end voltage at different constant currents for the YBCO coil at 40 K. The quench current was between 25.0 and 25.5 A

Table 1.6 summarizes the quench currents and critical current as a function of temperature. It shows that the LN has a big impact on the ability to remove the heat from the current leads and allows for a high quench current. While the current leads are an issue to be addressed, voltages across

Table 1.6. Summary of critical currents and quench currents as a function of temperature for the YBCO coil

Temperature, K	Critical current, A	Quench current, A	Cooling conductions
77	25	25.8	Liquid nitrogen
40		25.0	Cryocooled
36		32.0	Cryocooled
30	100		Cryocooled

splices within the pancake were constant at 36 K and 40 K and suggest that the coil quench current could be higher.

1.5.7 Thermal Runaway for SuperPower Cu-Stabilized YBCO Tapes

A fundamental question in the stability and ac loss of YBCO tapes is the amount of copper required to effectively stabilize the tape. While work has shown how adjacent copper can improve the tolerance of YBCO tapes to overcurrent pulses and changes in the system operating current, its functional dependence has not been examined on an experimental basis. A series of tapes were provided from SuperPower, Inc. as part of the SuperPower/ORNL CRADA with nominal critical currents between 64 and 73 A and with different levels of copper-surround stabilizer: 20 μm (40 μm total) and 38 μm (76 μm total). Samples were mounted onto a G10 block and were instrumented with a series of voltage taps (Fig. 1.46).

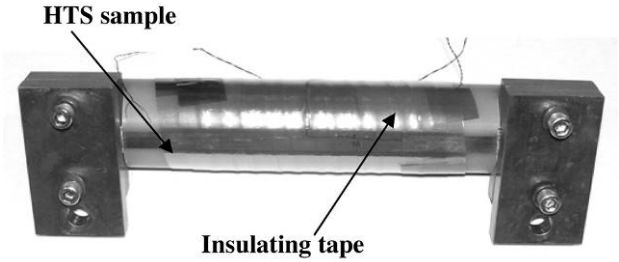

Fig. 1.46. Test setup for measurement of fault current limitation of Cu-surround stabilized YBCO tapes that were provided by SuperPower.

The sample was then insulated with several layers of dielectric tape and immersed in LN. After the sample critical currents were measured, a constant current was applied and the voltage was monitored to observe when runaway occurs. Thermal runaway is defined as the moment when the voltage as a function of time starts to go nonlinear. Figure 1.47 shows a set of different currents for a sample with 20 μm of surround copper stabilizer, which show that small changes in current cause the sample to run away sooner.

For the samples that were tested, the critical currents were 64 A for the unstabilized YBCO tape, 68.3 A for the YBCO tape with 40 μm of surround stabilizer, and 72.8 A for the sample with 20 μm of surround stabilizer. To better understand the differences between the observed thermal runaways, the times to thermal runaway were plotted as a function of the ratio of applied current to critical current (I/I_c) (Fig. 1.48). As expected, the sample with 38 μm of stabilizer could be operated at higher fractions of critical current than the other samples. However, the sample with 20 μm of surround stabilizer was closer to the fraction of critical current for the 38 μm surround-stabilized sample than the bare unstabilized YBCO tested. This is expected since the normal state resistance of tapes at 77 K decreases an order of magnitude when 20 μm of copper surround-stabilizer is added (0.13 Ω/m to 0.011 Ω/m) and the resistance only goes down by a factor of 2 when the surround stabilizer is increased from 20 μm to 38 μm (0.011 Ω/m to 0.005 Ω/m).

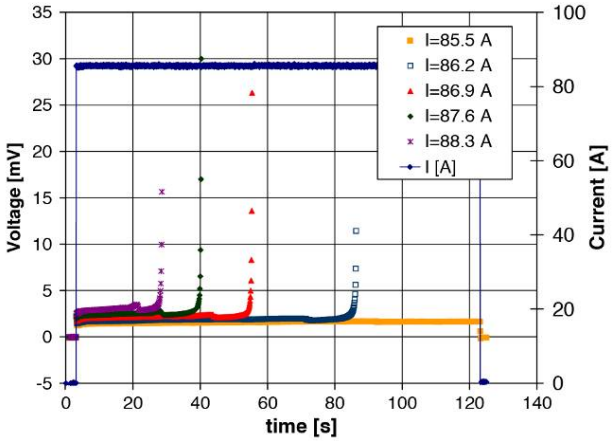

Fig. 1.47. Example of observed thermal runaway at 77 K for a SuperPower tape with 20 μm of surround copper stabilizer and a critical current of 72.8 A at 77 K.

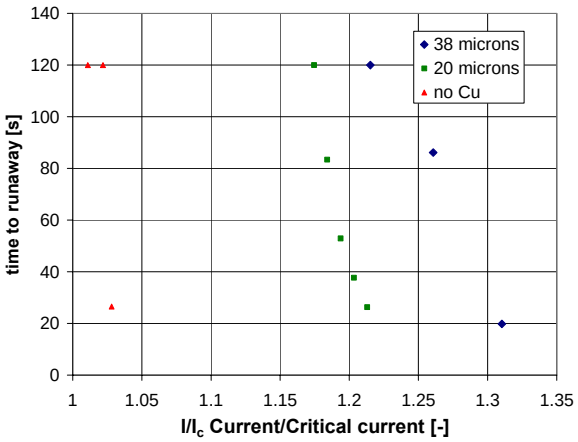

Fig 1.48. Time to runaway as a function of applied current to critical current for different thicknesses of copper stabilizer.

1.5.8 Stability Limits in SuperPower Cu-Surround Stabilized YBCO Tapes

To characterize the stability of an HTS with a specified tape geometry, two operation modes are often examined: constant currents and fault currents. A series of experiments were carried out to determine the effect of copper stabilization in Cu-surround stabilized YBCO tapes that were provided by SuperPower. With the expectation of using YBCO in HTS applications due to the requirements listed in the Superconducting Power Equipment solicitation in FY 2007, the understanding of the role of copper stabilization will improve the optimization of the YBCO in these applications. With respect to the two operation modes, constant current operation is a quench mode that is most often observed in superconducting rotor coils. The second operation mode is short-duration fault currents, which occur in applications such as superconducting cables and transformers. This fault typically consists of a short-duration (< 1 s) overcurrent, which is much greater than the device critical current. The results for the second operation mode, fault currents, will be reported here. Each sample was placed onto a G10 former and was isolated from the atmospheric LN bath using several layers of dielectric tape, as shown in Fig. 1.46. A set of voltage taps at intervals of 1.5 cm were placed to monitor the voltages across the sample width and quantify the uniformity of the sample critical current along its length, which in this case was 25 cm.

To test the ultimate limits of the YBCO tape as a function of Cu-surround stabilizer thickness, a series of separate overcurrent pulses were applied until degradation in the critical current of the sample occurred. The 0.25 s overcurrent pulses were followed by an operating current (< 10% of the critical current) for 30 s to monitor the sample resistance during the recovery of the current pulse without additional heating to the sample. Figure 1.49 shows an example of the current waveform for a sample with 38 μm of Cu-surround stabilizer and the resultant degradation in the tape performance upon application of the maximum current pulse is illustrated in Fig. 1.50.

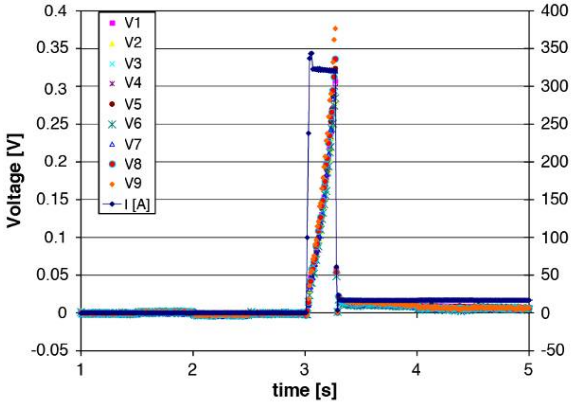

Fig. 1.49. Typical voltage response of a 4-mm-wide YBCO tape with 38 μm of Cu-surround stabilizer.

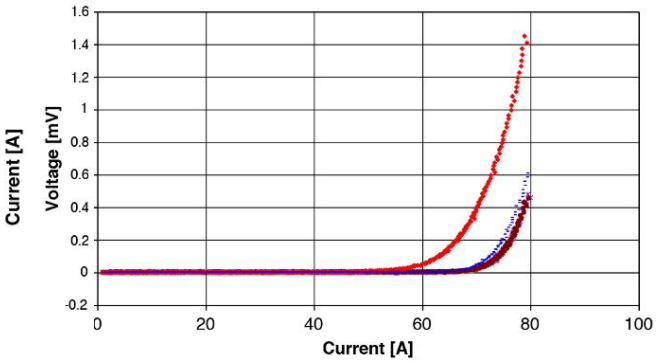

Fig. 1.50. Degradation of critical current in a Cu-surround stabilized 4-mm-wide YBCO tape with 38 μm of copper surround stabilizer.

Table 1.7 summarizes the overcurrent limits as a function of current pulse and Cu-surround stabilizer thickness. In addition, the normal state resistance at room temperature and critical current of each sample at 77 K is given. From these data, the amount of current that the sample can tolerate appears to be a function of the normal resistance of the tape. If the ratio of the overcurrent pulse to the critical current is multiplied by the resistance of the tape at room temperature, the difference between the product for the 20 μm of Cu-surround stabilizer and 38 μm of Cu-surround stabilizer is small. Given the short duration of pulse and the fact that entire tape was taken well above room temperature, the resistance of the tape becomes the limiting factor instead of the thermal conductivity of the tape, which was seen in previous measurements for long-duration, constant dc currents.

Table 1.7. Maximum overcurrent as a function of three different YBCO tapes with three different amounts of Cu-surround stabilizer

Copper surround thickness (μm)	I_c (A)	I_{pulse} (A)	I_{pulse}/I_c (-)	R/l (300 K) (Ω/m)	$C = (R/l)\ (I_{pulse}/I_c)$
0	64	76.7	1.20		
20	72	262.3	3.64	0.094	0.0034
38	68	432	6.35	0.055	0.0035

1.5.9 Normal Zone Formation in SuperPower Cu-Surround Stabilized YBCO Tapes

To better understand normal zone formation, it is necessary to look at the voltages along the sample length in closer detail. For each sample characterized, the voltages were recorded at intervals of 1.5 cm to 2.0 cm during the constant current pulses and the two-stage overcurrent pulses. An example of the normal zone growth in a sample with a constant operating current above the critical current is given in Fig. 1.51. For this sample the end-to-end critical current was 72.8 A with standard deviation of 1.2 A (2%) and a minimum critical current of 72 A and a maximum critical current of 77 A. All of the tape is generating heat, but it takes a finite amount of time for the heat to lead to thermal runaway. Even with uniform generation only four sections out of the nine sections of the conductor show a significant change in voltage before the power supply is shut down. This would seem to indicate that the normal zone growth is still rather slow.

This slow normal zone growth was confirmed in a measurement of a sample with 38 μm of Cu-surround stabilizer. Normal zones were induced with a short duration overcurrent pulse and were monitored with an operating current at a fraction of the critical current. The magnitudes of the overcurrent

and operating current were adjusted until propagation occurred. This was possible in the YBCO tape with 38 μm of surround Cu-stabilizer due to a nonuniform critical current, 64 A end-to-end critical current with a standard deviation of 5.1 A (7%) and a minimum critical current of 62 A and a maximum critical current of 73 A. Figure 1.52 shows an example of normal zone propagation where the propagation speeds were between 0.57 cm/s to 0.7 cm/s.

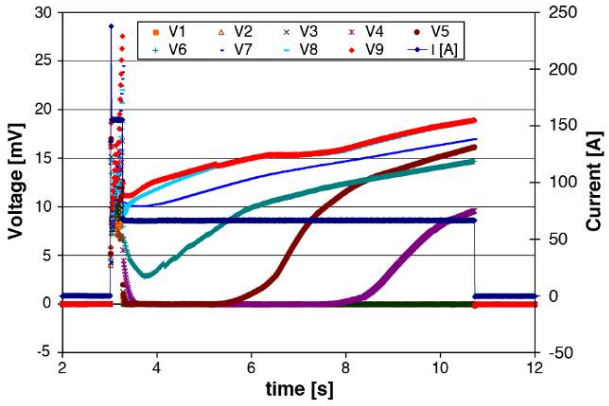

Fig. 1.51. Normal zone propagation at 77 K for a 4.4-mm YBCO tape with 38 μm of surround copper stabilizer when a 0.25-s 155.2-A overcurrent pulse is applied and followed by an operating current of 66.6 A. This is slightly less than the tape critical current at 77 K of 68 A.

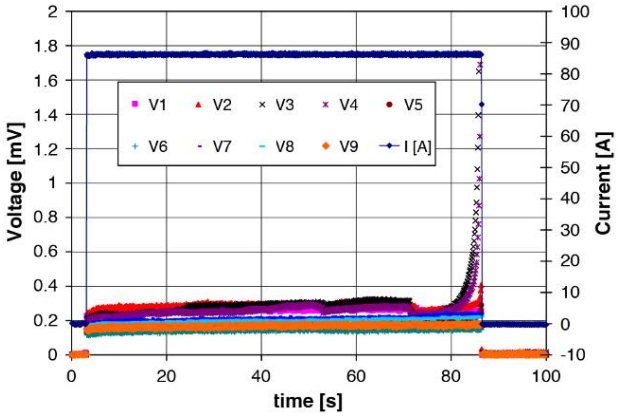

Fig. 1.52. Voltage distribution in a 4-mm-wide SuperPower tape with 20 μm of surround copper stabilizer when a constant current of 86.2 A is applied at 77 K. The tape end-to-end critical current was 72.8 A.

Table 1.8 displays the propagation speeds as a function of operating current (I_{op}), and overcurrent pulse (I_{pulse}), for the YBCO tape with 38 μm of Cu-surround stabilizer at 77 K. From these results, it is clear that the operating current after the overcurrent pulse has a greater influence on the propagation speed than the overcurrent pulse magnitude. Attempts were made to induce normal zone propagation in the other samples, but the uniformity of the critical currents along the sample length limited the opportunities.

Table 1.8. Normal zone propagation speeds at 77 K for YBCO tapes with 38 μm of Cu-surround stabilizer as a function of overcurrent pulse magnitude and operating current
The sample critical current was 68 A at 77 K.

I_{pulse} (A)	I_{pulse}/I_c (-)	I_{op} (A)	I_{op}/I_c (-)	Propagation speed (cm/s)
155.2	2.28	66.6	0.98	0.58
157.1	2.30	66.6	0.98	0.70
165.0	2.43	59.8	0.87	0.46
165.0	2.43	56.4	0.82	0.27
165.0	2.43	53.2	0.78	0.19

1.5.10 Effect of Long Length and Splices on Stability of Insulated SuperPower Cu-Surround Stabilized YBCO Tapes

While the stability of short samples can help with the understanding the impact of tape geometry on stability, experiments on long-length samples can give insight as to how the concepts identified on short samples (10–20 cm) translate to longer samples (1–2 m). A set of thermal runaway experiments were carried out on a 1-m-long, 4-mm-wide YBCO tape with a Cu-surround stabilizer thickness of 38 μm. A

constant dc current was applied until the voltages of the sample change rapidly at which point the current was removed. The YBCO tape was wound at large pitch onto a 60-cm-long, 2.54-cm diameter G10 rod and was insulated with the same radial build of dielectric tape that was used in the previous short length testing. This was done so that the cooling conditions with respect to the tape face were approximately the same to that used in the short length experiments. Voltage taps were attached at intervals of 10 cm at the ends and 5 cm near the sample center to monitor voltage developments at the points furthest away from the current leads and the LN bath. In Fig. 1.53**,** an example of the observed runaway in the 1-m-long YBCO tape with 38 μm of Cu-surround stabilizer is given. The thermal runaway occurred at 80 A after approximately 50 s and is localized in approximately 10 cm of the 1-m length. The fraction of conductor length, which exhibited runaway, was a significantly smaller percentage of the total length than was observed in the short length, 38 μm of Cu-surround stabilized samples. After modifying the current and measuring the thermal runaway current as a function of time to thermal runaway, these data were added to a previous short sample plot of the thermal runaway current as a function of time in Fig. 1.54.

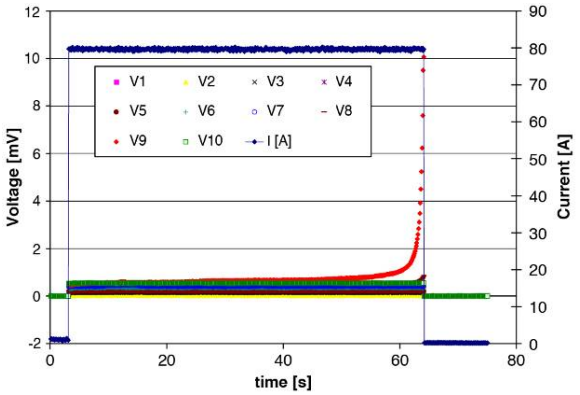

Fig. 1.53. Thermal runaway at 77 K for a 4.4-mm-wide, 1-m-long YBCO tape with 38 μm of Cu-surround stabilizer. The current was 80 A, which is greater than the critical current of 69 A.

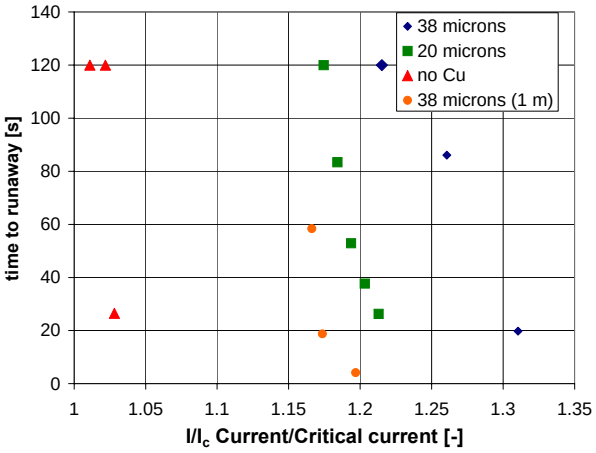

Fig. 1.54. Thermal runaway current as a function of time at 77 K for 4.4-mm-wide, 25-cm, and 1-m-long YBCO tapes with 38 μm of Cu-surround stabilizer.

The shift suggests that, as the length is increased further, the thermal runaway current could either approach the critical current or be less than the critical current. This would be consistent with some cryocooling experiments in BSCCO rotor coils, but additional experiments are needed to confirm this theory. After the sample was warmed up, a splice was added to the center of the 1 m sample. The splice was a double lap joint, which consisted of a 4-cm-long piece of 4-mm-wide YBCO with 38 mm of Cu-surround stabilizer that was soldered with Sn-Bi solder to a break at the center of the 1-m-long sample. The motivation was to observe whether the stability of the sample was impacted by a low-resistance section, which is of use to magnet manufacturers, as well as low ac loss configurations with low-resistance bridges. The sample was reinsulated and cooled back down to 77 K; a splice resistance of 0.5 μΩ was observed. Figure 1.55 gives the voltage profile for the sample as a function of time at a constant current of 74.4 A. The source of the runaway came from the damaged superconducting sections not the splice voltages, which were fairly constant over a long period. The interesting thing to note about the runaway is that the thermal runaway current of 74.4 A, which is shown is only slightly less than the nonspliced thermal runaway current of 74.8 A (assuming the same runaway time). Additional investigations through modeling and experiments are needed to determine the extent to which the splice remains stable at these conditions.

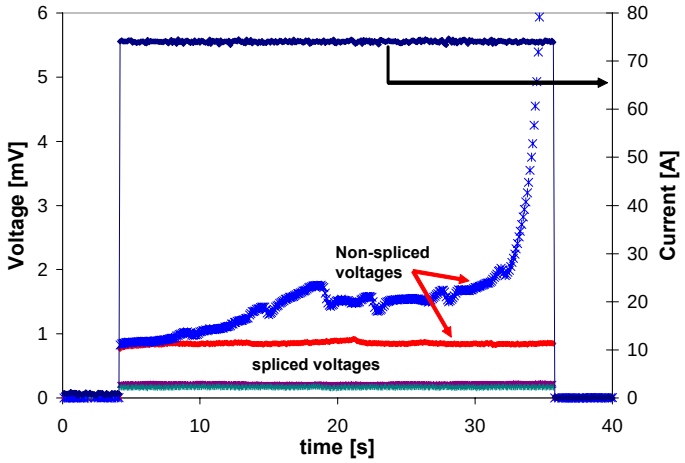

Fig. 1.55. Thermal runaway current as a function of time at 77 K for 4.4-mm-wide, 25-cm, and 1-m-long YBCO tapes with 38 μm of Cu-surround stabilizer.

1.5.11 Alternating Current Loss in Spliced and Stacked Narrow-Width YBCO Tapes

Filamentization has been shown to reduce ac losses, but practical alternatives need to be examined to determine whether stacks of YBCO tapes can provide an economical alternative to creating filaments. To accomplish this, a set of ten 2-mm-wide YBCO tapes, with lengths of 1 m, were provided by SuperPower to ORNL to look at low ac loss in assembled conductor geometries. Each 2-mm-wide YBCO tape had a critical current between 25 and 30 A. In addition, 4-mm-wide YBCO tapes with a critical current of 60 A were provided to baseline the improvements that were observed from the ac loss in the 2-mm-wide assembled conductor. Each tape had only a 2–3 μm silver stabilizing layer but no Cu-surround stabilization. This was done to minimize the gap between the YBCO layers in each configuration.

Two different geometries were considered initially, each consisting of a stack of two 2-mm-wide tapes, as shown in Fig. 1.56. The restriction to two 2-mm-wide tapes was because multiple stacks of conductors could pose complications with stability and current transfer. A separate set of samples are needed to consider these issues in more detail. The motivation of the spliced stack of YBCO tapes was based on previous results reported by Ashworth for low-ac-loss conductors, which were observed when low-resistance bridges were inserted into filamentary YBCO conductors. While joining two 2-mm YBCO tapes consecutively might be effective, it introduces questions as to the strength of the final conductor. Adding a second continuous tape to the separated tape should provide some additional mechanical strength and should provide a lower-resistance joint when current is passed through the tape stack. For the purposes of the discussion, sample A is the insulated two 2 mm YBCO tape stack, sample B is the spliced two 2-mm-wide YBCO tapes with a low-resistance indium solder, and sample C is the spliced two 2-mm-wide YBCO tapes with a high-resistance solder. Each has a low melting point and should not cause damage to the YBCO. Each sample had a total length of 7 cm, which

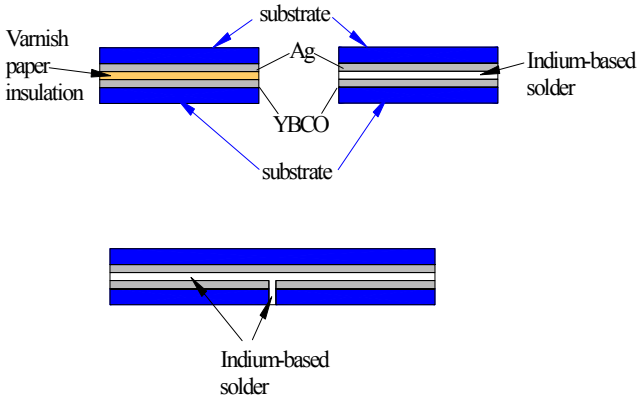

Fig. 1.56. Schematic of stack configuration for two 2-mm-wide YBCO tapes in insulated and spliced configurations.

kept the field in the bore of the ac solenoid mostly uniform across the face of the sample. The sample length also allowed for characterization of the ac losses thermally.

After each sample was made, it was instrumented with a heater and thermometer. Each of these components was made from twisted copper wire because the thermocouples have a tendency to see induced electromotive force while the ac field is applied. A 100 mA current was provided as excitation to the thermometer to measure the change in resistance at 77 K. It was estimated that the thermometer with 100 mA added about 0.001 W/m and was well below the sensitivity of the experiment at those temperatures. Figure 1.57 shows the 100 mT ac coil in which each sample was characterized and a typical thermal measurement setup for each sample. The heater calibrates the change in voltage of the thermometer against a known heat loss and when the ac field is applied to the sample, the change in voltage is matched to the calibration to find the total ac loss of the sample.

Fig. 1.57. Alternating current field coil (left) and example of ac loss measurement setup (right).

The comparison of the ac loss as a function of perpendicular field for a 4-mm-wide YBCO tape, a 2-mm-wide YBCO tape, and the insulated two 2-mm-wide YBCO tape stack (sample A) is given in Fig. 1.58. With a 0.1-mm gap, the ac losses for sample A are smaller than the single 4-mm-wide YBCO tape across the entire measurement range and above the single 2-mm. The reduction of ac loss in the stack of tapes is the result of the shielding of the field along the tape edges that occurs when the tapes are close to each other and is consistent with work done by Grilli and Ashworth [3]. Although only the 60-Hz-losses are shown in Fig. 1.58, variable frequency measurement of the ac losses indicated that they were primarily hysteretic.

Further reduction in the ac loss was observed when data for the splice stack of 2-mm-wide tapes were plotted as a function of ac field as shown in Fig. 1.59. A factor of four reduction was observed in

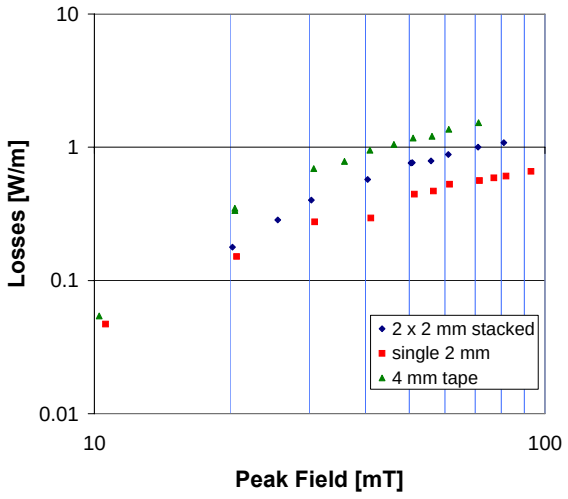

Fig. 1.58. Alternating current losses at 60 Hz and 77 K as a function of perpendicular applied ac field for different configurations of 2-mm- and 4-mm-wide YBCO tapes.

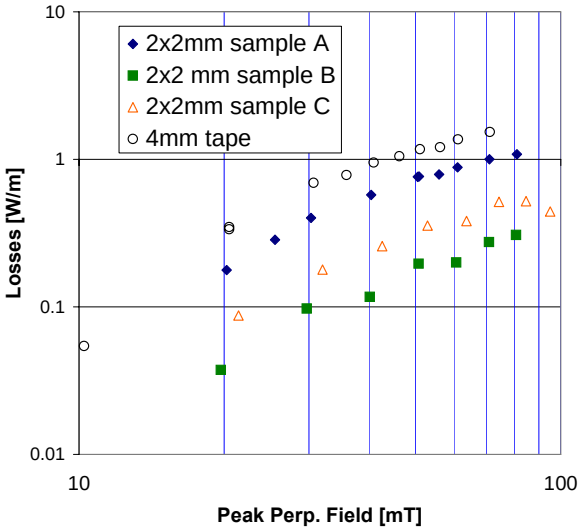

Fig. 1.59. Comparison of ac losses at 60 Hz and 77 K as a function of perpendicular ac field for a single 4-mm-wide YBCO tape to a set of two 2-mm-wide YBCO stacked configurations.

sample B, which conceivably has the lowest resistance due to the concentration of indium in as compared to sample C. This difference would support the Ashworth model for reduction by low resistance bridges, but the spliced tape results are slightly less than or the same as the single 2-mm-wide YBCO tape result. Even with the splice, the continuous portion of the YBCO tape of the splice should have registered the same losses as the single 2-mm-wide tape. However, if there were some benefits gained from the presence of the second spliced tape, further measurements and modeling are needed to determine if the splice tapes suffered handling issues, which could have degraded the critical current of the tape during soldering.

Reduction in ac loss has been achieved through the stacking of two 2-mm-wide tapes in different configurations. The use of splices to create low resistance bridges shows a promising way to reduce the ac loss when compared to a single 4-mm-wide YBCO tape. The ac losses were reduced from 1.5 W/m for a 4-mm-wide YBCO tape at 70 mT to 0.3 W/m for a two 2-mm splice configuration with a high indium concentration solder. The comparison of the results to 2-mm-wide tape suggest that further modeling and measurements are needed to confirm whether there was any damage done to the conductor. This concept will be investigated further to determine how the solder material and field orientation impact the feasibility of this concept. In parallel fields, the splice configuration could result in additional coupling losses, which may offset the reduction seen in ac loss in ac perpendicular fields.

1.5.12 Alternating Current Loss in Filamentary YBCO Samples Produced by Inkjet Deposition

As an alternative to mechanical and chemical methods to produce filamentary YBCO conductors, an inkjet deposition method has been developed. Starting with a YBCO solution used in spin coating, filaments were deposited onto fully-buffered Rolling Assisted Biaxially Textured Substrate (RABiTS™) by a single inkjet nozzle facility (Fig. 1.60). Figure 1.61 shows an example of a fully converted YBCO sample with filament widths of 800 μm and filament gaps of 100 μm that had a critical current density of 0.5 MA/cm^2.

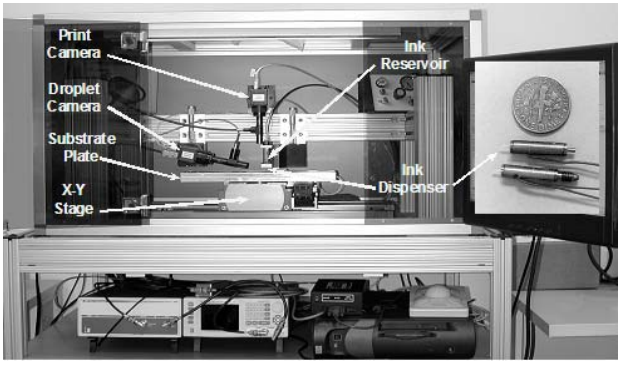

Fig. 1.60. Solution inkjet deposition facility at ORNL.

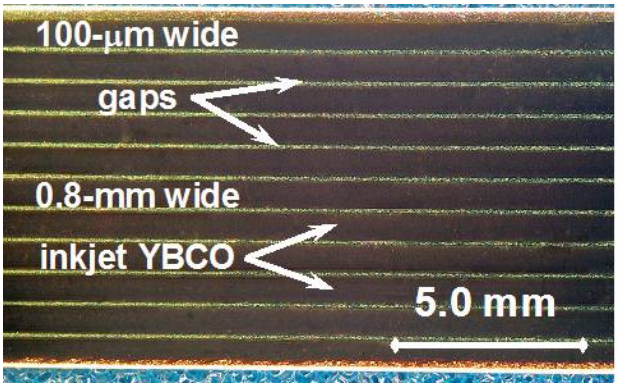

Fig. 1.61. Example of fully converted YBCO filaments on 1-cm-wide RABiTS™.

To prepare the sample for ac loss measurement in the test facility that is shown in Fig. 1.57, an aluminum oxide coating was added to insulate the sample and a thermometer and heater were epoxied to the sample. To qualify the test setup to measure a reduction in ac loss as a function of perpendicular ac field, filamentary YBCO samples were created from the same solution that was used in the inkjet deposition; one sample had filaments created through laser scribing. The nominal critical current of the samples before scribing was 0.4 MA/cm^2 and the YBCO thickness was 0.9 μm. From the results given in Fig. 1.62, a reduction in ac loss was measured with characteristics that were consistent with the dependence of the ac loss on the filament geometry and field dependence for hysteretic ac loss.

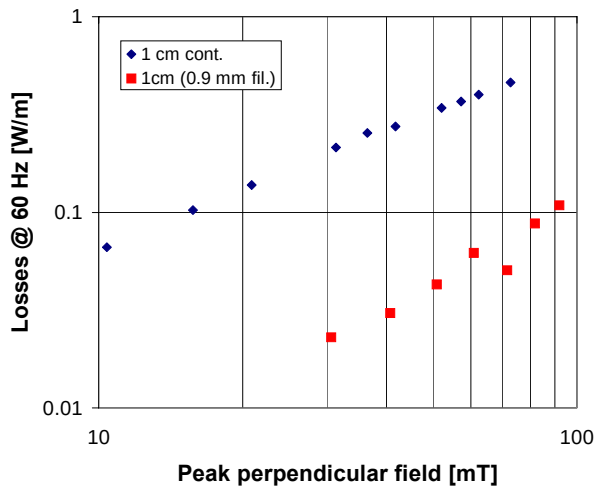

Fig. 1.62. Alternating current losses as a function of perpendicular ac field at 60 Hz and 77 K for a 1-cm-wide YBCO sample without filaments and a laser-scribed YBCO sample with 0.9-mm-wide filaments.

Initial attempts on inkjet filamentary conductors were not successful at reducing ac loss. In Fig. 1.63, the ac losses in a 1-cm-wide sample with 100 μm-wide filaments were significantly higher than the hysteretic loss that is predicted by theory. This increase in loss was attributed to the narrow filament width when compared to the grain size of YBCO on RABiTS™. When the filament width was increased to nearly 1 mm, only a slight reduction in ac loss was observed (Fig. 1.64) when compared to a 1-cm-wide continuous YBCO sample. When the ac losses were measured as a function of frequency, the dependence of the ac losses with respect to perpendicular field in Fig. 1.65 indicate the source of the ac losses were primarily coupling. From the slope of the line, the effective resistivity was 2.0×10^{-10} Ω-m, which was consistent with the length of the sample (4 cm) and the filament to filament shorting observed on each end.

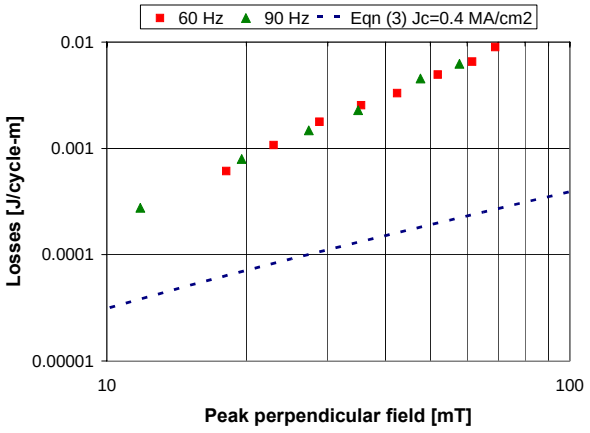

Fig. 1.63. Alternating current losses as a function of perpendicular ac field at 60 Hz and 77 K for a 1-cm-wide YBCO sample with inkjet deposited 100 μm-wide filaments.

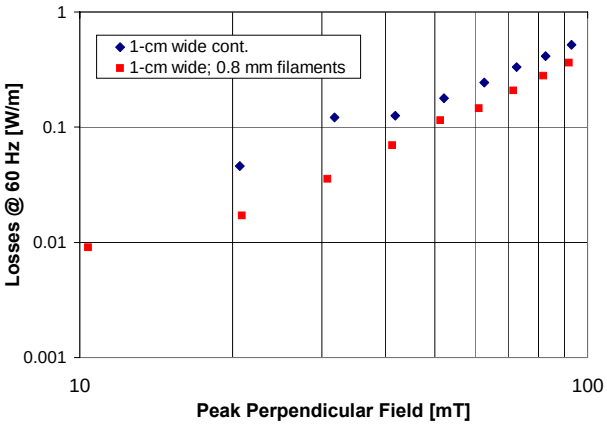

Fig. 1.64. Alternating current losses as a function of perpendicular ac field at 60 Hz and 77 K for a 1-cm-wide YBCO sample without filaments and a YBCO sample with 0.8-mm-wide inkjet deposited filaments.

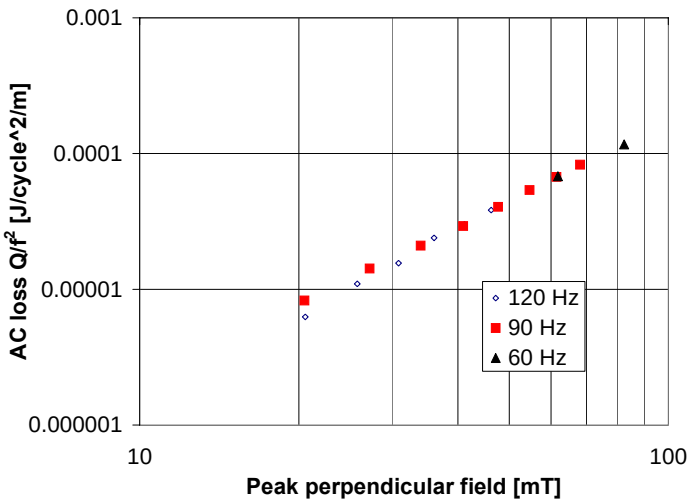

Fig. 1.65. Alternating current losses divided by the square of the frequency as a function of perpendicular ac field at 60 Hz and 77 K for a 1-cm-wide YBCO sample with 0.8-mm-wide inkjet-deposited filaments.

1.5.13 High-Voltage Performance of YBCO Tapes from American Superconductor

Based on previous measurements of high-voltage breakdown across YBCO tapes with Cu-surround stabilizer, experiments were carried out to determine whether the nature of the copper stabilization affects high-voltage breakdown. To characterize the dielectric properties for the sample tapes, a cross configuration (Fig. 1.66) was chosen because the test conditions should be fairly reproducible and should minimize the statistical variation associated with the test setup. A test where the breakdown is measured for two adjacent tapes or a side-by-side configuration is extremely affected by variation of the distance between the tape along the length, defects that occur along the tape length, and the end voltage connections to the tape. A picture of the test equipment, which allows for testing of multiple samples with one single ground tape, is shown in Fig. 1.67. In addition, this setup permits for some deviation in the straightness of the sample without affecting the electric field profile between the tapes. Breakdown is recorded once a short occurs between the two tapes and the voltage drops to zero.

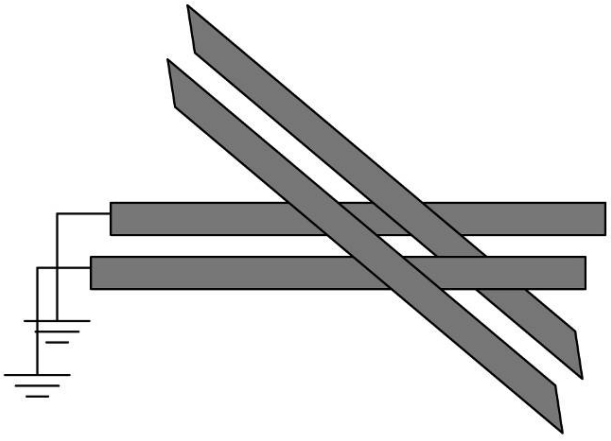

Fig. 1.66. Cross configuration used to test voltage breakdown between a pair of YBCO-coated conductors.

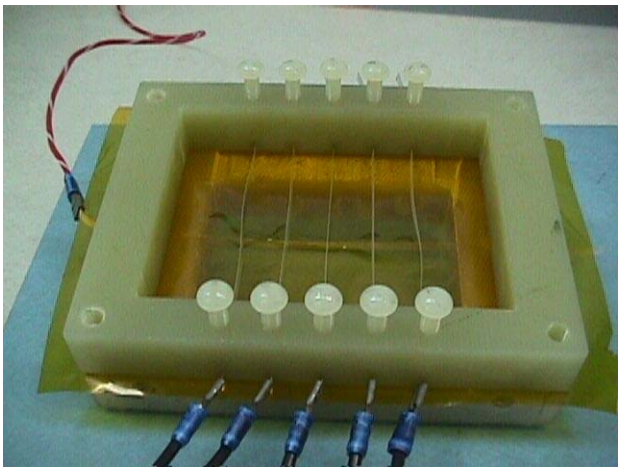

Fig. 1.67. Experimental high-voltage test setup for cross-configuration breakdown.

A 0.001-in.-thick piece of Kapton® was placed between the two tapes, as shown in Fig. 1.67, and the relative height of the sample was adjusted until each tape was flush to the Kapton® surface. This entire setup was immersed in an oil bath to allow for systematic testing of multiple samples. The dielectric strengths of the oil and the Kapton® prevent high-voltage leakage between the voltage-biased tapes and adjacent grounded samples and allow for the electric field to remain concentrated between the two tape edges. The tests were performed on copper-laminated YBCO tapes that were provided by AMSC. Each tape, which was taken from a representative sampling of AMSC's 344 superconductor, had a nominal width of 4.4 mm and a total thickness of 0.16 mm, of which 0.1 mm was taken up by two opposing layers of 50-μm-thick copper stabilizer.

To better appreciate the distribution of the voltage breakdown within the sample set, the Weibull distribution of the high-voltage breakdown for the copper-laminated YBCO tape is given in Fig. 1.68. The average breakdown voltage for the tape was 7.0 ± 0.9 kV. Previous reported results for other YBCO tapes had an average breakdown voltage of 6.7 ± 0.2 kV for copper-surround stabilized tapes and 6.0 ± 2.2 kV for as-slit YBCO tapes. Each uncertainty is the standard deviation of the high-voltage breakdown across the entire sample set. When the results were plotted on a Weibull plot to determine probability of breakdown at a given voltage, the 10% probability of breakdown is projected to be at 5.3 kV, greater than previous results of 2.0 kV for the as-slit YBCO tapes, but slightly less than 6.5 kV for the copper-surround stabilized YBCO tapes.

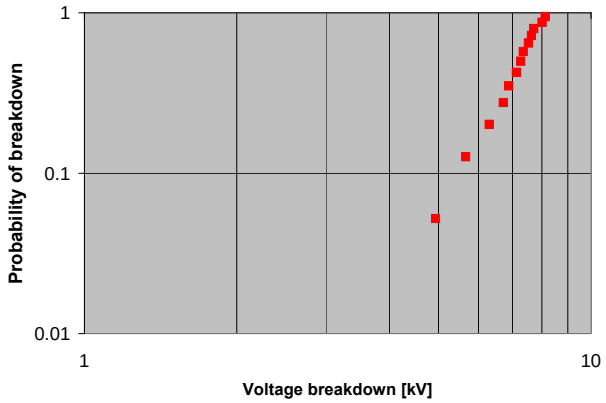

Fig. 1.68. Weibull plot of voltage breakdown at room temperature for copper-laminated YBCO tapes across a 25-μm-thick piece of Kapton®.

While the average value was higher, the increase is not statistically significant due to the standard deviations. However, the copper-laminated tapes show improvement as compared to the as-slit YBCO tape with respect to the 10% probability breakdown and the standard deviation of breakdown voltage. This improvement is likely due to the copper lamination defining the area across which the high-voltage breakdown occurs. Since the lamination extends beyond the tape edge slightly, it defines the cross sectional to a smaller area than what would be defined if only the YBCO tape was exposed. Additional measurements are needed on samples with different thicknesses to determine whether the deviation of the average voltage breakdown can be associated with either an increase or decrease in the stressed area.

1.5.14 Effect of Cu-surround Stabilizer of YBCO Tapes from SuperPower in Coil-Wound Geometries

While it has been demonstrated that Cu-surround stabilized YBCO tapes have improved high-voltage characteristics than as-slit YBCO in a fundamental sense, the high-voltage performance of Cu-surround stabilized YBCO-coated conductors was compared with the performance of nonplated YBCO-coated conductor in a winding geometry to determine whether any tangible improvement remained. To characterize the dielectric properties for the sample tapes in a coil-winding geometry, the final design consisted of mounting two tapes in a nearly parallel geometry as shown in Fig. 1.69. The tapes were positioned so that the distance of closest approach occurred away from the tape end, which could trigger premature breakdown due to the sharp edges. An ac voltage at a frequency of 60 Hz was ramped across the tapes until a breakdown occurred. Each sample consisted of two 4-mm-wide YBCO tapes with nominal lengths of 10 cm and gap spacing that ranged between 0.1 to 1.0 mm. Each pair of tapes was placed on a glass cloth and then held in place by Kapton® along the sample edges away from the test region. This glass cloth works with the Stycast W19 as is vacuum-impregnated to allow for the tape to be separated from the nylon former. After a visual inspection was done to determine whether any bubbles

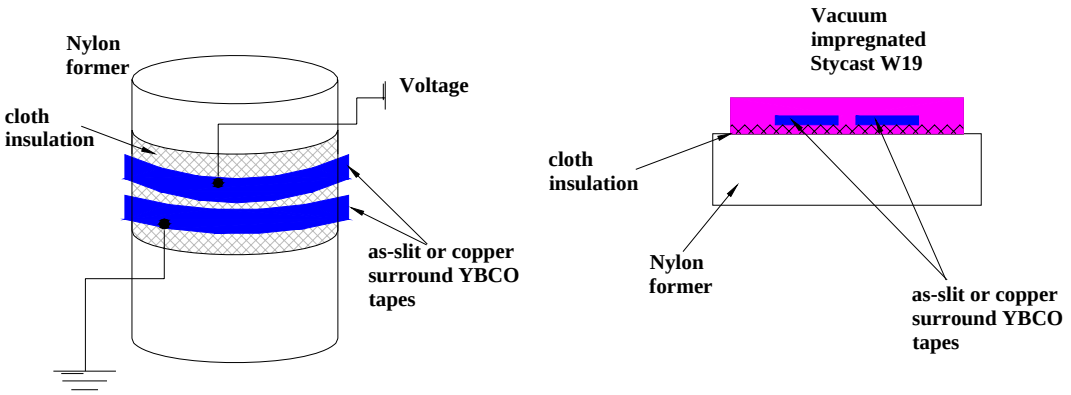

Fig. 1.69. Sketch of cross-configuration used to test voltage breakdown between a pair of YBCO-coated conductors.

had formed, each sample was placed in a room-temperature oil bath and the breakdown was measured. After breakdown, the gap in the region where the breakdown occurred, usually shown by a carbon arc, was measured to normalize the data with respect to the gap dimensions.

Table 1.9 summarizes the voltage breakdown that occurred for the as-slit and Cu-surround stabilized YBCO tapes. While the average breakdown was higher for the Cu-surround YBCO tapes than the as-slit YBCO tapes, the standard deviation of the Cu-surround stabilized tapes was higher because the breakdown stretched across a larger range than the as-slit YBCO tapes. A better way to look at the data is to generate a Weibull plot (Fig. 1.70) where the improvement with the Cu-surround stabilizer is more clearly shown. The Cu-surround stabilized YBCO tapes have higher breakdown voltages at all probabilities, so there is some level of improvement that can be gained for coil applications. While changing the epoxy itself may change the absolute numbers of the voltage breakdown, the improvement with the Cu-surround stabilizer should still be apparent. One test to follow this would be to repeat the test geometry in LN temperatures to see whether there is a change in the data spread.

Table 1.9. Statistical set of voltage breakdown data taken for Cu-surround stabilized and as-slit YBCO tapes in a coil geometry

Run	Breakdown in nonplated YBCO (kV/mm)	Breakdown in Cu-surround stabilized YBCO (kV/mm)
1	17.2	128.0
2	30.0	31.8
3	46.5	199.0
4	30.0	24.3
5	22.0	174.4
6	26.5	34.7
7	3.5	83.3
8	14.1	68.5
9	41.3	81.0
10	63.3	24.3
11	29.2	
Avg	29.4 ± 16.4 kV/mm	84.9 ± 63.1 kV/mm

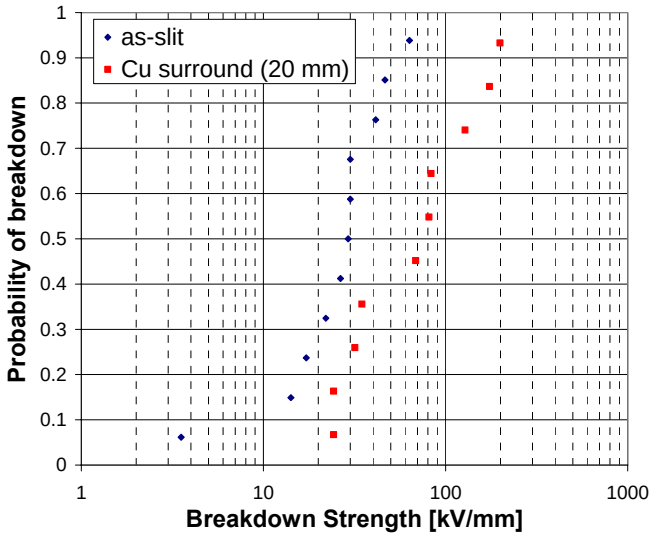

Fig. 1.70. Weibull plot of voltage breakdown at room temperature in an oil bath for as-slit and Cu-surround stabilized YBCO tapes.

1.5.15 Splice Resistances in BSCCO and YBCO Tapes

1.5.15.1 General Overview

ORNL, in collaboration with Rockwell Automation of Cleveland, Ohio, has been investigating the splice resistance of both first-generation Bi-2223 PIT tape and second-generation YBCO-coated conductor. The purpose of the experimental investigation is to study the splice resistance of both first-generation tape and second-generation coated conductor as a function of (a) surface preparation condition, (b) flux type, (c) solder type, (d) sheath materials, (e) operating temperature, (f) thermal cycle, and (g) magnetic field. Understanding the splice resistance with its corresponding variation as a function of surface preparation and operating conditions is essential to the practical implementation of electric utility devices (e.g., motors, generators, transformers). Several splice configurations are possible, but we have limited our study thus far to a common lap joint in which one superconducting tape is laid flat over the second. The interface region, referred to here as the "overlap distance," is a key factor in determining the magnitude of the splice resistance. Current is passed from one conductor through the splice joint and finally through the second conductor. The voltage drop is measured with a precision digital multimeter (DMM) at voltage taps that span the splice joint. Several data points (typically between 50 and 100) are recorded in 1 power-line cycle repetition rates, averaged to determine an average value with its corresponding standard deviation.

1.5.15.2 Results

Some preliminary results at 77 K are shown in Figs. 1.71 and 1.72. Shown in Fig. 1.71 is the contact resistance for a splice joint using 60Sn-40Pb solder, no surface preparation, and a 0.25 in. overlap distance. Shown in Fig. 1.72 is the contact resistance for a splice joint using Sn60-40Pb solder, paste-type flux, and a 0.25 in. overlap distance. Results are shown in both figures as a function of thermal cycle and applied current flowing through the joint. In general, little degradation is observed from thermal cycle to thermal cycle, indicating that mechanical degradations due to thermal cycling are limited. Furthermore, contact resistance can be lowered by almost 30 to 50% with the use of flux paste and appropriate cleaning of the surface prior to joint fabrication, as can be seen in Figs. 1.71 and 1.72. As the study continues, we also plan to investigate second-generation YBCO-coated conductor as a function of temperature and magnetic field to determine their effects on splices in practical operating environments anticipated for electric utility applications.

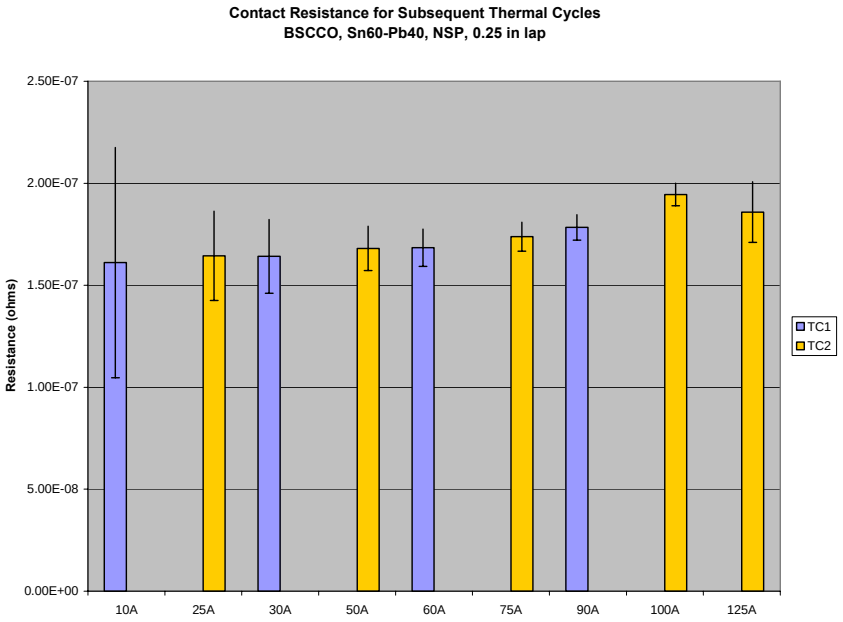

Fig. 1.71. Contact resistance for a Bi-2223 splice joint with no surface preparation, 60Sn-40Pb, a 0.25-in. overlap as both a function of thermal cycle and current.

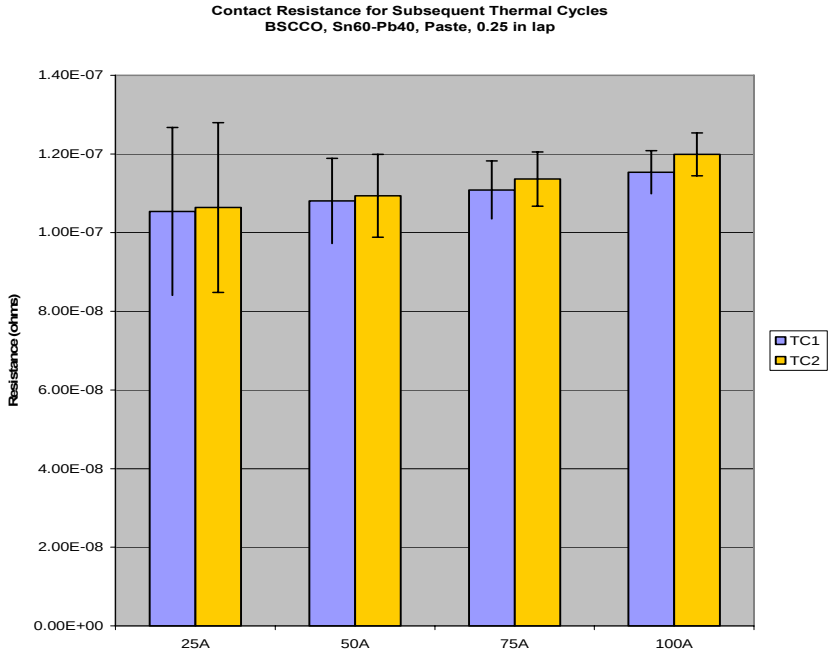

Fig. 1.72. Contact resistance of a Bi-2223 splice joint with a 60Sn-40Pb solder, paste flux, a 0.25-in. overlap as both a function of thermal cycle and current.

1.5.16 YBCO Coil Testing

ORNL, in collaboration with AMSC, and Cryomagnetics, Inc., has designed, fabricated, and tested a solenoid coil fabricated with second-generation YBCO-coated conductor tape. The purpose of the project was to study the quench protection and propagation characteristics in the new second-generation YBCO coils. A fundamental understanding of the quench phenomena is crucial in the future design and operation of HTS-based electric utility applications and devices.

1.5.16.1 Coil Construction

The second-generation YBCO coil design and construction details have been reported in previous quarterly reports. A brief summary is provided in Table 1.10.

Table 1.10. Second-generation YBCO coil key parameters
Conductor type: RABiTS™, second-generation YBCO 344

Quantity	Value
Inner diameter (mm)	35
Outer diameter (mm)	102
Height (mm)	35
Single pancakes	6
Total turns	582

1.5.16.2 Liquid Nitrogen Tests (Thermal Cycle 1)

The YBCO coil was initially tested at 77 K in a bath of pool boiling LN. Transport critical current measurements (I-V) were made using standard four-terminal techniques. Using an electric-field criterion of 1 μV/cm (i.e., V_c ~ 12 mV terminal-to-terminal or 2 mV per single-pancake), results showed a critical current of ~ 31 A, which corresponded to a central B-field in the coil of 0.32 T (reported previously).

Conduction Cooling Tests (Thermal Cycles 2–4.) After the initial testing at 77 K in an LN bath, the YBCO coil was modified to accommodate additional copper end rings that were attached to the original aluminum end rings of the coil. The new copper ends rings were used to facilitate mounting of the coil to the cryocooler cold head for the conduction cooling test. The new copper-top end ring of the YBCO coil was then mounted on a brass spool piece, which attached to the cold finger of an Al-330 G-M cryocooler. To keep the top and bottom of the YBCO coil as close to the same temperature as possible, thermally conductive flexible copper straps were attached to the top and bottom end plates of the additional copper end ring. During the modification and subsequent mounting of the YBCO coil for the conduction cooling test, it was noted that a small kink had appeared in the entering and exiting leads of the second-generation YBCO conductor. The kinks in the YBCO leads were most likely the result of out-of-plane bending that occurred during the conduction cooling modification. An attempt was made to repair the kinks in the entering/exiting leads with the addition of stabilizing Bi-2223 HTS conductor.

During the second thermal cycle, the coil was slow to reach thermal equilibrium using the conduction cooling apparatus. The YBCO coil was allowed to cool down for more than 24 h prior to the start of the critical current testing. After reaching final thermal equilibrium the temperature sensors on the coil were recorded as follows: (1) T_{top} ~ 45 K and (2) T_{bottom} ~ 51 K. After reaching a thermal equilibrium point, transport critical current measurements were taken using a wide variety of ramp rates ranging from 0.01 to 0.5 A/s. Results showed a range of critical current values from 22 to 27 A, depending upon the ramp rate used in the test. The results indicated that all single pancakes were experiencing large amounts of heat generation during the current excitation. Since higher critical currents were anticipated based on the earlier LN test results, three hypotheses were put forth to explain the disappointing results. First, the global YBCO conductor in the coil was actually at a warmer temperature than was being recorded at the top and bottom end rings, or there was a localized hot spot from impinging thermal radiation. Second, there was excessive heat generation in the coil caused by large ac loss, which was not observed during the

original LN testing. Finally, some type of global damage or degradation had occurred to the coil as a result of the conduction cooling modification or repeated thermal cycling. The critical current tests were halted, the cryocooler was turned off, and the YBCO coil was allowed to warm overnight. Upon warm-up of the YBCO coil, a trickle current was passed through the coil to observe the corresponding superconducting transition temperature. The transition temperature of the coils was measured to be ~ 90 K, as would be expected. As a result of the warm-up testing, the hypothesis of the (global) temperature of the YBCO coil being at a significantly higher temperature than the top and bottom end rings was ruled out, although a localized hotspot was not.

To test the hypothesis that the YBCO coil had either been damaged during modification or degraded as a result of thermal cycling, the critical current of the YBCO coil was once again tested (third thermal cycle) in a bath of pool boiling LN. After reaching a thermal equilibrium point, transport critical current measurements were taken using a wide variety of ramp rates, ranging from 0.01 to 0.5 A/s. Using the same electric field criterion of 1 μV/cm across the terminals (V_t), results showed a critical current value ranging from 28 to 30 A, depending upon the ramp rate used in the test. Although, the critical current was slightly lower (by 1 to 2 A) than the previous LN test, it was concluded that no global damage or degradation was apparent. Upon more careful inspection of the YBCO coil, it was noticed that the exposed outer turns of the coil were covered in Kapton® tape. It was speculated that the Kapton® tape's emissivity was quite poor and that it may be acting like a black body absorber on the outermost turns of the coil, causing these outer turns to be at a warmer temperature than the inner windings (i.e., a localized hotspot), resulting in a lower overall critical current for the coil. Therefore, it was determined that a radiation shield around the YBCO coil might reduce this deleterious effect.

Prior to the cooldown on the fourth thermal cycle, two modifications were made to the conduction cooled experimental setup. First, an additional Si diode was placed inside the bore of the solenoid against the inner copper winding mandrel to more accurately assess the temperature gradient along the axis of the YBCO coil. Second, a radiation shield consisting of two layers of aluminum foil and six layers of aluminized MLI was wrapped around the coil and attached to the Al-330 cold head. Another thermal cycle was initiated. This time, however, with the inclusion of the MLI, the second-generation YBCO coil cooldown took less than 6 h. After reaching final thermal equilibrium, the temperature sensors on the coil were recorded as follows: (1) T_{top} ~ 34.2 K, (2) T_{bottom} ~ 34.8, and $C_{center\text{-}bore}$ ~ 36 K (the rated accuracy of the Lakeshore Si diodes is +/- 1 K.) With the inclusion of the MLI, the final equilibrium temperature of the YBCO coil was more than 10 K lower than the previous thermal cycle with the ΔT between the top and bottom end ring less than 1 K. After reaching a thermal equilibrium point, transport critical current measurements were taken using a wide variety of ramp rates, ranging from 0.01 to 5 A/s (see Fig. 1.73). Subsequently, to measure the I-V characteristics of this coil at another temperature, the LN radiation shield of the test cryostat vessel was emptied to raise the baseline temperature of the YBCO coil. After the LN was removed from the test cryostat radiation shield, the second-generation YBCO coil thermal equilibrium temperature was ~ 45–46 K across all 3 Si diodes (see Fig. 1.74).

Transport I-V measurements at varying ramp rates were once again measured. In addition, two other types of current ramps were studied: (a) rapid "on/off" square wave pulses and (b) symmetrical triangular shaped current ramps. For the square wave pulses, duration at full current varied between 2 and 5 s, depending upon the magnitude of the current pulses. Current pulses starting at 60 A were made in 10 A increments all the way to 100 A, which corresponds to ~ a 1-T B-field in the central bore of the coil. After the high on/off type current pulses, the second-generation YBCO coil was tested at ramp rates varying from 0.01 to 5 A/s with symmetrical triangular-shaped current ramps.

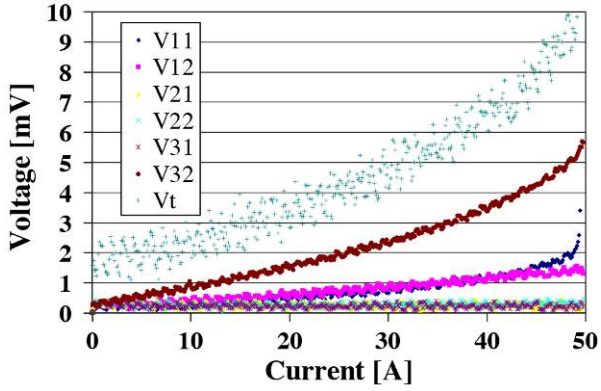

Fig. 1.73. I-V measurement of the second-generation YBCO coil at 34 K with a ramp rate of 0.1 A/s. The nomenclature Vij refers to the i(th) double pancake and the j(th) single pancake coil.

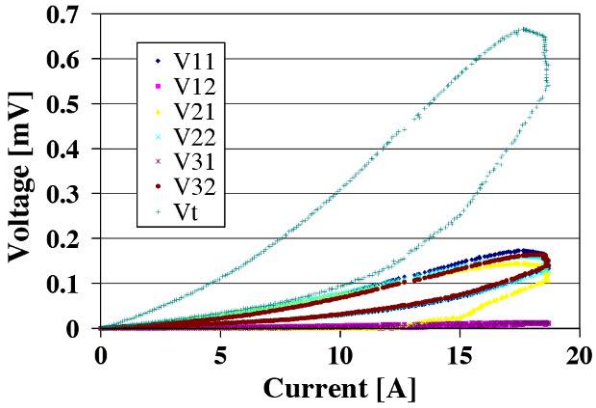

Fig. 1.74. I-V measurement of second-generation YBCO coil at 45 K for all six pancake coils below the critical current. The hysteresis loops that develop during the conduction cooling tests with triangular current ramps.

1.5.16.2 Results

Shown in Fig. 1.75 is the I-V measurement for the second-generation YBCO coil at ~ 34 K with an increasing ramp rate of 0.1 A/s. The nomenclature used to denote the subscripts in voltage measurement are as follows: (a) the first number refers to the double pancake coil, (b) the second number refers to the single pancake coil, and (c) the subscript V_t refers to the end-to-end terminal voltage of the second-generation YBCO coil. Hence, V_{11} refers to the first single pancake of the first double pancake coil, V_{12} refers to the second single pancake in the first double pancake coil, and so on. Thus, V_{11}, V_{21}, and V_{31} all contain the single pancake to single pancake splice, while V_{12}, V_{22}, and V_{32} do not. For the data taken in Fig. 1.73, the shape of the applied current was saw-toothed with a decreasing ramp rate of 10 A/s. Shown in Fig. 1.74 is the current vs voltage for all six single pancake coils at 45 K at a ramp rate of 0.05 A/s. For this particular measurement, the applied current for both increasing and decreasing currents was symmetrical, i.e., triangular shaped. Using the same electric field criterion of 1 μV/cm across the coils terminals (V_t), results showed a critical current value ranging from 38 to 44 A, depending upon the ramp rate used in the test. The hysteresis in the I-V loops in Fig. 1.74 develop at the higher temperature and the slower (triangular) ramp rates.

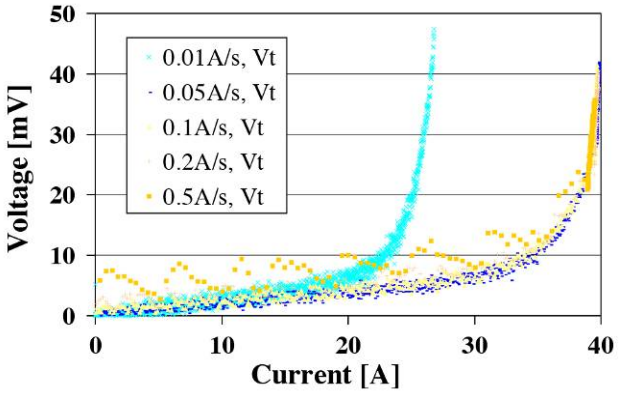

Fig. 1.75. Current vs terminal voltage (V_t) measurement of second-generation YBCO coil at 77 K for ramp rates varying between 0.01 and 0.5 A/s.

1.5.16.3 Discussion

The I-V measurements performed on the first thermal cycle in pool boiling LN were consistent with the calculated value using the calculated maximum perpendicular B-field component and the measured short sample critical current at 77 K. Subsequent measurements, taken in the conduction cooling configuration at 34 and 45 K, showed a steady-state I_c ~ 45–49 A and 38–44 A, respectively. These values were significantly lower than the calculated value assuming a literature-derived temperature-dependent critical current of the second-generation YBCO tape. For the I-V data collected at 34 K, using

slow ramp rates between 0.05 and 0.5 A/s and a 1 μV/cm criteria across the voltage terminals, the I_c was measured to be between 45 A and 49 A in the top most pancake coil (see Fig. 1.75). The 45 K data show similar disappointing results with measured critical currents between 38 and 44 K in the top most pancake coil (see Fig. 1.76). It is believed that these lower than expected critical currents at that temperature are caused by the nonsuperconducting splices (both internal an external) which result in excessive Joule heating which cannot be carried away fast enough in the conduction cooling mode of cooling. The extremely slow ramp rates further exacerbate the problem during the conduction cooling tests by allowing the heating cause by the splices to continually build and not removed fast enough by conduction cooling. Evidence for this can be seen in Fig. 1.75, where hysteresis loops in the I-V measurements were observed during the 45 K tests and triangular shaped current ramps. As a result of this heating not being offset by the available cooling, the YBCO conductor is becoming more resistive and a portion may have a small normal zone develop as evidenced by the sharp/sudden change in slope of the I-V curve. In addition, an interesting ramp rate dependence of the coil's I-V characteristics was observed at 77 K. For ramps rates greater than 0.05 A/s, all I-V curves converge with an $I_c \sim 31$-34A, while at very slow ramp rates the critical current appears to decrease significantly. This drop in critical current for the lower ramps rate (opposite of what would be expected from ac loss mechanisms) may be due to splice joint heating accumulating in the winding pack.

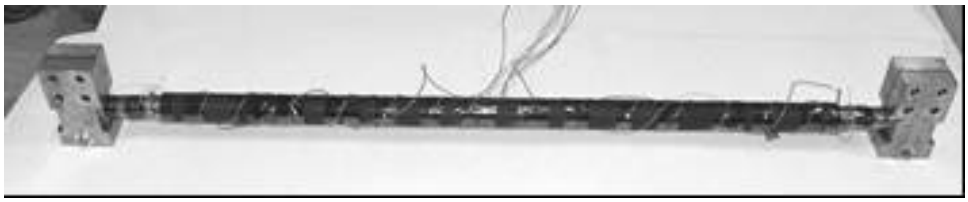

Fig. 1.76. The 1.25-m YBCO cable ready for testing. The copper end connections for the external copper cables are on each end.

1.5.16.4 Conclusion

It has not been determined whether the root cause of the lower than expected steady state critical currents is an intrinsic characteristic of the second-generation YBCO conductor in a perpendicular B-field or an extrinsic result of the many internal and external splices or possibly localized damage caused during coil modification. The critical currents of the top and bottom pancake coils are measured to be the lowest, a finding that is consistent with the fact that these pancakes experience the peak radial B-field. Hence this is an intrinsic limitation of the YBCO conductor in this solenoid coil configuration. There may be extrinsic factors limiting the critical current of the coil such as the splices (both internal and external) as well as the observed "kinks" in the entering/exiting leads of the coil. The hysteresis observed with triangular current ramps at ~ 45 K (Fig. 1.74) and the unusual ramp rate dependence at 77 K (Fig. 1.75), are indicative a problem with internal heating from splices.

1.5.17 YBCO Cable Testing

ORNL has designed, built, and tested a 1.25-m-long, prototype HTS power cable made from second-generation YBCO-coated conductor tapes (Fig. 1.76). YBCO tapes provided by AMSC, coated conductor Cu-laminated tapes, have a 75-μm-thick substrate made from Ni5at%W alloy with a 0.2 μm buffer layers, a 0.8-μm-thick YBCO layer, 2 to 3 μm of Ag, 10 μm of solder, and 50 μm of hardened Cu stabilizer on both sides, giving a total thickness of about 200 μm. This tape is called "344 superconductor" by AMSC due to the 3-ply construction and 4.4 mm width. The two-layer cable was built by Ultera with the Cu-laminate side nearest to the YBCO superconductor facing down in both layers for ease of attachment to the 25.4 mm diam copper end plugs. This configuration ensured that the current transfer was not through the higher-resistance NiW substrate. Each layer had sixteen 4.4-mm-wide YBCO tapes wound on a 25.4-mm-diameter former made of G-10 fiberglass epoxy.

Electrical tests of the cable were performed in LN at 77 K. Direct current testing of the HTS cable included determination of the V-I curve with a critical current of about 2100 A, which was consistent with the critical currents of the two layers of 4.4-mm-wide YBCO tapes. Alternating current testing of the cable was conducted at currents up to about 1500 A_{rms}. The ac losses were determined calorimetrically by measuring the response of a calibrated temperature sensor placed on the former and electrically by use of a Rogowski coil with a lock-in amplifier. Figure 1.77 shows the ac loss in the YBCO cable that was obtained by the electrical method (solid squares). The thermal measurements were somewhat higher and need to be confirmed. The ac loss determined electrically was 1.26 W/m at an I_{peak} of 2100 A, corresponding to $I_{peak}/I_c \sim 1$. Monoblock model calculations predict an ac loss of about 1.1 W/m for this I_{peak}/I_c ratio (~1) and layer geometry. The measured results are somewhat greater than the monoblock model predictions.

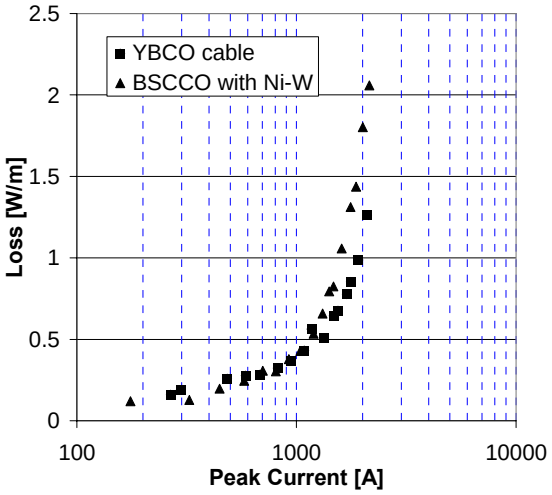

Fig. 1.77. Alternating current loss of the 1.25-m YBCO cable.

Figure 1.78 includes data (solid triangles), on the ac losses of a two-layer BSCCO cable that was wound with 50-µm Ni-5at%W tapes to simulate the presence of a Ni-5at%W substrate. As can be seen in Fig. 1.78, the ac loss of the BSCCO and YBCO cables are comparable up to about 1200 A peak and beyond that the YBCO cable loss is somewhat lower. The cable was wound on the same size former (25.4 mm diam) and had approximately the same critical current (2200 A) as the YBCO cable that was measured in this paper. At low peak currents the ferromagnetic contributions of both cables was about the same and this is due to the fact that the amount of Ni-5at%W exposed to axial and azimuthal ac fields was about the same in each case.

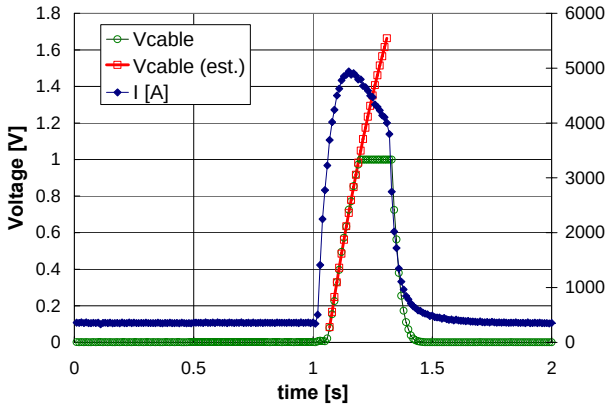

Fig. 1.78. Overcurrent pulse of 4.9 kA applied to the YBCO cable.

Fault overcurrent simulation tests were performed on the YBCO cable. Pulse lengths of 0.3 to 0.5 s were used to simulate 18 to 30 cycles of short-circuit faults in a 60-Hz line. This is a typical time for action by a second contingency fault protection device. During the first series of 0.5-s pulse length tests, the maximum pulse current was limited to between 3 and 3.5 kA. In the second series of 0.3 s pulse length tests, the maximum pulse current was increased to 4.9 kA (over twice the critical current) after V-I measurements showed no degradation from the lower pulse currents. Fig. 1.78 shows the overcurrent waveform for a peak current of 4.9 kA for a nominal duration of 0.3 s on the YBCO cable. The cable survived with a modest temperature rise of a few K at the end of the pulse. This commercial-grade HTS cable demonstrated the feasibility of second-generation YBCO tapes in an ac cable application.

1.6 Cryogenic Dielectrics Initiative

I. Sauers, D. R. James, A. E. Ellis, M. O. Pace (UT-K), S.W. Schwenterly and E. Tuncer

1.6.1 Workshop on Cryogenic Dielectrics

A workshop on cryogenic dielectrics was held on Sunday, October 16, 2005, in conjunction with the Institute of Electrical and Electronics Engineers, Inc., (IEEE) Conference on Electrical Insulation and Dielectric Phenomena (CEIDP), October 16–19, 2005, in Nashville, Tennessee. The workshop brought together many experts in the field of cryogenic dielectrics from the United States, Europe, and Asia. There were ten presentations, followed by a panel discussion on future needs. The organizers were Dr. Isidor Sauers and Dr. Randy James, from ORNL; Dr. Alan Wolsky from Argonne National Laboratory; and Dr. Toshikatsu Tanaka, from Waseda University, Japan. Financial support came from the IEEE Dielectrics and Electrical Insulation Society (DEIS) and the International Energy Agency Implementing Agreement on Superconductivity. There were approximately 50 attendees, making the workshop one of the most successful workshops hosted by the CEIDP and DEIS. A photograph from the workshop is shown in Figure 1.79. There was broad agreement on the need for the DOE Cryogenic Dielectrics Initiative to advance this enabling technology for superconducting grid applications.

Fig. 1.79. Photograph taken at the Workshop on Cryogenic Dielectrics, October 16, 2005.

1.6.2 Breakdown Survival Probability with Aging

The probability of breakdown after successive shots of impulse voltage has been considered to attempt to assess the safety factor needed for dielectric materials when testing requires multiple withstands (e.g., ten positive and ten negative withstand impulse voltages). Figure 1.80 shows the survival

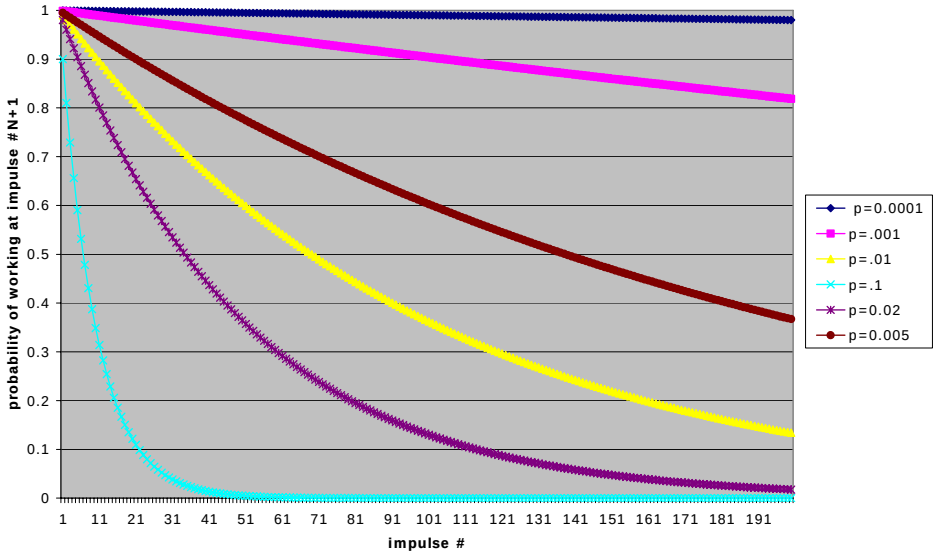

Fig. 1.80. Survival probability as function of number of impulses for different single shot breakdown probabilities.

probability for successive shots for different single shot breakdown probabilities ranging from p = 0.0001 to p = 0.1. An aging factor is also included in Fig. 1.81 for the case of p = 0.01, which shows a decrease in the survival probability.

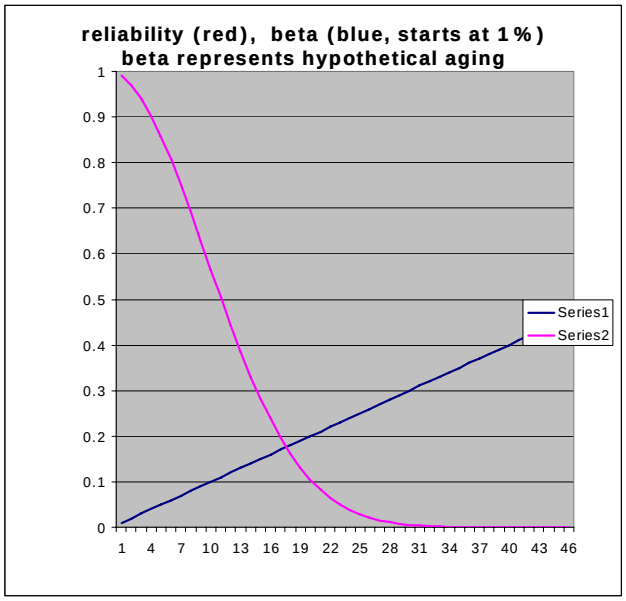

Fig. 1.81. Survival probability for the case of p=0.01 including an arbitrary aging factor (shown by the straight line).

1.6.3 Breakdown Statistics

Electrical breakdown of dielectric materials is a statistical process due largely to undefined factors in the manufacture and processing of these materials (including, for example, impurities and voids). Therefore it is important to understand the statistical nature of breakdown and use the statistical methods that can best describe the data and can afford the engineer the tools needed to determine appropriate safety factors in the dielectric design. Here we investigate the dielectric breakdown data of polyimide at 77 K and focus on the applicability of the Weibull distribution. A new distribution function is also proposed, and its utility and strength are illustrated distinctly by employing the Monte Carlo method. The proposed expression is shown to be superior to the Weibull one as shown explicitly with the presented numerical procedure.

The Weibull statistics is based on an empirical survival probability Ps(x) [4, 5],

$$Ps(x) = 1 - F(x) \tag{1}$$

where, F(x) is the failure probability. The survival probability Ps(x) in Eq. (1) is given as follows for the Weibull statistics [5],

$$W(x) = \exp[-A(x - x_W)^B] \tag{2}$$

where $x \geq x_W$ and A, B, and x_W are fitting parameters on the measurement of observable x. The data are sorted from the lowest observable value to the highest one, and the indices, *I*, of the sorted observables are later used to assign the failure probability $F(x_i)$ of the appropriate observed value x_i [6],

$$F(x_i) = (i - 0.3)(N_d + 0.4)^{-1} \tag{3}$$

where N_d is the total number of observables. The data are sorted before the computation in Eq. (3). They are later analyzed as plotted in the scale

$$\ln (\ln[1- F(x_i)]^{-1}) \text{ vs } x_i \text{ or } \ln(x_i) \tag{4}$$

A nonlinear curve fit algorithm shall yield the free parameters (A, B, x_W) in Eq. (2), where the significant engineering design parameter, the lower bound for the failure probability, is given by x_W. Since the Weibull expression in Eq. (2) is an empirical expression, another, more suitable expression can also be adopted as the failure probability F(x). We therefore propose an exponential function for the failure probability:

$$G(x) = \alpha\, x^{-1} \exp(-\beta(x-x_G)) \tag{5}$$

where $x \geq x_G$ and the free parameters α, β, and x_G are acquired from the same nonlinear curve fit algorithm. Expressions similar to Eq. (4) are extensively used in investigating the resistivity of ionic conductors [7]. The numbers of unknowns in Eq. (2) and Eq. (4) are actually equal, meaning that the number of degrees of freedom are the same for two expressions for a given set of observables. The survival probability, Ps, for values lower than x_G and x_G is one, $Ps(x < x_j) = 1$ for j = (W, G).

The validity of the expressions mentioned above was tested on actual breakdown measurement data. The measurements were performed on polyimide samples, which were 25 μm thick. The breakdown experiments were performed with a ramp alternating voltage with a fixed ramp rate of 500 Vs^{-1} at 77 K; in an LN environment. In the analysis part of the paper the breakdown voltage V_{bd} data is assigned as observable x.

In Figs. 1.82 and 1.83 the mean values of the obtained fit parameters are presented with error bars, which are their standard deviation. It is striking that as the number of the observables are decreased both expressions indicate quite different characteristics. The results for the Weibull expression are only shown for large N_d (> 20) due to large error bars, which do not vary considerably as N_d is lowered. First, the mean values for the lower bound of the Weibull statistics x_W do not change smoothly as in the proposed expression, $3.2 \leq x_W \leq 4.1$. However, the deviation in the values is increasing quite absolute, which raises questions about validity and trustworthiness of this expression. Second, the other fit parameters, A and B, also follow similar trends, an increase in standard deviation with decreasing N_d.

The proposed expression in Eq. (4) on the other hand shows a more desirable tendency, where the unknown parameters α, β, and x_G do not vary significantly when the number of the observables, N_d, are close to the whole number of data points (N = 37), the standard deviations are small. It is surprising that the free fit parameter β is very close to 2, which might be used to characterize the behavior of different materials and breakdown processes and should be kept in mind for future investigations. Unlike the Weibull expression, the proposed one illustrates a significant dependence on the number of observable N_d used when the number of observables are decreased; the dependencies of the mean and standard deviation appear to be N_d dependent. This sort of behavior is expected and might be desired because the statistical uncertainty is increased with decreased N_d . Therefore, it can be comprehended that the model parameters of Eq. (4) converge to some finite value as N_d approaches to higher values than the one we have for the polyimide. Also, the ratio of relative errors obtained for the two models, x^2_G, $(x^2_W)^{-1}$, yield approximately nine out of ten cases in the Monte Carlo analysis that are less than one, meaning that the proposed expression is more likely to express the polyimide breakdown data than the Weibull expression. We have also assumed that N = 19 and repeated the numerical procedure on this set of data, and we have observed a similar behavior for both expressions.

One concrete implementation of the presented method and the proposed expression is that when we make a new set of measurements and increase the total number of observables, the Weibull statistics yield different fit parameters than the analysis with fewer data points for a given material. The proposed expression on the other hand would not differentiate the old analysis values with low number of observables. Therefore it might be more appropriate to use the proposed expression to describe the

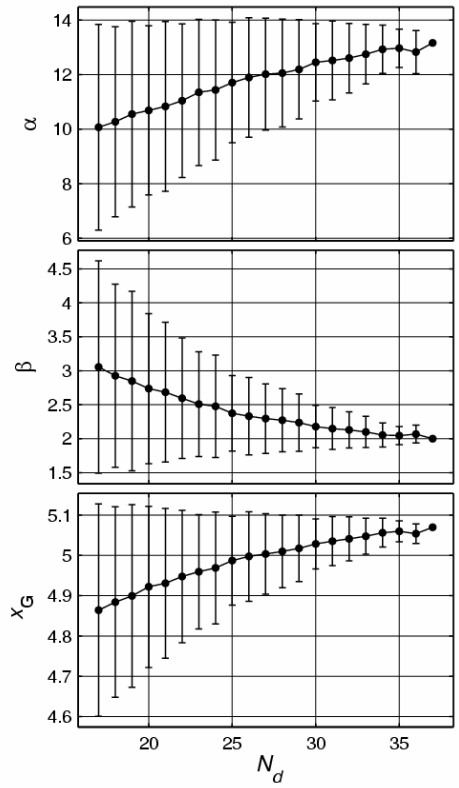

Fig. 1.82. Mean of fitting parameters as a function of number of observables N_d in the Monte Carlo method for the Weibull expression in Eq. (2). The data are presented as error bars which are calculated from the standard deviation of the data.

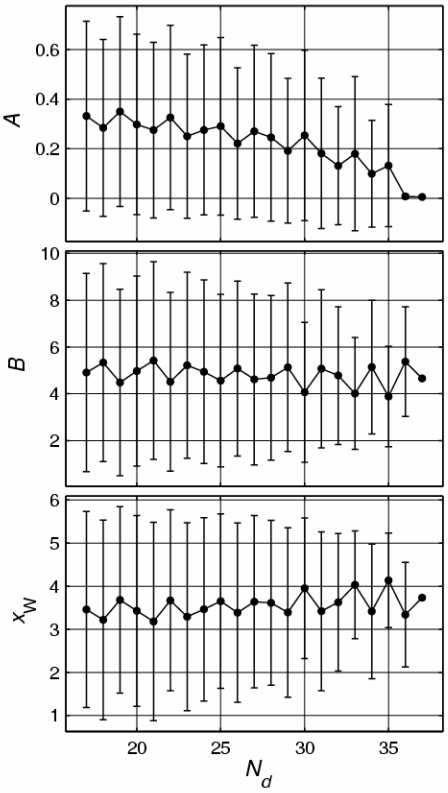

Fig. 1.83. Mean of fitting parameters as a function of number of observables N_d in the Monte Carlo method for the proposed expression in Eq. (4).

breakdown properties of materials. Due to the presented differences between both models, we are confident that the proposed expression is superior to the Weibull expression when the statistics of the data are challenged by the Monte Carlo method.

1.6.4 Kapton® and PVA Breakdown

Breakdown measurements of Kapton® (polyimide) and polyvinyl alcohol (PVA) films were made. Silver electrodes were evaporated onto the films in a vacuum evaporator, and a mask was used to make multiple electrodes on the same film (Fig, 1.84). The Kapton® breakdown was done at room temperature in an oil bath. The PVA was measured in an open LN bath. A multiple electrode arrangement was used to permit making multiple measurements without disturbing the sample in LN (Fig. 1.85). The breakdown data for Kapton® (Fig. 1.86) showed good consistent results. Figure 1.87 shows breakdown data for PVA in LN.

Fig. 1.84. Kapton® film with 19 silver electrodes.

Fig. 1.85. PVA sample in open LN bath.

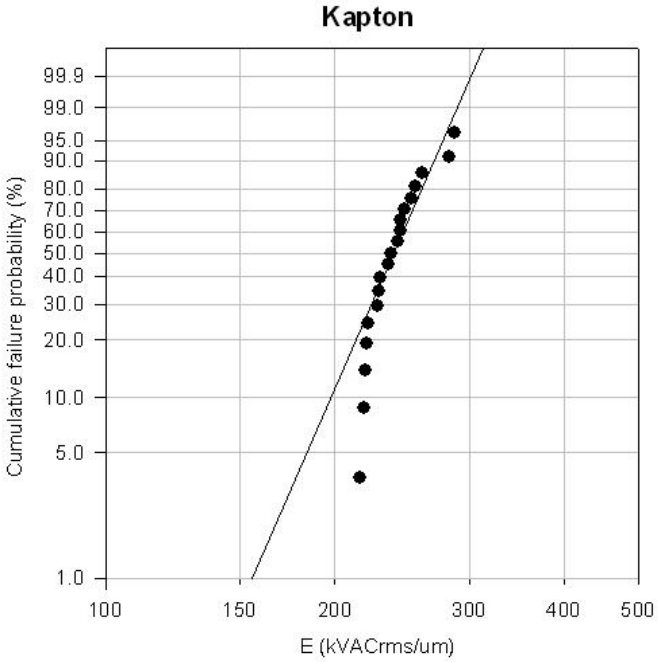

Fig. 1.86. Weibull plot of Kapton® breakdown.

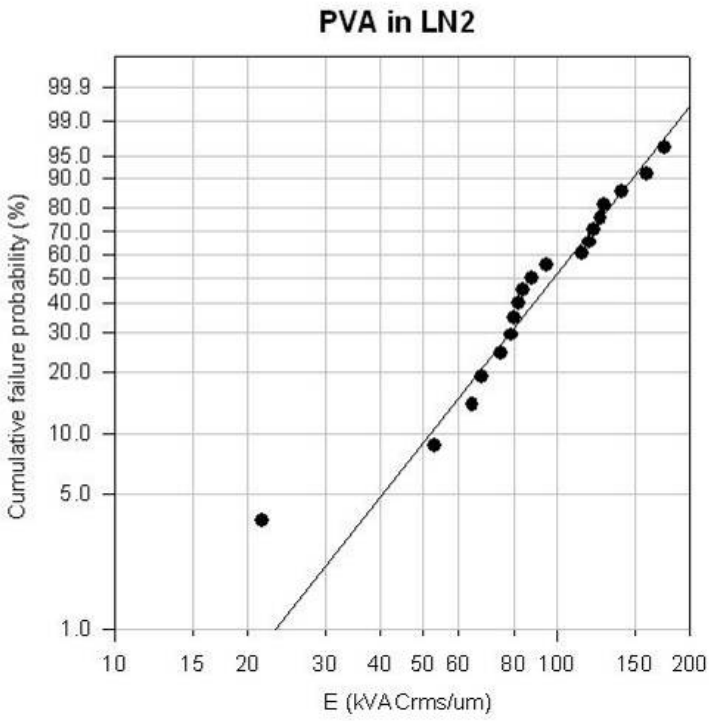

Fig. 1.87. Weibull plot of unfilled PVA breakdown data in LN.

1.6.5 Keith Nelson Visit

Professor Keith Nelson from Rensselaer Polytechnic Institute in New York visited ORNL and presented a talk on his recent work on nanocomposite dielectrics. One of the applications discussed was composite dielectrics that work at cryogenic temperatures using nanoparticle fillers.

1.6.6 Partial Discharge Analyses for the 5-m Triaxial Cable

Data analyses have been performed on the PD patterns that were measured for the 5 m cable high-voltage tests that were performed last spring. Background noise coming from the cryogenic system pump inverter circuits was subtracted and the data were analyzed as the total number of pulses for integrated charge amplitudes as a function of phase angle as shown in Fig. 1.88. PD is observed to increase above 33.1 kV_{rms}. A plot of the total number of counts as a function of applied voltage is shown in Fig. 1.89.

1.6.7 Polyvinyl Alcohol Breakdown Test

PVA is a polymeric material for which the breakdown strength increases with decreasing temperature. Experiments have been conducted on PVA composites using nanoparticle filler at cryogenic temperature (open bath LN at 77K). In this case the filler is TiO_2 formed in situ from $TiCl_3$. In general, when particles of micron size or larger are added to a dielectric material, the breakdown strength decreases. However, the nanoparticle composite increased in strength over the pure PVA. This is a significant finding, indicating that breakdown strength can be increased through the addition of nanometer-sized particles. Figure 1.90 shows the increase in breakdown strength of PVA from approximately 95 kV/mm for the unfilled polymer film, to approximately 135 kV/mm for the nanoparticle composite, at a weight fraction of 0.08. At higher concentrations there is a gradual decrease in breakdown strength with increasing particle content.

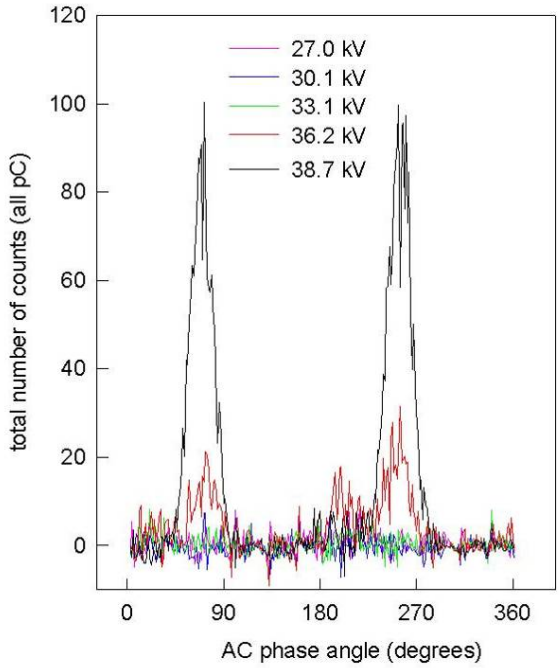

Fig. 1.88. PD as expressed by total number of pulses integrated over all pulse amplitudes as a function of phase angle at several applied voltages.

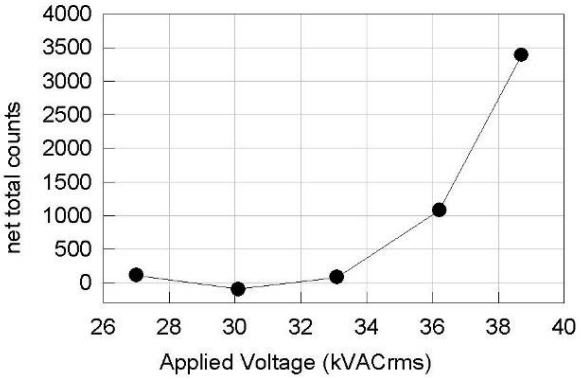

Fig. 1.89. Plot of total PD pulses as function of applied voltage after background noise is subtracted, leaving true PD signal, and showing threshold above 33 kV_{rms}.

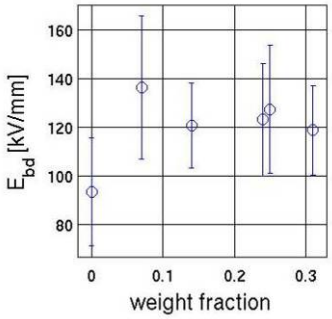

Fig. 1.90. Breakdown strength as a function of nanoparticle filler content.

1.6.8 HV Testing of New Dielectric Tape Materials

High-voltage (ac breakdown) testing was conducted on a candidate synthetic tape provided by WES that can be used either in conventional transformer or in a HTS transformer at cryogenic temperatures. Initial testing was conducted at room temperature in air and in oil. The ORNL tape tester consists of five pairs of electrodes for multiple breakdown measurements (Fig. 1.91). Data were obtained for the synthetic tape in air and immersed in oil, plotted in the form of a Weibull probability distribution plot (Fig. 1.92). The tape had a significantly higher breakdown strength when tested immersed in oil than it had when tested in air, indicating that the tape is, indeed, impregnated with the oil to provide the full insulation strength of the tape. For comparison, Fig. 1.92 depicts air breakdown at the same gap as the tape thickness (0.076 mm). The air breakdown value is consistent with the Paschen curve for breakdown in air at the small gap employed in these measurements. Table 1.11 summarizes the mean breakdown strengths. The breakdown strength of the oil-impregnated synthetic candidate tape is 56.99 ± 5.75 kVrms/mm. The non-oil-impregnated tape is only 15.16 ± 4.63 kVrms/mm, which is smaller by nearly a factor of 4. High-voltage testing of the tape will also be conducted in LN. It will be interesting to see whether the tape fully impregnated with LN will show comparable or higher dielectric strength.

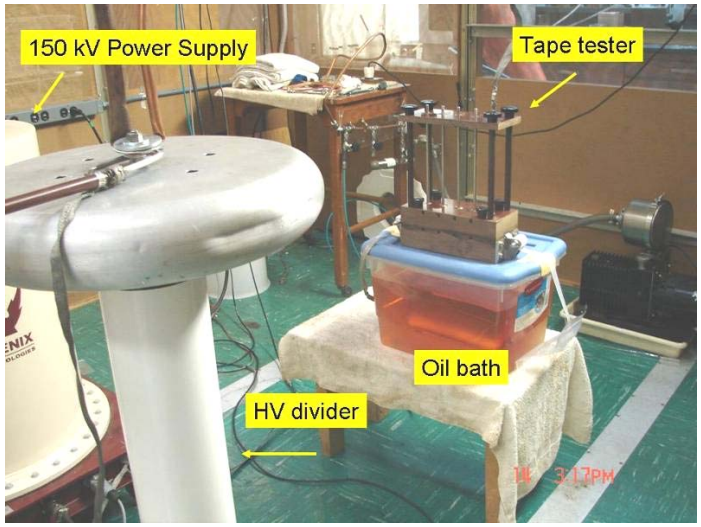

Fig. 1.91. High-voltage testing set-up using ORNL tape tester.

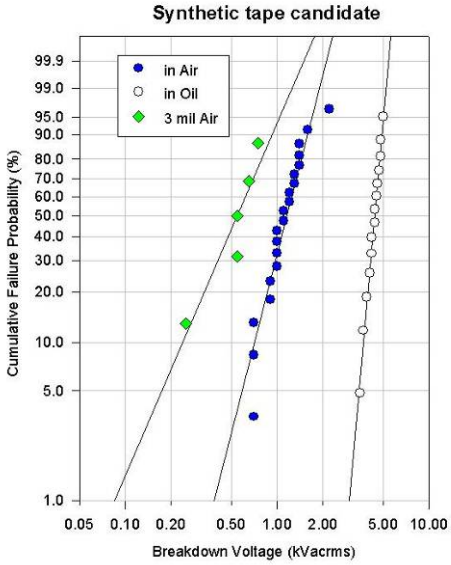

Fig. 1.92. Breakdown data, in the form of a Weibull probability distribution plot, obtained for a synthetic tape candidate immersed in oil (white circles) and compared with breakdown in air (blue circles). Also plotted is air breakdown (no tape) at a gap of 0.076 mm (green diamonds).

Table 1.11. Mean breakdown strength of candidate synthetic tape (ST)

Sample type	BD, kV/mm	STDEV, kV/mm
Air	7.22	2.45
ST in air	15.16	4.63
ST in oil	56.99	5.75

1.6.9 Nanocomposite Dielectrics

Previously prepared nanocomposite dielectric samples composed of PVA and TiO_2 were made with two separate aqueous solutions; one for PVA and one for TiO_2. The structural analysis of a sample using this approach showed that the particles were poly-dispersed, and there were several large (around 200 nm), needle-like particles. The particles might negatively influence the dielectric properties of the composite sample. To improve the quality of nanoparticles and to have a uniform monodispersed particle-polymer mixture, the sample preparation method has been altered.

Now samples are prepared by a second method, in which all the components are mixed in the same jar for a short time. A thin film was drop-cast, and unlike the previous samples, the samples made using the second method were completely transparent. The dielectric breakdown strength was measured and was compared with the previous sample. It was observed that there is a small amount of further improvement in the breakdown strength of the PVA-TiO_2 composite. Figure 1.93 illustrates the improvement, showing the unfilled PVA and composites prepared with two methods and are shown in a Weibull breakdown statistics plot. The first filled sample that was made contained 27 wt % TiO_2; the second sample contained 26 wt %TiO_2 .

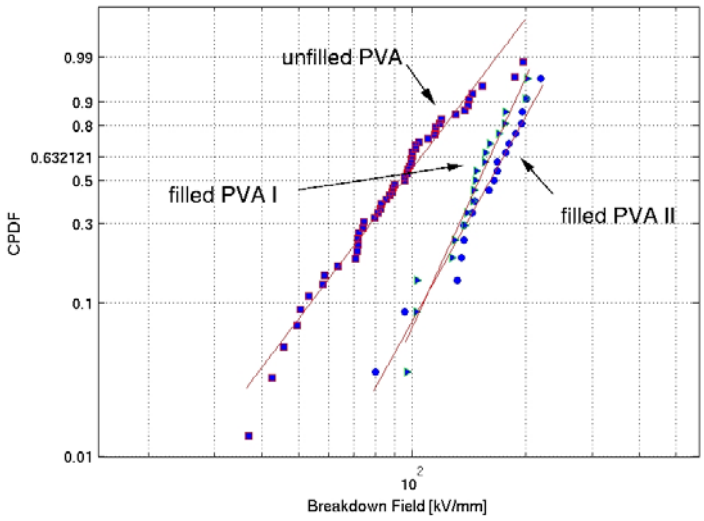

Fig. 1.93. Weibull breakdown probability plot of pure and nano-filled PVA. There are two sets of data for the filled PVA, as indicated in the plot, where the filled PVA using the refined method shows further improvement in the breakdown field strength.

1.6.10 Breakdown Strength of LN and of Solid Materials in LN

Data on generic materials were analyzed and were prepared for publication in two conference papers. Breakdown voltages of some commonly used cryogenic dielectric materials were reported for several practical electrode geometries that might be encountered in HTS applications. The goal is ultimately to come up with useful design rules to make the high-voltage design of cryogenic power equipment more routine and reliable. The results here have been done mostly in a bath of LN at atmospheric pressure, which allows bubbles to form. Since bubble formation can reduce dielectric strength, the values reported here should be considered "worst case" for design purposes. One of the most commonly used materials is G-10, a commercially available formulation of fiberglass reinforced plastic known for its good electrical insulation strength and mechanical strength. The glass content reduces its thermal contraction and expansion so that it performs well at cryogenic temperatures without cracking. Table 1.12 gives the breakdown strength for three different cylinders. The strength decreases with an increase in wall thickness, which is consistent with the so-called volume effect where the strength is dependent upon distribution of defects throughout the material. Other commercially available materials such as Ultem (polyetherimide) and G-10 disks were also studied.

Table 1.12. Impulse breakdown strength of G-10 fiberglass-reinforced plastic cylinders
Cylinder dimensions: 203 mm (8 in) × 89 mm (3.5 in) inside diam

Cylinder thickness, mm (in.)	Air			LN		
	Strength, V/mm	Breakdown	Pressure, bar	Strength, kV/mm	Breakdown	Pressure, bar
1.6 (1/16)	250	Flashover	1	47.9	Puncture	1
1.6 (1/16)	---	---	1	48.5	Puncture	1
3.2 (1/8)	---	---	1	40.0	Puncture	6
12.7 (1/2)	---	---	1	25.4	Flashover	6

Figure 1.94 shows breakdown voltages for LN gaps for sphere-plane geometry. Relatively large gaps were studied to determine how effective increasing the gap would be toward increasing the breakdown voltage in LN. It is known that increasing the surface area of the electrode or stressed volume of the LN reduces the breakdown strength. It was found in this work that increasing the gap did not increase significantly the breakdown voltage or surface flashover (SFO) beyond a certain gap. Other means for holding off higher voltages need to be investigated systematically such as the design of the triple-junction area (electrode, liquid, solid junction) for SFO, the role of barriers or partitions, and controlling the initiation of the discharge in the critical highly stressed areas.

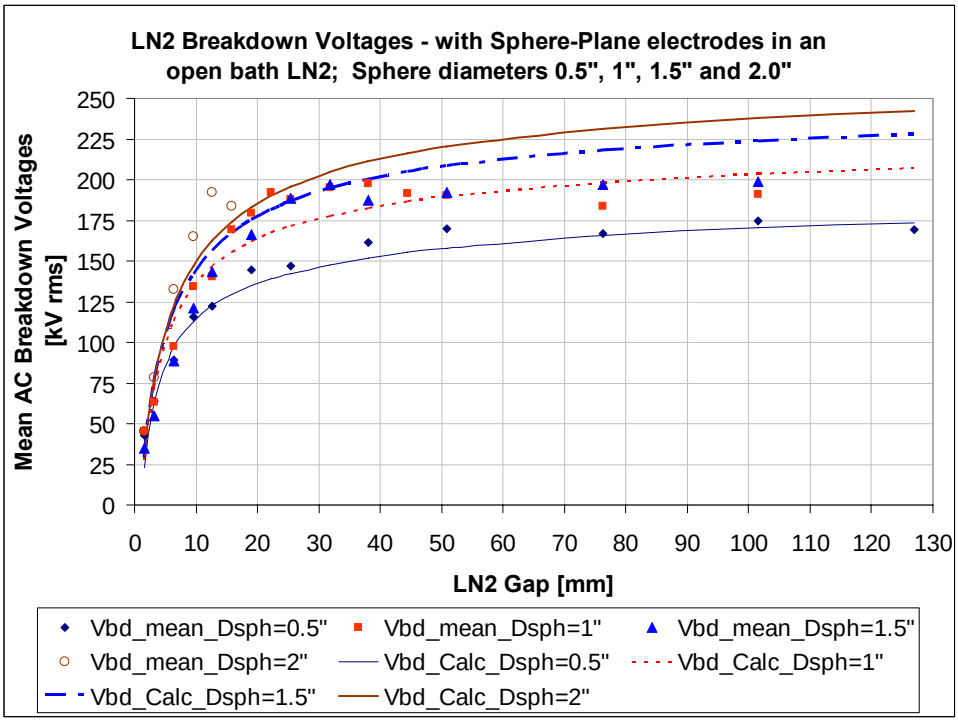

Fig. 1.94. Breakdown voltages of LN gaps for sphere-plane geometry. The curves are power law fits to the data.

1.7 SPI Oversight/Readiness Reviews

M. J. Gouge

M. J. Gouge presented a talk (*Superconducting Grid Applications and Cryogenic Dielectrics*) at the Cryogenic Dielectrics Workshop on October 16, 2005 in conjunction with the IEEE Conference on Electrical Insulation and Dielectric Phenomena (CEIDP), October 16–19, 2005 in Nashville, Tennessee. No readiness reviews were conducted in this period. ORNL supported DOE-HQ by providing feedback on questions from potential vendors on DOE OE SBIR proposal topics. M. J. Gouge organized a second-generation conductor requirements session and a cable issues session for the 2006 Wire Development Workshop.

No readiness reviews were conducted by ORNL in this period. ORNL supported DOE-HQby providing technical reviews of DOE:OE SBIR proposals in the cryogenics area. M. J. Gouge organized a second-generation conductor requirements session and a cable issues session at the 2006 Wire Development Workshop in St. Petersburg, FL. One of the recommendations from the 2005 SPI project(s) peer review was for the three cable project teams to look at generic technical issues in HTS cables. A generic cable issues session was organized on February 1, 2006 at the Wire Development Workshop and all three SPI cable teams participated. Real progress was made towards understanding external (fault currents due to grid shorts) and internal (such as loss of vacuum in the cryostat) faults and their impact on the LN cooling system. A presentation was also made on cryostat reliability and lightning protection issues.

1.8 References

1. Gockenbach, E. and W. Hauschild, *IEEE Electrical Insulation Magazine* **16** (6), 11–16, 2000.

2. A. O. Ijaduola, *Physica C* **403**, 163.

3. F. Grilli, S. P. Ashworth, and S. Stavrev, *Physica C* **434**,185.

4. E. J. Gumbel, *Statistics of Extremes*, Columbia University Press, New York, 1958.

5. W. Weibull, *J. Appl. Mech*. **18**, 293–97, 1951.

6. L. A. Dissado, *J. Phys. D: Appl. Phys.* **23**, 1582–91, 1990.

7. E. Tuncer et al., *J. Chem. Phys.* **122**, 084901, 2005.

2. Technical Progress in Wire Development

2.1 Superconductor Wires

M. Parans Paranthaman

High-Temperature Superconductor (HTS) wires are so efficient that they can carry up to 140 times the power of conventional copper wires of the same size. The potential uses for HTS wires in electric power applications include underground transmission cables, oil-free transformers, superconducting magnetic-energy storage units, fault current limiters, high-efficiency motors, and compact generators. Electricity grid losses have grown to be more than 10% of all electricity generated due to resistance and other losses in conventional equipment, and blackouts highlighted transmission bottlenecks in the United States in 2003. Efficiency and reliability will be enhanced when new transmission technologies are used that have reduced line losses and that have the capability to carry more current for a given size of conductor. Superconductors have virtually no electrical resistance; therefore they can carry current with no electrical energy loss. They come in two types, namely, low- and high-temperature superconductors. Low-temperature superconductors (LTSs) work at only very frigid temperatures: near –452°F. Equipment made with LTS wires can be expensive to operate because they need to be chilled with liquid helium. Equipment made with high-temperature superconductor (HTS) wires, however, work at relatively warmer temperatures (near –320°F) and require less-expensive liquid nitrogen to operate.

Oxide HTSs, discovered in the late 1980s, are moving into the second generation of their development. The first generation relied on bismuth strontium calcium copper oxide ($[Bi,Pb]_2Sr_2Ca_2Cu_3O_{10}$, abbreviated as BSCCO or 2223); the second generation is based on yttrium barium copper oxide ($YBa_2Cu_3O_{7-x}$, abbreviated as YBCO or 123), which has the potential to be less expensive and to perform better. One of the main challenges in developing high-performance superconductors has been the brittleness of many of the most promising materials because they need to be drawn into wires that can carry current. Yet recent developments allow fabrication of superconductor wires and tapes. This article describes the present state of superconductor wires and tapes, successes and challenges, and projected applications.

Following the discovery of HTSs, notably BSCCO and YBCO, researchers all around the world have searched for ways to fabricate affordable flexible wires that will carry high current density. The U.S. Department of Energy's (DOE's) target cost for the conductor is close to the current copper wire cost ($10/kA-meter). The near-term goal is to achieve HTS wire in 100-m lengths with current-carrying capacity of 300 A. Robust, high-performance HTS wire will certainly revolutionize the electric power grid and various other electric power equipment as well. American Superconductor Corporation (AMSC) and Sumitomo (Japan) have been widely recognized as the world leaders in manufacturing the first-generation (1G) HTS wires based on BSCCO materials and the oxide-powder-in-tube (OPIT) process. Typically, 1G HTS wires carry critical currents (I_c) of greater than 125 A in piece lengths of several hundreds of meters at the standard 0.41-cm width and ~210-μm thickness. However, due to the higher cost of 1G wire and the intrinsic properties of YBCO, the researchers shifted their efforts toward the development of second generation (2G) YBCO wires or tapes. One of the main obstacles to the manufacture of commercial lengths of YBCO wire has been the phenomenon of weak links (i.e., grain boundaries formed by the misalignment of neighboring YBCO grains are known to form obstacles to current flow). Low angle boundaries between superconducting YBCO grains, which are produced by careful alignment of the grains, allow more current to flow. In fact, below a critical misalignment angle of 4°, the critical current density (J_c) approaches that of YBCO films grown on single crystal substrates. The schematics of the 1G and 2G HTS wire architectures are shown in Fig. 2.1. Typically, 2G HTS wires have three components: a flexible metal substrate, buffer layers, and YBCO superconductor layers. Several methods were developed to obtain biaxially textured metal substrates suitable for fabricating high-performance YBCO coated conductors. They are ion-beam assisted deposition (IBAD), Rolling-Assisted

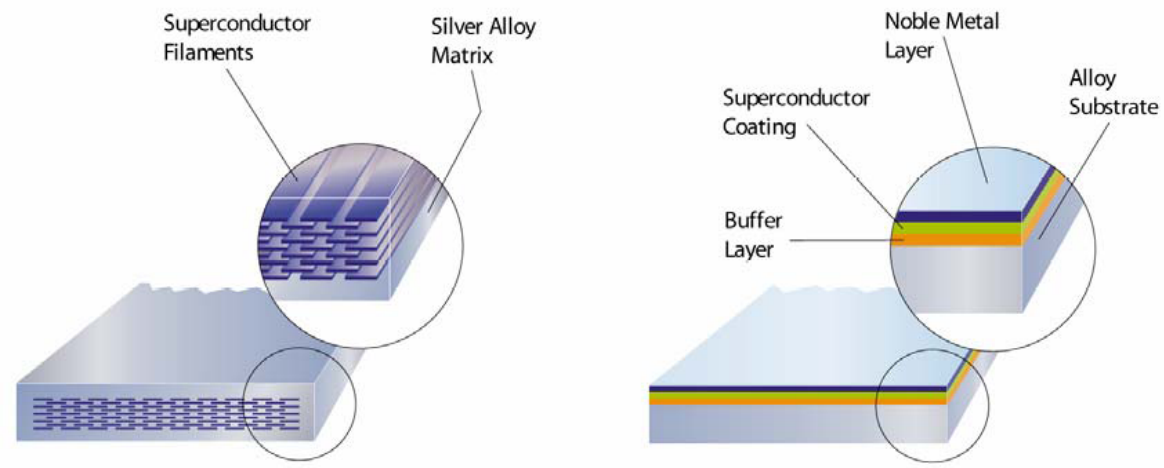

First-generation BSCCO wire multifilamentary composite

Second-generation YBCO coated conductor tapes Courtesy: American Superconductor

Fig. 2.1. The schematics of the first- and second-generation HTS wires.

Biaxially Textured Substrates (RABiTS™) and inclined-substrate deposition (ISD). The industry standard for characterizing the 2G wire is to divide the current by the width of the wire. For example, for both a 3-μm-thick YBCO layer carrying a critical current density of 1 MA/cm^2 and a 1-μm-thick YBCO layer carrying a critical current density of 3 MA/cm^2, the electrical performance would be 300 A/cm-width. When converted to suit the industry standard of 0.4-cm-wide HTS wire, the value would correspond to 120 A, which is comparable to that of the commercially available 1G wire. Further increase in YBCO film thickness or critical current density, or finding a way to incorporate two layers of YBCO in single wire architecture (either double sided coating or joining two YBCO tapes face to face) would then give performance exceeding 1G wire; i.e., a high overall engineering critical current density (J_E) at 77 K. The other important advantages of 2G wires over 1G wire are that YBCO has better in-field electrical performance at higher temperatures, it is produced by a potentially lower-cost process, and its alternating-current (ac) losses are low.

In the IBAD process, the ion beam is used to grow textured buffer layers onto a flexible but untextured metal, typically a nickel superalloy. After the initial announcement of the IBAD process to grow textured yttria-stabilized zirconia (YSZ) layers by Iijima et al. (Fujikura Ltd., Japan, 1992), researchers at Los Alamos National Laboratory (LANL 1995) perfected the process and achieved high performance YBCO films on IBAD-YSZ templates. To date, three IBAD templates, namely YSZ, gadolinium zirconium oxide ($Gd_2Zr_2O_7$, GZO) or magnesium oxide (MgO), are being used to make YBCO tapes. The RABiTS™ process developed at Oak Ridge National Laboratory (ORNL 1996) uses thermomechanical processing to obtain flexible, cube-textured nickel-alloy substrates. Both buffers and YBCO superconductors are then deposited epitaxially on the textured nickel alloy substrates. The starting substrate serves as a structural template for the YBCO layer, which has substantially fewer weak links. For comparison, wires made by the OPIT process (1G wire) are limited to a higher cost because the majority component is high-purity silver. However, in the RABiTS™ process or IBAD process, silver is replaced by a low-cost nickel alloy, which allows for fabrication of less-expensive HTS wires. In the ISD process, the textured buffer layers are produced by vacuum-depositing material at a particular angle on an untextured nickel alloy substrate. After the discovery of the ISD-YSZ process by Hasegawa et al. (Sumitomo, Japan, 1996), THEVA/Technical University of Munich, Germany perfected the reel-to-reel MgO buffer layer texturing by ISD on Hastelloy tape (2003). Recently, several industries have demonstrated that they can produce 2G wires in 10- to 100-m lengths with critical currents ranging from 50 to 300 A/cm-width based on either IBAD or RABiTS™ technology. Very recently, the THEVA group has produced its first 40-m-class YBCO-tape-based ISD-MgO technology (2005). The 37-m-long, 10-mm

wide wire based on a nonmagnetic Hastelloy C276 steel tape with ISD aligned MgO buffers exhibited an average critical current of 158 A. This demonstration would correspond to 5846 A-m (158 A × 37 m).

Methods to produce textured templates for growing high-performance YBCO coated conductor wires include IBAD-YSZ, IBAD-MgO, IBAD-GZO, ISD-MgO, and RABiTS™. These five templates are being used with high-deposition-rate YBCO processes such as trifluoroacetate-based metal-organic deposition (MOD), metal-organic chemical vapor deposition (MOCVD), and high-rate pulsed-laser deposition (PLD) to deposit the superconductor films. The main challenge is to combine the oriented template concept and superconductor deposition process and fabricate HTS tapes in kilometer lengths. Industries from the United States and Japan are leading in this area while industries from Europe, Korea, and China are trying to catch up with them. The present status of the 2G HTS wires is summarized in Table 2.1.

Table 2.1. Present status of the 2G HTS wire technology (as of July 2005)

Country/Organization	Length (m)	Critical current at 77K (A/cm width)	Substrate/ HTS deposition process
US- American	34	186	RABiTS™/MOD
Superconductor	10	272	RABiTS™/MOD
	short samples	~400	RABiTS™/MOD
US- SuperPower	100	70	IBAD/PLD
	97	104	IBAD/MOCVD
	short samples	407	IBAD/MOCVD
Japan-Sumitomo	35	175	RABiTS™/PLD
	short samples	357	RABiTS™/PLD
	10	130	RABiTS™/MOD
	short samples	196	RABiTS™/MOD
	105	NA	RABiTS™
Japan- Showa Electric	6	69	IBAD-GZO/MOD
	230	NA	RABiTS™ (Ni-W)
Japan-Fujikura	105	126	IBAD-GZO/PLD
	short samples	~300	IBAD-GZO/PLD
	255	NA	IBAD-GZO
Japan-ISTEC	100	159	IBAD-GZO/PLD
	4	270	IBAD-GZO/MOD
	short samples	413	IBAD-GZO/MOD
	220	NA	IBAD-GZO
Europe-THEVA	37	158	ISD-MgO/Evap.
	5	237	ISD-MgO/Evap.
	1	422	ISD-MgO/Evap.
Europe-Edison Spa	2	120	RABiTS™/Coevap.
	short samples	220	RABiTS™/Coevap.
Korea- KERI	4	97	RABiTS™/Coevap.
	1	107	RABiTS™/PLD

RABiTS™ = Rolling-Assisted Biaxially Textured Substrates; MOD = Metal Organic Deposition; IBAD = Ion-Beam Assisted Deposition; PLD = Pulsed Laser Deposition; MOCVD = Metal Organic Chemical Vapor Deposition; GZO = Gadolinium Zirconium Oxide, $Gd_2Zr_2O_7$; ISD = Inclined-Substrate Deposition; MgO = Magnesium Oxide; Evap. = Electron Beam Evaporation; Coevap. = Electron Beam Co-evaporation.
Courtesy: Oak Ridge National Laboratory and Los Alamos National Laboratory

The following choices can enhance 2G wire attributes:

- substrate
  - mechanical properties (especially critical tensile stress)
  - ferromagnetism (ac loss due to ferromagnetic loss)
  - resistivity (eddy current loss)
  - grain size (hysteretic loss)
- HTS deposition process
  - throughput
  - availability of long piece lengths
  - in-field performance, especially perpendicular to tape
  - thick films (small aspect ratio for less hysteretic loss)
- stabilizer
  - surround stabilizer, fully encapsulating wire or stabilizer on one side
  - rounded edges for direct dielectric integration
  - sharp edges

A number of issues related to the development of power applications for 2G HTS wires by the year 2010 were identified at the DOE Coated Conductor Development Roadmapping Workshop II (Washington D.C., July 28–29, 2003). They included low ac loss, design and current-carrying capacity of the stabilizer, conducting substrates, and alternate conductor designs. (See Table 2.2 for specifications.)

Table 2.2. Specifications for 2G HTS wires to be developed for power applications by 2010

Geometry	Face-to-face; neutral axis; two-sided coating
Length (m)	100–1000
Width (mm)	≤ 4.1
Bend diameter (cm)	2–3.5
Stress (MPa)	200 (300 @ 77 K)
Irreversible strain limit (%)	
Tension	0.4–0.6
Compression (for magnets)	0.3–1
J_E (A/cm^2)	10,000–20,000 at 30–65 K and 3 T (or at operating conditions)
I_c (A)	100–200 at operating conditions
I_c (A/cm-width)	1000 @ 77 K and self-field
ac loss (W/kA-m)	0.25
n value	≥ 14
Large-volume price ($)	10/kA-m

Source: U.S. Department of Energy Coated Conductor Development Roadmapping Workshop II, Washington D.C., July 28–29, 2003.

In summary, five different templates, IBAD-YSZ, IBAD-GZO, IBAD-MgO, ISD-MgO and RABiTS™, have been developed and superconductivity companies around the world are in the process of taking the technology to the pilot scale to produce commercially acceptable 100-m lengths. In addition, three different deposition methods, MOD, MOCVD, and high-rate PLD, have been used to demonstrate high critical current in 100-m lengths of YBCO coated conductors. The current research in the area of HTS wire technology is to increase the flux-pinning properties of YBCO superconductor wires and to reduce the ac loss in these wires for various military applications.

2.1.1 Outlook

DOE has funded three different Superconductivity Partnership Initiative (SPI) projects to demonstrate the use of HTS power cables for electric transmission and distribution. They are Long Island HTS power cable, Albany HTS power cable, and Columbus HTS power cable. The goal of the Long Island HTS power cable project is to demonstrate a 610-m, 600-MW HTS power transmission cable

operating at 138 kV in the Long Island Power Grid, the first ever installation of a superconductor cable in a live grid at transmission voltages. The goal of the Albany HTS power cable project is to demonstrate the technical and commercial viability of HTS cables by operating a 350-m superconducting cable, including a 30-m section made from 2G HTS wire, between two Niagara Mohawk substations. The goal of the Columbus HTS power cable project is to complete the development, installation, and testing of a 200-m, three-phase HTS power cable at a substation in Columbus, Ohio. This project will demonstrate how a triaxial HTS cable may be used in the future to replace existing oil-filled underground copper cables and to greatly increase the capacity of the power link. The future of HTS wire technology research depends heavily on the successful demonstration of these power cables.

2.1.2 References

M. P. Paranthaman and T. Izumi, Editors, "High-Performance YBCO-Coated Superconductor Wires," *MRS Bulletin* 29, No. 8, August 2004.

Y. Iijima, N. Tanabe, O. Kohno, and Y. Ikeno, *c*60 , 769, 1992.

X. D. Wu, et. al., *Appl. Phys. Lett.* 67, 2397, 2995.

A. Goyal, et. al., *Appl. Phys. Lett.* 69, 1795, 1996.

K. Hasegawa, et. al., *Appl. Supercond.* 4, 487, 1996.

W. Prusseit, et. al., *Physica C* 392, 801, 2003

J. L. Macmanus-Driscoll, et. al., *Nature Materials* 3, 439, July 2004.

2.2 Deposition of Rare Earth Tantalate Buffers on Textured Ni-W Substrates for a YBCO Coated Conductor Using CSD Approach

M. S. Bhuiyan, M. Paranthaman, A. Goyal, L. Heatherly, and D. B. Beach

Thin films with pyrochlore structures have been used as potential buffer layers for YBCO coated conductors, due to their thermal stability and their chemical and structural compatibility with the substrates and superconducting layers. Due to the extensive compositional range of the compounds which exhibit the pyrochlore structure with an $A_2B_2O_7$ stoichiometry, there are a variety of actual and potential applications for these materials. Examples include dielectric materials, catalysts, solid electrolytes, thermal barrier coatings as well as actinide host phases for nuclear waste encapsulation. The pyrochlore structure under study has the chemical formula A_3BO_7, where A (Lu to La) is a larger trivalent cation and B (Ta) is a pentavalent cation.

During the last two decades, lot of effort has been made to prepare superconducting YBCO-coated conductors using different physical and chemical deposition methods. Such conductors generally consist of a YBCO film grown on a metallic substrate with intermediate buffer layers. Buffer layers act as chemical barriers between the YBCO layer and the substrate in order to prevent the metal diffusion into YBCO as well as the oxidation of the metallic surface during YBCO film deposition. Highly textured YBCO films are essential to obtaining high critical currents. In the Rolling-Assisted Biaxially Textured Substrate (RABiTS™) approach, starting from a perfect textured metallic substrate the buffer layers have to transfer the textured structure of the substrate onto the YBCO layer, providing an improved lattice matching. For industrial applications long lengths of coated conductors are required. As an alternative to the relatively higher cost and complexity of vacuum deposition techniques, chemical solution deposition (CSD) techniques have emerged as viable low-cost nonvacuum methods for producing ceramic oxide powders and films. These processes offer many desirable aspects, such as precise control of metal oxide precursor stoichiometry and composition, ease of formation of epitaxial oxides, relatively easy scale-up of the film and possibly low cost.

CSD can be applied to grow both buffer and superconducting layers for long coated conductors. Highly textured nickel-based RABiTS™ is mostly used for such solution-based processes. Different

chemical routes are available to develop precursor solution chemistry. These are mainly the well known classical sol-gel route and the metal-organic decomposition (MOD) route, distinguished by the chemical reactivity of the starting chemicals toward water. Sol-gel routes commonly start from metal alkoxides, whereas water-insensitive starting substances such as metal carboxylates or metal β-diketonates are mainly used for MOD methods. Details about the different CSD routes are available in the literature. The precursors are normally applied onto various substrates using dip, slot die, or spin coating; both slot die and dip coating are particularly useful for the preparation of films in longer lengths. Although many buffer layers have been developed in the last few years using CSD or physical vapor deposition, none can act as a single layer buffer to perform all the necessary functionalities. Recently, we have demonstrated that rare earth niobate can be used as a single-layer buffer.

Here, we report for the first time the successful growth of textured film of rare earth tantalates (RE_3TaO_7) on Ni-W substrates, its texture, and microstructural analysis. Various rare-earth oxides and rare-earth pyrochlore films have been grown epitaxially on biaxially textured Ni and Ni-3 at.% W (Ni-W) substrates by solution-based methods as buffer layers for YBCO coated conductors. We demonstrated previously that RE_3NbO_7 can be used as a single buffer layer for YBCO coated conductor. Therefore, we believe that solution-deposited RE_3TaO_7 films with good epitaxy are potential candidates for use as a single buffer layer in RABiTS™ architecture.

The precursor solutions for the rare earth tantalates were prepared via two different routes, namely sol-gel and metal-organic decomposition (MOD), depending on the solution chemistry. Solution chemistry can play an important role on film orientation, morphology, and oxygen diffusivity. Using the sol-gel precursor route, La, Eu, and Gd tantalates were prepared; using the MOD precursor route, Ce tantalate was prepared. All solution manipulations for the sol-gel precursor were carried out under an atmosphere of argon using standard Schlenk techniques. The starting reagents were weighed in an argon-filled inert-atmosphere glove box. The chemical reagents lanthanum isopropoxide (Alfa, La 40%), tantalum ethoxide (Alfa, 99.999%) and 2-methoxyethanol (Alfa, spectrophotometric grade) were used as received from Alfa Aesar; Eu acetate and Gd acetate were purified beforehand. For the purification of Eu acetate first, Eu acetate was prepared by the reaction of europium oxide (Alfa, 99.99%) with a fivefold excess of 25% acetic acid at 80°C for 1 h. The resulting clear solution was filtered, and the solvent was removed. The precipitate was dried at 120°C under dynamic vacuum for 16 h. Finally a small amount of sample was allowed to react with excess water and was then dried to constant weight at 35°C to form the hydrated sample. The weight gain of this sample allowed us to estimate that the degree of hydration of the europium acetate after vacuum drying is about 1.5 ± 0.2. A similar procedure was followed for the purification of Gd acetate.

A solution of europium and tantalum methoxyethoxide in 2-methoxyethanol for the Eu_3TaO_7 film was prepared in a 250-mL flask by weighing 1.1107 g of europium acetate, 0.457 g of tantalum ethoxide, and 20 mL of 2-methoxyethanol. The flask was refluxed for 1 h at 130°C, and the contents were rediluted with additional 2-methoxyethanol. The distillation/redilution cycle was repeated twice more to ensure complete formation of europium and tantalum methoxyethoxide. The final concentration was adjusted to produce 15 mL of a 0.3 M stock solution.

The MOD precursor solution was prepared in ambient atmosphere. The reagents Ce acetylacetonate (Alfa, hygroscopic), tantalum ethoxide (Alfa, 99.999%), acetic acid (Alfa, 99.9985%) and methanol (Alfa, 99.9%) were used as received from Alfa Aesar. The precursor solution for Ce tantalate was prepared by dissolving 1.3123 g of Ce acetylacetonate in acetic acid and methanol with continuous stirring for 10 min in a hot plate at 60°C. Then, 0.4063 g of tantalum ethoxide was added, and the final volume of the solution was adjusted to obtain a 0.4 M precursor solution. The chemical reagents, solvents ,and the molarities for all the precursors are listed in the Table 2.3.

Table 2.3. Starting chemicals, solvents and molarities for the RE_3TaO_7 precursors (10 mL)

Rare earth tantalates	Chemical reagents	Stoichiometric quantity (g)	Solvent and reactant	Final molarity (M)
La_3TaO_7	La-isopropoxide/ Ta-ethoxide	0.9485/0.4063	2-methoxyethanol	0.4
Ce_3TaO_7	Ce-acetylacetonate/ Ta-ethoxide	1.3123/0.4063	Acetic acid and methanol	0.4
Eu_3TaO_7	Eu-acetate/ Ta-ethoxide	0.7405/0.3045	2-methoxyethanol	0.3
Gd_3TaO_7	Gd-acetate/ Ta-ethoxide	1.0032/0.4063	2-methoxyethanol	0.4

The solutions were spin-coated onto 2 × 1 cm short cube-textured Ni-W substrates at 4000 rpm for 30 s, followed by heat treatment in a reducing atmosphere of Ar-4% H_2. After a 5-min purge with an Ar-4% H_2 gas mixture at room temperature, the samples were introduced into a preheated furnace. Then, at the end of heat-treatment cycles, the samples were quenched to room temperature in the same atmosphere. The heating and cooling rates were in the range of 350 to 400°C/min, annealing time 15 to ~60 min, and annealing temperatures were 1050 to ~1100°C. The lanthanum tantalate film was heat-treated at 1100°C for 60 min. Ce and Gd tantalates were heat-treated 1100°C for 15 min. Eu tantalates were heat treated at 1050°C for 15 min.

The RE_3TaO_7 films were characterized by using X-ray diffraction (XRD) for phase purity and texture, scanning electron microscopy (SEM) for homogeneity and microstructure and atomic force microscopy (AFM) for surface roughness analysis. A Philips model XRG3100 diffractometer with CuKα radiation was used to record the θ–2θ XRD patterns. The texture analysis was performed using a Picker 4-circle diffractometer. Phase analysis was done using XRD patterns, and the lattice parameters were determined using the MDI-JADE 6 program. The microstructure analyses of these samples were performed using a Hitachi S-4100 field emission SEM and Digital Instruments nanoscope AFM in contact mode.

X-ray diffraction patterns for the solution-deposited RE_3TaO_7 films grown on Ni-W substrates were collected at room temperature. From the XRD patterns, it was found that the tantalates of La, Ce, Eu, and Gd grow epitaxially with a pyrochlore structure. Room temperature XRD patterns for the pyrochlore-phase RE_3TaO_7 thin films deposited on Ni-W substrates are shown in Fig. 2.2. Due to highly *c*-axis (004) oriented films, there are no (222) peaks present in the patterns. There is a clear indication of (004) peak shifting to the right as a result of decreasing ionic radii of the rare earth elements. Therefore, the lattice parameters of the pyrochlore phase increases with an increase in ionic radii.

Figure 2.3 shows the cell parameters of the RE_3TaO_7 pyrochlore as a function of the ionic radii, and as expected, the cell parameters decrease linearly with decrease in ionic radii (*x*-axis) from left to right. The data in Fig. 2.3 are the actual experimental values calculated from the XRD patterns using MDI-JADE 6 program. From the linear equation shown inside the graph, cell parameters for other RE_3TaO_7 pyrochlores, can be easily calculated. From La to Gd tantalates the cell parameter decreases from 11.0544 Å to 10.6883 Å, which is about 3.3% decrease.

To grow a textured film by a chemical solution deposition, a highly textured substrate is very important. Cube-textured Ni-W substrates serve the purpose with an excellent in-plane (ϕ scan) and out-of-plane (ω scan) texture of full width at half maximum (FWHM) about 8.0° and 5.5°, respectively. All the RE_3TaO_7 films grown by solution deposition on Ni-W substrates have an out-of-plane texture with FWHM value in the range of 3.6 to 7.2° in the rolling direction (RD; $\phi = 90°$), 3.8 to 11.4° in the transverse direction (TD; $\phi = 0°$) and the in-plane texture in the range of 7.5 to 8.5°. The ω (out-of-plane) and ϕ (in-plane) scans of La_3TaO_7 films on the Ni-W substrates are shown in Fig. 2.4. The La_3TaO_7 film has a good out-of-plane and in-plane texture with FWHM of 3.6° and 7.5°, respectively. These values indicate that the La_3TaO_7 film has improved texture compared with that of Ni-W substrates ($\Delta\omega = 5.4°$, $\Delta\phi = 7.8°$). A list of FWHM values for the RE_3TaO_7 films is given in Table 2.4. Table 2.4 shows that with

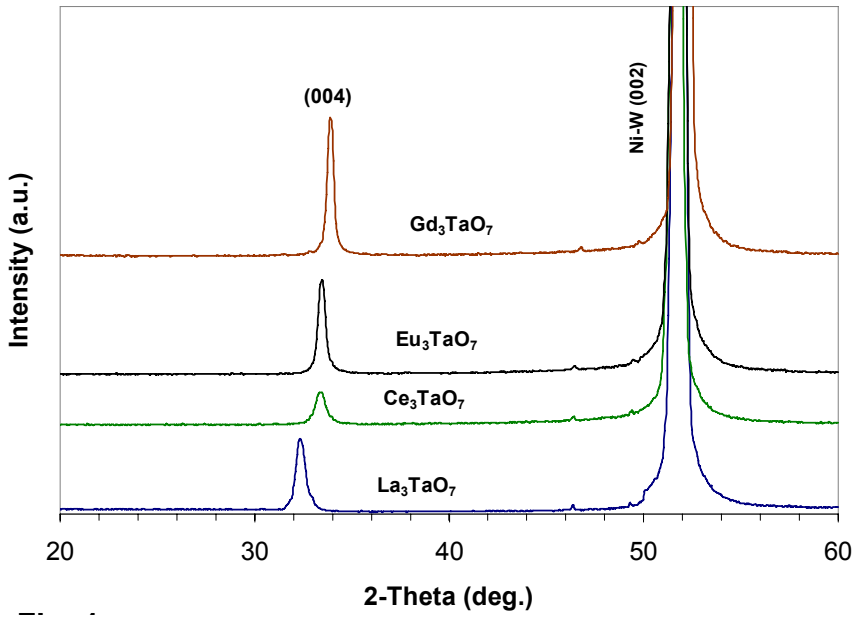

Fig. 2.2. A typical θ-2θ scan for 20-nm-thick RE_3TaO_7 (RE = La, Ce, Eu, and Gd) films grown on biaxially textured Ni-W substrates using chemical solution deposition. RE_3TaO_7 films have preferred c-axis orientation.

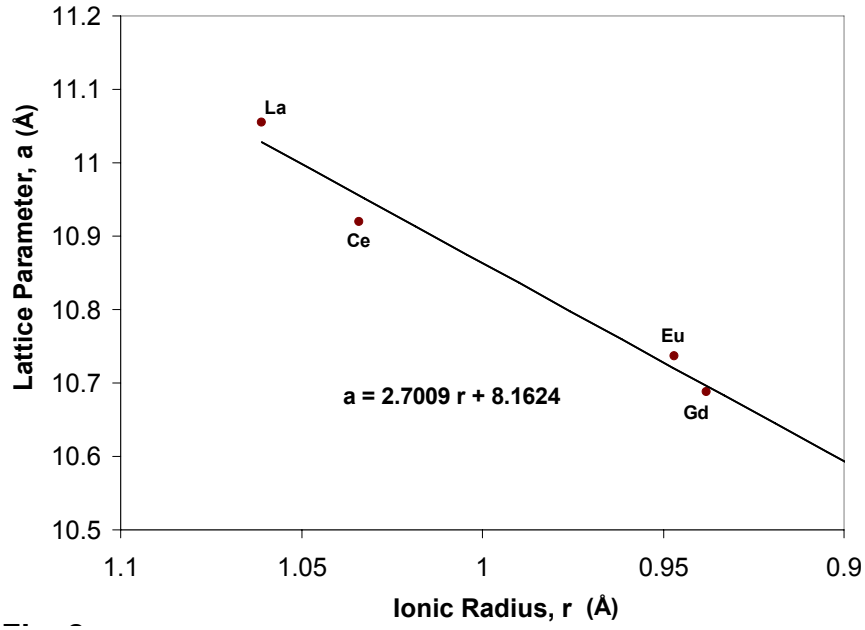

Fig. 2.3. Lattice parameters of the solution grown RE_3TaO_7 films on Ni-W substrates. All data points represent experimental value calculated by MDI-JADE6 software.

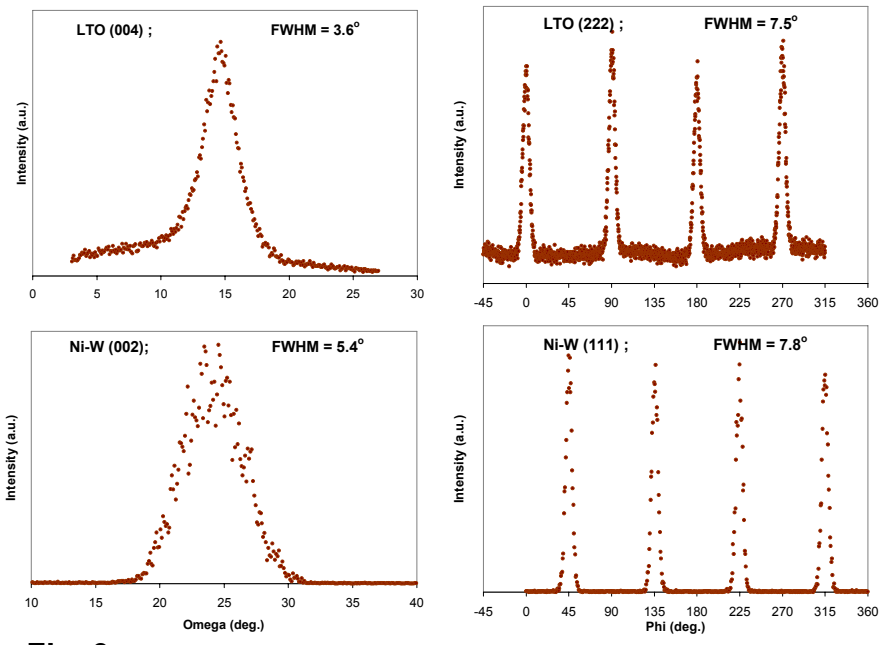

Fig. 2.4. The ω and ϕ scans obtained for La_3TaO_7 film grown on textured Ni-W substrate. The FWHM values for each scan are shown inside the patterns.

Table 2.4. Texture data of RE tantalate films on Ni-W substrates

Rare earth tantalates	FWHM of RE_3TaO_7			FWHM of Ni-W substrates		
	Δω (ϕ = 0) (deg.)	Δω (ϕ = 90) (deg.)	Δϕ (deg.)	Δω (ϕ = 0) (deg.)	Δω (ϕ = 90) (deg.)	Δϕ (deg.)
La_3TaO_7	3.8	3.6	7.5	7.6	5.4	7.8
Ce_3TaO_7	8.0	5.4	7.8	7.6	5.2	7.4
Eu_3TaO_7	9.9	7.0	8.6	8.2	5.4	7.7
Gd_3TaO_7	11.4	7.2	8.5	8.2	5.5	7.6

the increase in ionic radii of the rare earth element, the RE_3TaO_7 films improve in texture quality. The reason for this behavior is not clear at this moment; however it can be the growth kinetics and /or interfacial relation between the substrate and the buffer layer.

The typical (222) pole figures for all the four RE_3TaO_7 films grown on the Ni-W substrate are shown in Fig. 2.5, which indicates single cube-on-cube epitaxy. Microstructure studies of the RE_3TaO_7 films exhibit a uniform, smooth and crack free surface morphology. SEM micrographs for RE_3TaO_7 films on textured Ni-W substrates using spin-coating is shown in Fig. 2.6. Most of the Ni-W grain boundary grooves on the Ni-W surface were found to be well covered. Figure 2.6 also shows that the film surface is continuous as well as crack free. AFM images of the RE_3TaO_7 films showed typical average surface roughness (Ra) of the RE_3TaO_7 films is around 2.5 nm, which is comparable to that of underlying Ni-W substrates. We observed large number of small particles at the surface of the tantalate films using AFM. They are crystallized tantalates and could be beneficial for achieving YBCO films with improved flux-pinning properties.

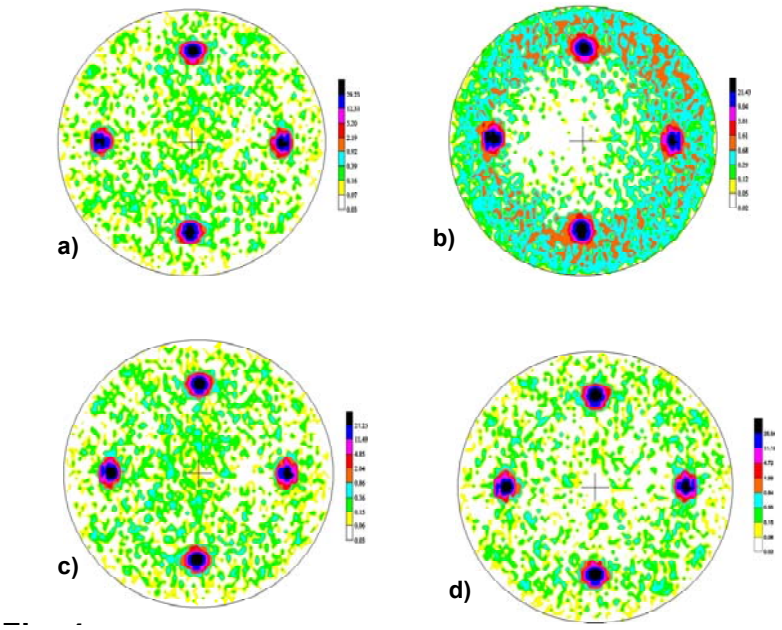

Fig. 2.5. The typical (222) log scale pole figures of 20-nm-thick (a) La_3TaO_7, (b) Ce_3TaO_7, (c) Eu_3TaO_7, and (d) Gd_3TaO_7 films grown on textured Ni-W substrate.

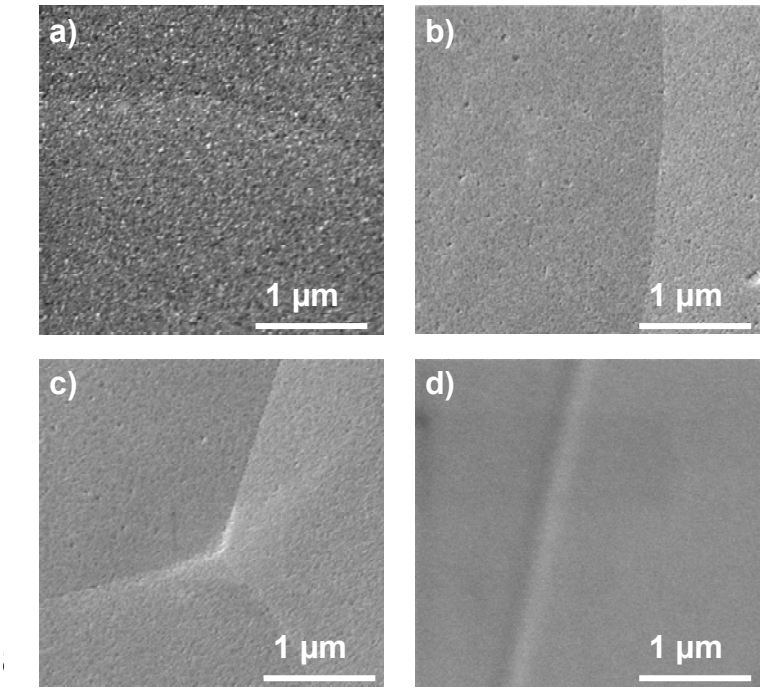

Fig. 2.6. EM micrographs obtained on 20-nm-thick films of (a) La_3TaO_7, (b) Ce_3TaO_7, (c) Eu_3TaO_7, and (d) Gd_3TaO_7.

Lattice matching between the substrates and the films plays a key role in the epitaxial growth. The pseudocubic cell parameters for the RE_3TaO_7 films closely follow that of the Ni-W substrates (see Table 2.5). Since the films were grown epitaxially with a 45° rotation with respect to the substrates, the pseudocubic cell parameters were calculated by dividing cubic cell parameter with $2\sqrt{2}$. The percentage

Table 2.5. Lattice parameters for RE_3TaO_7
(Ni; a = 3.524 Å, YBCO; a = 3.823 Å, b = 3.887 Å, c = 11.68 Å)

Rare earth tantalates	Lattice parameter, a (Å)	Pseudo lattice parameter, a/2√2 (Å)	Lattice mismatch vs Ni (%)	Lattice mismatch vs YBCO (%)
La_3TaO_7	11.054	3.908	10.91	2.37
Ce_3TaO_7	10.92	3.861	9.56	1.12
Eu_3TaO_7	10.737	3.796	7.72	-0.58
Gd_3TaO_7	10.688	3.779	7.23	-1.02

lattice mismatch between these films and the substrates is 7.2 to 10.9%. Surprisingly, although film containing higher-ionic-radii rare earth elements has a higher lattice mismatch, it gives better epitaxy. A careful study of interface and growth kinetics is necessary to understand this phenomenon. The advantage of tantalates over other oxides such as niobates is twofold: Ta^{5+} is very stable compared with Nb^{5+} under reducing conditions; and reactive sputtering of tantalates should be easier than sputtering niobates because alloy targets are readily available. The lattice mismatch between the tantalate buffers and YBCO is much smaller than that of YSZ buffers and YBCO. Because the lattice mismatch between YBCO and RE_3TaO_7 is in the range of -0.6% to +2.4%, it offers the possibility of using RE_3TaO_7 films as buffer layers for coated conductors. Efforts are under way to deposit YBCO by PLD/MOD techniques on these films.

In summary, for the first time, we have grown textured RE_3TaO_7 (RE = La, Ce, Eu, and Gd) films on cube textured Ni-W substrates using chemical solution deposition. A trend in improved texture was observed in RE_3TaO_7 films containing rare earth elements having higher ionic radii. Also, sharper texture was found in La_3TaO_7 films than in Ni-W substrates. Microstructural studies of the RE_3TaO_7 films deposited on rolled Ni-W substrates using a solution process reveal a smooth, dense, and crack-free surface. Average surface roughness was well comparable to that of underlying Ni-W substrates. Such epitaxial, dense, and crack-free RE_3TaO_7 buffer layers can be used as suitable buffer candidates for YBCO coated conductors.

2.3 All MOD Buffer/YBCO Approach to Coated Conductors

M. P. Paranthaman, S. Sathyamurthy, L. Heatherly, P. M. Martin, A. Goyal (ORNL), T. Kodenkandath, X. Li, C. L. H. Thieme, and M. W. Rupich (AMSC)

The main objective of this research is to develop an all-solution buffer/YBCO process to fabricate potentially lower-cost, high-performance second-generation coated conductors, with a DOE goal to demonstrate a critical current of 300 A/cm width for all-solution buffers on RABiTS™. Efforts are being made to replace the existing three-layer architecture of all-physical vapor deposition (PVD) Y_2O_3/YSZ/CeO_2 with simplified layers comprising multiple-functional buffers deposited by industrially scalable methods such as chemical solution deposition. Chemical solution deposition offers significant cost advantages over PVD processes. Solution coating is amenable to complex oxides. Slot-die coating and ink-jet printing techniques can be used to scale up solution processes. Both $La_2Zr_2O_7$ (LZO) and CeO_2 buffers have been identified as potential candidates for this study. The challenge is to match the performance of American Superconductor's current PVD buffer stack with a performance of 250 A/cm in short lengths with buffers deposited using non-vacuum-based solution techniques. Last year, we demonstrated a transport critical current density of 1.75 MA/cm^2 on 0.8-μm-thick metal-organic deposition (MOD) YBCO films grown on all MOD CeO_2 (one coat)/LZO(three coats)/Ni-3W substrates.

These translate to a critical current of 140 A/cm-width at 77 K and self-field. The lattice mismatch between LZO and Ni-W substrate is about 7.9 %. The performance of the LZO layer has been further enhanced by reducing the lattice mismatch; texture was also improved, by inserting a thin Y_2O_3 seed layer. Here, we report our recent results obtained on the improved MOD-CeO_2/$La_2Zr_2O_7$ templates.

Biaxially textured Ni-W (5 at. %) substrates were obtained by annealing the as-rolled substrates in the presence of Ar/H_2 (4%) gas at 1100 to 1150°C for 1 h. The substrates used were 1 cm wide and 75 μm thick. All the textured substrates were sulfurized by annealing at 750°C in a 1×10^{-5} Torr of H_2S gas atmosphere to get the desired sulfur c (2 × 2) superstructures at the Ni-5W surface. Reel-to-reel electron beam evaporation was used to deposit 10-nm-thick Y_2O_3 seed layers. The LZO precursor solution was prepared from lanthanum isopropoxide (Alfa, La 40% assay), zirconium n-propoxide in n-propanol (Alfa, 70%), and 2-methoxyethanol (Alfa, spectrophotometric grade). The details of the solution preparation were reported earlier. A total cation concentration of about 0.75 M was used to grow 100-nm-thick LZO films in a single coat. Spin-coating was used to deposit LZO at a spin rate of 2000 rpm for 30 s. The spin coated films were then crystallized at 1100°C for 15 min in a flowing mixture Ar/H_2 4% gas. To obtain thicker LZO films, the coating and crystallization steps were repeated several times. American Superconductor's proprietary process was used to deposit about 60-nm-thick MOD-CeO_2 and 0.8-μm-thick MOD-YBCO on MOD-LZO

X-ray Diffraction (XRD) was used to characterize the phase purity and texture of the films; atomic force microscopy (AFM) was used to observe the microstructure of both buffers and YBCO. The resistivity and transport critical current density were measured by using a standard four-point probe technique.

Typical θ-2θ XRD patterns for both single-coat (100-nm-thick) and two-coat (200-nm-thick) $La_2Zr_2O_7$ films on Y_2O_3-seeded Ni-5W substrates are shown in Fig. 2.7. These scans indicate the presence of a strong *c*-axis (004) aligned films. The ω and ϕ scans for a 200-nm-thick $La_2Zr_2O_7$ film grown on Y_2O_3-seeded Ni-5W substrates are shown in Fig. 2.8. The full width at half-maximum (FWHM) values for $La_2Zr_2O_7$ (004) and Ni-5W (002) were 4.7° and 5.9°, respectively. Similarly, the FWHM values for $La_2Zr_2O_7$ (222) and Ni-5W (111) were 6.7° and 7.7°, respectively. Both in-plane and out-of-plane textures of $La_2Zr_2O_7$ layers were improved over 1° as compared to the underlying Ni-5W substrates. This improvement in $La_2Zr_2O_7$ texture is mainly due to the insertion of PVD-Y_2O_3 layer. The (222) X-ray pole figures for 200-nm-thick $La_2Zr_2O_7$ film grown on Y_2O_3-seeded Ni-5W substrate are shown in Fig. 2.9. The presence of a fourfold symmetry indicates the presence of a single cube-textured $La_2Zr_2O_7$ film.

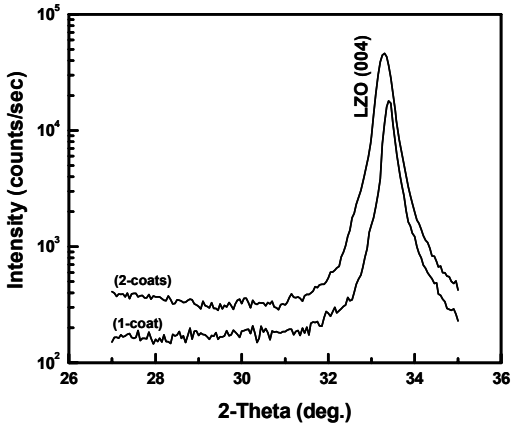

Fig. 2.7. A typical θ-2θ scan for 100-nm-thick (one-coat) and 200-nm-thick (two-coat) $La_2Zr_2O_7$ films grown on 10-nm-thick Y_2O_3 buffered Ni-5W substrates using metal-organic deposition. $La_2Zr_2O_7$ has a preferred *c*-axis orientation.

Highly textured MOD-CeO_2 and MOD-YBCO films were grown on 200-nm-thick $La_2Zr_2O_7$/Y_2O_3-seeded Ni-5W substrates. As shown in Fig. 2.10, the typical θ-2θ scan for a 0.8-μm-thick YBCO film grown on MOD-CeO_2/MOD-$La_2Zr_2O_7$/Y_2O_3/Ni-5W substrate indicated the presence of a strong *(00l)* reflection of YBCO films. In addition, small impurities of $NiWO_4$, NiO, unreacted BaF_2, $BaCeO_3$, and polycrystalline YBCO were also present. The transport properties of the MOD-YBCO film on MOD-buffer template are shown in Fig. 2.11. The self-field critical current of 200 A/cm (J_c = 2.5 MA/cm^2) was achieved. From the angular measurement data (right side of the Fig. 2.11), a strong *ab*-plane peak with a very small *c*-axis peak was observed at 77 K and 1 Tesla. The enhancement of critical current from 140 A/cm (last year) to 200 A/cm (this work) is mainly due to the combination of both thin e-beam Y_2O_3 and MOD-$La_2Zr_2O_7$

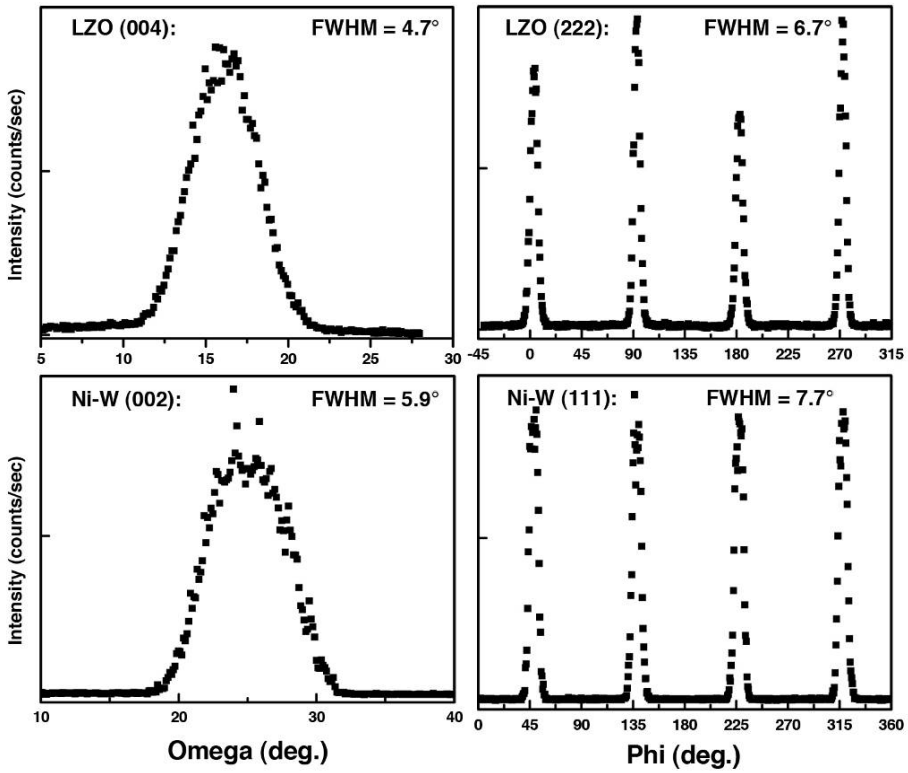

Fig. 2.8. The ω and ϕ scans for a 200-nm-thick $La_2Zr_2O_7$ film grown on 10-nm-thick Y_2O_3 buffered Ni-5W substrates using metal-organic deposition. The FWHM values for each scan are shown inside the scans.

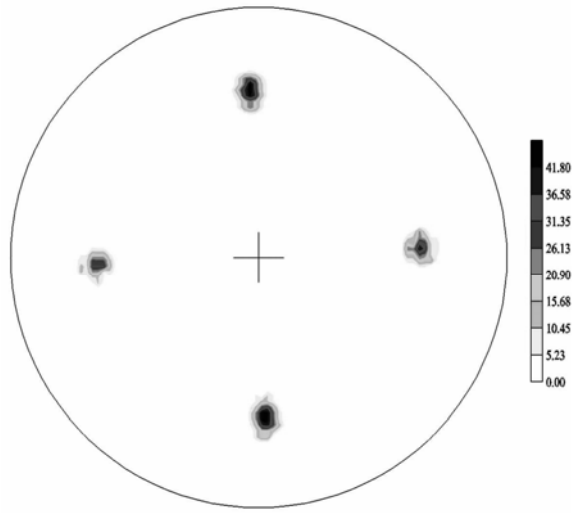

Fig. 2.9. (222) pole figure for a 200-nm-thick $La_2Zr_2O_7$ film grown on 10-nm-thick Y_2O_3 buffered Ni-5W substrates using metal-organic deposition.

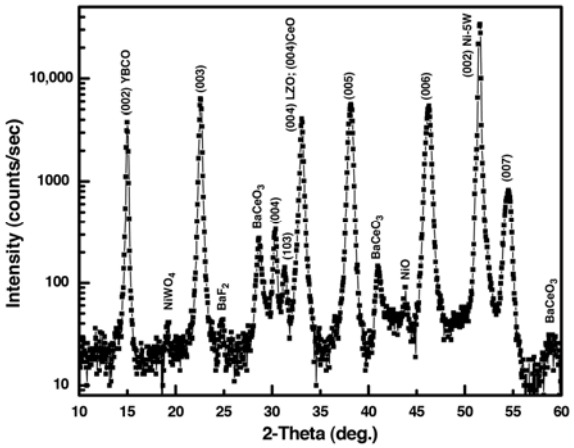

Fig. 2.10. Typical θ-2θ scan for a 0.8-μm-thick YBCO film grown on MOD-CeO_2/MOD-$La_2Zr_2O_7$/Y_2O_3/Ni-5W substrate using metal-organic deposition. YBCO film has a preferred *c*-axis orientation. In addition, small amounts of $NiWO_4$, BaF_2, $BaCeO_3$, and NiO impurities and polycrystalline YBCO peaks were also identified.

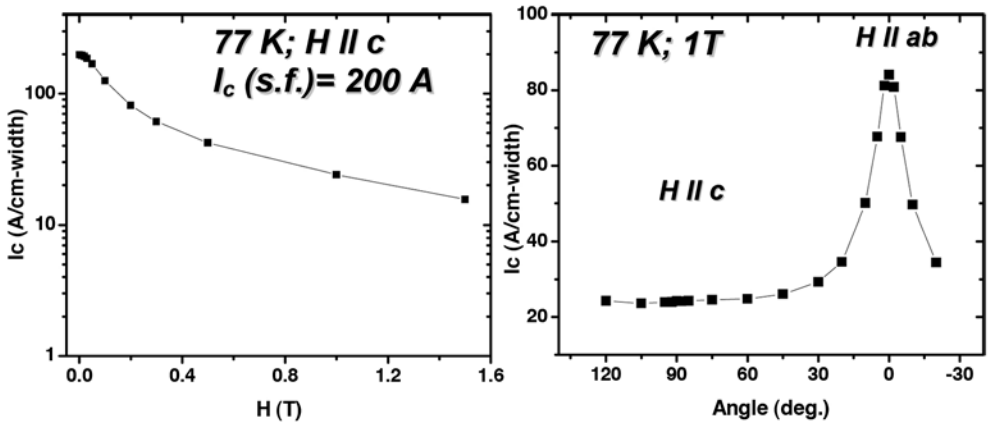

Fig. 2.11. The field dependence critical current for a 0.8-μm-thick YBCO film grown on MOD-CeO_2/MOD-$La_2Zr_2O_7$/Y_2O_3/Ni-5W substrate using metal-organic deposition (left side). The self-field critical current density of 2.5 MA/cm^2 (I_c = 200 A/cm) at 77 K and self-field was obtained. The angular dependence critical current at 77 K and 1 Tesla for the same film is shown on the right side. A minimum critical current of 20 A/cm was obtained at all angles.

layers with improved texture. However, to find out whether the performance of the template was limited by MOD-$La_2Zr_2O_7$ or MOD-CeO_2 compared to all PVD templates with a performance of 250 A/cm, we replaced the MOD-CeO_2 with a sputtered CeO_2 cap. MOD-YBCO films grown on sputtered-CeO_2/MOD-$La_2Zr_2O_7$/Y_2O_3/Ni-5W carried a critical current of 255 A/cm (J_c = 3.2 MA/cm^2). This demonstrates that the barrier properties of MOD-$La_2Zr_2O_7$/Y_2O_3 layers are comparable to that of PVD-YSZ layers. Detailed X-ray characterization of MOD-CeO_2 and PVD-CeO_2 cap layers indicated that there was no big difference in the texture between the two templates. However, reaction of MOD-CeO_2 with YBCO films resulted in increased amounts of $BaCeO_3$ formation as compared to that on PVD-CeO_2. The main reason for increased $BaCeO_3$ formation could be due to the slight roughening of the MOD-CeO_2 surface as compared to that of PVD-CeO_2. Further optimization of the MOD-CeO_2 layers is in progress.

In summary, we have developed process conditions to deposit 100-nm-thick MOD-$La_2Zr_2O_7$ layers in a single coat using spin-coating on 10-nm-thick Y_2O_3-seeded Ni-5W substrates. To improve the texture, so that the lattice mismatch with the Ni-5W substrate is reduced and the performance of MOD-$La_2Zr_2O_7$ is enhanced, we have inserted a 10-nm-thick Y_2O_3 seed layer. MOD-YBCO film with a critical current of 200 A/cm was achieved on MOD-CeO_2/MOD-$La_2Zr_2O_7$/Y_2O_3/Ni-5W substrates. These results demonstrate that the performance of MOD buffers is approaching that of PVD buffers.

2.4 Effect of Relative Humidity on the Crystallization of Sol-Gel Lanthanum Zirconium Oxide Films

S. Sathyamurthy, K. Kim, T. Aytug, and M. Paranthaman

Sol-gel processing is a versatile solution-based approach for the synthesis of a variety of ceramic oxides. The main attraction of this process is the flexibility and control it offers in terms of stoichiometry, microstructure, and crystallographic texture. This process has been used to synthesize a whole variety of technologically important oxides; e.g., $PbTiO_3$, $BaTiO_3$, $Pb(Zr,Ti)O_3$ (PZT), $SrBi_2Ta_2O_9$ (SBT). In our work, we have extended this processing approach to deposit highly oriented films of RE_2O_3 (e.g., RE-zirconates, RE-niobates, RE-tantalates) on biaxially textured Ni-alloy substrates. In the area of coated-conductor fabrication, there is a need for highly oriented films that can act as a buffer layer to prevent interdiffusion between the metal substrate and the $YBa_2Cu_3O_{7-d}$ (YBCO) superconductor film. A nonvacuum, scaleable process such as sol-gel processing could be ideally suited for the deposition of these buffer layers over long lengths of tapes because of the significant cost advantages it offers.

However, for it to be viable as a stable manufacturing process, a complete understanding of the various process variables that need to be regulated is imperative. In this paper, we investigate the effect of relative humidity during the coating step on the texture and microstructure of sol-gel–processed lanthanum zirconium oxide (LZO) thin films.

The sol-gel precursor solution was prepared from alkoxides of lanthanum and zirconium. Lanthanum isopropoxide (Alfa, La 40% assay), zirconium n-propoxide in n-propanol (Alfa, 70% w/w) and 2-methoxyethanol (Alfa, spectrophotometric grade) were used as received. For 20 mL of a 0.75 M solution, stoichiometric quantities of lanthanum isopropoxide (2.37 g) and zirconium n-propoxide (3.51g) were dissolved in 2-methoxyethanol and refluxed in 40 mL of excess 2-methoxyethanol using a Schlenk-type apparatus. After multiple solvent exchanges, the final volume of the solution was reduced to 20 mL. LZO films were prepared by spin-coating the precursor solution onto Ni-5at.%W substrates (1 × 1 cm) with a 75-nm Y_2O_3 seed layer using a spin speed of 2000 rpm for 30 s. The spin-coating was carried out in a controlled-humidity environment (ETS Model 5100 humidifier) with relative humidity changing from 10% to 80% at 23ºC. The coated films were crystallized at temperatures from 900 to 1100ºC for 15 min in a flowing atmosphere of Ar-4%H_2 gas. The phase purity and texture of the samples were analyzed using X-ray diffraction (XRD) with a Philips XRG3100 diffractometer and a Picker four-circle diffractometer, respectively, using Cu-K_α radiation. The microstructure of the samples was characterized using a field emission scanning electron microscope (FESEM). The surface crystallinity and roughness of the samples were characterized using reflection high-energy electron diffraction (RHEED) and atomic force microscopy (AFM) in contact mode, respectively.

XRD patterns obtained for samples spin-coated under relative humidity ranging from 10% to 80%, and processed at 1100ºC for 15 min are illustrated in Fig. 2.12. The intensity of the LZO (222) peak, which gives an estimate of the amount of random polycrystalline fraction in the film decreases as the relative humidity during the coating process is increased, dropping to background levels when relative humidity above 40% is used. Similar trends were also seen at 900ºC and 1000ºC process temperatures. Figure 2.13 illustrates the percentage of random polycrystalline material in the films as a function of relative humidity at various temperatures. The effect of humidity on the percentage of random polycrystalline material seems to be less exaggerated at lower temperatures. However, since all samples were processed only for 15 min, the lower amount of random material at lower temperatures could be due to slower crystallization kinetics. As the amount of random-oriented material decreases, a concomitant increase in the amount of cube-textured material [calculated using the pole figures from the LZO (222) peak] is observed. This is illustrated for samples processed at 1100ºC for 15 min in Fig. 2.14. Figure 2.15 shows the RHEED patterns collected from samples processed at 900ºC and 1100ºC after coating at 20% and 40% humidity levels. Samples coated at 40% relative humidity show a clean spot pattern, showing a fully oriented material at both temperatures. The pattern obtained from the sample coated at 20% relative humidity and processed at 1100ºC shows a mixture of spots and rings, suggesting a mixture of oriented and random material at the surface of the sample. In contrast, the sample coated at 20% relative humidity and processed at 900ºC for 15 min shows no diffraction pattern, suggesting that the surface of the film is completely amorphous. This observation is consistent with the observations using XRD, suggesting that at lower humidity levels, the LZO film is not completely crystallized at 900ºC. Apart from the differences in electron and XRD patterns of samples coated under different relative humidity levels, a clear difference was also observed in the microstructure of the films. Figure 2.16 shows the SEM microstructures of two LZO films processed at 1100ºC for 15 min coated at two different humidity levels (Fig. 2.16(a): 20%; Fig. 2.16(b): 50%). In samples coated with optimal humidity levels a pronounced granularity was seen at the surface, while samples processed at lower humidity showed a mostly smooth surface with a few particulates distributed randomly on it. The amount of particulates observed was found to decrease with the processing temperature. For samples coated under optimal humidity, the granularity in the microstructure was found to be less severe with a decrease in processing temperature (Fig. 2.17). This is consistent with AFM roughness measurements, where the surface roughness decreased from 2.0 nm to 1.2 nm to 0.5 nm for samples processed at 1100ºC, 1000ºC, and 900ºC, respectively.

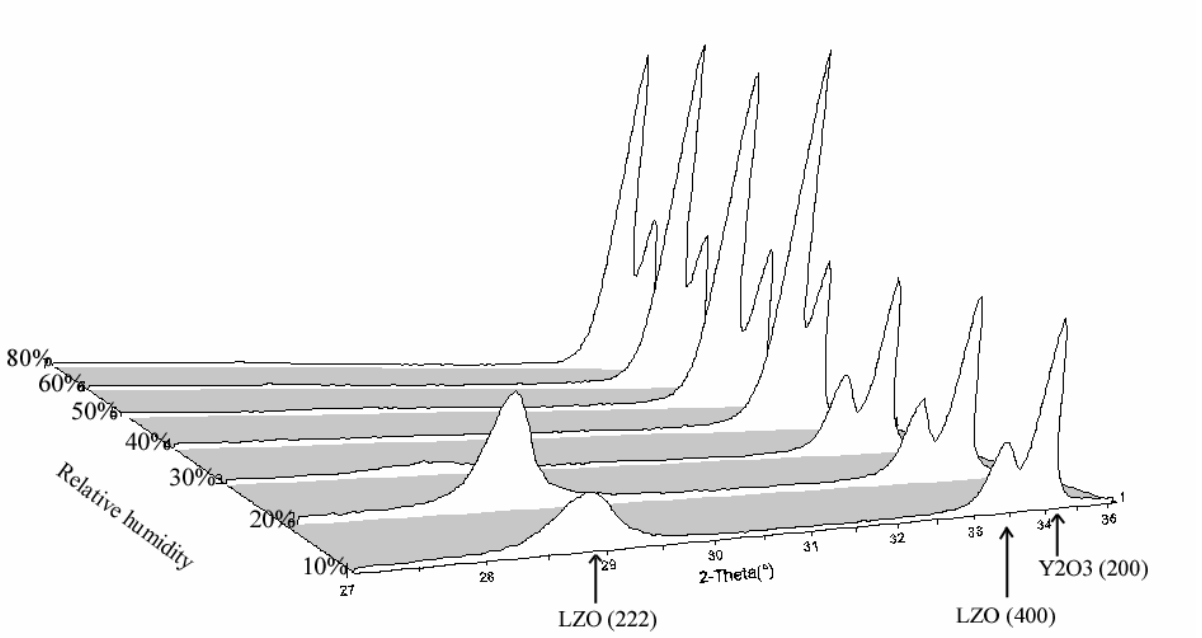

Fig. 2.12. XRD patterns of samples coated under different relative humidity levels (10%–80%) and processed at 1100ºC for 15 min.

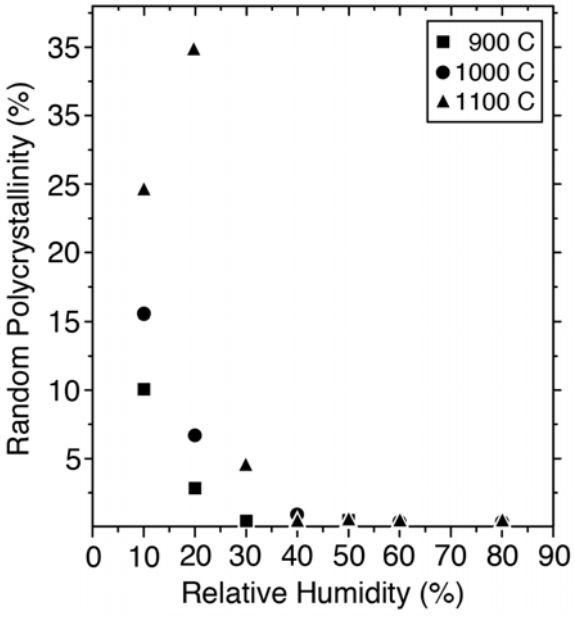

Fig. 2.13. Variation of percent random-polycrystalline material as a function of relative humidity during coating for a series of processing temperatures.

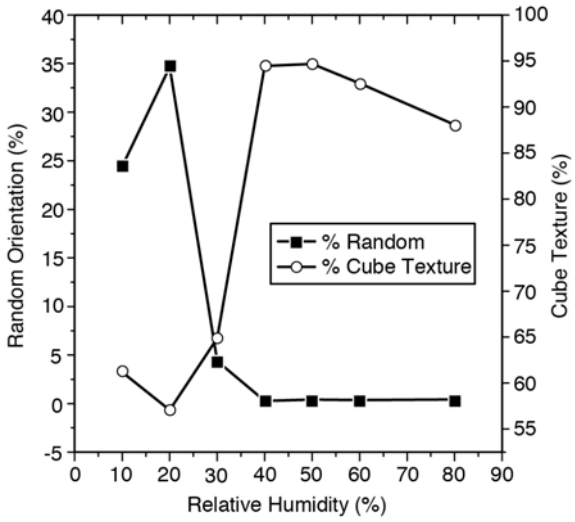

Fig. 2.14. Variation of percent random-oriented and cube textured material in the films as a function of relative humidity for samples processed at 1100ºC for 15 min.

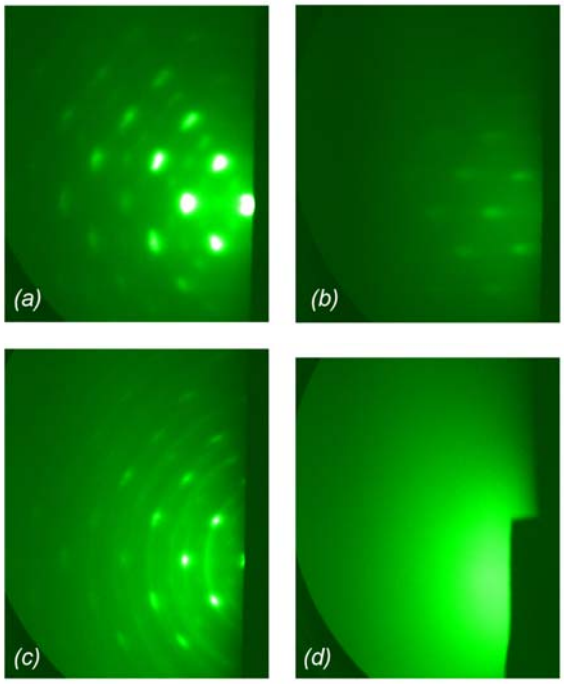

Fig. 2.15. RHEED patterns for LZO samples processed at (a) 40% relative humidity, 1100ºC; (b) 40% relative humidity, 900ºC; (c) 20% relative humidity, 1100ºC; (d) 20% relative humidity, 900ºC.

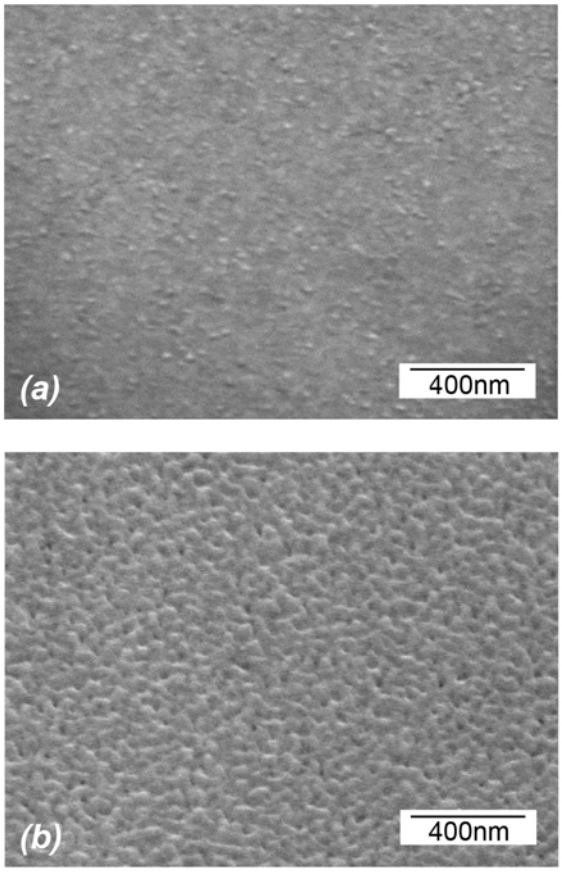

Fig. 2.16. Effect of relative humidity during coating on the microstructure.

To understand the effects of the relative humidity on the film crystallization behavior observed in this work, a closer look at the thermodynamics of nucleation and growth is necessary. Figure 2.18 schematically illustrates the difference in the variation of free energy as a function of temperature for the amorphous films (sol-gel precursor film), the supercooled liquids, and the crystal. The energy difference between the amorphous phase and the crystal (ΔG_v) is the driving force for crystallization at any given temperature. Standard nucleation and growth theory provides the relationship between the thermodynamic driving force for crystallization and the energy barriers for homogeneous and heterogeneous nucleation, as described by

$$\Delta G^*_{homo} = 16\pi\gamma^3/3(\Delta G_v)^2 \quad (1)$$

$$\Delta G^*_{hetero} = (16\pi\gamma^3/3(\Delta G_v)^2)\, f(\theta), \quad (2)$$

where γ is the interfacial energy and $f(\theta)$ is a function related to the contact angle, θ. Nucleation at the interface with the substrate (heterogeneous nucleation) would lead to epitaxial material; nucleation in the bulk of the film (homogeneous nucleation) and at the film surface (heterogeneous nucleation) would lead to random polycrystalline material. The difference in the barrier height for the various modes of nucleation depends on the driving force, surface energy, and the contact angle. Depending upon the

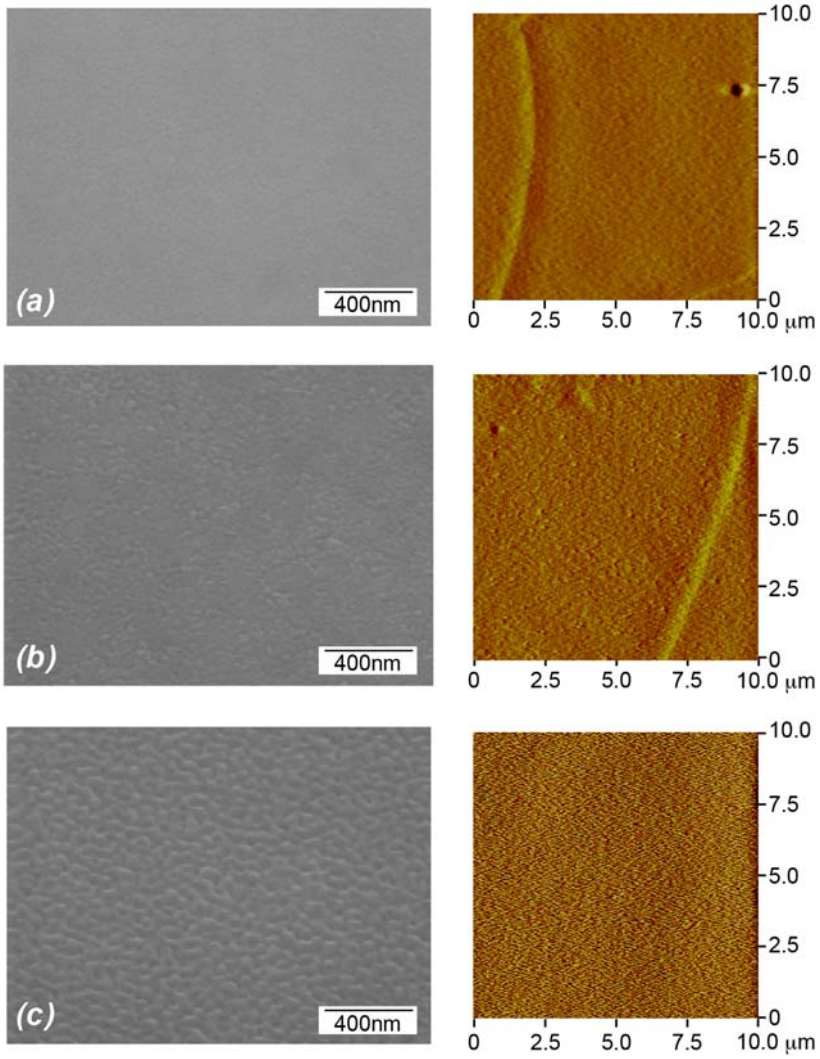

Fig. 2.17. Effect of processing temperature on the microstructure (left) and surface roughness (r_a) of the samples coated at 40% relative humidity.

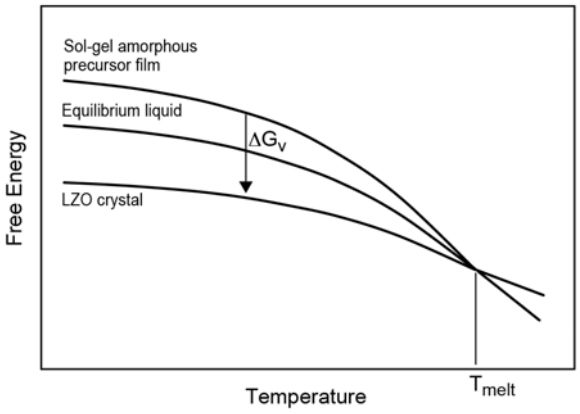

Fig. 2.18. Schematic illustration of the free energies for the sol-gel precursor film, ideal supercooled liquid, and the crystalline LZO phase as a function of temperature.

thermal input during the heat treatment and the processing conditions, along with the interface nucleation (which is the most energetically favored), surface and bulk nucleation modes may also be active during the crystallization.

The effect of hydrolysis water on the orientation and microstructure of sol-gel films has been studied on several oxides such as $PbTiO_3$, $LiNbO_3$, PZT, and $Ba_xSr_{1-x}TiO_3$. In all these studies, typically, hydrolysis has been reported to cause a decrease in epitaxy by promotion of homogeneous nucleation, which competes with the heterogeneous nucleation at the substrate surface (film-substrate interface). The effect seen here is quite different from the hydrolysis effects reported by others. This

suggests that the effect of relative humidity should not be due to hydrolysis. The present results seem to indicate that humidity during coating aids crystallization. In samples coated at low humidity there could be a nonuniform distribution of moisture through the thickness of the film with the lowest concentration at the interface with the substrate. This would lead to crystallization of the film at the surface and in the bulk of the film along with crystallization at the interface. That is, since the moisture content would be lowest close to the film-substrate interface, the amount of nucleation at the interface (which would be the epitaxial component of the film) will also be low. On the other hand, above a threshold humidity level, there would be a uniform distribution of moisture throughout the thickness, and, because epitaxial nucleation and growth initiated from the substrate surface are energetically favored, the dominant mode of crystallization should be through nucleation at the substrate surface. Further studies on the changes to the chemical nature of the amorphous precursor film as a function of coating humidity may help elucidate the reasons for the effects reported in this work.

2.5 MOD Buffer/YBCO Approach to Fabricate Low-Cost Second Generation HTS Wires

M. P. Paranthaman, S. Sathyamurthy, M. S. Bhuiyan, P. M. Martin, T. Aytug, K. Kim, M. Fayek, K. J. Leonard, J. Li, A. Goyal, T. Kodenkandath, X. Li, W. Zhang, and M.W. Rupich

2.5.1 Introduction

Both Rolling-Assisted Biaxially Textured Substrates (RABiTS™) and ion-beam assisted deposition (IBAD) approaches have emerged as leading techniques for the fabrication of 2G HTS wires in 100 meter lengths [1–5]. The current RABiTS™ architecture used by American Superconductor consists of a starting template of biaxially textured Ni-W (5 at. %) with a seed layer of 75-nm Y_2O_3, a barrier layer of 75-nm YSZ, and a cap layer of 75-nm CeO_2 [5]. In this architecture, all the buffers have been deposited by reactive sputtering. To reduce the initial investment cost of buying 2G pilot-scale production equipment, it is essential to either reduce the number of layers or to replace some of the sputtered buffer layers with solution-deposited buffers. The metal-organic deposition (MOD) process offers a significant potential cost advantage over physical vapor deposition (PVD) processes. Solution coating is amenable to complex oxides and the materials utilization is almost 100%. A slot-die coating process has been chosen to scale up solution buffer layers.

The main objective of this research is to match or exceed the performance of the all-PVD buffers using MOD buffers. Both $La_2Zr_2O_7$ (LZO) and CeO_2 buffers have been identified as potential candidates for this work. Sputtered Y_2O_3 seed layers improve the texture relative to the substrate texture. However, there is no improvement in texture when MOD LZO layers were grown directly on textured Ni-W substrates. The lattice mismatch between LZO and Ni-W substrate is about 7.9%. We have reduced the lattice mismatch, improved the texture, and enhanced the properties of LZO by inserting a thin Y_2O_3 seed layer. Y_2O_3-seeded MOD-LZO templates with either MOD-CeO_2 or sputtered-CeO_2 cap layers have yielded MOD YBCO films with critical currents of 200 and 255 A/cm-width [6,7]. In this paper, we have used both X-ray diffraction (XRD) and transmission electron microscopy (TEM) techniques to understand the role of MOD vs sputtered CeO_2 cap layers. In addition, we have further modified the LZO process conditions and demonstrated the performance of MOD buffers to exceed the performance of PVD buffers.

2.5.2 Experimental Procedure

Biaxially textured Ni-W (5 at. %) substrates with reactively sputtered Y_2O_3 seeds were provided by American Superconductor Corporation (AMSC). The substrates used were typically 1 cm wide, slit from 4-cm-wide, 75-μm-thick tapes. The LZO precursor solution was prepared from lanthanum isopropoxide (Alfa, La 40% assay), zirconium n-propoxide in n-propanol (Alfa, 70%), and 2-methoxyethanol (Alfa, spectrophotometric grade). The details of the solution preparation were reported earlier [8]. About 0.75 M total cation concentration was used to grow LZO films with a thickness of 100 nm in a single coat. Spin coating was used to deposit LZO at a spin rate of 2000 rpm for 30 s and an ambient relative humidity of

40 to 60%. The spin-coated films were then heat-treated at 900 to 1100°C for 15 min in a flowing mixture of Ar/H_2 4% gas. To obtain thicker LZO films, the coating and crystallization steps were repeated several times. About 60-nm-thick MOD-CeO_2 and 0.8-μm-thick MOD-YBCO were deposited on MOD-LZO using AMSC's proprietary trifluoroacetate (TFA) process [9].

The films were characterized for phase purity and texture using XRD. Microstructural analysis was done by cross-section TEM. Secondary ion mass spectroscopy (SIMS) depth profile analyses were carried out to study the metal and oxygen diffusion properties of buffers. The resistivity and transport critical current density were measured using a standard four-point probe technique.

2.5.3 Results and Discussion

LZO films with improved texture were grown on 10-nm-thick Y_2O_3-seeded Ni-5W substrates using our standard 1100°C process conditions. These LZO films capped with MOD-CeO_2 cap layers supported MOD-YBCO films with a critical current of 200 A/cm-width (J_c = 2.5 MA/cm^2) [6,7]. As shown in Fig. 2.19, typical θ-2θ scans for a YBCO film grown on MOD-CeO_2/MOD-$La_2Zr_2O_7$/Y_2O_3/Ni-5W substrate indicated the presence of a strong *(00l)* reflection of YBCO. In addition, small impurities of $NiWO_4$, NiO, unreacted BaF_2, $BaCeO_3$, and polycrystalline YBCO were also present. However, MOD-YBCO films grown on sputtered-CeO_2/MOD-$La_2Zr_2O_7$/Y_2O_3/Ni-5W carried an increased critical current (I_c = 255 A/cm-width; J_c = 3.2 MA/cm^2) [6,7]. Detailed XRD studies indicated that there was no big difference in texture between MOD-YBCO on MOD-CeO_2 and sputtered-CeO_2 cap layers. However, the $BaCeO_3$ formation was less in sputtered-CeO_2 cap films as compared to that on MOD-CeO_2 cap films (Fig. 2.19). This could be due to the increased surface roughness for MOD CeO_2 as compared to that of sputtered-CeO_2 cap layers.

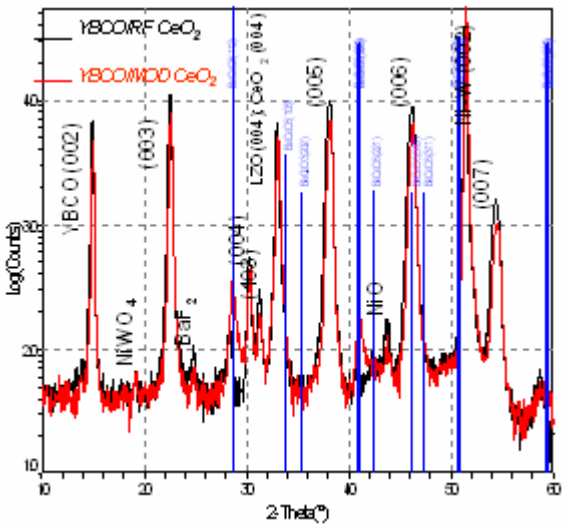

Fig. 2.19. Typical θ-2θ scans for 0.8-μm-thick YBCO films grown on 60-nm-thick MOD-CeO_2/200-nm-thick MOD-$La_2Zr_2O_7$/10-nm-thick Y_2O_3/Ni-5W (marked in black) and 75-nm-thick rf-sputtered-CeO_2/200-nm-thick MOD-$La_2Zr_2O_7$/10-nm-thick Y_2O_3/ Ni-5W (marked in red) substrates using metal-organic deposition. YBCO film has a preferred *c*-axis orientation. Small amounts of $NiWO_4$, BaF_2, $BaCeO_3$, and NiO impurities and polycrystalline YBCO peaks were also identified. Additional $BaCeO_3$ formed on MOD-CeO_2 cap layers.

The transport properties of MOD-YBCO films on both MOD-CeO_2 and sputtered-CeO_2 cap layers are shown in Fig. 2.20. Sputtered CeO_2 cap layers improved the performance of MOD-YBCO by 25% compared to that of MOD CeO_2 cap layers. The in-field properties are typical of a standard MOD-YBCO film.

A cross-sectional TEM image of a MOD-YBCO film on MOD-CeO_2/MOD-$La_2Zr_2O_7$/Y_2O_3/Ni-5W substrate carrying a critical current of 200 A/cm-width sample is shown in Fig. 2.21. Polycrystalline NiO and $NiWO_4$ phases are present at the Ni-W substrate/Y_2O_3 interface. Also, MOD-CeO_2 was completely converted to $BaCeO_3$ due to the reaction of CeO_2 cap with YBCO. However, the rf-sputtered CeO_2 cap layer is intact and the CeO_2 cap/YBCO interface is clean for MOD-YBCO films grown on sputtered-CeO_2/MOD-$La_2Zr_2O_7$/Y_2O_3/Ni-5W substrate carrying a critical current of 255 A/cm-width sample (as shown in Fig. 2.22). These findings confirmed the presence of increased $BaCeO_3$ content with MOD-CeO_2 cap layers as compared to that of sputtered-CeO_2 cap layers in XRD patterns (Fig. 2.19).

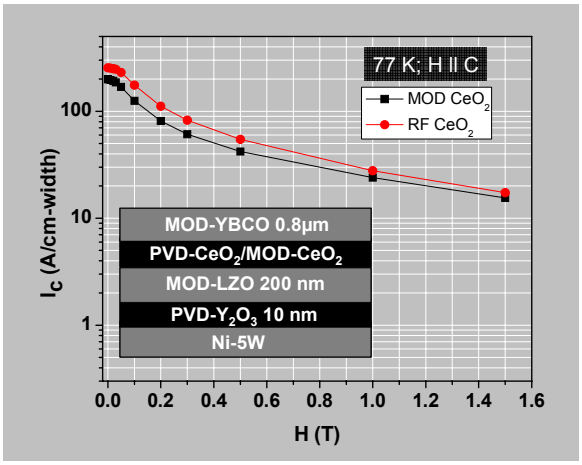

Fig. 2.20. The field dependence critical current for 0.8-μm-thick YBCO film grown on MOD-CeO_2/MOD-$La_2Zr_2O_7$/Y_2O_3/Ni-5W and rf-sputtered-CeO_2/MOD-$La_2Zr_2O_7$/Y_2O_3/Ni-5W substrates using metal-organic deposition. J_c = 2.5 MA/cm^2 (I_c = 200 A/cm) for MOD-CeO_2 cap; J_c = 3.2 MA/cm^2 (I_c = 255 A/cm) (for sputtered-CeO_2 cap) at 77 K, self-field.

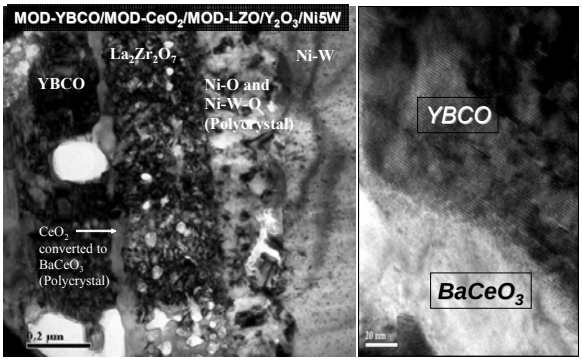

Fig. 2.21. Cross-sectional TEM image of 0.8-μm-thick YBCO film grown on MOD-CeO_2/MOD-$La_2Zr_2O_7$/Y_2O_3/Ni-5W substrates using metal-organic deposition. The higher magnification image on the right shows the presence of $BaCeO_3$ at the CeO_2/YBCO interface.

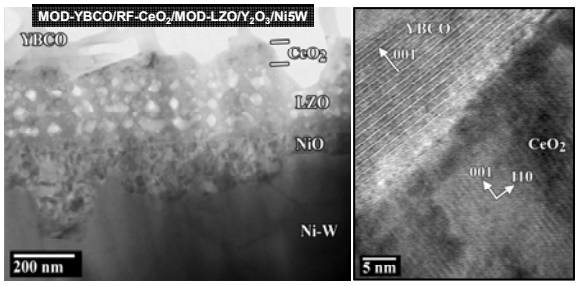

Fig. 2.22. Cross-sectional TEM image of 0.8-μm-thick YBCO film grown on rf-sputtered-CeO_2/MOD-$La_2Zr_2O_7$/Y_2O_3/Ni-5W substrates using metal-organic deposition. The higher magnification image on the right shows the clean CeO_2/YBCO interface.

SIMS depth profile studies on 1100°C as-processed MOD LZO films showed the diffusion of Ni into the LZO layers. A minimum of 75-nm-thick LZO layer is necessary to prevent Ni diffusion. To match the performance of MOD buffers with PVD buffers, we need to improve the diffusion properties of LZO layers and to reduce the surface roughness of LZO layers. Also, to make the MOD process a viable manufacturing process, we need to process LZO films below 950°C in a short time (15 min). Hence, we started focusing on processing LZO at lower temperatures. Recently, we found that, by controlling the ambient relative humidity during the spin-coating process, the crystallographic texture and microstructure of the LZO films can be changed significantly. The effects of humidity on the microstructure, surface roughness, and texture of the films were studied and reported elsewhere [10]. By lowering the process temperature of LZO films to 900°C, highly textured and smooth LZO films were obtained. MOD-YBCO films grown on sputtered-CeO_2 capped MOD-LZO films processed at 900°C supported a critical current of 336 A/cm-width (J_c = 4.2 MA/cm^2) at 77 K and self-field (as shown in Fig. 2.23). This performance exceeded the performance of all-PVD buffers. Efforts are being made to deposit both MOD-CeO_2 and MOD-YBCO on MOD-LZO films processed at 900°C.

2.5.4 Summary

In summary, we have demonstrated the barrier properties of MOD LZO and that the performance of MOD LZO layers exceeded that of PVD YSZ layers. MOD LZO films processed at 900°C should further improve the properties of MOD-CeO_2 cap layers in the future. This work promises a route for producing long lengths of YBCO coated conductors using MOD buffer layers.

2.5.5 References

1. M. P. Paranthaman, "Superconductor wires," pp. 319–22 in *McGraw-Hill 2006 Yearbook of Science and Technology*, McGraw-Hill Publishers, New York (2006).
2. M. P. Paranthaman and T. Izumi, editors, *MRS Bulletin*, **29**, 533–36 (2004).
3. P. N. Arendt, and S. R. Foltyn, *MRS Bulletin*, **29**, 543–50 (2004).
4. Y. Iijima, et. al., *MRS Bulletin*, **29**, 564–71 (2004).
5. A. Goyal, M. Paranthaman, and U. Schoop, *MRS Bulletin*, **29**, 552–61 (2004).
6. S. Sathyamurthy, et. al., *J. Mater. Res.* **21**, 910–14 (2006).
7. M. P. Paranthaman, *Physica C* **445–48**, 529–32 (2006).
8. S. Sathyamurthy, *J. Mater. Res.* **17**, 1543–49 (2002).
9. M. W. Rupich, *MRS Bulletin*, vol. 29, pp. 572-578, 2004.
10. S. Sathyamurthy et al., *Chem. Mater*. (submitted 2006).

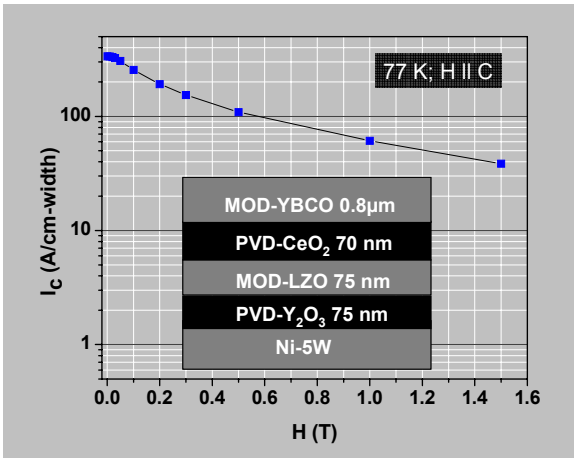

Fig. 2.23. The field dependence critical current for 0.8-μm-thick YBCO film grown on 75-nm-thick rf-sputtered-CeO_2/100-nm-thick MOD-$La_2Zr_2O_7$ (processed at 900°C)/75-nm-thick Y_2O_3/Ni-5W using metal-organic deposition. J_c = 4.2 MA/cm^2 (I_c = 336 A/cm) at 77 K, self-field.

2.6 Slot Die Coating and Conversion of LZO on Rolling Assisted Biaxially Textured Ni-W Substrates with and without a Very Thin Seed Layer in Low Vacuum

L. Heatherly, H. Hsu, S. H. Wee, J. Li, S. Sathyamurthy, M. Paranthaman and A. Goyal

2.6.1 Introduction

The production of thin-film HTSs requires buffer layers to be placed between the starting metal substrate and the final YBCO superconductor. These layers are needed to prevent metal cations from interacting with and degrading the superconductor and to prevent oxygen from reaching the metal substrate. In the Rolling-Assisted-Biaxially-Textured-Substrate (RABiTS™) process, critical requirements for these layers are that they must be epitaxial with respect to the biaxially textured substrate and that they must be compatible with the adjacent layers [1].

Most current methods by which buffer layers are deposited result in the production of quite good superconductors, but they involve expensive high-vacuum systems and high temperatures, and the deposition rates are not extremely fast. Also, materials are not efficiently used in these methods because the efficiency during deposition is low. The work reported in this paper deals with a buffer deposition process that is fast and less expensive, and in which the starting materials are very efficiently utilized. This MOD-based method involves the slot-die coating of liquid precursors onto metal substrates, which are in the form of RABiTS™ tapes. The precursors are then converted to crystalline LZO, which forms epitaxial diffusion barrier buffer layers on the textured substrates. When capped with an epitaxial CeO_2 layer, substrates that are fabricated are good templates for the deposition of high-current-carrying HTS films.

2.6.2 Experimental Procedure

The procedure for producing biaxially textured Ni-alloy substrates has been well established and published [1]. Essentially, the process involves subjecting a metallic alloy to a tremendous amount of deformation by cold rolling to greater than ninety percent reduction in thickness. The rolled tape is then heated to nearly its melting temperature, where recrystallization occurs. As the crystals nucleate and grow, they are highly aligned in both the out-of-plane and in-plane directions.

The alloy used in this study was a Ni-3at.%W powder metallurgy processed material custom rolled by a commercial rerolling vendor in the highly deformed as-rolled condition. After the tape was degreased and dried, it was loaded into a reel-to-reel high vacuum (10^{-8} Torr) chamber, which contained a radio-frequency induction-heated furnace. The tape was pulled through the hot zone of the furnace at a rate that heated each part to 1250°C for 20 min with a partial pressure of hydrogen sulfide gas of ~3×10^{-7} Torr in order to form a sulfur c(2×2) superstructure on the surface of the tape. It has been reported previously that this superstructure promotes epitaxial growth of a Y_2O_3 buffer layer, which is routinely deposited to prevent oxygen diffusion into the metal substrate during subsequent processing steps [1]. A 10-nm layer of Y_2O_3 was deposited on part of the metal tape using an electron beam evaporation process, which has been described previously [1]. These tapes were used as the starting materials or substrates for the slot-die coating of the LZO buffer layers.

The LZO precursor solution was prepared by refluxing a stoichiometric mixture of lanthanum isopropoxide and zirconium *n*-propoxide in 2-methoxyethanol in a Schlenk-type apparatus. A total cation concentration of 0.75 M was used in this work. Details of the preparation procedure have been described in a separate publication [2].

The LZO deposition was performed using a commercial slot die coater, which was adapted for our purpose and was installed in an environmentally controlled box, as shown in Fig. 2.24. The box was attached through a quartz tube to a 2-m long tube furnace, which allowed the tape to be heated slightly for drying or to high temperatures for atmospheric-pressure conversion of the precursor immediately after it came out of the slot-die coater. The tape speed for the coatings was 2 m/min, which was determined previously to be a suitable speed for the precursor described above [2]. The atmospheric pressure conversion was performed in a flowing forming gas mixture (Ar-4%H_2) for 15 min at a temperature of 1050°C.

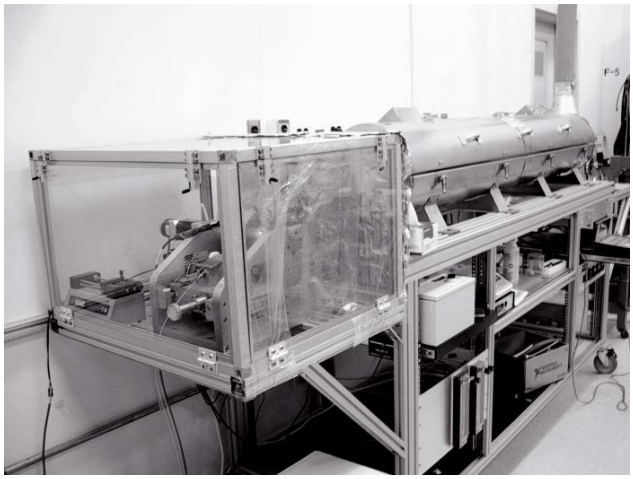

Fig. 2.24. Slot-die coater in an environmentally controlled box with a 2-m-long tube furnace attached.

The vacuum conversion of the LZO precursor was performed in a turbomolecular pumped high vacuum (~10^{-9} Torr) chamber, which contained a radio-frequency induction furnace with an inert platinum-rhodium susceptor. The chamber was instrumented with a differentially pumped residual gas analyzer (RGA), precision variable leak valves and a reel-to-reel tape-handling system. A computer data acquisition and control system controlled the tape travel speed and tension, the RGA and the temperature of the furnace. Tapes as long as 2 m have been uniformly deposited and converted; however, the process should be scalable to extremely long lengths.

Once converted, the tapes were characterized using a reel-to-reel 4-circle X-ray diffraction system, which allowed θ-2θ scans, rocking curves, ϕ-scans, pole figures and various tape scans to be performed on long lengths of tape.

2.6.3 Results and Discussion

It was determined that the slot-die LZO precursor deposited on a thin Y_2O_3 "seed" layer could be converted either in flowing forming gas at near atmospheric pressure or under high vacuum conditions with very similar results. Figure 2.25 shows typical XRD data for a forming-gas or a vacuum-converted 100-nm-thick LZO film incorporating a thin Y_2O_3 seed layer. The θ-2θ scans show no detectable signal from the LZO(222), indicating the absence of any untextured material in films converted under either condition. Also, the intensity of the LZO(400) and the widths of the rocking curves are essentially the same for each film, indicating that the film thickness and texture are very similar for the two conditions.

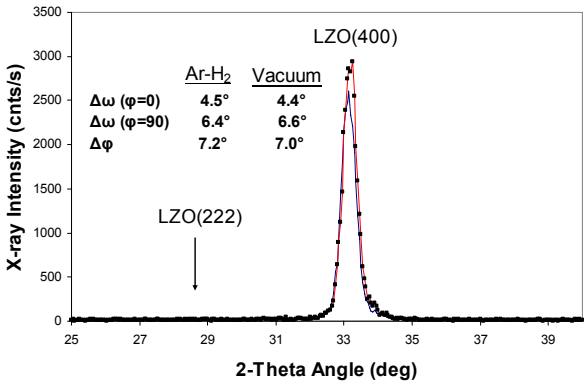

Fig. 2.25. The θ-2θ and rocking curve data show the Ar-H_2 and vacuum conversions produce similar results.

Figures 2.26(a) and (b) show the XRD data from two single coat (50 nm) LZO films converted in forming gas at nearly atmospheric pressure. The data shown in Figs. 2.26(a) and (b) were collected on a film with and without a thin Y_2O_3 film, respectively. It can be seen that the presence of the very thin (10 nm) Y_2O_3 greatly improves the texture of the slot-die-coated LZO film. The intensity of the (400) diffraction peak is ~50% greater, and the spread in the out-of-plane texture (Δω) is considerably smaller. It is expected that this amount of texture improvement should have a beneficial effect on the current-carrying capacity of the resulting YBCO superconductor.

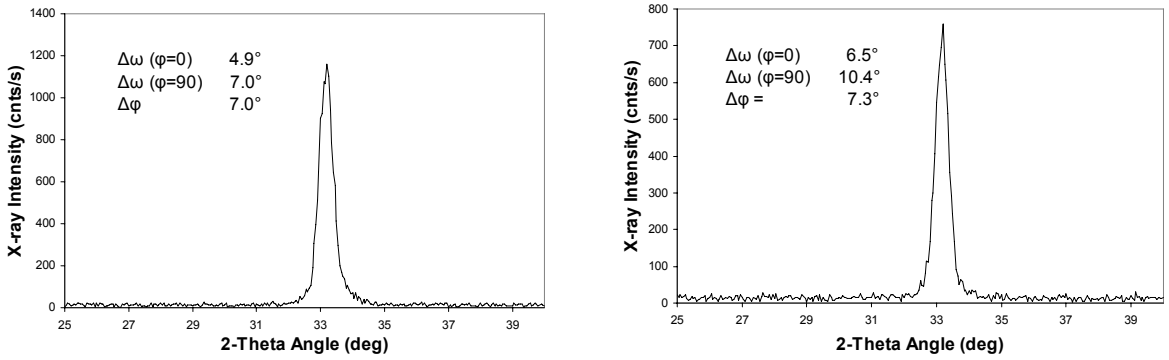

Fig. 2.26. θ-2θ scan and the rocking curve and phi scan results. (a) A sample with a Y_2O_3 seed layer converted in Ar-H_2. (b) A sample without a Y_2O_3 seed layer converted in Ar-H_2.

The effect of the Y_2O_3 layer is even more dramatic when the precursors are converted under high-vacuum conditions, as shown in Fig. 2.27. When the LZO was deposited with the seed layer and converted in vacuum, the results were very similar to the near-atmospheric conversions. However, if the seed layer is not used, vacuum conversion results in little or no properly oriented LZO, as shown in Fig. 2.27, when using the same conversion parameters as in the samples containing Y_2O_3. The extremely low signal intensity and the absence of the LZO(400) peak indicate that the LZO precursor crystallized very little, and the crystals were randomly oriented.

Transmission electron microscopy (TEM) characterization was performed on 100-nm-thick vacuum-converted samples using a Philips CM 200 microscope equipped with a field emission gun (FEG). TEM cross section samples were prepared using a dual beam focus ion beam (FIB) microscope [3]. Figure 2.28

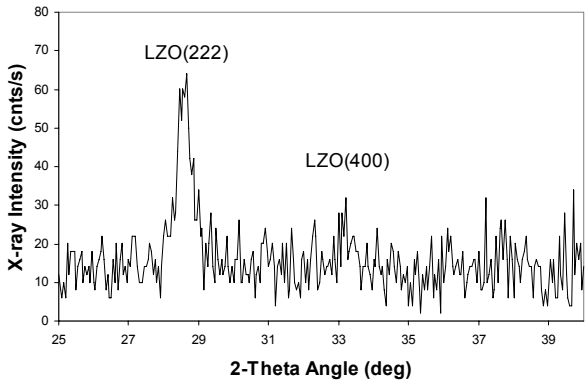

Fig. 2.27. A θ-2θ scan from a vacuum-converted LZO precursor without a Y_2O_3 seed layer.

07

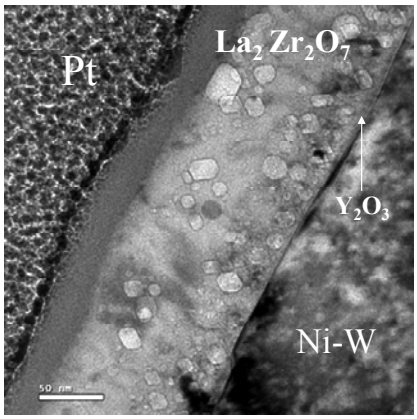

Fig. 2.28. A cross-section TEM showing the two phases present in the converted LZO film.

shows a cross-section TEM image of the Y_2O_3 seed layer and the LZO film that reveals two distinct phases present throughout the film. The electron diffraction pattern displayed in Fig. 2.29 shows that the LZO film is composed of a combination of the pyrochlore $La_2Zr_2O_7$ (matrix) and fluorite $La_2Zr_2O_7$ (La-rich/Zr-deficient coherent particles). The XRD technique cannot distinguish between these phases because the data for the two look very similar.

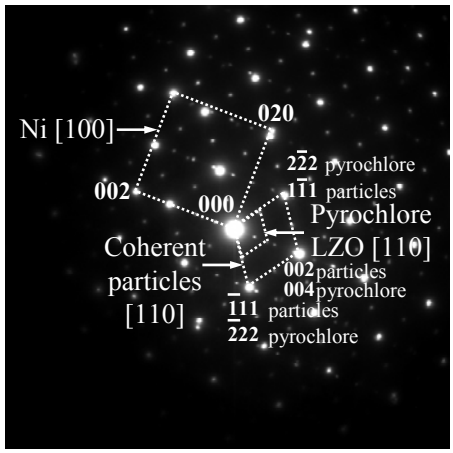

Fig. 2.29. Electron diffraction patterns from LZO film identifying the pyrochlore and fluorite phases present throughout the film.

CeO_2 cap layers were deposited on several of the 100-nm-thick converted LZO films that incorporated the Y_2O_3 seed layer using standard deposition techniques reported previously [2]. YBCO superconducting films were then deposited and processed using the same conditions as for the standard vacuum-deposited buffer layers. The measured current-carrying capacities of the samples were similar to those of the standard samples processed with vacuum-deposited buffer layers, so the prospect of a more-efficient and less-expensive method of buffer layer deposition looks encouraging.

2.6.4 Conclusion

It has been shown that slot-die LZO films can be deposited that are suitable for producing high-current-carrying HTS tapes. The LZO precursors can be converted with similar results in Ar-H_2 forming gas at near-atmospheric pressure or in high vacuum. Under all conditions tested, a Y_2O_3 seed layer is needed to get highly textured films needed for good superconducting films. This slot-die technique is an alternate buffer layer deposition process, which could be simpler and more economical to utilize than the techniques currently being used.

2.6.5 References

1. A. Goyal, M. Paranthaman, and U. Schoop, *MRS bulletin* **29** (8), 552–61 (2004).

2. S. Sathyamurthy, et. al., *J. Mater. Res* **17** (9), 21–84 (2002).

3. J. Li, A. et. al., *J. of Mater. Res.*(submitted).

2.7 Growth of Thick $YBa_2Cu_3O_{7-\delta}$ Films Carrying a Critical Current of 272 A/cm on $LaMnO_3$-Buffered Ion-Beam Assisted Deposition MgO Substrates using Metal-Organic Chemical Vapor Deposition

M. Paranthaman, T. Aytug, and A. Goyal (ORNL) and X. Xiong, Y. Chen, J. Reeves, and V. Selvamanickam (SuperPower)

$LaMnO_3$ (LMO) has been identified as an excellent cap layer for ion-beam assisted deposition (IBAD)-MgO templates because of its excellent compatibility with both IBAD-MgO and $YBa_2Cu_3O_{7-\delta}$ (YBCO) and because of its high deposition rate, thinner layer, and wide process temperature window. RF sputtering was used to deposit epitaxial LMO layers in IBAD-MgO templates in both short and long lengths. Using metal-organic chemical vapor deposition (MOCVD), YBCO films with a critical current density of ~2.5×10^6 A/cm^2 at 77 K and self-field for a film thickness of 1.1 μm has been achieved on sputtered CeO_2/$LaMnO_3$-buffered IBAD MgO substrates in short lengths. This corresponds to a critical current of 272 A/cm-width. In addition, we have also fabricated 25-m lengths of MOCVD-grown YBCO tape using LMO-buffered IBAD-MgO and achieved a critical current of 142 A/cm. This promises a route for fabricating IBAD-MgO based second generation YBCO tapes with LMO cap layers in a pilot-scale production.

The main objective of this research is to develop a compatible cap layer for ion-beam assisted deposition (IBAD)-MgO template/metal-organic chemical vapor deposition (MOCVD) $YBa_2Cu_3O_{7-\delta}$ (YBCO) based second-generation (2G) high temperature superconductor wires for various electric-power applications. In the IBAD process, the ion-beam is used to grow textured buffer layers onto a flexible but untextured metal, typically a nickel superalloy. After the initial announcement of the IBAD process to grow textured yttria-stabilized zirconia (YSZ) layers by Iijima et al. (Fujikura Ltd., Japan, 1992), researchers at Los Alamos National Laboratory (LANL 1995) improved the process and achieved high-performance YBCO films on IBAD-YSZ templates. Wang et al. (Stanford University 1997) showed that IBAD-MgO required only 10 nm to develop texture comparable to that of IBAD-YSZ at 1-μm thickness, which, for equivalent deposition rates, translates to a process that is ~100 times faster than IBAD-YSZ. To date, three materials systems, namely YSZ, gadolinium zirconium oxide, $Gd_2Zr_2O_7$ (GZO) (recently developed by Iijima et al., Fujikura Ltd., Japan, 2001) or magnesium oxide, MgO, are being used to fabricate IBAD-template-based long lengths of YBCO tapes. Both strontium titanium oxide, $SrTiO_3$ (STO) and strontium ruthenium oxide, $SrRuO_3$ (SRO) cap layers have been developed as a potential cap layers for IBAD-MgO templates, and high-current-density YBCO films were demonstrated on these cap layers using pulsed laser deposition (PLD). However, these buffer cap layers were not suitable for high-throughput processing of buffers on IBAD MgO templates and compatibility with MOCVD-YBCO. For manufacturing 2G conductors based on an IBAD-MgO template, there is a critical need to find an alternate material to STO and SRO layers. Hence, we focused on developing a suitable cap layer for IBAD-MgO that is also compatible with MOCVD-YBCO. In the alternate Rolling-Assisted Biaxially Textured Substrates (RABiTS™) approach, a three-layer architecture of CeO_2/YSZ/Y_2O_3/Ni-W is used to fabricate long lengths of buffered tapes. The RABiTS™ process, as developed at Oak Ridge National Laboratory (ORNL), utilizes thermomechanical processing to obtain the flexible, biaxially oriented nickel-alloy substrates. Both buffers and YBCO superconductors are then deposited epitaxially on the textured nickel alloy substrates. The starting textured substrates serve as structural templates for the YBCO layer, which has substantially fewer weak links. In our strategic research, we developed an

alternative single $LaMnO_3$ (LMO) buffer layer architecture for RABiTS™-based YBCO coated conductors. We have demonstrated the growth of YBCO films with a critical current density of over 1.2 MA/cm^2 at 77 K and self-field on single $LaMnO_3$-buffered Ni-W substrates using PLD. $LaMnO_3$ has also been identified as a good diffusion barrier for Ni. $LaMnO_3$ is an orthorhombic perovskite with lattice parameters a = 5.533 Å, b = 5.722 Å, and c = 7.694 Å. The pseudocubic lattice parameter of 3.88 Å is closely matched to YBCO: the lattice mismatch is less than 0.8 %. Following the initial success of our $LaMnO_3$ buffer layer with RABiTS™ approach, we extended this strategic research to IBAD MgO as well. In order to determine the compatibility of $LaMnO_3$ with MgO surfaces, $LaMnO_3$ buffers were initially deposited on MgO (100) single-crystal substrates. A zero-field critical current density of more than 4×10^6 A/cm^2 at 77 K was obtained on YBCO films grown on $LaMnO_3$-buffered MgO single-crystal substrates using both PLD and ex situ BaF_2 processes. This demonstrates that LMO buffers are highly compatible with MgO surfaces. Recently, we have demonstrated the growth of 1.65-µm-thick YBCO films with a critical current density of 1.4×10^6 A/cm^2 at 75 K and self-field on $LaMnO_3$-buffered MgO IBAD/Ni-alloy substrates using PLD. This corresponds to an critical current of 231 A/cm-width. In this paper, we report our first successful demonstration of the growth of thick YBCO films on $LaMnO_3$-buffered IBAD-MgO templates using MOCVD. In addition, we have demonstrated that LMO buffers can be deposited in very high deposition rates and in a wider process window, and we have achieved high critical currents on MOCVD-grown YBCO films in long lengths.

We have grown 25- to 300-nm-thick LMO buffer layers on IBAD MgO templates on Ni-alloy by rf-magnetron sputtering. The oxide sputter targets were made from the single phase of LMO powders, prepared by solid-state reaction and loosely packed in a 4-in. copper tray. Typical sputter conditions consisted of 2 to 5×10^{-5} Torr of H_2O with a total pressure of 3 mTorr forming gas (Ar/H_2 4%). The LMO films were grown at a substrate temperature of 625 to 775°C. The water pressure is sufficient to oxidize the film to form stoichiometric $LaMnO_3$. The MgO template consists of a polished hastelloy C276/amorphous Al_2O_3 barrier layer (80 nm)/nano-crystalline Y_2O_3 seed layer (7 nm)/IBAD MgO layer (10 nm)/homo-epitaxial MgO layer (30 nm). The schematic architecture of the IBAD-MgO/MOCVD-YBCO 2G conductors is shown in Fig. 2.30. Detailed processing conditions for the preparation of IBAD MgO template were published earlier. YBCO films were deposited using MOCVD. The details of the YBCO deposition were also reported earlier. The typical YBCO thickness is 1.1 µm. J_c was measured using a four-point probe configuration at 77 K in self-field. The texture of the samples was quantified using X-ray diffraction (XRD), and sample microstructure was examined using both scanning electron microscope (SEM) and cross-sectional transmission electron microscope (TEM).

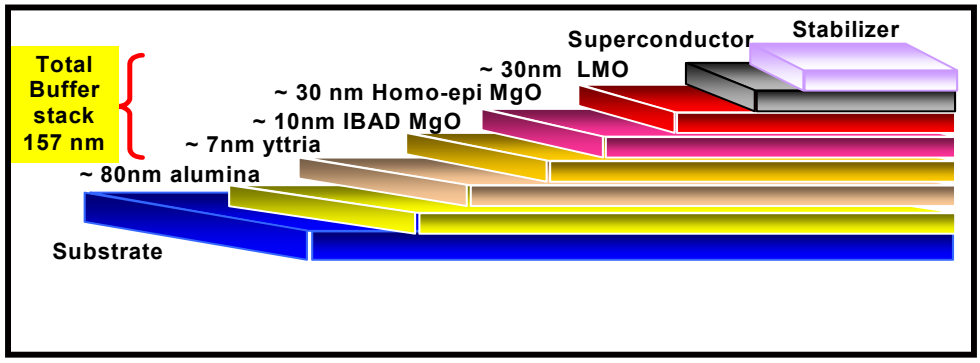

Fig. 2.30. Schematic architecture of IBAD-MgO/MOCVD-YBCO 2G conductors.

Typical θ-2θ scans of a 300-nm-thick LMO film grown on homo-epitaxial MgO layers indicated the presence of a highly c-axis-oriented LMO phase. Initially, CeO_2 cap layers were deposited on some of the LMO-buffered IBAD-MgO templates using rf sputtering. Since LMO layers are compatible with

MOCVD-grown YBCO films, it is not necessary to deposit CeO_2 cap layers. As shown in Fig. 2.31, the XRD results from ω and ϕ scans on CeO_2/$LaMnO_3$/IBAD-MgO revealed good epitaxial texturing. The full-width half-maximum (FWHM) values for $LaMnO_3$ (002) and CeO_2 (004) are 3.2° and 3.0°, and those of $LaMnO_3$ (110) and CeO_2 (222) are 7.7° and 5.3°, respectively. The textures of both CeO_2 in-plane and out-of-plane improves significantly compared to the IBAD-MgO template layers. This is mainly due to the planarization of the growing surfaces and proves $LaMnO_3$ as the ideal buffer layer for high-performance superconductor coatings. Typical θ-2θ scans of a 1.1-μm-thick YBCO film grown on CeO_2/$LaMnO_3$-bufffered IBAD-MgO templates using MOCVD are shown in Fig. 2.32. These scans indicated the presence of *c*-axis-aligned YBCO films. The superconducting properties of a 1.1-μm-thick YBCO film grown on CeO_2/$LaMnO_3$-buffered IBAD-MgO templates using MOCVD is also shown in Fig. 2.32.

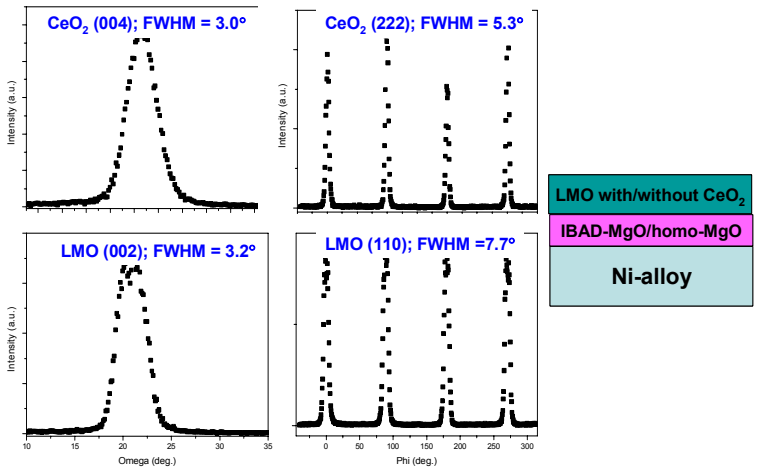

Fig. 2.31. The ω and ϕ scans for a 60-nm-thick CeO_2/300-nm-thick $LaMnO_3$-buffered IBAD-MgO templates using rf sputtering. The FWHM values for each scan are shown inside the scans.

As from the current-voltage (I-V) curve, a critical current of 272 A/cm-width was measured (J_c = ~2.5 MA/cm^2) at 77 K and self-field . This is the highest critical current measured on a typical 1.1-μm-thick MOCVD-grown YBCO film on IBAD-MgO templates. Using reel-to-reel pilot-scale buffer deposition process, LMO buffers were deposited on IBAD-MgO templates in various thicknesses ranging from 25 to 125 nm and at various deposition temperatures (ranging from 625 to 775°C) using rf sputtering with a deposition rate of over 10 m/h. YBCO films with a thickness of 1.0 μm were deposited on the LMO layers using MOCVD. The superconducting properties are reported in Fig. 2.33.
YBCO films with a critical -current range of 175 to 195 A/cm-width were achieved on LMO layers deposited at 650 to 775°C in short lengths. In addition, we have also achieved a critical current of 175 A/cm-width for MOCVD-grown YBCO films on 25-nm-thick LMO layers in short lengths. This demonstrates that LMO has a wide process temperature window, thinner buffer cap layers, and high deposition rates. Based on these results, we have fabricated 25-m lengths of MOCVD-YBCO/LMO cap/IBAD-MgO templates and achieved an end-to-end critical current of 142 A/cm-width. The critical current measured at every meter interval is shown in Fig. 2.34. These results demonstrate that uniform critical currents can be achieved on LMO-buffered IBAD-MgO templates. Efforts are being made to fabricate 250-m lengths of $LaMnO_3$-buffered IBAD-MgO templates with high throughput rates; the results will be published soon.

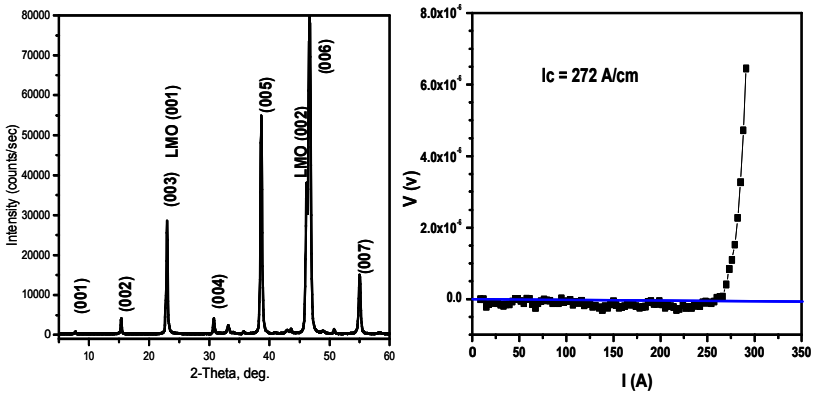

Fig. 2.32. A typical θ-2θ scan for a 1.1-μm-thick YBCO film grown on CeO_2/$LaMnO_3$-buffered IBAD-MgO templates using MOCVD. YBCO film has a preferred *c*-axis orientation. The transport current-voltage (I-V) characteristics for the same film is also shown. A critical current of 272/cm-width was measured.

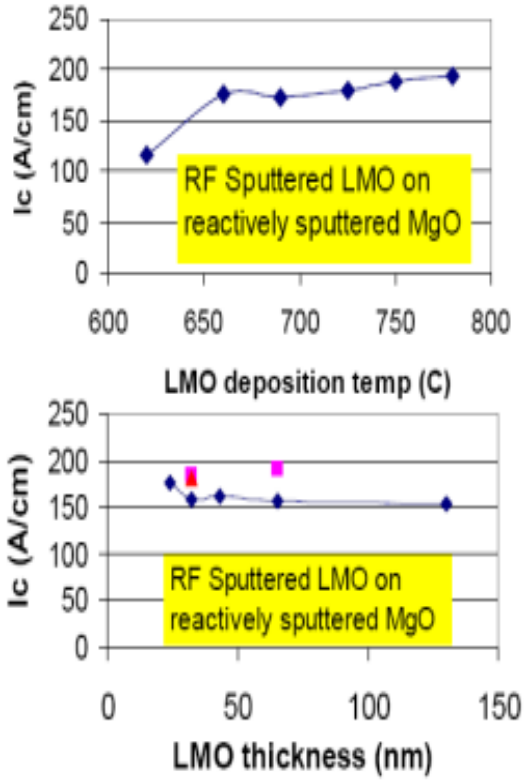

Fig. 2.33. Superconducting properties of a 1.1-μm-thick YBCO film grown on $LaMnO_3$-buffers deposited at various temperatures and various thicknesses on IBAD-MgO templates in short lengths using MOCVD in a reel-to-reel configuration.

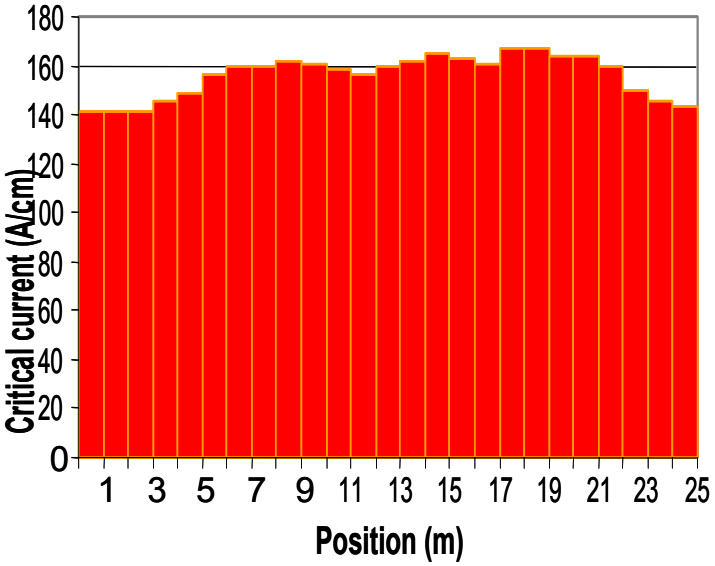

Fig. 2.34. Superconducting properties of a 1.1-μm-thick YBCO film deposited in 25-m lengths of $LaMnO_3$-buffered IBAD-MgO templates with all high throughput buffer layers. IBAD-MgO was deposited at 10 m/h; reactively sputtered homo-epitaxial MgO was deposited at 10 m/h; rf-sputtered LMO was deposited at 10 m/h; and finally MOCVD-YBCO was deposited at 10 m/h (2 passes). The critical current was measured at every meter interval.

In summary, we have demonstrated the feasibility of $LaMnO_3$ buffer layers with IBAD-MgO templates that yield very high current density MOCVD-YBCO films. A transport critical current density of ~2.5×10^6 A/cm^2 was obtained on 1.1-μm-thick YBCO films grown on CeO_2/$LaMnO_3$/IBAD-MgO templates. This corresponds to a critical current of 272 A/cm-width at 77 K and self-field. This performance is the best result achieved on IBAD-MgO template in short lengths for a YBCO thickness of 1.1 μm. In addition, we have demonstrated that very thin LMO buffers can be deposited at very high rates and in a wider processing window and still achieve high-current-density YBCO films. We have also shown that LMO buffers can be deposited in 25-m lengths and that they have an end-to-end critical current of 142 A/cm-width. This promises a route for fabricating long lengths of YBCO coated conductors using an easily scaleable IBAD-MgO template and $LaMnO_3$ buffer layer technology.

2.8 Effects of Preannealing on the Conversion of $YBa_2Cu_3O_{7-\delta}$ Precursor Films Made by E-beam Co-evaporation

Y. Zhang (ORNL and The University of. Tennessee), R. Feenstra and D. K. Christen (ORNL)

Great achievements have been made during last ten years in the development of the technology for fabricating $YBa_2Cu_3O_7$ (YBCO) coated conductors for energy efficient electric-power applications. Biaxially textured substrate templates can now be fabricated using techniques such as RABiTS™ or IBAD. The properties of YBCO films made by either in situ or ex situ methods have been significantly improved, and the performance requirements are being approached by laboratory short samples. Efforts are being made in industries and laboratories for scaling up the process and fabricating long-length wires with properties similar to short samples. The goal, for example, is to make 1000-m tapes with critical current (77 K, self-field) reaching 1,000 A/cm-width by 2010.

While industries are making progress in the scaling-up of the process, there are still many technical challenges to produce practically viable, long-length coated conductors with a low cost. The main challenges include (1) finding simpler, therefore more economical ways of making substrate/buffer template, (2) improving the existing techniques or developing new deposition methods to achieve higher throughput of YBCO film, (3) realizing end-to-end property uniformity for long wires, and (4) attaining critical currents that scale with film thickness.

Two major ex situ approaches, namely TFA-MOD and e-beam co-evaporation, have been intensely investigated for fabricating high-critical current YBCO films. Unlike the TFA-MOD approach in which a long-time low-temperature calcination is indispensable to make the precursor film, e-beam co-evaporation is an easier approach to deposit dense, homogeneous, and thicker precursors. The main difficulty of this technique, also known as BaF_2 process, is in the precursor conversion: there are many parameters that are effectively involved so that control of the conversion is not straightforward; the optimized processing window is small so that the film quality depends strongly on the processing conditions; the conversion rate is relatively low, which complicates the long-length, thick-film processing. Moreover, the mechanism of the conversion reaction and the film formation is yet not fully understood.

The thermodynamics and kinetics of the conversion reaction and YBCO film formation are basically determined by the structural and chemical states of the precursors as well as the processing conditions. For a fixed processing condition, the precursor conversion behavior differs when the precursor state is changed. It is therefore possible to make the precursor more "conversion-friendly" by enhancing the precursor conversion characteristics through certain modification of the precursor structure and chemistry. While great efforts have been made in studying the conversion annealing and optimizing the processing parameters, there has been little investigation of the modification of the e-beam evaporated precursors. It was once reported that a thin layer of Ag coating on the precursor surface prior to the conversion could help enhance the YBCO orientation [1]. On the other hand, for solution-based MOD technique, precursor modification has been pursued explicitly with variation of the solution chemistry and optimization of the calcination. From the baseline TFA method, modified precursors such as reduced-fluorine precursors have emerged, adding further options and potential.

The precursor modification can be implemented not only through the deposition, but also after the deposition. In this study, an intermediate low-temperature (400 to ~500°C) anneal was given to the e-beam co-evaporated precursors after the deposition and prior to the high-temperature conversion. The preannealed and the as-deposited precursors were converted under the same condition, and the results were compared for evaluating the effects of the precursor modification through the preannealing. The precursors and the converted films were characterized for understanding the effects of the preannealing. XRD and TEM were used for the structural analysis, and X-ray photoelectron spectroscopy (XPS) was used to compare the elemental chemical states of precursors that convert differently.

2.8.1 Experimental

Stoichiometric YBCO precursor films (< 1.5 μm thick) were deposited on single-crystal (100) $SrTiO_3$ (STO) substrates, CeO_2 buffered single-crystal YSZ, and on CeO_2/YSZ/Y_2O_3 buffered RABiTS™ at ~100 °C by e-beam co-evaporation of Y, BaF_2 and Cu at a deposition rate of about 1 nm/s. The oxygen pressure for the deposition was about 5×10^{-6} Torr. The precursor preannealing was carried out in a quartz tube furnace at 400 to ~500°C for 30 to ~60 min, under 1 atm pressure with various oxygen content. The precursors that undergo the intermediate lower-temperature annealing are referred as "preannealed" precursors. The as-deposited and preannealed precursors were processed in a low-pressure system in which oxygen partial pressure, $P(O_2)$, and water partial pressure, $P(H_2O)$ were carefully controlled [2].

The critical current densities of YBCO films were measured by a Quantum Design MPMS 7 SQUID magnetometer, where the magnetic field was applied perpendicular to the film surface. The critical-current-density values were determined by the application of the Bean critical state model, $J_c = 30\Delta M/d$, where ΔM is the magnetization hysteresis (emu/cm^3) and d is the lateral size of the sample (cm). X-ray

photoelectron spectroscopy (XPS) was carried out using a PHI 5600 system with a nonmonochromatic Al K_α source. The X-ray beam spot size was about 0.8 mm in diameter. The electron binding energy scale was calibrated using the Au 4f7/2 and Cu 2p3/2 lines from pure Au and Cu.

2.8.2 Results and Discussion

Earlier work has shown that high-critical-current-density YBCO films can be made through a low-pressure conversion of e-beam co-evaporated precursors [2]. However, the structure and properties of the films were sensitive to the processing parameters, especially the processing temperature and $P(H_2O)$. It was found that more aggressive processing conditions implemented by higher temperature and higher water partial pressure normally lead to the formation of more randomly oriented YBCO, which deteriorates the properties. To achieve high critical current density, the conversion for the as-deposited precursors had to be conducted under less reactive conditions with the conversion rate limited to < 1 Å/s. The slow conversion rate, which limits the throughput of the processing, becomes the bottleneck for the scaling-up of the technique. The effect of $P(H_2O)$ on YBCO film orientation, indicated by the film surface SEM morphology, is shown in Fig. 2.35.

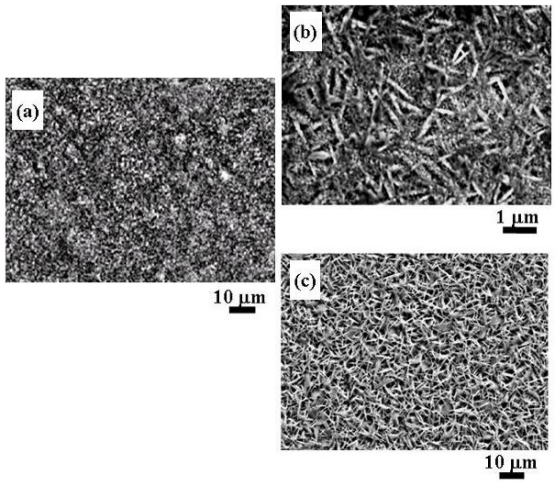

Fig. 2.35. SEM surface morphology of YBCO films converted from the as-deposited precursors under three water vapor partial pressures. $P(H_2O)$ = (a) 1 mTorr, (b) 5 mTorr, and (C) 10 mTorr. The substrates were CeO_2 buffered YSZ.

A comparison study of TFA-MOD and e-beam co-evaporated precursor conversion revealed that the conversion behaviors of the two types of precursors are different [3]. In brief, typical TFA-MOD precursors require more reactive conditions to be converted, compared with the e-beam precursors. As a rule, a low-temperature (~400°C) calcination in oxygen-containing ambient is used to make these solution-based MOD precursors, which has been found to be determinative to the precursor conversion characteristics. An interesting question is what change would be if the e-beam precursors undergo a similar low-temperature annealing before being converted. To evaluate the possible effects of the preannealing, e-beam precursor films deposited on single-crystal STO substrates, with and without a pre-annealing after the deposition, were processed under the same conditions. Typically, a series of conversions were conducted under the same $P(O_2)$, about 100 mTorr at 760°C but with different water $P(H_2O)$. For the as-deposited precursors, high-critical-current-density film can only be obtained when $P(H_2O)$ was limited to 0.2 to ~1 mTorr. Using higher $P(H_2O)$, such as 2 to ~10 mTorr, yielded the formation of more randomly oriented YBCO, which greatly degrades critical current density. The preannealed precursors, in contrast, can be converted at higher $P(H_2O)$ without degradation of the properties. The critical current density vs processing time relationship in Fig. 2.36 shows that the preannealed precursor can tolerate more aggressive processing conditions, which results in much faster effective conversion.

A similar preannealing effect was also observed for the e-beam co-evaporated precursors deposited on CeO_2 buffered YSZ and standard RABiTS™ substrates. The conversion behavior difference for the precursors with and without the pre-annealing is larger when higher $P(H_2O)$ is used. XRD pole figure analysis indicated that higher critical current density of the films converted from the preannealed precursors is due to their better film texture. In fact, the preannealed precursor not only tolerates higher $P(H_2O)$ but also higher processing temperature. Therefore, the processing window for making high-critical-current-density YBCO films is extended compared with that for the as-deposited precursors. By using higher temperature and higher $P(H_2O)$, the effective conversion rate for the preannealed precursors can be as high as 12 Å/s. Preliminary experimental results have also shown that the preannealing effect is

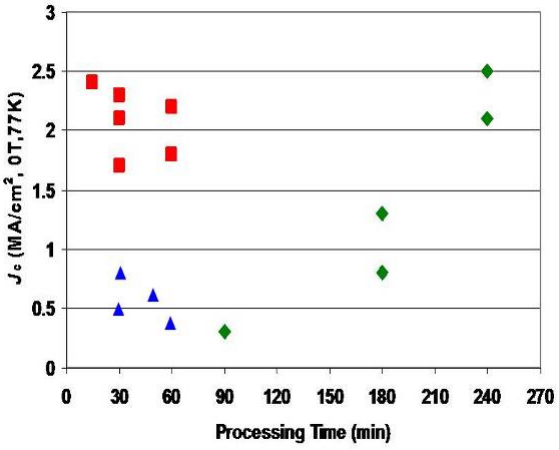

Fig. 2.36. Critical current density (self field, 77 K) vs processing time relationships.
Precursor conversion conditions:
■ Preannealed, converted at higher P(H_2O)
▲ As-deposited, converted at higher P(H_2O)
♦ As-deposited, converted at low P(H_2O)

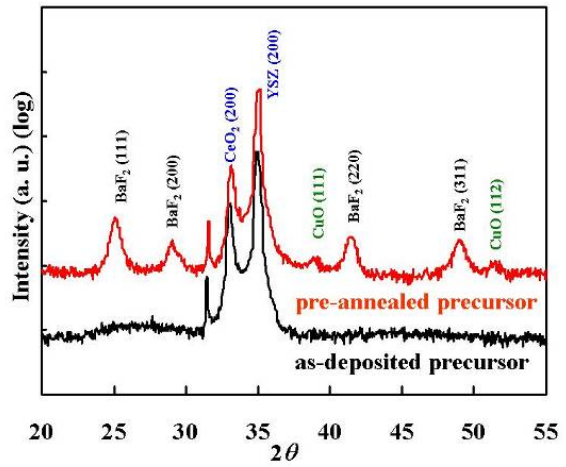

Fig. 2.37. XRD θ-2θ scan patterns for the as-deposited and preannealed e-beam precursors on CeO_2-buffered YSZ substrates.

not strongly sensitive to the preannealing condition. An intermediate treatment at a temperature between 400 to ~500°C and in an atmosphere with oxygen content varying from 10 to ~100 % facilitates faster conversion of the e-beam co-evaporated precursors for both low-pressure and atmospheric-pressure conversions [4,5].

To understand the preannealing effect, the preannealed and as-deposited precursors were studied using XRD, TEM and XPS. The inspections focused on the differences in the precursor structure and chemistry, which could account for their different conversion behaviors. The XRD θ-2θ scan patterns of a preannealed precursor and an as-deposited precursor are shown in Fig. 2.37. The precursors were deposited on CeO_2-buffered YSZ substrates. Apparently, the as-deposited precursor is basically amorphous, with no peaks shown in the diffraction pattern except that from the substrate. For the preannealed precursor, which was annealed in pure oxygen of atmospheric pressure at 500°C for 60 min, has crystallized BaF_2 and CuO. From the Sherrer equation, the size of the nano-crystallites of BaF_2 and CuO were calculated to be about 15 nm. This size is close to that of BaF_2 and CuO in calcinated TFA-MOD precursors [5]. The formation of the nano-crystallites due to the preannealing was further confirmed by transmission electron microscopy (TEM). The essentially amorphous structure of the as-deposited precursor is one of the basic reasons that it is more reactive under aggressive processing conditions. A precrystallization may help stabilize the precursor.

XPS, which is sensitive to the elemental chemical state, was used for investigating the precursors and their conversion, to assess whether the different conversion behavior may result from the difference in precursor chemistry. For comparison, pure BaF_2 films deposited in the same *e*-beam evaporated system were also inspected. It was found that the chemical states of barium in the pre-annealed and the as-deposited precursors are the same, and close to that in the pure BaF_2 film. This implies that under the preannealing condition, BaF_2 does not decompose; instead, more stable BaF_2 nano-crystallites form.

In Fig. 2.38 are the Cu2p XPS spectra for the surfaces of the (a) preannealed and (c) as-deposited precursors; (b) and (d) are the Cu2p XPS spectra of two copper films, one in the as-deposited state and the other was annealed under the same condition for the preannealing of the precursors. For comparison, the Cu films were deposited in the same system and under the same conditions as the precursors. It can be seen that the chemical states of copper are similar for the precursors and the copper films when they are either at the annealed state or at the as-deposited state. Based on whether the spectrum contains the so-called "shake-up satellites," which are the signature of Cu^{2+}, it is seen that Cu at the surface of the preannealed precursor and the annealed Cu film are in the state of Cu^{2+} as in CuO, while no CuO exists at

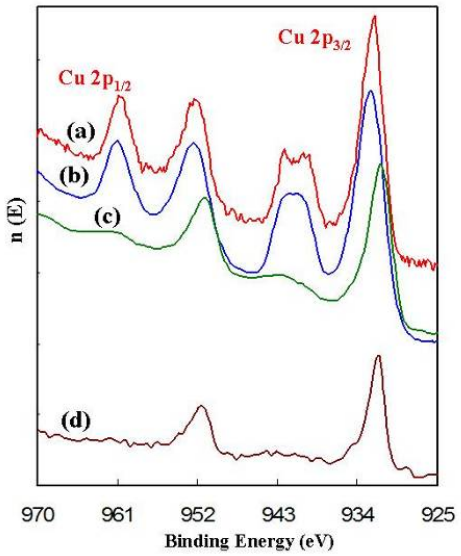

Fig. 2.38. Cu2p XPS spectra from the surfaces of (a) the preannealed precursor, (b) the annealed Cu film, (c) the as-deposited Cu film, and (d) the as-deposited precursor.

the surface of the as-deposited precursor and the as-deposited Cu film. Further investigation indicated that the Cu oxidation state difference extends from surface through the thickness. The conversion behavior difference is partially attributed to the variation in the Cu oxidation state.

2.8.3 Summary

E-beam co-evaporated YBCO precursor films were processed with and without an intermediate anneal prior to their conversion to superconducting films. The preannealing was conducted at 400 to ~500 °C. It was demonstrated that preannealing has significant effects on the conversion characteristics. In contrast to the as-deposited precursors, preannealed precursors can be processed under more reactive conditions, implemented with higher temperature and higher water partial pressure, leading to a faster conversion rate, while still forming predominantly *c*-axis–oriented YBCO films. The precursors with and without the preannealing were characterized using XRD, XPS, and TEM. It is indicated that the precursor has both structural and chemical change through the preannealing. The strong effects of the precursor preannealing imply that a further modification in the e-beam co-evaporated precursors could help achieve faster processing and higher critical currents.

2.8.4 References

1. T. Clausen, et. Al., *Appl. Phys. Lett.* **65**, 2350 (1994).

2. Y. Zhang, et. al., *Supercond. Sci. Technol.* **17**, 1154–59 (2004).

3. Y. Zhang, et. al., *IEEE. Trans. Appl. Supercon.* **15**, 2659 (2005).

4. R. Feenstra, et. al., *IEEE Trans. Appli. Supercond.* **15**, 2803 (2005).

5. Y. Zhang, "*Ex-Situ* Epitaxial YBCO Films: Precursor Conversion and Film Characterization," Doctoral Dissertation, The University of Tennessee, Knoxville (December 2006).

2.9 Characterization of Phase Evolution in YBCO Coated Conductors Produced by the Ex Situ BaF_2 Process

R. Feenstra, F. A. List, Y. Zhang, and D. K. Christen (ORNL); V. A. Maroni and D. J. Miller (ANL); and D. M. Feldmann (University of Wisconsin)

The ex situ conversion of BaF_2 containing precursors is a leading technique for production of $YBa_2Cu_3O_7$ (YBCO) coated conductors, because of the potential for economic scale-up and because of the ability to yield large values of the critical current. The method relies on the fast deposition of a precursor film containing the essential metallic ingredients and the subsequent growth of epitaxial YBCO by means of a high-temperature furnace anneal. During the anneal, Ba-F phases are chemically decomposed by a reaction with water vapor, leading to the release of HF gas. Numerous reports have appeared in recent years on the complex chemistry and kinetics associated with this conversion process, in particular for solution-based precursors produced by metal-organic deposition of trifluoroacetates (MOD-TFA).

An interesting recent result from research on physical-vapor-deposited (PVD) precursors has been the identification of a strong effect of intermediate annealing (400–500ºC) on properties of the film after high-temperature conversion. This low-temperature anneal resembles the solvent burnout commonly applied to MOD precursors. Because of the absence of organic solvents, however, such anneal is optional for PVD precursors. When 1-µm-thick precursors with and without an intermediate anneal were compared, it was found that the former were able to convert well into *c*-axis YBCO at high rates (> 5Å/s), whereas the as-deposited films did not. Preannealed precursors yielded YBCO films on RABiTS™ with high critical current density and a nearly linear increase of critical current with YBCO layer thickness (*d*). Subsequent research on 0.35-µm-thick precursors using X-ray photo-emission spectroscopy (XPS) confirmed that the intermediate anneal increased the Cu valence near the surface as well as in the interior of the film.

This report expands on the previous research as we investigate the thickness dependence of the conversion rate (using constant process parameters) and as we characterize in detail the nucleation process for ~2-µm-thick films. At that thickness, strong deviations from the linear I_c-*d* relation are found to occur. The main techniques for the latter research are Raman microprobe spectroscopy (RM) and scanning electron microscopy (SEM) augmented with energy dispersive spectroscopy (EDS) and focused ion beam milling (FIB) capabilities. To obtain a through-thickness view of nucleation events and evolution, quenched samples were prepared and subsequently thinned to various step heights by Ar ion milling on a low-temperature stage. Preliminary indications from the research are that the thick precursors contain oxygen concentrations near the substrate that are too low to enable formation of a dense array of *c*-axis YBCO nuclei, leading to undesirable non-*c*-axis growth, especially at the top of the film. Precursor layers of variable thicknesses were prepared by electron-beam evaporation of Y, BaF_2, and Cu sources, as we have previously described. The films were deposited on RABiTS™ templates, provided by American Superconductor Corporation (AMSC). These templates feature a Ni-5at.%W metal tape coated with a stack of Y_2O_3, yttria-stabilized zirconia (YSZ), and CeO_2 buffer layers. The substrate temperature during deposition was 100ºC or less; the oxygen background pressure was < 10^{-5} Torr. Typical conditions for the intermediate oxidation anneal were a temperature of 400ºC, duration of 0.5 h, and oxygen pressure of 0.1 atm. High-temperature conversion was performed in a tube furnace with flowing gases at 1 atm, using monitored amounts of H_2O and O_2 according to the "fast" process we have described previously. The conversion temperature was set at 780ºC, and the H_2O partial pressure was set at ~0.015 atm. The O_2 pressure was varied between 0.00018 and 0.00032 atm. These conditions yield conversion rates of 7 to 12 Å/s for small-area films (0.3 cm^2) with thickness in the range of 0.2 to 2 µm. Quenching was performed by turning off the furnace power and opening the top of the clamshell furnace, which results in a temperature drop of > 100ºC during the first minute.

Select experiments to monitor the conversion process in real time were performed in a low-pressure apparatus equipped with in situ X-ray diffraction (XRD) capability. The sample size in this case is 3 × 1 cm. The substrates were ORNL-produced RABiTS™, featuring buffer layers similar to the AMSC RABiTS™ but deposited on textured Ni-3at%W tape. As in the previous report on fast conversion with this low-pressure system, the temperature was set at 780ºC, using a ramp rate of 50ºC/min. The total pressure was 500 mTorr, $p(O_2)$ = 200 mTorr, $p(H_2O)$ = 10 mTorr, and Ar was used as the ballast gas (290 mTorr). The conversion rate was determined with ±10% accuracy from the observed linear increase in YBCO (002) peak intensity and simultaneously occurring variations in the BaF_2 (111) intensity.

Figure 2.39 compiles thickness-dependent data for the YBCO conversion rate measured with the in situ XRD low-pressure system and self-field critical current values at 77 K of the corresponding samples after final oxidation. Also included in Fig. 2.39, indicated by the data points of lighter shading, are critical current values obtained with the 1-atm conversion system for films ranging between 0.2 and 2 µm deposited on AMSC RABiTS™. The latter provide an update of data presented in Ref. [1] with improved performance for films of several thickness values: $I_c \cong$ 450 A/cm for a 1.7-µm film, ~300 A/cm for a 1.1-µm-thick film, and >300 A/cm for several films of 1.8to 2 µm. The nearly linear I_c-*d* increase in the range 0.2 to 1.7 µm suggests a constant critical current density value of about 2.5 MA/cm^2 (with higher values for some exceptional films). In more detail, critical current density decreases from a maximum of

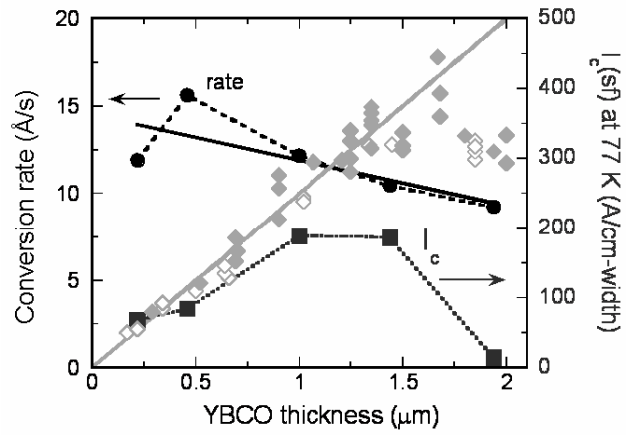

Fig. 2.39. Dependence of the conversion rate for a fixed set of processing parameters on film thickness deduced from in situ XRD measurements in a low-pressure conversion system (black circles, left-hand scale). Corresponding values of the critical current (I_c) are indicated by the black squares (right-hand scale). Grey diamonds are I_c values of YBCO films produced by ex situ conversion in the standard 1-atm furnace. Open symbols are for nearly stoichiometric compositions; filled symbols are for Y-doped compositions. The grey straight line corresponds to J_c = 2.5 MA/cm^2. All films were deposited on RABiTS™ templates.

3.5 to 4 MA/cm^2 for $d \cong 0.12$ μm to 2.5 MA/cm^2 for $d \cong 0.5$ μm. The reason for this initial decrease in critical current density remains under investigation.

Mimicking the 1-atm converted films, the low-pressure films exhibit a ~linear increase with d as well, up to about 1 μm. For larger d, however, critical current rolls over and decreases abruptly for a 1.9-μm film. This tendency for a "breakdown" in conversion results for a fixed set of processing parameters is also evident for the 1-atm converted films, although the effect in Fig. 2.39 is subdued by the application of minor adjustments to the processing parameters for the thickest films and inclusion of best data.

Significantly, the average conversion rate stays nearly constant over the full thickness range, decreasing in the thick films by no more than 20 to 30% compared to a 0.2-μm thin film. The absence of strong thickness dependence suggests that the conversion rate in these experiments is controlled primarily by the H_2O and HF gas exchange at the film surface and is affected only weakly by through-thickness diffusion of those species. The data also show that the sharp drop in critical current for the 1.9-μm film is not due to a significant change in the conversion rate.

On the contrary, similar to the in situ XRD data reported in Ref. [1], the present data suggest the existence of a structural and/or chemical difference between 1- and 2-μm precursors prepared in a similar manner. While in the previous study improved growth and critical current performance resulted from insertion of an intermediate anneal (compared to as-deposited precursor), the conversion rate was unaffected by the precursor condition. Adding to the correspondence, XRD analysis of the low-pressure converted films of Fig. 2.39 indicate complete *c*-axis epitaxy for the films up to 1 μm, and systematically increasing amounts of non-*c*-axis YBCO in the 1.4- and 1.9-μm films. These observations agree well with the critical current results. We conclude that the primary reason for the performance "breakdown" in the 1.5- to 2-μm films is a precursor characteristic, necessitating either a different preparation history (possibly including the deposition step) or adjusted conversion parameters.

The conversion properties of the thick films were further characterized by SEM analysis. Figure 2.40 shows SEM images of a 2-μm-thick film that was quenched from the conversion temperature (780ºC) after a hold of 4 min. At an average conversion rate of 9 Å/s, this duration represents about 10% of the full conversion time.

Displayed are images at three levels through the thickness of the film: the top surface (step 1), a central thickness of about 1.1 μm (step 3), and a bottom step of about 0.5 μm thick (step 5). Included with each step are the fluorine and oxygen EDS maps of the imaged regions. A one-to-one correlation exists between local areas of fluorine depletion and oxygen enrichment and surface features in the secondary electron images. These features, apparently, correspond to nuclei where a conversion reaction took place. Thus, Fig. 2.40 illustrates the formation of nearly round 10- to 20-μm nuclei near the substrate interface (step 5). RM analysis [Fig. 2.41(a)] identifies these nuclei as *c*-axis YBCO. At that level inside the film, relatively few tilted YBCO nuclei were found. A spectrum for an isolated example is included in Fig. 2.41(a). Higher up in the precursor (step 3 and the top surface, step 1), various nuclei are seen as

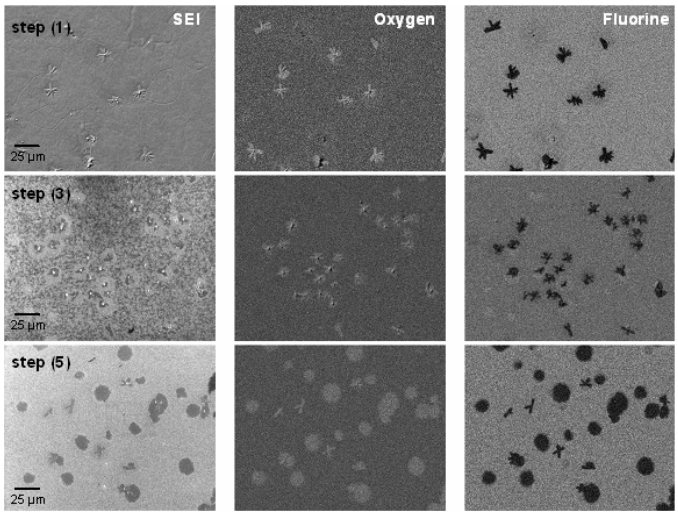

Fig. 2.40. SEM images and oxygen and fluorine EDS maps illustrating YBCO nuclei at three levels within a quenched, partially processed 2-µm-thick film. Step 1 is the film top surface, step 3 is approximately midway through the precursor, step 5 is approximately 0.5 µm above the substrate interface. Light shadings in the EDS maps indicate a high concentration. Note the spatial correlation between the islands of F depletion and O enrichment, the surface features in the secondary electron images, and the different shapes and sizes of those features on the different steps.

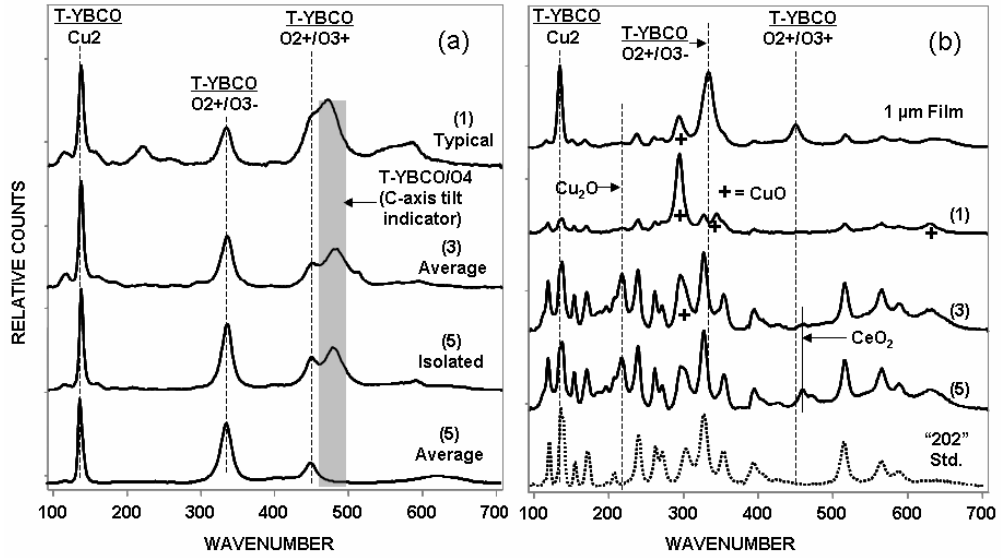

Fig. 2.41. Raman microprobe spectra of YBCO nuclei (a) and unconverted matrix (b) in the three steps imaged in Fig. 2.40 through the thickness of a partially processed 2-µm-thick precursor. In (a), the spectrum for step 1 is typical for the nuclei that were observed; spectra for steps 3 and 5 were averaged over several nuclei. The spectrum for an isolated tilted nucleus in step 5 is also shown. Included in the bottom of (b) is the spectrum for a bulk $Y_2Cu_2O_5$ standard (dotted line). Peaks corresponding to CuO are indicated with a + symbol. Topmost spectrum in (b) is an average surface spectrum for a similarly processed, quenched 1-µm-thick film.

well. However, most of the nuclei have different shapes, resembling a flower with a central core and "petals" extending outward. Higher-magnification images show the central core protruding upward from the "petals" at the surface. These nuclei are no longer *c*-axis YBCO, but as indicated by the RM data [Fig. 2.41(a)], consist of tetragonal YBCO with tilted orientations. The number density of nuclei does not vary much between the steps. The density is highest near the substrate, but still substantial toward the film surface. This suggests that either there is a changeover of growth properties midway through the thickness or a second nucleation mechanism. We discuss this point further below.

Outside the nuclei [Fig. 2.41(b)] the precursor matrix consists of intermediate phases such as CuO and $Y_2Cu_2O_5$ (hereafter referred to as "202" phase). These phases are precursors for the final conversion into YBCO. Note the strong intensity of the 202 phase in steps 3 and 5 near the substrate and the much weaker intensity near the surface in step 1. No YBCO intensity is detected in either of the matrix spectra, consistent with a complete segregation of material into YBCO nuclei and unconverted matrix. However, while the surface of the film contains a strong CuO signal, the intensity decreases deeper into the precursor, where it is replaced with a growing Cu_2O signal. Cu_2O is not a dominant precursor phase of YBCO as the Cu valence averaged over the three Cu-O lattice planes in the oxygen-deficient $YBa_2Cu_3O_6$ unit cell equals 1.67 (assuming full oxidation of Y and Ba). It is very likely that the reduced oxygen concentration in the bottom of the film is responsible for a reduced YBCO nucleation at the substrate interface and for the relatively small nuclei density observed in Fig. 2.40.

The significance of this observation is illustrated by the fact that the surface Raman spectrum of a 1-μm film processed and quenched under identical conditions displays a complete absence of monovalent Cu and already contains strong *c*-axis YBCO intensity [Fig. 2.41(b)]. The latter signal presumably comes from densely populated *c*-axis YBCO nuclei that have grown in close proximity to the film surface. Although oxidation effects during transport and storage in air preclude firm conclusions regarding the presence of Cu_2O in the near-surface region, the fact that a small Cu_2O signal is observed for the 2-μm film and not for the 1-μm film indicates a systematic difference in the oxygen concentration profiles of the two films, consistent with the different thickness. Figures 2.41(a) and (b) suggest that YBCO nucleation occurs while much of the Cu is still being oxidized to the divalent state in the 2-μm film, whereas sufficient oxygen is present near the substrate interface in the 1-μm film during the critical moment of initial nucleation.

The RM data presented above provide a possible explanation for the poor conversion properties of the 2-μm films. Starting from the observation of large amounts of monovalent Cu deep inside the film, and consistent with effects described in Ref. [2], we postulate that a low oxygen concentration impedes the formation of *c*-axis YBCO nuclei, leaving large spaces between them. Remarkably, no incubation time is observed in the in situ XRD measurements for the thicker films, suggesting that *c*-axis nucleation occurs immediately on a local scale wherever sufficient oxygen is present. Due to the large spacing between nuclei, coalescence is delayed and the nuclei tend to grow upward where more O is present. In this growth mode, tilted YBCO either nucleates on top of the *c*-axis YBCO or spontaneously at locations away from the substrate ("homogeneous nucleation"). Although some tilted YBCO may nucleate at the substrate interface, the SEM and RM data are consistent in the observation that most of tilted YBCO originates at higher levels in the precursor film. Using FIB milling, we have dissected several of the flower-like nuclei in search of their spatial origin. However, the evidence provided by the images is inconclusive because several modifications of the flower-like structures appear to exist and because complex segregations (of cations and anions) occur inside and around the nuclei at different levels in the precursor. These complex phenomena require further investigation.

An apparent remedy for the poor *c*-axis growth of the thicker films would be the introduction of more oxygen deep inside the precursor to bring about prolific *c*-axis nucleation at the substrate interface. Attempts to accomplish this by extending the duration of the intermediate anneal (to 1 h) or increasing the oxygen pressure (to 1.0 atm) and temperature (500ºC), however, did not lead to significant properties improvement and minor effects were observed by RM. Based on a recent study by Solovyov et al. [2] on the conversion of even thicker films (in the 3- to 4-μm range), it may be more promising to increase the oxygen pressure during the conversion process. In that study, however, narrow windows of optimal

oxygen pressure were identified, which varied with the film thickness. This raises questions about reproducibility and practicality. In our study, only minor effects from variations in the conversion oxygen pressure (0.00018–0.00032 atm) were observed in RM. We conclude by noting that preliminary RM studies on quenched 1.5-μm-thick MOD precursors indicate full oxidation of Cu to a divalent state throughout the precursor thickness. MOD and PVD precursors thus form interesting counterpoints, and a detailed comparison between the two may shed valuable light on the role of oxygen on nucleation and growth during the conversion process.

We used a fixed set of processing parameters to obtain an approximately linear increase in critical current with layer thickness in the range 0.2 to 1.5 μm for YBCO films on RABiTS™ produced by ex situ conversion of e-beam evaporated precursors. An abrupt deviation from the linear dependence was observed, however, for films in excess of 1.5 μm thickness. It is found that the origin of this abrupt deviation does not reside in a strong dependence of the conversion rate on thickness. Rather, a systemic oxygen deficiency in deep portions of thick films leads to anemic *c*-axis nucleation rates, leaving the opportunity for other parts of the film to undergo random nucleation. The results suggest an important role of controlled oxygen supply near the substrate during the early stages of the conversion process, which may be achievable by precursor modification and/or adjustments in the conversion parameters.

2.9.1 References

1. R. Feenstra, et al., *IEEE Trans. Appl. Supercond*. **15** (2), 2803–2807 (2005)

2. V. F. Solovyov, H. J. Wiesmann, and M. Suenaga, *Supercond. Sci. Techn*. **18**, 239 (2005).

2.10 Control of Flux Pinning in an MOD YBCO-Coated Conductor

W. Zhang, Y. Huang, X. Li, T. Kodenkandath, M. W. Rupich, U. Schoop, D. T.Verebelyi, C. L. H. Thieme,and E. Siegal (AMSC); T. G. Holesinger, B. Maiorov, and L. Civale,(LANL); D. J. Miller and V. A. Maroni (ANL); J. Li, P. M. Martin, E. D. Specht, A. Goyal, and M. P. Paranthaman (ORNL)

2.10.1 Introduction

The development of second-generation (2G) YBCO HTS wire has transitioned from a demonstration of the technical feasibility and evaluation of potential manufacturing processes to the scale-up of a commercially viable 2G HTS wire manufacturing technology. For many applications, such as cables and fault current limiters, the self-field critical current is the important parameter. However, for other applications, such as motors and generators, the wire performance in applied magnetic fields is very important. In addition, the dependence of the critical current on the field orientation is critical for maximizing the wire performance in coil applications.

Pulsed-laser deposition (PLD) has been widely used to study the incorporation of pinning centers into YBCO films.

MacManus-Driscoll [1] studied the relationship between pinning and the variance of RE ion size in the Yx(RE1−x)Ba2Cu3Oy system. The addition of BaZrO3 particles has been shown to result in strong pinning behavior in the *H*//*c* direction [2,3]. Matsumoto showed that by decorating the substrate surface with nanodots, YBCO films grown by PLD inherit the defect structure, resulting in tremendous pinning forces along the *H*//*c* direction [4]. All these studies focused on the introduction of random point pinning or correlated pinning along the *H*//*c* direction.

In this work, we report on different types of pinning centers that can be incorporated in MOD YBCO films and their effects on the pinning force as a function of the field orientation. We also report the results of increased pinning both in *H*//*c* and *H*//*ab* directions through RE additions to YBCO films and through the process control of Y(RE_x)BCO superconductors.

2.10.2 Experimental

American Superconductor's 2G manufacturing approach is based on the YBCO(MOD)/RABiTS™ technology. The coated conductor architecture discussed here is based on textured Ni(5at%W) substrates where heteroepitaxial buffer layers of Y_2O_3, YSZ, and CeO_2 are deposited by high-rate reactive sputtering. On top of the buffer layers, a metal trifluoroacetate-based precursor is deposited by MOD [5]. The precursor film is then dried and decomposed to form a mixture of metal oxy-fluorides. A subsequent high-temperature heat treatment is used to convert the precursor into a crack-free, nominally 0.8-µm YBCO superconducting film. The composition of the films was varied from $Y_{1-x}(RE_x)BCO$ (RE = Yb, Eu, Gd, Ho, Sm and $x = 0 – 0.33$) to $Y(RE_x)BCO$ (RE = Er, Dy, Ho, and $x = 0 – 0.5$). The critical current was measured by the standard four-probe method. In-field performance was tested at 65 K and 77 K up to 7 Tesla.

2.10.3 Results and Discussion

2.10.3.1 Origin and control of 124-type intergrowths

MOD-derived YBCO films grow with a laminar structure. This microstructure contrasts sharply with the columnar structure typically seen in PVD processes, such as PLD [5,6,7] and is responsible for the unique properties of the films. The MOD-derived YBCO films have a significant current enhancement with the magnetic field oriented in the *ab*-plane, as shown in Fig. 2.42, due to the existence of a high density of planar defects [6]. Understanding the formation of the planar defects is important since it controls the H//*ab* plane performance.

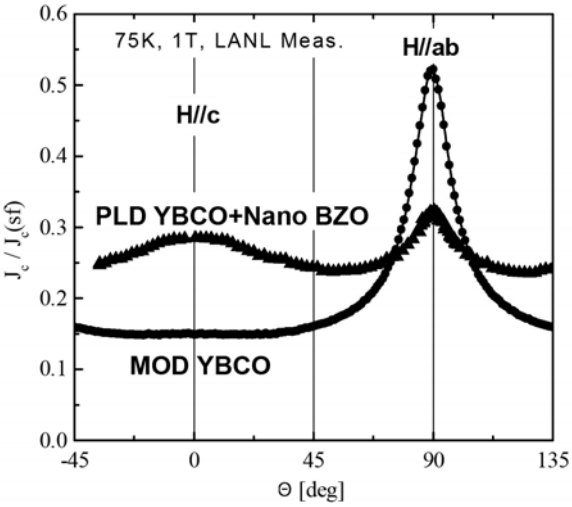

Fig. 2.42. Angular dependence of MOD YBCO/RABiTS™ and PLD films YBCO+$BaZrO_3$ addition.

High-resolution transmission electron microscope (HRTEM) studies of the oxygenated films showed that the planar defects have a lattice parameter of 13.7Å, corresponding to a $YBa_2Cu_4O_x$ type lattice as shown in Fig. 2.43. A Z-contrast image (Fig. 2.44) showed that the planar defects have lower average Z, consistent with $YBa_2Cu_4O_x$ layers. X-ray (2-θ) analysis of YBCO films at various stages of processing show a broadening of (002) and (003) peaks (Fig. 2.45) during the oxygenation step (400–500°C). This peak broadening has been shown to correspond to the density of 124-type intergrowths in the YBCO films [8].

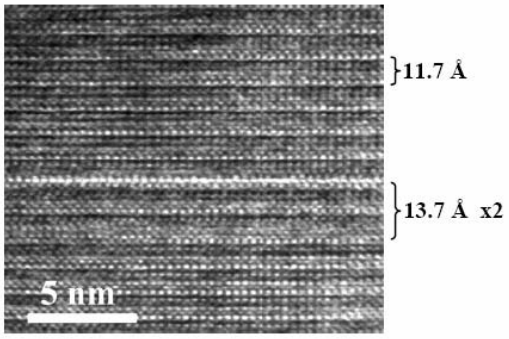

Fig. 2.43. HRTEM shows the lattice of 123 and the intergrowth.

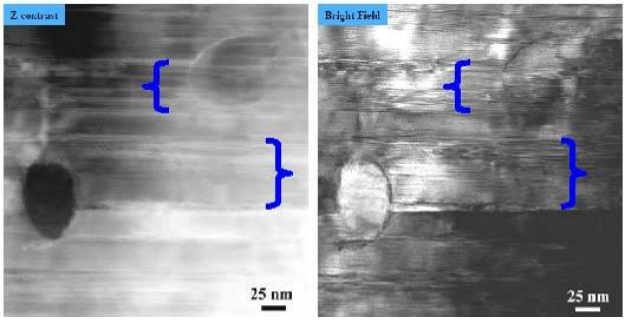

Fig. 2.44. TEM images of YBCO sample with Z-contrast and bright field images. 124 type intergrowths emanate from Ba-Cu-O particles.

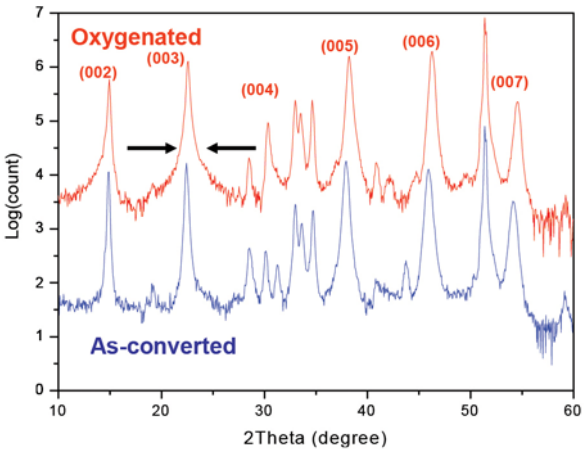

Fig. 2.45. XRD of as converted and oxygenated films.

TEM analysis of the intergrowths shows that they frequently form in groups, emanating from a common particle as shown in Fig. 2.45. Raman, HRTEM and EELS analysis of as reacted YBCO film, in which the intergrowths are just forming, show the particles associated with the intergrowths CuO and $Y_2Cu_2O_5$ are generally not associated with the intergrowths. Raman microscopy measurements [9] also indicate the involvement of a cuprous entity in the as-reacted MOD film. However, the detailed structure and composition of this cuprite phase has not been identified in this study.

2.10.3.2 Control of random pinning

Although the performance of the MOD-based YBCO films is suitable for cable and fault-current-limiter applications requiring high self-field critical current, it is desirable to improve the performance in perpendicular fields present in coil-based applications. One approach to enhancing the pinning of the MOD-based YBCO films is to introduce random pinning to increase the overall pinning force. Fig. 2.46(a) shows the microstructure of the pure YBCO composition. The microstructure shows the presence of porosity and secondary phases. The primary and largest secondary phase, identified by EDS analysis, is predominately a barium cuprate phase. Other secondary phases, with sizes of 10 to 50 nm, include $Y_2Cu_2O_5$ and Y_2O_3.

From the pinning view point, small particles have better pinning effects than large particles and therefore are preferred. In order to increase the density of the small secondary phases, we added additional RE to the film by adjusting our overall composition of Y(RE_x)BCO. Figure 2.46(b) shows the microstructure of a film with the composition Y($Dy_{0.5}$)BCO. EDS analysis of the Dy doped film indicated the secondary phase particles were primarily RE_2O_3 and $RE_2Cu_2O_5$ (RE =Y and Dy) with a significantly reduced amount of barium cuprite. TEM analysis shows the 20- to ~50-nm RE_2O_3 and $RE2Cu_2O_5$ nanoparticles were uniformly distributed in the YBCO matrix as shown in Fig. 2.47.

The introduction of these nanoparticles results in a significant increase in the random pinning compared to that of an undoped YBCO film, as shown in Fig. 2.48. Although the Dy-doped sample shows a significant increase in critical current for $H//c$, the ratio of I_c $[H//ab]/I_c[H//c]$ falls to ~1.3 from ~4.5 in the undoped YBCO film. These changes in the pinning properties are independent of the RE identity as seen in Fig. 2.48, which also shows the angular dependence of Y($Er_{0.5}$)BCO and Y($Ho_{0.5}$)BCO films.

Figure 2.49 shows that both the enhancement in the random pinning and decrease in ab-plane pinning vary with the level of RE doping, with the effect saturating around Y($RE_{0.5}$)BCO. This decrease in the *ab*-plane pinning correlates to the decrease in the 124-type stacking fault density as shown in Fig. 2.50, which can be monitored and modeled by the broadening of the 002 and 003 peak-broadening in the 2-θ scans of the YBCO. This decrease in 124-type intergrowths is believed to be associated with reduction in the amount of the cuprite phase formed in the presence of the increased RE concentration.

The compositional analysis of the RE-doped films indicated that the Y site in the 123 phase is partially substituted with the RE. To evaluate whether the substitution of Y by RE element contributes to the increased random pinning, we tested films prepared with substitution of Y by RE with the composition of Y_{1-x}(RE_x)BCO. The in-field measurements showed that with up to 33% substitution of Y by Yb, Eu, Gd and Sm, no substantial pinning enhancement is observed compared with pure YBCO samples. Therefore, it is clear that the pinning increase with RE addition is due to the introduction of the RE-based nanodots observed by TEM.

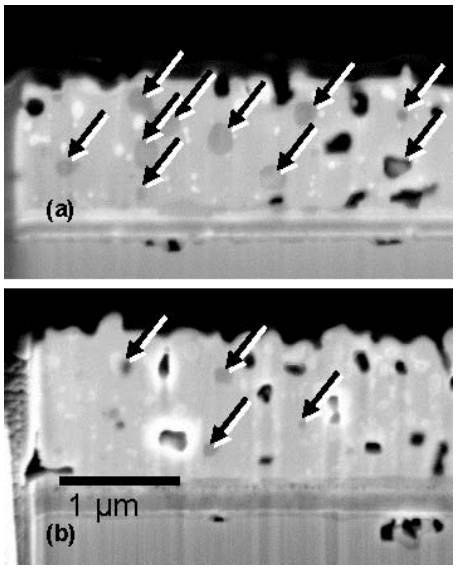

Fig. 2.46. SEM micrographs of (a) YBCO and (b) Y(Dy0.5)BCO films showing differences in second phase particles. Arrows point to Ba-Cu-O phase in both micrographs.

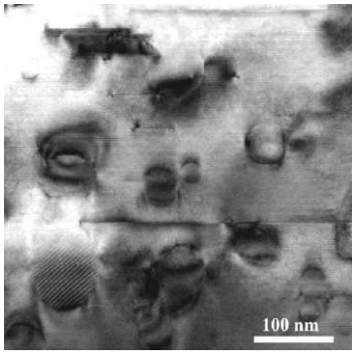

Fig. 2.47. TEM image of nano-particles in Y(Dy0.5)BCO.

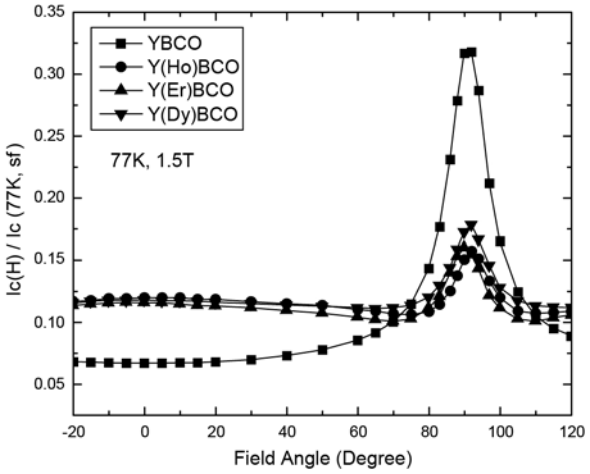

Fig. 2.48. Angular dependence of YBCO and Y(RE0.5)BCO (RE = Dy, significant increase in the random pinning compared to that of Ho, Er) at 77K, 1.5T.

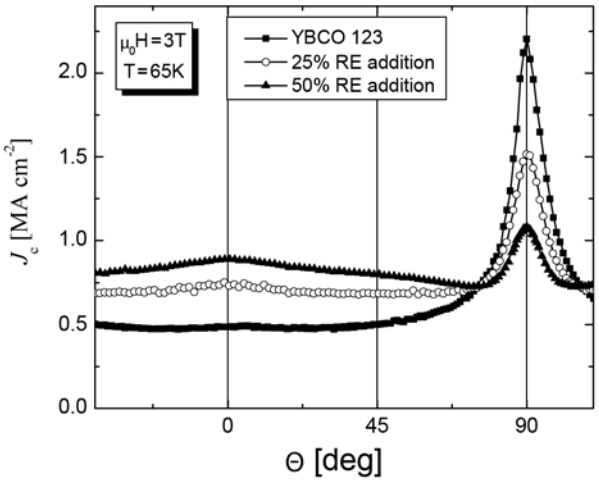

Fig. 2.49. Angular dependence YBCO and Y(Erx)BCO (x = 0.25 and 0.5) films.

2.10.3.3 Engineering the pinning through design of a hybrid superconductor

Although the RE-doped YBCO films show a significant enhancement in the random pinning, most coil applications require $I_c[H//ab]/I_c[H//c]$ ratios of ~2 to accommodate differences in the relative strengths of the magnetic field as a function of position in the coil. One approach to controlling this ratio is to adjust the RE doping level as shown earlier. Alternately, we can engineer a hybrid film constructed of an undoped YBCO layer with strong *ab*-plane pinning and a RE-doped layer with enhanced random pinning. The hybrid films in this study were made with a bottom layer of $Y(Dy_{0.5})BCO$ and a top layer of YBCO with nominal thicknesses of 0.8 and 0.6 μm, respectively. The hybrid film was prepared by

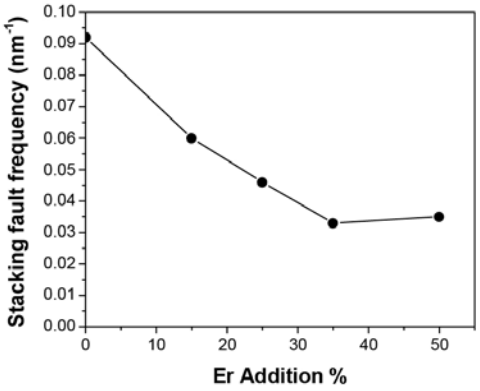

Fig. 2.50. Stacking fault density as a function of Er additions.

depositing and decomposing the layers individually and reacting the 1.4-μm film in a single step. Through process optimization, a well-tuned high-critical-current hybrid superconducting wire was produced with a critical current of 508A/cm-width (77 K, self-field). Figure 2.51 shows the angular dependence of this hybrid conductor along with that of undoped YBCO and Y($Dy_{0.5}$)BCO films. The ratio of I_c [*H*//*ab*)/I_c[*H*//*c*] is ~1.8 for the hybrid film. Microstructural analysis of the hybrid film shows a high density of $RE_2Cu_2O_5$ and RE_2O_3 nanoparticles in the bottom layer [Fig. 2.52(a)] and a high density of 124-type intergrowths in the top layer [Fig. 2.52(b)]. These results show that by varying the RE-doping levels and relative thickness of the individual layers, it is possible to selectively tune the anisotropy of the 2G wire to meet the field and temperature requirements of the targeted applications.

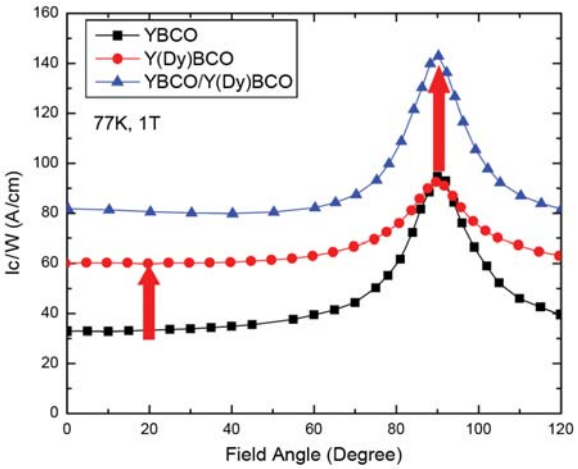

Fig. 2.51. Angular dependence of YBCO (0.8μm) and Y(Dy0.5)BCO (0.8μm) and a hybrid superconductor Y(Dy0.5)BCO/YBCO (0.8μm/0.6μm).

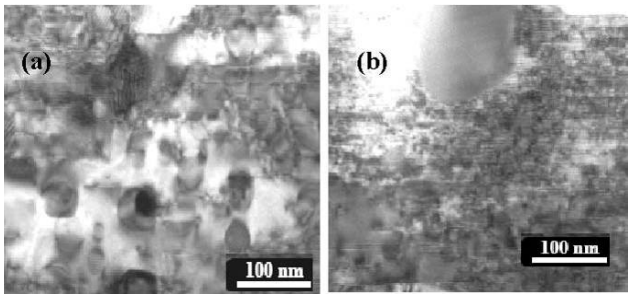

Fig. 2.52. TEM images of hybrid film. (a) Bottom Y(Dy0.5)BCO layer. (b) Top YBCO layer.

2.10.4 Conclusions

Two different types of defect structures have been identified and characterized in MOD-based YBCO films. RE addition to the YBCO films resulted in the formation of nanodots in the YBCO matrix, which can serve as uncorrelated pinning centers, enabling a significant increase in pinning in all field angles. On the other hand, the 124-type intergrowths, which are present in a high density in undoped YBCO films, are responsible for the large peak in the *H*//*ab* direction. A high-critical-currrent hybrid film, containing individual Y($Dy_{0.5}$)BCO and YBCO layers was demonstrated. This novel hybrid 2G conductor provides a path for selective tuning of the anisotropy of the 2G wire for targeted application requirements.

2.10.5 References

1. J. L. MacManus-Driscoll, et al., *Applied Physics Letters* **84**, 5329–31 (2004).

2. J. L. MacManus-Driscoll, et. al., *Nature Materials* **3**, 439–43 (2004).

3. S. Kang et al., "High-performance high-T_c superconducting wires," *Science* **311**, 1911–14 (2006).

4. K. Matsumoto, et. Al., *Physica C: Superconductivity* **426–31**, 1091–95 (2005).

5. M. W. Rupich, et. al., *MRS Bulletin* **29**, 572–78 (2004).

6. T. G. Holesinger, et. al., "Nano-engineered microstructure for tunable high temperature superconducting wires" (submitted).

7. L. Civale, et. al., *Physica C* **412–414P2**, 976 (2004).

8. E. D. Specht, et. al., "Measurement of stacking fault density in $YBa_2Cu_3O_x$ using X-ray diffraction" (submitted).

9. K. E. Gray, D. J. Miller, V. A. Maroni, "Coordinated characterization of coated conductors," presented at the Superconductivity for Electric Systems 2006 Annual Peer Review, July 25–27, 2006, Washington, D.C. (http://www. energetics. com/meetings/supercon06/agenda. html).

2.11 Critical Currents of Ex Situ $YBa_2Cu_3O_{7-\delta}$ Thin Films on Rolling-Assisted Biaxially Textured Substrates: Thickness, Field, and Temperature Dependencies

A. O. Ijaduola and J. R. Thompson (UTK and ORNL); R. Feenstra, D. K. Christen, and A. A. Gapud (ORNL); and X. Song (University of Wisconsin)

2.11.1 Introduction

Ex situ synthesis of YBCO coatings is a promising method for fabricating YBCO coated conductors for large-scale applications [1]. A physical vapor deposition (PVD) BaF_2 ex situ process for YBCO epitaxial film growth has been under development for coated-conductor applications since at least 1998. More recently, efforts have focused on defining new processing parameters to enable faster conversion of the precursor into YBCO and to increase the critical current. Here, the critical current density flowing in thin $YBa_2Cu_3O_{7-\delta}$ (YBCO) films of various thicknesses (d) has been studied magnetometrically, both as a function of applied field (H) and temperature (T), with a central objective to determine the dominant source of vortex pinning in these materials. The films, grown by a BaF_2 ex situ process and deposited on buffered RABiTS™ substrates of Ni-5%W, have thicknesses ranging from 28 nm to 1.5 μm. Isothermal magnetization loops, $M(H; T)$, and remanent magnetization, $M_{rem}(T)$ in $H = 0$, were measured with the applied field normal to film plane ($H \parallel c$-axis).

Good pinning properties, i.e., strong vortex pinning forces in superconducting thin films, are an important feature in order to obtain high critical current density and to allow their use in electronic and power applications. For the materials studied here, we find that the vortex pinning originates predominately from large, randomly distributed inclusions such as Y_2O_3 and Y-Cu-O of sizes ranging from ~5 to 65 nm. Pinning by large, sparse defects has been described by the theory of strong pinning of Ovchinnikov and Ivlev [2], as extended by van der Beek et al. [3]. After summarizing predictions of this theory in the next section, we show the observed nanostructure in the YBCO. Finally, experimental results for $J_c(H,T,d)$ are compared with the theoretical model.

2.11.2 Theoretical background

The theoretical development by Ovchinnikov and Ivlev [2] treats the case of large but relatively sparse pinning sites. We find that this development describes reasonably well the field, temperature, and thickness dependencies of the critical current density in films that contain such pinning sites. In building this theory, they assumed that in order to obtain the critical current density for sparse pins, one should not start from a statistical average of the pinning forces of the different defects as in weak collective pinning [4], but rather evaluate the probability that a vortex line will encounter a pinning site at all. The following summarizes the theoretical results of Ovchinnikov and Ivlev, as extended and implemented by van der Beek et al. in analyzing YBCO films (deposited by pulsed laser deposition) on single-crystal substrates. With this and additional assumptions, the following $J_c(B)$ relationships were obtained for various regimes of the magnetic flux density B, for $H \parallel c$-axis.

$$J_c \approx 0.28 n_i^{1/2} J_0 \frac{[D_i^z F(T)]^{3/2}}{2\varepsilon} \quad \text{for } B << B^* \tag{1}$$

$$J_c \approx 0.0866 n_i J_0 \frac{[D_i^z F(T)]^{9/4}}{\varepsilon^{5/4} \xi^{1/2}} \left(\frac{\Phi_0}{B}\right)^{5/8} \quad \text{for } B^* << B << B_a \tag{2}$$

$$J_c \approx 0.375 n_i J_0 D_i^z F(T) \frac{\Phi_0}{B} \quad \text{for } B >> B_a \tag{3}$$

where

n_i is the defect density,

$J_0 = (B_c / 3\sqrt{6}\pi\lambda)(4\pi / \mu_0)$ is the depairing current density (~ 3×10^8 A/cm^2 at low temperature),

ε is the anisotropy parameter ($\varepsilon \approx 1/5$ for YBCO),

ξ is the in-plane coherence length,

D_i^z is the extent of the defects along the field direction and D_i is their transverse extent.

Also, $F(T) = \ln[1 + D_i^2 / 2\xi^2(T)]$ is a temperature-dependent factor that, from force-balance considerations, is approximately $F(T) \approx (4 / D_i^z)(U_p / \varepsilon_0)$. Also, U_p and Φ_0 are the pinning energy per defect and the flux quantum, respectively. Eq. (1) gives the critical current density in the single-vortex (low-field) limit that is realized for fields lower than a characteristic value B^*, which is given by

$$B^* \equiv \pi\Phi_0 n_i (U_p / \varepsilon_0) \tag{4}$$

Here $\varepsilon_0 = (\Phi_0 / 4\pi\lambda)^2 (4\pi / \mu_0)$ is the scale of the vortex line energy per unit length, which is written in SI units as are all of these expressions. In Eqs. (2) and (3), B_a is a crossover field at which the maximum allowed lateral vortex displacement, u_0, becomes comparable to the vortex spacing, a_0. The $J_c(B)$ departs from a 5/8 power law dependency near B_a, where

$$B_a = 0.41\Phi_0 \xi^{4/3} \left(\varepsilon \frac{\varepsilon_0}{U_p} \right)^{10/3} .$$

In a simplified development based on the work of Vinokur et al. [5], van der Beek et al. [3] developed alternative expressions for the critical current density in the intermediate field regime with interacting vortices, obtaining

$$J_c = 0.087 n_i J_0 \frac{[D_i^z F(T)]^2}{\varepsilon} \left(\frac{\Phi_0}{B} \right)^{1/2} \quad \text{for fields } B << \tilde{B}_a \tag{5}$$

where the characteristic field is given by

$$\tilde{B}_a = \Phi_0 \left(\varepsilon \frac{\varepsilon_0}{U_p} \right)^2 \tag{6}$$

As a function of thickness d, the Ovchinnikov and Ivlev-based prediction is that $J_c \propto d$ for very thin films ("thin-thin films"), with

$$J_c = n_i \frac{D_i^z}{4\xi} F(T) \frac{U_p}{\Phi_0 \varepsilon^2} d \tag{7}$$

This differs from the constant $J_c(d)$ predicted for 3D weak collective pinning [4]. For thicker films ("thick thin-films"), the J_c is predicted to reach a maximum, thickness-independent value above a crossover thickness d^*. The crossover from the "thin thin-film" to the "thick-thin film" limit occurs near the thickness

$$d^* = \left(\frac{\varepsilon^2 \varepsilon_0}{\pi n_i U_p} \right)^{1/2} \tag{8}$$

which is determined by considerations of the trapping area in either limit. For thin-thin films, the probability for a vortex to be trapped by an inclusion is determined by its ability to bend sufficiently within the film thickness.

In this study, we show that YBCO thin films deposited on RABiTS™ substrate can carry significant critical current density at relatively high temperature and magnetic fields. We then analyze these dependencies to understand better the dominant pinning mechanisms and vortex properties in these technically important materials. The resulting findings, together with correlations with the microstructure of the coated conductors, should provide guidance for future approaches to improve the level of critical current density in these materials.

2.11.3 Experimental aspects

YBCO films of various thicknesses *d* were prepared on buffered Ni-W substrates using an ex situ process. RABiTS™ substrates used in this study were provided by American Superconductor Corporation (AMSC). They feature a 75-μm-thick Ni-5%W deformation-textured metal template with average grain size of ~25 μm, and epitaxial Y_2O_3, YSZ, and CeO_2 buffer layers. Prior to mounting in the precursor deposition chamber, the buffered substrates were annealed in flowing N_2 gas (containing < 80 ppm O_2) to temperatures in the range of 700 to 750°C for 30 min. The YBCO constituents were deposited by simultaneous electron-beam evaporation from sources of Y, BaF_2 and Cu, during which quartz crystal monitors (QCMs) were used to measure and control the three individual evaporation rates. The ex situ conversion was performed in a standard annealing system using flowing gases at atmospheric pressure. The "fast" process (described by Gurevich, unpublished) was used for all samples in this study, featuring a conversion temperature of 780°C and water partial pressure of ~ 0.015 atm. The annealing duration was increased in proportional to the film thickness, based on an average growth rate of 0.7 nm/s. The final YBCO thickness was inferred from the total of the QCM readings, using a previously determined calibration. The films have thicknesses from 28 to 1500 nm. A detailed description of the fabrication process is presented elsewhere [6].

In order to see detailed microscopic features of the films, transmission electron microscopy (TEM) studies were performed on representative samples. The TEM images were taken looking from above, along the axis of film deposition (plan-view images). The images revealed various secondary phases (inclusions) in the YBCO films, whose size distribution and density were determined. In addition to the secondary-phase inclusions of Y_2O_3 and Y-Cu-O present in the films, there are also twin planes with spacings in the range of 35 to 50 nm and large spherical pores faceted along the (110) and (100) planes of YBCO grains. Figure 2.53 shows a TEM image from a 117-nm-thick film. An analysis of the defect sizes revealed a roughly log-normal distribution, with about two-thirds of the particles having diameters in the range 28 (± 11) nm. The density of defects is approximately 4.8×10^{21} m^{-3}, based on the observed areal density of defects and the estimated thickness of the TEM sample. These values are typical of the materials in the entire series of films. The size and density of defects corresponds to about 6% volume fraction in these materials.

The critical current density values were magnetically determined by applying the modified critical state model [7,8] to the magnetic hysteresis via the "sandpile" relation:

$$J_c = \frac{2\Delta M}{a\left(1 - \frac{a}{3b}\right)} \tag{9}$$

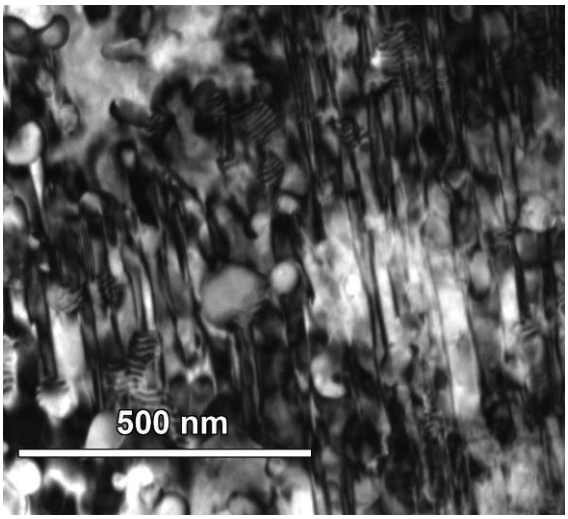

Fig. 2.53. Plan-view TEM image showing the microstructural composition of a YBCO film with a thickness of 117 nm as synthesized. For TEM, the coated conductor was thinned through the metal substrate and buffer layers. Spherical and oval defects correspond to non-superconducting Y_2O_3 or Y-Cu-O precipitates inside the YBCO matrix. The areal density of defects is ~ 2.4×10^{14} m^{-2}; combining this with an estimated thickness of 50 nm of YBCO in the microscopy specimen yields a defect density $n_i \approx 4.8 \times 10^{21}$ m^{-3}. Many twin planes are visible in the image, tilted slightly counterclockwise from vertical, with spacings of 35 to 50 nm.

This sandpile relation applies to a rectangular solid with field perpendicular to a face with sides $b > a$. Here $\Delta M = (M^- - M^+)$) is the magnetic hysteresis, where M^- (M^+) is the magnetization at temperature T measured in decreasing (increasing) field H history, respectively. These measurements were done in a superconductivity quantum interference device (SQUID)-based magnetometer with a maximum field of 7 T, (Quantum Design model MPMS-7). Both isothermal magnetization loops $M(H, T)$ and remanent magnetization $M_{rem}(T)$ in $H = 0$ were measured. With these thin superconductors in a perpendicular field geometry, the flux density, B, can be replaced by $\mu_0 H$ to a close approximation in all but the smallest applied fields. For the isothermal magnetization measurements, fields in the range of 0 to 6.5 tesla were applied at different fixed temperatures (5–95 K) and the moment generated by the induced flowing current in the film was measured. For the remanent magnetization measurement, a large field (~0.5 tesla) was first applied to set up currents in the film. This field was then gradually taken off, thereby inducing critical currents flowing in the opposite direction. Before beginning measurements, the magnet was "reset" to eliminate any trapped flux, to ensure that H was truly zero, and to provide a very quiet measurement environment. Signals of the reversible background magnetization from the ferromagnetic substrate were subtracted out before computing the critical current density These two ways of determining the critical current density at self-field yielded very similar results.

In order to determine the superconducting transition temperature, T_c, for the films, temperature-dependent measurements of $M(T)$ were made in an applied field of 1 m tesla (10 Oe), after cooling to 5 K in zero applied field. The resulting values for the onset temperature T_c range from 88 to 91 K.

In some cases, complementary studies of the current density were conducted using standard four-probe transport methods. In particular, this provided information on critical current density as a function of field orientation (i.e., the angle θ between the field direction and the YBCO *c*-axis). For these measurements, the magnetic field was oriented perpendicular to the current, in the full Lorentz force configuration. Also measured was the critical current density in self-field at 77 K. A comparison of these values with those from the magnetic study showed the transport results to be larger by a factor of ~1.3, relative to the magnetization values. This difference arises almost completely from curvature in the (current density J – electric field E) characteristics, coupled with strongly differing E-field criteria in the two investigative methods.

2.11.4 Results and discussion

In a superconductor, nearly any irregularity that disrupts the translational symmetry within the material can pin vortices, in principle. Hence there are many differing models appropriate to various defect morphologies. Here we seek to identify the dominating source of vortex pinning for the present materials, which we will find is the array of strong, sparse defects. First, though, we consider briefly two other major candidates. One of the most cited is weak collective pinning [4], such as that arising from

vacancies or site-antisite defects. Such atomic-scale defects doubtlessly exist in the YBCO films. However, the observed magnitude of critical current density is so large in these materials that the longitudinal correlation length, L_c, from the theory is extremely short, only one to a few unit cells. This conflicts with the observed thickness dependence of critical current density that, as will be shown, varies over a thickness range much larger than the calculated L_c. Furthermore, to invoke weak collective pinning would be to ignore the presence of the large and potentially very effective defects that are visible by TEM in Fig. 2.53. Hence we rule out weak collective pinning as the dominant mechanism in these materials.

A second major possibility is pinning by some type of correlated disorder [9], such as columnar defects or twin planes. Indeed, Fig. 2.53 shows the presence of twin boundaries, and it is possible that a dense forest of *c*-oriented dislocations could be generated in the YBCO by the substrate and/or the various inclusions [10]. In addition, irregularities in the substrate surface (either naturally occurring or deliberately introduced as nano-islands [11,12]) can propagate up through the YBCO and form roughly linear defects. The angular dependence of critical current density, shown in Fig. 2.54 for a 700-nm film, provides a good test of these possibilities; the figure shows critical current density at $T = 77$ K as a function of the angle θ between the applied field and the *c*-axis. As these results show, however, there is no evidence for pronounced, angularly selective pinning near the *c*-axis; rather, $J_c(\theta)$ is quite featureless for $\theta \approx 0$. Thus we rule out correlated disorder as the dominant source of pinning for $H \| c$-axis. On the other hand, the peaks in critical current density for H near the *ab*-planes do give evidence for pinning by correlated disorder in this angular region, most likely by "intrinsic pinning," by layered intergrowths such as Y-124, or a combination of these.

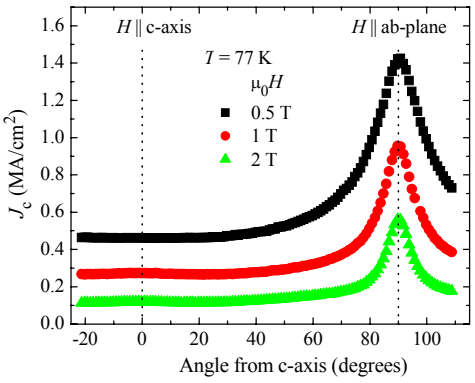

Fig. 2.54. Angular dependence of the critical current density for a 700-nm YBCO film at 77 K. The transport measurements were conducted in applied fields of 0.5, 1, and 2 tesla, with the field always perpendicular to the current direction (maximum force configuration).

Next we analyze the experimental results for $J_c(H,T,d)$ using the theory from Ovchinnikov and Ivlev [2] and van der Beek et al. [3].

2.11.4.1 Field dependence of critical current density

In the following analysis of experimental results, we test the appropriateness and applicability of the formulation of Ovchinnikov-Ivlev and van der Beek et al. In particular, we ask whether the models can describe critical current density and the characteristic fields with values for the defect size and density that are comparable with the TEM observations for these materials. We start this discussion by considering the field dependence of critical current density at the various temperatures studied. Figure 2.55 shows representative critical current density vs magnetic results for films of several different thicknesses. The first observation is that in all cases, there is a low-field region of single vortex pinning, where the critical current density is nearly independent of field, as described by Eq. (1). In Fig. 2.56 is shown, for several films, the temperature dependence of B^*, the boundary field where critical current density becomes field-dependent. As the temperature decreases, the values first rise and then become nearly constant in the range of 50 to 30 K, with similar values for all thicknesses. For $T \leq 20$ K, B^* abruptly rises, which may originate in additional pinning from point-like defects that are relatively ineffective at higher temperatures. The reasonableness of this conjecture is illustrated by the dashed curve in Fig. 2.56, showing the boundary $B_{sb}(T)$ for single vortex pinning estimated from weak collective pinning theory. Thus for analysis of pinning by strong, sparse defects using Ovchinnikov and Ivlev theory, we focus on the region $T \geq 30$ K, where B^* varies from ~0.12 tesla at 30 K to ~0.04 tesla at 77 K.

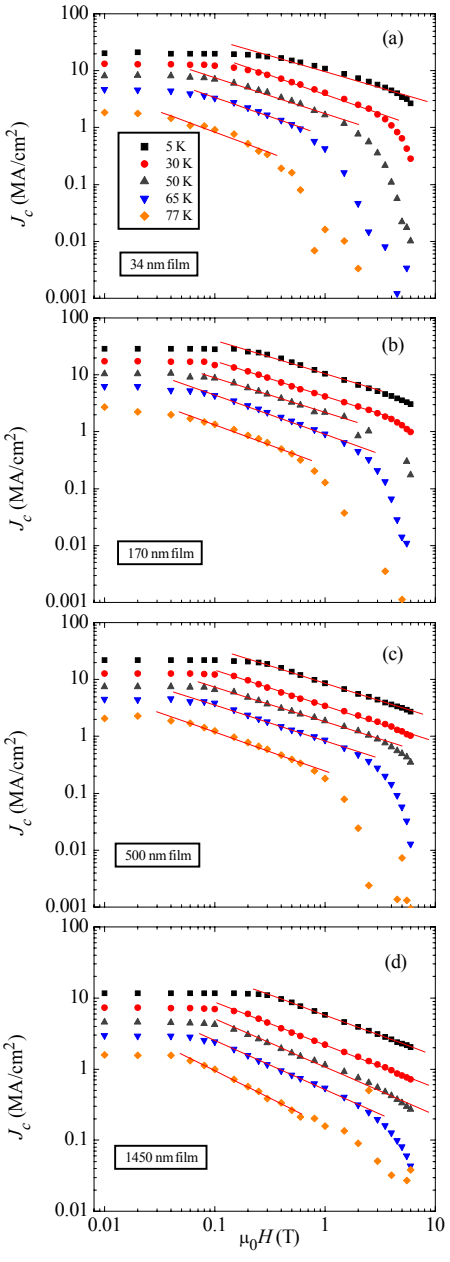

Fig. 2.55. (a) Field dependence of the critical current density at temperatures 5, 30, 50, 65, and 77 K for a 34-nm-thick film. From the lines drawn on each set of data, we obtain the exponent α in $J_c \propto H^{-\alpha}$ in the intermediate field range. For all the materials, $\alpha \sim 0.56 - 0.69$. (b) The same, for a 170-nm-thick film, (c) a 500-nm-thick film, and (d) a 1450-nm-thick film.

From Eq. (4) and the preceding discussion, we have $B^* \sim \ln[1 + D_i^2 / 2\xi^2(T)]$. In this and subsequent analyses, we take the defects to be roughly equiaxed, so that $D_i \approx D_i^z$. The temperature dependent $B^*(T)$, shown as a solid line in Fig. 2.56, gives a reasonable description of the data at intermediate and higher temperatures. We have taken $D_i^z = 10$ nm to obtain self-consistency in both this estimation and in the magnitude of critical current density, as discussed below. Then with $B^* = 0.12$ tesla for the films at moderate temperatures (30–50 K), the expression Eq. (4) for B^* yields a defect density $n_i = 2.4 \times 10^{21}$ m^{-3} . In the same low-field single vortex limit, we alternatively calculate using Eq. (1) (again with $D_i^z = 10$ nm) with the experimental value $J_c \approx 15 \times 10^6$ A/cm^2 and obtain $n_i = 3.1 \times 10^{21}$ m^{-3} . These estimates are reasonably consistent internally and are comparable with the defect density of 4.8 × 10^{21} m^{-3} obtained directly from the TEM study.

An alternative explanation of the field-independence of critical current density is that B^* is simply the self-field of the film, B_{self}. For thin sample geometry, we have $B_{self} \approx \mu_0 J_c d / 2$ [13]. Therefore the self field (at fixed temperature, with critical current density varying little with d) must increase greatly over the range of film thicknesses d = 28–1450 nm; in contrast, however, the experimental values of B^* are nearly independent of film thickness. More quantitatively, one estimates at T = 30 K that $B_{self} \sim 0.05$ tesla for d = 500 nm and ~0.02 tesla for d = 170 nm. The values for B^* are larger by a factor of 2.5 to 6, meaning that the field-independent critical current density originates largely from single vortex pinning rather than self-field effects. (However, the large value(s) of B^* in Fig. 2.56 for the 1450 nm film at low temperatures probably do contain contributions from the self field.)

A particularly interesting feature in the $J_c(H)$ data in Fig. 2.55 occurs in the intermediate field range, where the current density falls off with a power law field dependence $J_c \propto H^{-\alpha}$ with exponent $\alpha \sim (0.56–0.69)$ for all the materials, for the entire temperature range studied. This power law coincides closely with the prediction of Ovchinnikov and Ivlev [2], who obtain in Eq. (2)

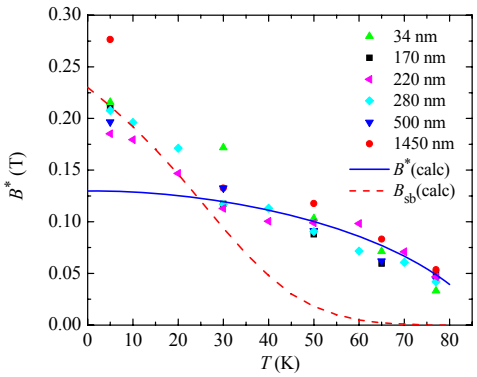

Fig. 2.56. Variation of the cross-over field B^* with temperature for films of thicknesses from 34 to 1450 nm. The solid line is the theoretical prediction for pinning by strong, sparse defects, as described in the main text. The dashed curve shows an estimated boundary $B_{sb}(T)$ for weak collective pinning by point-like disorder.

for $J_c(H)$ that $\alpha = 5/8$ (0.625). A similar field dependence was reported recently for YBCO ($d = 200$ nm) deposited epitaxially on $SrTiO_3$ substrates by pulsed laser deposition (PLD) [14]. As for the magnitude of critical current density estimated from Eq. (2), the values obtained (using the same defect density and size described above) exceed those measured in these YBCO thin films by about a factor of 20. This overestimation of J_c has been attributed [3] to an assumption that a vortex line will encounter at least one defect (see further explanation in footnote 27 in ref. 3). In addition, the presence of some weak links also reduces somewhat the current densities below the levels expected in equivalent single crystal films, as the present materials are realistically quasi-single crystals consisting of a series-parallel network of predominantly low-angle grain boundaries. However, for high-quality coated conductors such as those studied here, the attenuation in critical current density is generally a factor of 2 or less and cannot account for the difference in estimated vs experimental critical current values. (Additionally, we note that there is accumulating evidence that for low-angle grain boundaries, the intergrain critical current density is proportional to the intragrain critical current density [15], meaning that dependencies on field and temperature are basically unaffected by residual grain-to-grain weak linkage.)

Similar difficulties with numerical estimates arise with the crossover field B_a, separating the $\alpha \sim 5/8$ and the $\alpha \sim 1$ regions in the Ovchinnikov-Ivlev theory. Estimates in the range of 0.01 tesla are obtained, compared with experimental values of 1 to 3 tesla.

For complementary estimates, we turn to the alternative, simpler development leading to Eqs. (5) and (6). In this case, the theoretical power law dependence with $\alpha = 1/2$ is slightly weaker than either the Ivlev-Ovchinnikov theory or the experimental findings. On the other hand, the magnitude of the current density lies much closer to that realized experimentally. From Eq. (5), we obtain $J_c \approx 19$ MA/cm^2 $\times$ (1 T/B)$^{1/2}$, again using the same defect parameters $n_i = 3 \times 10^{21}$ m^{-3} and $D_i^z = 10$ nm. The resulting estimate for critical current density lies within about a factor of 3 of the experimental values, which is relatively good agreement for such estimates.

One may also evaluate the cross-over field $\tilde{B}_a$ separating regions with power law behavior with $\alpha =$ 1/2 and $\alpha = 1$, using Eq. (6). This leads to the estimate $\tilde{B}_a \approx 1.4$ tesla, which is close to the experimental values in Figs. 2.55(a) through (d) for the films of various thicknesses. Finally, as we approach the irreversibility line (where the films lose their ability to carry any significant amount of supercurrent), the current collapses progressively more quickly with increasing temperatures. The associated increasing rate of flux creep, coupled with experimental difficulties of thin film measurements in large magnetic fields, preclude a detailed, quantitative analysis of properties in fields above $\tilde{B}_a$. Qualitatively, however, it is clear that the critical current density falls off earlier in the thinnest films, most likely due to faster flux dynamics.

2.11.4.2 Thickness dependence of critical current density

Useful, complementary information can be obtained from the dependence of critical current density on film thickness, d. Understanding this dependence is vital to gaining insights for improving the total

current-carrying capabilities of a coated conductor. It is widely recognized that for thicker films, the experimental critical current density decreases as thickness is increased; this has been attributed, at least in part, to degraded film morphologies and/or differences in defect structure between the thinner and the thicker films [16]. One potential way to circumvent this problem is based on extrapolating the $J_c(d)$ dependence to very thin films, which suggests the possibility of extremely high critical current density values; then fabricating a stack of very thin layers may lead to a very high overall critical current densities. On the other hand, materials-related problems may lead to very small critical current density in thin films on RABiTS™. These were some of the motivations for undertaking this study. In fact, a recent report by Foltyn et al. [17] illustrates that high critical currents may indeed be obtained from a multilayer approach when pulsed laser deposition is used to grow the films.

Although extensive studies have been reported to investigate the d dependence of critical current density in YBCO thick films on single crystalline [18] and buffered metallic substrates [19,20,21] as well as for thin films on single crystalline substrates, no work has been reported for thin films on buffered (RABiTS™) substrates. From our results, the $J_c(d)$ data can be divided into two regions viz: thin–thin films and thick thin films. In Fig. 2.57(a) is shown a plot of the experimental $J_c(d)$ measured in self – field; in the first region of thin "thin films" described by Eq. (7), we find that the critical current density first increases with thickness d; it then reaches a peak around ~120 to 140 nm and decreases thereafter. This behavior is independent of temperature as the same effect is found at low (5 K) and high (77 K) temperature. This temperature independence implies that the thickness where the peak critical current density occurs is not directly related for these materials to the penetration depth λ_{ab}, as suggested in an earlier work [16]. In addition, the similarity of $J_c(d)$ at high and low temperatures also argues against explanations based on thermal depinning of thickness-limited vortex segments to account for the decreased critical current density observed in the thinnest films [22]. Interestingly, similar plots in Figs. 2.57(b) and (c) for applied fields, $\mu_0 H$, of 0.2- and 0.5-tesla fields reveal the same features found in the self – field data with single vortex pinning: even in the regime of collective effects with the $\sim B^{-5/8}$ power law dependence, $J_c(d)$, peaks at a similar thickness.

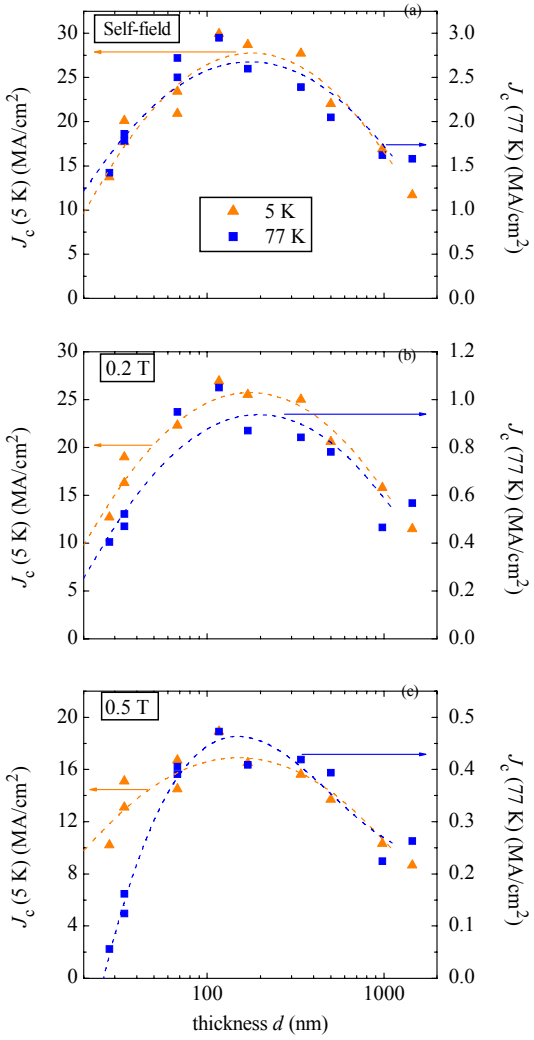

Fig. 2.57. (a) Thickness dependence of critical current density. A semi log plot of $J_c(d)$ shows that critical current density increases initially with thickness, attains a peak, then decreases thereafter. This feature is seen in both the 5 K and 77 K data. Here, there is no applied field. Thickness dependence of critical current density in applied fields, with (b) H = 0.2 tesla (2 kOe) and (c) with H = 0.5 tesla (5 kOe). The peak critical current density is at the same thickness, d, of the films in all cases.

The similarity in data at 5 and 77 K appears to fail, however, for conditions approaching the irreversibility line, e.g., the thinnest films at 77 K in 0.5 T, where creep effects become pronounced.

Continuing, the theory predicts a linear dependence of J_c on d in the thin-thin region, as seen in Eq. (7). Examination of the experimental data in Fig. 2.58(a) (T = 5 K) and Fig. 2.58(b) (T = 77 K) reveals an initial linear rise in J_c as shown by the dashed lines; with further increases in thickness, the J_c dependence rolls over and peaks near 120 nm, as discussed above. In the thin-thin region, the experimental data have a slope at low temperature of $J_c/d = 5.7\times10^{18}\,\mathrm{A/m^3}$, which can be compared to the theoretical value $n_i D_i^z F(T) U_p \big/ \Phi_0 \varepsilon^2\, 4\xi$ predicted by Eq. (7). This yields for the defect density a value $n_i = 1\times10^{21}\,\mathrm{m^{-3}}$, which is roughly consistent with the values obtained in earlier analyses of the $J_c(B)$ relationship and the cross-over field in the single vortex limit. Lastly, using this latter value n_i in Eq. (8) gives a crossover film thickness $d^* \approx 40$ nm, which lies near the thickness where the $J_c(d)$ data depart from their initial linear dependence.

A shortcoming of the Ovchinnikov and Ivlev theory is that it provides no insight into the falloff of $J_c(d)$ for $d > 120$ nm. One characterization of this decrease is shown by the solid lines in Fig. 2.58 that illustrate a $d^{-0.4}$ power law dependence, which is comparable in form with the falloff observed in coated conductors prepared by various methods [19,20]. In principle, the observed falloff could arise from a loss in density or size of pinning centers for $d > \sim$ 120 nm; however, if this were the only operative factor, it seems improbable that materials fabricated by different methods (e.g., ex situ BaF_2, PLD) should experience similar deteriorations in pinning morphology with increasing thickness. Clearly, a better understanding of this unwanted falloff is needed, and it remains a topic of continuing investigation. In an alternative theoretical approach, Gurevich [22] has suggested 2D collective pinning to explain this falloff with d, as it has $J_c \propto 1/\sqrt{d}$; at still larger thicknesses, the system then crosses over to 3D collective pinning where the critical current density becomes independent of d. It has been difficult, however, to reconcile the implication of such large correlation lengths, L_c, with the observed high levels of critical current density. This latter difficulty may be circumvented by incorporating the effect of finite defect size into the theory (Gurevich, unpublished).

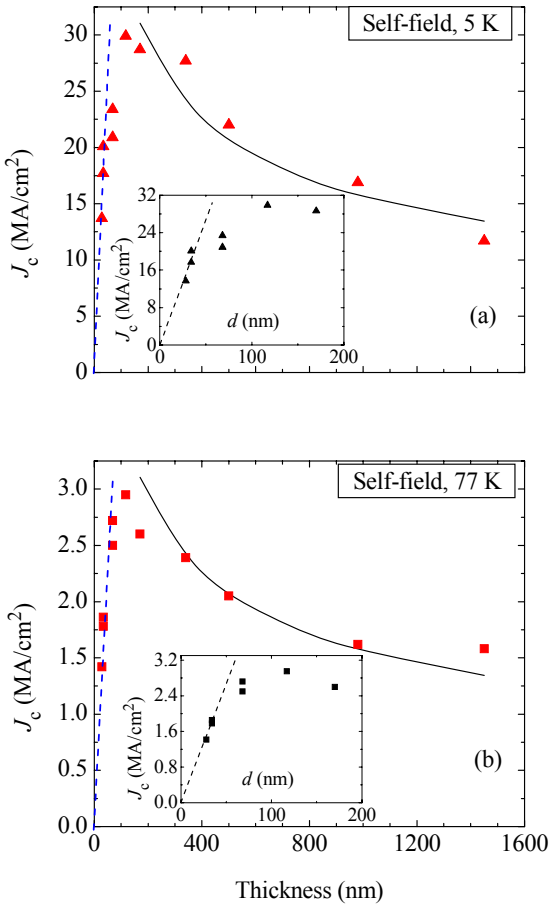

Fig. 2.58. Plots of critical current density vs thickness, *d*. The critical current density values are in self-field, (a) at 5 K and (b) at 77 K. Dashed lines show an initial dependence $J_c \propto d$ as in Eq. (7). The solid line is an empirical $d^{-0.4}$ fit to the data in the thick thin film region. Insets show expanded views of the low-thickness region.

2.11.4.3 Temperature dependence of critical current density

In type II superconductors, pinning results from spatial variations of the Ginzburg-Landau (GL) coefficient (traditionally denoted as α); the spatial variation may be associated with disorder in the T_c

and/or from spatial variations in the charge carrier mean free path, *l*, near lattice defects. These two sorts of pinning are usually called "δT_c *pinning*" and "δl *pinning*" (in some publications, "δl pinning" is called "δκ pinning"). The type of pinning in high-T_c superconducting materials can give insights into the vortex structure as each of them is governed by different regimes of the GL free energy functional [23]. In the single vortex regime, which is the region of interest for the present analysis, the critical current density can be expressed as a function of the reduced temperature $t = (T / T_c)$ as [23]

$$J_c(t) \propto (1-t^2)^{7/6} \tag{10a}$$

$$J_c(t) \propto (1-t^2)^{5/2} \tag{10b}$$

Equation (10a) holds for "δT_c *pinning*" while Eq. (10b) holds for "δl *pinning*". In Figs. 2.59(a) through (d), we present the critical current density in self-field as a function of temperature normalized to the T_c for the 34-, 117-, 500-, and 1450-nm-thick films. These results are representative of all the films. The log-log plots of J_c vs [1- $(T/T_c)^2$] have slopes near T_c that range from n = 1.2 to 1.4. These values coincide within experimental error with the theoretical exponent 7/6 (1.2) in the theoretical model Eq. (10a) for "δT_c *pinning*". This finding of "δT_c *pinning*" is entirely consistent with the observed large precipitates of materials such as Y_2O_3 and Y-Cu-O in the materials, as these insulating precipitates are completely nonsuperconductive.

2.11.5 Conclusions

We have investigated the dependence of the inter-grain critical current density flowing in ex situ processed YBCO thin films deposited on RABiTS™ substrates as a function of film thickness, field magnitude, and temperature. The dependencies on magnetic field (field-independent critical current density in low field, crossing over in intermediate fields to a power law falloff $B^{-\alpha}$ with $\alpha \approx 5/8$) and on film thickness (thin film limit) are consistent with the theory of Ovchinnikov-Ivlev and van der Beek et al. for strong pinning by sparsely distributed, nonsuperconducting inclusions. The deduced size (~10 nm) and density [(1–3) × 10^{21} m^{-3}] of pins are semiquantitatively consistent with the values obtained from TEM, 28 nm and 5 × 10^{21} m^{-3}, respectively; in each case, the deduced values are smaller by a factor of 2 to 4. Thus we conclude that, for $H \parallel c$-axis, the most important pinning sites in these films are the large precipitates (e.g., Y_2O_3, Y-Cu-O) revealed by TEM. Consistent with this observation, temperature-dependent studies show that "δT_c" pinning, in which the T_c is locally suppressed at the pinning sites, dominates in these materials.

In similarity with results from previous work [16], the thickness dependence study shows that critical current density increases initially with thickness, reaches a peak near 120 nm, and then decreases as the films get thicker. The new finding, however, is the temperature and field dependence of this feature. We find that this behavior is independent of temperature and field (up to at least 0.5 tesla or 5 kOe) and the peak occurs at the same thickness at both high and low temperatures. Thus one concludes that the thickness at the peak is not directly related to the in-plane penetration depth, λ_{ab}, as suggested earlier. One shortcoming of the Ovchinnikov and Ivlev theory, however, is that it provides no insight into the falloff of critical current density for thicknesses greater than the peak value. This falloff has important technological ramifications and needs better understanding.

In summary, the pinning analysis as reinforced by TEM imaging demonstrates that the dominant mechanism for immobilizing vortices near the *c*-axis in these YBCO materials is strong pinning by large, sparse defects, rather than by weak collective pinning or pinning by strongly correlated disorder.

2.11.6 Appendix

In this appendix, we outline the use of theory for weak collective pinning in anisotropic superconductors to estimate the impact of point-like disorder on the experimentally determined boundary of single vortex pinning (see Fig. 2.56. In the review of Blatter et al. [24], the boundary for weak collective pinning, denoted as B_{sb}, is given by Eq. (2.173); this and subsequent equation numbers refer to the review article. Taking the experimentally observed value $B^* = 0.23$ T at $T = 0$ as B_{sb} thus implies a critical current density j_c *due solely to point-like disorder* of ~ 0.12 MA/cm^2. Continuing, Eq. (3.74) relates j_c to the dimensionless pinning parameter (δ/ε). For δT_c pinning, Eq. (3.78) has $(\delta_\alpha/\varepsilon) \propto [n_i (d^2T_c/dn_i^2)]^2$ where n_i is the density of point-like defects. Assuming these defects are predominantly oxygen vacancies, we obtain that $(d^2T_c/dn_i^2) \approx 5\times10^{-41}$ K cm^6 from the data of Ossandon et al. and finally arrive at the value $n_i \approx 2.3\times10^{19}$ cm^{-3}. This corresponds to ~ 0.004 oxygen vacancies per unit cell in YBCO, which is credible for nominally fully-oxygenated thin film materials [25].

The temperature dependence of B_{sb} for weak collective pinning is given by Eq. (2.178) in Blatter et al.[2] The dominant T-dependence is the factor

$[1+T/\tilde{T}^s_{dp}]^2 \times \exp[-2c(\alpha+T/\tilde{T}^s_{dp})^3]$, where c and α are constants of order unity. For the present modeling, we set $c = \alpha = ½$. and estimate the vortex depinning temperature $\tilde{T}^s_{dp} = 50$ K. The resulting boundary, shown as a dashed curve in Fig. 2.56, represents the data at low temperatures relatively well. Overall, these estimates show the possibility that point-like disorder, with reasonable parameter values, can account for the observed elevation of $B^*(T)$ at low temperatures. Let us note, however, that while this procedure treats independently the pinning by point-like disorder and by strong, sparse pins, it is clear that some interplay between them is needed to support the high levels of current density experimentally observed below ~ 30 K in small fields.

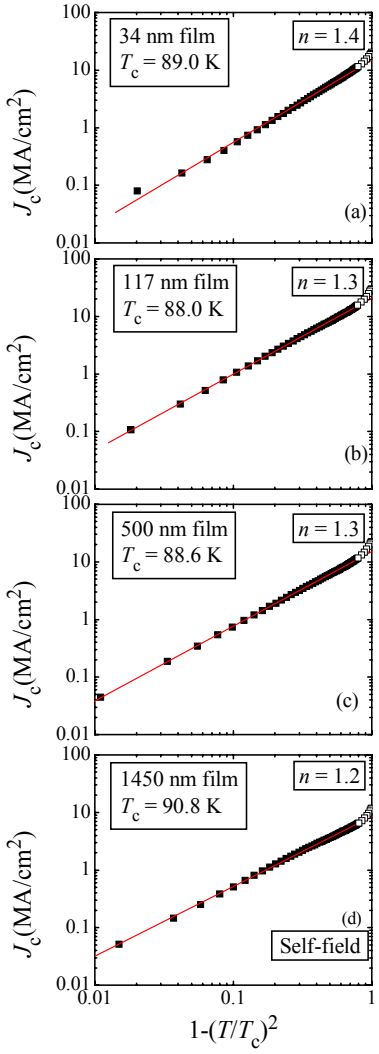

Fig. 2.59. Log-log plot of J_c vs [1-(T/T_c)^2] to show the temperature dependence. Critical current density values are those at self-field in order to ensure single vortex regime. Straight lines are best fits to data for $T/T_c > 0.55$ (filled symbols), to obtain slopes n. Open symbols show lower-temperature data. From theoretical models, values of the slope n point to "δT_c pinning" for all materials. (a) 34-nm film; (b) 117-nm film; (c) 500-nm film; and (d) 1450-nm film.

2.11.7 References

1. R. Feenstra, U.S. Department of Energy Wire Development Workshop, St. Petersburg, Fla. (1998).

2. Y. N. Ovchinnikov and B. I. Ivlev, *Phys. Rev. B* **43**, 8024 (1991).

3. C. J. van der Beek, et. al., *Phys. Rev. B* **66**, 024523 (2002).

4. A. I. Larkin and Yu Ovchinnikov, *J. Low Temp. Phys.* **21**, 409 (1979).

5. V. M. Vinokur, et. al., *Physica C* **295**, 207 (1998).

6. R. Feenstra, et. al., *IEEE Trans. Appl. Supercond.* **15**, 2803 (2005).

7. C. P. Bean, *Rev. Mod. Phys.* **36**, 31 (1964).

8. A. M. Campbell and J. E. Evetts, *Advances in Physics* **21**, 199 (1972).

9. D. R. Nelson and V. M. Vinokur, *Phys. Rev. B* **48**, 13060 (1993).

10. T. G. Holesinger, et. al., *J. Mater. Res.* **20**, 1216 (2005).

11. T. Aytug, et. al., *J. Appl. Phys.* **98**, 114309 (2005).

12. P. Mele, K. Matsumoto, T. Horide, O. Miura, A. Ichinose, M. Mukaida, Y. Yoshida and S Horii, *Supercond. Sci. Technol.* **19**, 44 (2006).

13. M. Daeumling and D. C. Larbalestier, *Phys. Rev. B.* **40**, 9350 (1989).

14. M. Puerla, H. Huhtinen, and P. Paturi, *Supercond. Sci. Technol.* **18**, 628 (2005).

15. A. Palau, et. al., *Appl. Phys. Lett.* **84**, 230 (2004).

16. C. Jooss, et. al., *Physica C* **266**, 235 (1996).

17. S. R. Foltyn, et. al., *Appl. Phys. Lett.* **87**, 162505 (2005).

18. Q. Li, et. al., *Appl. Phys. Lett.* **84**, 3528 (2004).

19. S. R. Foltyn, et. al., *Appl. Phys. Lett.* **63** 1848 (1993).

20. S. R. Foltyn, et. al., *Appl. Phys. Lett.* **75**, 3692 (1999).

21. S. R. Foltyn, et. al., *Appl. Phys. Lett.* **82**, 4519 (2003).

22. A. Gurevich, *Condensed Matter* 0207526 (2002).

23. R. Griessen, et. al., *Phys. Rev. Lett.* **72**, 1910 (1994).

24. G. Blatter, et. al., *Rev. Mod. Phys.* **66** 1125 (1994).

25. J. G. Ossandon, et. al., *Phys. Rev. B.* **45**, 12534 (1992).

2.12 Local Epitaxy of $YBa_2Cu_3O_x$ on Polycrystalline Ni Measured by X-Ray Microdiffraction

E. D. Specht, A. Goyal, and W. Liu

2.12.1 Introduction

While high-critical-current YBCO superconductors are most easily made by epitaxial growth on single-crystal substrates, practical devices require long conductors made by epitaxial growth on polycrystalline substrates [1–5]. This epitaxy has been intensively studied by conventional X-ray diffraction techniques, which provide a statistical measure of the epitaxy over a large area but not the orientation of individual grains. Electron backscatter diffraction (EBSD) analysis is a complementary probe, providing a detailed map of the orientation of surface grains, but giving no information about the underlying substrate [6]. EBSD and transmission electron microscopy can measure epitaxy of cross-sectional samples, but only a few grains per sample are observed [6]. Multiple EBSD images taken as the surface of a sample is ion-milled from the film down to the substrate have been used to measure grain boundary meander [7], and grain alignment [8]. This technique requires extensive sample preparation and a smooth surface, and measures grain orientation with limited angular resolution.

X-ray microdiffraction can provide a complete description of epitaxy with no sample preparation, no limitation on surface roughness, and with high angular resolution. A penetrating 0.7-μm beam measures the orientation of both substrate and overlayer. Budai et al. [9] used this technique to analyze the growth modes of CeO_2 grown on polycrystalline, biaxially textured Ni (RABiTS^{TM}). CeO_2 grows by island nucleation at low temperatures and by ledge growth at high temperatures. The CeO_2 orientation is close to the Ni orientation at low temperatures, while at high temperatures the CeO_2 grains are rotated with respect to the underlying Ni, with the [001] direction lying closer to the surface normal direction. In both cases, there is a high correlation between the Ni and CeO_2 orientations. The epitaxy has only a small random component, so the film orientation can be well controlled by manipulating the substrate orientation. An unexpected conclusion is that using a larger-misfit film can lead to better alignment to the surface normal.[9]

Since superconducting properties depend strongly on the orientation of the YBCO layer, it is important to see how epitaxy extends from the cubic CeO_2 barrier layer to the orthorhombic YBCO superconductor. However, the techniques used to determine crystallographic orientation from X-ray microdiffraction patterns [9] have not been successfully applied to YBCO films. When illuminated by polychromatic radiation, a crystal grain produces a Laue pattern, in which each reflection determines the direction of a crystal plane: the difficult step is "indexing" (i.e., assigning the proper crystal plane to each reflection). Microdiffraction patterns from materials like Ni substrates and CeO_2 films are readily indexed by algorithms that match the angles between reflections to the angles between crystal planes in the known structure [10,11].

Diffraction patterns from YBCO do not consistently exhibit sharp peaks from which well-defined orientations may be extracted. This most likely results from the more complicated microstructure of YBCO films. Almost invariably, orthorhombic YBCO forms a twinned structure with a misorientation of ~0.7° between the variant twins. Further misorientation and peak broadening are introduced by other defects, including second-phase particles and stacking faults. Figure 2.60 shows polychromatic laue patterns for (a) original data and (b) YBCO scattering with the nickel filtered out. While a YBCO diffraction pattern [Fig. 2.60(b)] is far more diffuse and noisy than a Ni pattern [Fig. 2.60(a)], the crystal orientation is nevertheless obvious: the pattern is dominated by two arcs corresponding to the [100] and [010] zone axes.

A novel algorithm is applied to a high-critical-current YBCO film grown on a multilayered RABiTS^{TM} substrate. While each Ni grain has a uniform orientation and diffracts as a single crystal, the orientation of the epitaxial YBCO film varies from point to point. Multiple measurements are used to determine both the average orientation of YBCO on each Ni grain and the variation in orientation—the single-grain crystal mosaic. The broadening of a YBCO reflection gives a more local single-point mosaic. The variations of all three quantities are found as a function of the tilt of the underlying Ni grain.

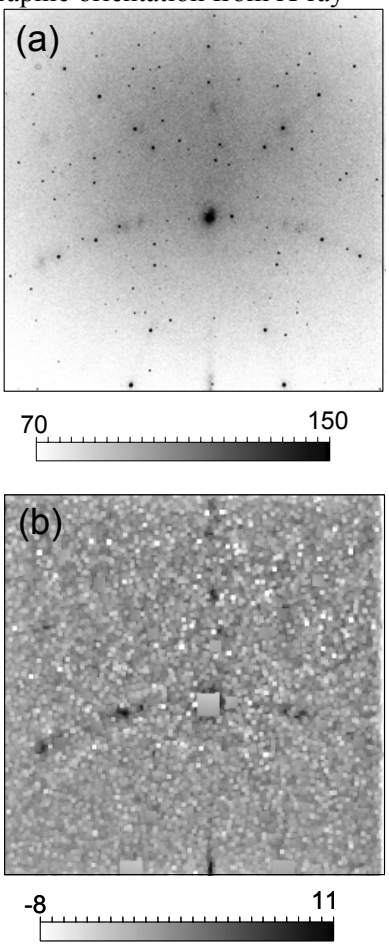

Fig. 2.60. Polychromatic Laue patterns. (a) Original data, with an intensity scale emphasizing the weak peaks. (b) YBCO scattering after a minimum filter is used to remove scattering from Ni.

2.12.2 Experimental

YBCO films having a thickness of 0.8 μm were deposited by metallorganic deposition (MOD) on RABiTS™ of configuration Ni-5at.%W (75 μm) / Y_2O_3 (75 nm) / YSZ (75 nm) / CeO_2 (75 nm). The transport critical current density at self-field and 77 K was 2 MA/cm^2. Details of RABiTS™ substrate preparation [12] and MOD YBCO preparation [13] can be found elsewhere.

Diffraction data were collected at the 34-ID-E microdiffraction facility at the Advanced Photon Source synchrotron. The instrumentation has been described in detail elsewhere [14]. Briefly, X rays are focused to a 0.5 × 0.7 μm^2 spot using Kirkpatrick-Baez mirrors. The beam hits the sample at a 45° glancing angle. A 2084 × 2084 pixel 16-bit Peltier-cooled charge-coupled device (CCD) detector collects diffraction patterns spanning a 59° × 59° solid angle of diffracted X rays. The center of the detector collects specularly reflected rays leaving the sample at a 45° glancing angle. Laue diffraction patterns are collected by using the full 8–24-keV bandpass of X rays reflected by the mirrors. The sample is mapped by rastering the sample in 5-μm steps over a square grid, 200 × 625 μm^2 in total area; 5125 patterns are acquired.

To determine the YBCO orientation, the strong, sharp scattering from the Ni substrate is first removed, using a low-pass filter. Fig. 2.60(a) shows one polychromatic X-ray diffraction pattern. Sharp peaks can be seen from five Ni grains, along with more diffuse scattering from the YBCO film. The stronger Ni peaks are off-scale in this image. If the full intensity range of the data was used, only Ni peaks would be visible. Fig. 2.60(b) shows the same image after filtering. Only the diffuse scattering from the YBCO film is visible. The pattern in Fig. 2.60(b) is not sufficiently well resolved to index the Bragg reflections, but two arcs are clearly visible. Conventional X-ray texture measurements show that YBCO grows with a (001)<100> orientation, so these arcs are the [100] and [010] zone axes, corresponding to the [0*kl*] and [*h*0*l*] families of reflections. The orientation of these zone axes, and thus of the YBCO film, are found using Hough transforms [15], following a similar technique for analyzing orientation using EBSD patterns [16].

2.12.3 Results

Using white-beam Laue patterns to measure Ni orientation and considering neighboring points with misorientation less than 0.1° to belong to the same grain, 202 Ni grains are observed, with an average area of 25 μm^2 (Fig. 2.61). While EBSD has shown that the Ni grain boundaries are sharp and well defined, the X-ray map shows some ambiguity in assigning grain orientation near the boundaries, where two grains give strong diffraction. This causes spurious single-pixel grains, which are ignored in the following analysis. The Ni is cube-textured, with FWHM ~6°, consistent with EBSD [6] and conventional X-ray texture [17] measurements (Fig. 2.62, blue dots).

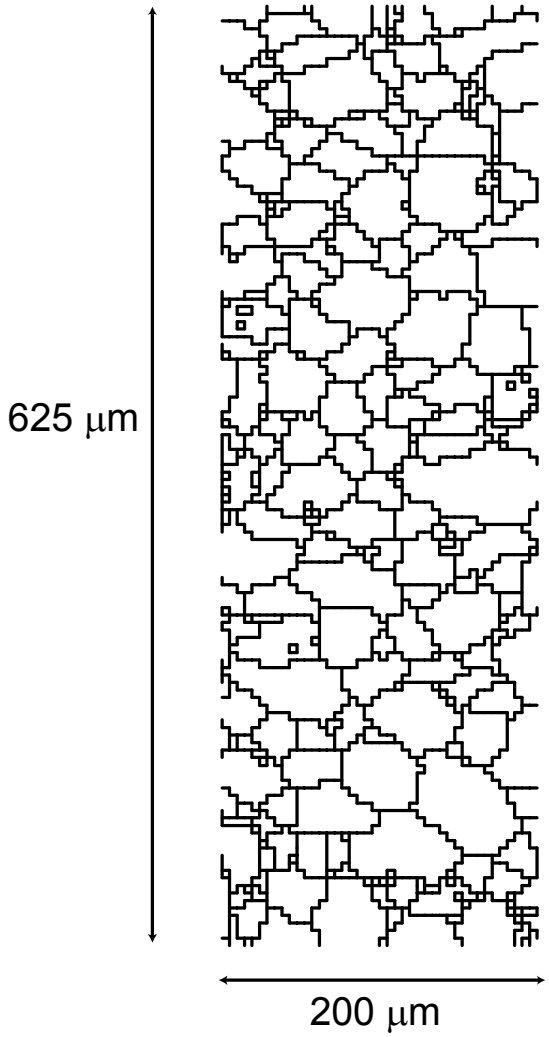

Fig. 2.61. Ni grain boundaries. Lines indicate misorientations > 0.1°.

We will consider variations of YBCO orientation on three length scales. The longest is the variation between Ni grains in the average orientation of the YBCO grown on each Ni grain. As for CeO_2/Ni [9], the orientations of YBCO and Ni are strongly correlated. The in-plane orientations are similar, but YBCO grows with the [001] direction closer to the surface normal than the Ni [001]; this may be seen graphically in a pole figure (Fig. 2.62). This rotation is shown more quantitatively in Fig. 2.63: the out-of-plane misorientation ψ_{YBCO} (the angle between the YBCO [001] direction and the surface normal) is only 0.58 that of the misorientation ψ_{Ni}.

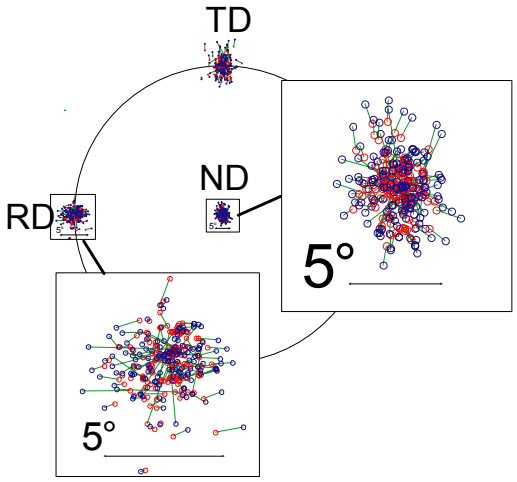

Fig. 2.62. Stereographic projection of Ni (100) (blue) and YBCO (100) and (001) (red) plane normals. Green lines connect the orientation of each Ni grain with the average orientation of the overlying YBCO. RD: rolling direction; TD: transverse direction; ND: normal direction.

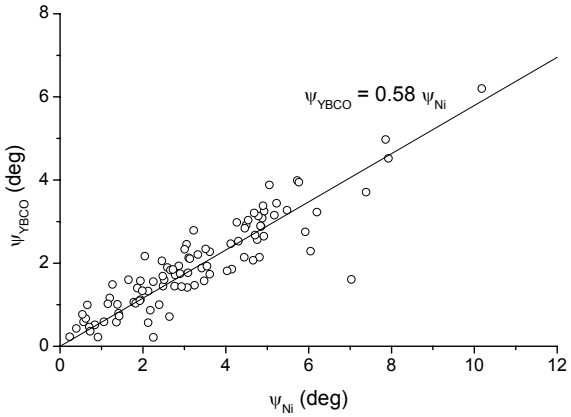

Fig. 2.63. Correlation of the angle ψ between the [001] direction and the surface normal for YBCO and Ni.

The intermediate length scale is the variation of YBCO texture among the points measured on each Ni grain. Depending on the size of the Ni grain, from 1 to 158 Laue diffraction patterns are measured per grain. YBCO orientation can be deduced from only 64% of the diffraction patterns; from 1 to 133 orientations are measured per grain. To get statistically significant results, the variation in grain orientation is considered only for grains over which YBCO orientation was measured at 10 or more locations; these 94 grains include 80% of the sample area. We would expect this variation in orientation to correspond to the diffraction rocking curve width for YBCO grown on a single crystal; to facilitate comparisons to x-ray rocking curves, we report the variation in terms of FWHM, equal to 2.355 times the standard deviation, assuming Gaussian statistics. This width is of practical interest because it represents the limiting alignment that would be produced on a highly textured substrate.

The average FWHM is $\langle \Delta\omega_R \rangle = 2.6^\circ$ for rotation about the rolling direction, $\langle \Delta\omega_C \rangle = 2.0^\circ$ for rotation about the cross direction, and $\langle \Delta\phi_R \rangle = 2.9^\circ$ for rotation about the normal direction. Since these three measures of alignment all exhibit similar behavior, we will report results for the three added in quadrature: $\Delta\Theta = \sqrt{\langle \Delta\omega_R \rangle^2 + \langle \Delta\omega_C \rangle^2 + \langle \Delta\phi \rangle^2}$. The distribution of $\Delta\Theta$ for the 94 grains is shown in Fig. 2.64. For the grains with the best-aligned YBCO, alignment approaches that reported for high-quality YBCO grown on oxide single crystals; for example, $\Delta\Theta = 1.8°$ for YBCO/Al_2O_3 [18]. Most of the grains would be expected to yield a high intergranular critical current, but there are eight outlier grains with $\Delta\Theta > 8°$.

What leads to the large mosaic of these outlier grains? The polycrystalline Ni substrate provides a combinatorial library of Ni grains with varying surface orientation and grain size (along with other properties, which we cannot readily measure). No correlation is apparent between Ni misorientation ψ_{Ni} and YBCO mosaic $\Delta\Theta_{YBCO}$. YBCO growing on smaller Ni grains, however, is significantly more likely to have a large mosaic. For grains with $\Delta\Theta_{YBCO} > 8°$, the average grain size is 797 μm^2, while for grains with $\Delta\Theta_{YBCO} < 8°$, the average grain size is 1202 μm^2 (Fig. 2.65). Within each Ni grain, YBCO orientation varies randomly, with no apparent correlations between nearby points.

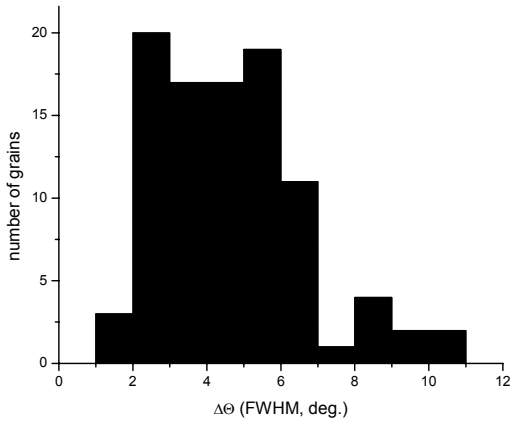

Fig. 2.64. Frequency distribution over 96 grains of the total variation in YBCO crystal orientation (rocking curve widths about three axes added in quadrature).

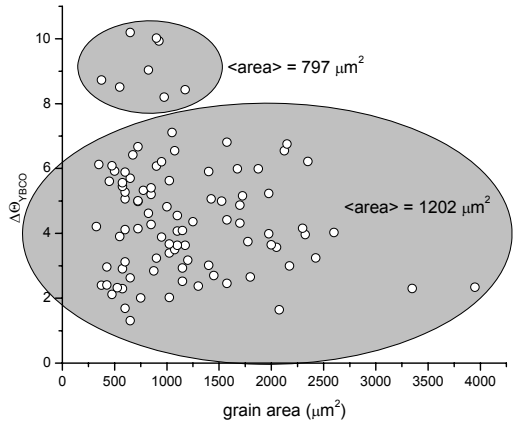

Fig. 2.65. Grains with high-YBCO mosaic (small ellipse) are significantly smaller than grains with lower mosaic (large ellipse).

The smallest length scale is the variation in YBCO orientation within the ~0.5-μm^2 area sampled by one diffraction measurement. Of the 5125 Laue patterns measured, 3276 (64%) contain YBCO diffraction patterns clear enough to determine orientation. For these patterns, the YBCO crystal mosaic is ~0.7°. Since YBCO thickness is known to be uniform, we conclude from the absence of clear YBCO diffraction that the local mosaic is significantly larger than at the other 44% of the points. While a better way to measure mosaic on the submicron length scale is clearly needed, we can make comparisons between Ni grains based on this crude measure: the fraction, *f*, of the grains for which YBCO diffraction can be measured.

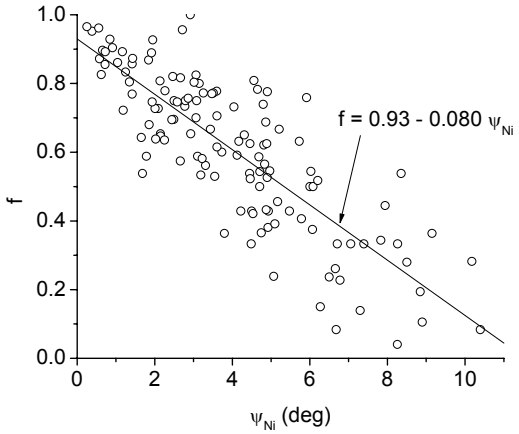

Fig. 2.66. Correlation between fraction *f* of patterns from which YBCO diffraction can be clearly observed and angle ψ_{Ni} of the <100> direction and the sample normal.

The mosaic of YBCO on a submicron length scale is well correlated with the tilt ψ_{Ni} of the Ni lattice (Fig. 2.66). For Ni grains in which the <100> direction is aligned to the surface normal to within 2°, YBCO can nearly always be indexed, from which we infer a mosaic near 0.7°. For Ni grains with $\psi_{Ni} > 8°$, the fraction *f* approaches zero, implying a higher YBCO mosaic. No significant correlation is observed between *f* and the size of the Ni grain.

2.12.4 Discussion

On the length scale of Ni grains, the average epitaxy of YBCO exhibits little random variation; the YBCO tilt depends only on the Ni tilt (Fig. 2.63). This is consistent with the EBSD result that the greatest improvement in alignment occurs for substrate grains with the largest out-of-plane tilts [8]. The relationship, $\psi_{YBCO} = 0.58\ \psi_{Ni}$, is consistent with that reported for CeO_2/Ni at higher temperatures, where growth proceeds by ledge propagation and lattice mismatch at atomic steps leads to reduced tilting [9]. This suggests that YBCO grows on the oxide buffer layers with good (001)||(001), <100>||<100> epitaxy. This is not the case for other YBCO/RABiTS™ films, in which YBCO grows with a smaller average tilt than the buffer layers [19]. Further study of grain-by-grain epitaxy is needed to understand the different growth modes of YBCO.

The variation of YBCO orientation among the measurements on a single grain has a weak dependence on grain size. Smaller Ni grains are more likely to support a large YBCO mosaic (Fig. 2.65), although most of the large variation in YBCO mosaic is uncorrelated with any measure of the underlying Ni grain. No mechanism is apparent by which Ni grain size would directly affect YBCO mosaic; more likely a common factor causes both. Grain growth in Ni is impeded by precipitates of trace impurities such as carbides. A higher density of precipitates could lead to both smaller Ni grains and a larger YBCO mosaic. Alternatively, variations in YBCO mosaic could be caused by variations in the dislocation density in Ni grains. Grain growth during recrystallization is driven by the energy gained as grains with a low dislocation density grow at the expense of grains with a high dislocation density [20], it is reasonable to expect there to be fewer dislocation in larger Ni grains, leading to a lower mosaic in the overlying YBCO.

The YBCO mosaic within the ~0.5-μm^2 area illuminated by the incident beam, measured indirectly by the frequency with which a YBCO diffraction pattern can be measured, is strongly correlated with the tilt of the underlying Ni grain. This can be accounted for by statistical fluctuations in this tilt. Consider for example a tilt ψ_{Ni} about the <100> axis, corresponding to a linear density $2\psi_{Ni}/a_0$ of steps of height $a_0/2$. If the steps are uncorrelated, the average number of steps in length x is $2\psi x/a_0$, with standard deviation $\sqrt{2\psi_{Ni}\, x / a_0}$. The standard deviation $\sqrt{\psi_{Ni} a_0 / 2x}$ in the tilt increases with the tilt. More variation in the tilt of the Ni grain will naturally produce a larger mosaic in the overlying YBCO.

Results from polychromatic X-ray microdiffraction and EBSD are generally consistent. The advantages of each technique are as follows. Because X rays are a penetrating probe, multiple layers can be analyzed with no sample preparation, whereas EBSD requires extensive and destructive sample preparation. However, this deep penetration leads to a signal from a thin film that is weak relative to the substrate, making analysis difficult; YBCO orientation could be measured with polychromatic X rays only for the better-oriented portions of the film, and buffer layer orientation could be measured only with time-consuming monochromatic-beam measurements. With proper sample preparation, EBSD can measure almost the entire surface. By measuring multiple layers simultaneously, the X-ray technique provides absolute registry of the position of the layers, while the multiple EBSD scans must be aligned by locating landmarks in the microstructure. The X-ray technique provides higher angular resolution (~0.01°) for the Ni substrate than EBSD (~0.25°); this is of limited use for epitaxial films with large mosaic.

At the present time, EBSD orientation maps typically provide higher resolution. Polychromatic X-ray microbeams have been made that are smaller than 100 nm [21], comparable in resolution to EBSD. However, the effective resolution in the X-ray measurements is most often limited by the time required to acquire and analyze data, limiting the number of data points that can be measured. Data acquisition is slowed by the use of CCD detectors with many pixels, to take advantage of the high angular resolution of the X-ray measurement and a large dynamic range to observe diffraction from a thin film over the large background scattering due to deep penetration into the substrate. Higher-rate detectors are under development and should soon facilitate the rapid acquisition of polychromatic X-ray diffraction patterns [22]. Analysis of X-ray diffraction patterns is currently slow (~1 min for X-ray vs ~1 s for electron

diffraction patterns) simply because the software has not been as highly optimized as it has for electrons; the analysis is not fundamentally more difficult.

2.12.5 Conclusions

Much of the variation in YBCO orientation can be correlated to variation in the Ni grains on which it grows. Increasing tilt of the Ni grain leads to increasing YBCO tilt, although the YBCO tilt is less than the Ni tilt. This affect appears to be caused entirely by the oxide buffer layers, with YBCO simply replicating the buffer layer orientation. Increasing tilt of the Ni grain also leads to larger local mosaic in YBCO on a submicron length scale. Smaller Ni grains are correlated with larger YBCO mosaic on a 5-μm length scale. An inhomogeneous distribution of precipitates in the Ni substrate is a possible cause of this variation.

2.12.6 References

1. Y. Iijima, N. Tanabe, O. Kohno, and Y. Ikeno, *Appl. Phys. Lett.* **60**, 769 (1992).

2. X. D. Wu, et. al., *Appl. Phys. Lett.* **67**, 2397 (1995).

3. D. P. Norton, et al., *Science* **274**, 755 (1996).

4. A. Goyal, et. al., *Appl. Phys. Lett.* **69**, 1795 (1996).

5. B. Ma, et. al., *Physica C* **366**, 270 (2002).

6. A. Goyal, et. al., *Micron* **30**, 463 (1999).

7. D. M. Feldmann, et. al., *J. Mater. Res.* **20**, 2012 (2005).

8. D. M. Feldmann, et. al., *J. Mater. Res.* **21**, 923 (2006).

9. J. D. Budai, et. al., *Nature Materials* **2**, 487 (2003).

10. J. S. Chung and G. E. Ice, *J. Appl. Phys.* **86**, 5249 (1999).

11. N. Tamura, et. al., *Appl. Phys. Lett.* **80**, 3724 (2002).

12. A. Goyal, et. al., *MRS Bull*. **29**, 552 (2004).

13. M. W. Rupich, et. al., *MRS Bull.* **29**, 572 (2004).

14. G. E. Ice, et. al., *J Synchrotron Radiat* **12**, 155 (2005).

15. R. O. Duda and P. E. Hart, *Commun Acm* **15**, 11 (1972).

16. N. C. K. Lassen, et. al., *Mater. Sci. Technol.* **12**, 837 (1996).

17. E. D. Specht, et. al., *Supercond. Sci. Tech.* **11**, 945 (1998).

18. B. F. Cole, et. al., *Appl. Phys. Lett.* **61**, 1727 (1992).

19. E. D. Specht, et. al., *Physica C* **382**, 342 (2002).

20. R. D. Doherty, et. al., *Mater. Sci. Eng. A* **238**, 219 (1997).

21. W. J. Liu, et. al., *Rev. Sci. Instrum.* **76**, 113701 (2005).

22. P. Coan, A. et. al., *J Synchrotron Radiat.* **13**, 260 (2006).

2.13 Stacking Faults in $YBa_2Cu_3O_{7-x}$: Measurement using X-Ray Diffraction and Effects on Critical Current

E. D. Specht, A. Goyal J. Li. P. M. Martin (ORNL), X. Li, and M. W. Rupich (AMSC)

2.13.1 Introduction

Epitaxial Y123 thin films can support high critical current when the magnetic field vortices are pinned; however, the responsible pinning mechanisms have not been clearly identified. Improved understanding and control of these pinning mechanisms will aid in the development of films for high-critical-current applications. Possible pinning mechanisms include the Y123 lattice (intrinsic pinning) [1] and naturally formed lattice defects such as precipitates [2], twins [3], grain boundaries [3], edge dislocations [4], screw dislocations [5], and stacking faults (SFs) [6].

SFs are of particular interest because they appear to be an important pinning mechanism for ex situ Y123 films prepared from BaF_2 precursors [6]. Such films, important for potential high-current applications, are grown in two steps: a precursor film is first deposited, then chemically converted to Y123 [7]. The *c*-axis stacking sequence of defect-free, fully oxygenated Y123 is BaO-CuO_2-Y-CuO_2-BaO-CuO [8]. The SFs that occur in ex situ Y123 films are believed to consist of an extra CuO plane: BaO-CuO_2-Y-CuO_2-BaO-CuO-CuO [6]. The $YBa_2Cu_4O_8$ (Y124) structure corresponds to such an SF in every Y123 cell [9], while the $Y_2Ba_4Cu_7O_{15}$ structure corresponds to SFs in alternate Y123 cells [10].

This paper is concerned with measuring SF density, *n,* in epitaxial Y123 films and the correlation between SFs and the critical current value when *H* is in the *ab* plane of the Y123 films. SFs are generally measured using transmission electron microscopy (TEM) [6,11–15]; however, sample preparation is time-consuming and destructive. In addition, only a small portion of the sample can be examined, so results may not be representative of the entire sample. We demonstrate that analysis of XRD line broadening can be used to provide a rapid, quantitative, nondestructive measure of *n* over a large area of the film.

2.13.2 Experimental Details

All samples were prepared on Rolling-Assisted-Biaxially Textured-Substrates (RABiTS^{TM}) [16] with the configuration Ni-5at%W (75 μm) / Y_2O_3 (75 nm) / YSZ (75 nm) / CeO_2 (75 nm). Details of substrate fabrication and characterization have been reported elsewhere [17].

Y123 and Dy-doped Y123 films were prepared using an MOD process. Films were reacted at ~750°C in a humidified, low-O_2 atmosphere, cooled to ambient temperature, and then oxygenated at < 600°C to form the orthorhombic phase. Complete details of processing parameters and conditions have been reported elsewhere [18]. Selected Y123 films were given an additional high-temperature oxygen anneal at 700 to 750°C in 500 ppm O_2 after the reaction step, then oxygenated at < 600°C to form the orthorhombic phase.

Critical current was measured by transport using a standard four-point-probe method with a voltage criterion of 1 μV/cm. The angular dependence of critical current was measured at 77 K with *H* applied perpendicular to the current (i.e., in the maximum Lorentz force configuration). TEM was carried out on a Hitachi HF-2000 and a Philips CM200 microscope, both with a field emission gun operated at 200 kV. XRD measurements were made using a standard Rigaku diffractometer with Cu K_α radiation.

For (001)-textured films, only (00*l*) XRD peaks are observed for Y123; peaks from the substrate and buffer layers are ignored. After annealing, the Y123 peaks are well described by a Lorentzian-squared lineshape:

$$L(2\theta) = A\left[1 + (2\theta - 2\theta_L)^2 / \kappa^2\right]^{-2}, \quad (1)$$

where the full-width at half-maximum (FWHM) $\Delta 2\theta = 1.29\kappa$ follows the form expected for an inhomogeneous strain:

$$\Delta 2\theta_L = 2\varepsilon \tan\theta_L , \tag{2}$$

where ε = 0.0038 is the FWHM of the strain distribution. In this case, the inhomogeneous strain is likely due to an oxygen stoichiometry gradient through the thickness of the film.

The diffracted intensity $F(2\theta)$ from a crystal with SF is given by Eq. (20) of Hendricks and Teller [19]. This model assumes that the structure consists of a random sequence of 1.361-nm Y124 layers, occurring with probability f_{124}, and 1.168-nm Y123 layers occurring with probability $f_{123} = 1 - f_{124}$. The bulk structures of Y123 and Y124 are used to find the scattering factors of each layer [8,9]. Each peak is modeled by a numerical convolution of the diffracted intensity, F, from an ideal randomly faulted crystal with the peak profile, L, from a real, unfaulted film, which is broadened due to instrumental effects and lattice parameter variation:

$$I(2\theta) = \frac{1+\cos^2\theta}{\sin^2\theta\cos\theta}\int_{-8\kappa}^{8\kappa} L(x)F(2\theta+x)dx , \tag{3}$$

where the first term is the Lorentz-polarization factor for powder diffraction [20], L, given in Eq. (1). A linear background is added. Each pattern is fitted by varying the intensity, A, of each peak, the probability f_{124} of SF, and the slope and intercept of the background; the widths, κ, are fixed from analysis of an annealed sample.

Because six Y124 layers are equal in thickness to seven Y123 layers to within 0.12%, the Y123 (006) reflection is not significantly broadened by faulting, and the convolution of Eq. (3) becomes difficult to perform. The (006) peak is modeled by a Lorentzian-squared lineshape [Eq. (1)], as are the unfaulted films. The lack of broadening of the (006) reflection is characteristic of Y124-type SF and supports the conclusion that it is the dominant SF in these films.

2.13.3. Results and Discussion

MOD Y123 films on RABiTS™ typically display a strong peak in the angular dependence of critical current on H at 77 K for H // *ab*-plane [18] (Fig. 2.67, ♦). However, the critical current for this field alignment drops dramatically in samples given the high-temperature oxygen anneal step, while there is no measurable change in the critical current with the field oriented along the *c*-axis (Fig. 2.67, ○). These data indicate that the pinning centers responsible for the high currents for H // *ab*-plane are eliminated by the high-temperature annealing.

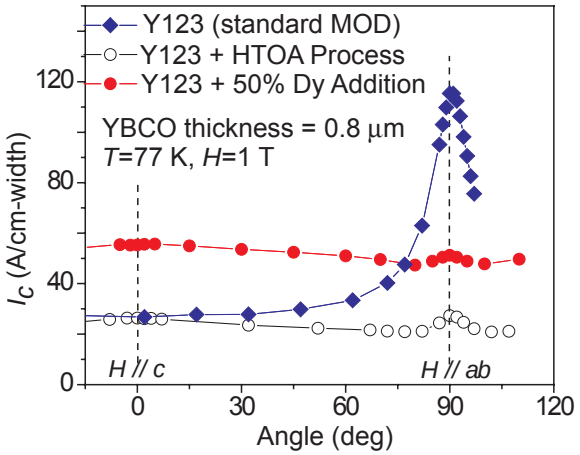

Fig. 2.67. Dependence of critical current on the orientation of *H* (1 tesla, 77 K). Y123 prepared with the standard MOD process (◆); Y123 film with high-temperature oxygen anneal (○); and Dy-doped Y123 (●). Calculated Y123 thickness is 0.8 μm.

XRD analysis (Fig. 2.68, ■) of the Y123 sample prepared with the standard process shows the presence of numerous 124-type defects with the best fitting model of $f_{124} = 0.08$ (dashed line), n = 0.068 nm^{-1}. TEM analysis of a similar sample [Fig 2.69(a)(b)] confirms the presence of the 124-type SFs. In contrast, XRD analysis of a sample after the high-temperature oxygen anneal process (Fig. 2.68, ○) shows the best fit is for $f_{124} = 0.01$ (solid line), n = 0.086 nm^{-1}, indicating that almost no SFs are present, which was confirmed by TEM [Fig. 2.69(c)]. These results suggest that the enhanced *ab*-plane pinning is due to the presence of the 124 SF.

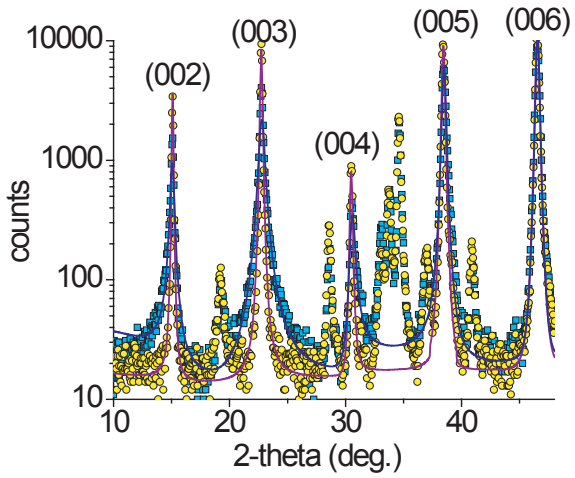

Fig 2.68. XRD scans and fit for Y123 films. Standard MOD processing (■) modeled with f124=0.08 (dashed line); after high-temperature oxygen anneal film (○) modeled with f124=0.01 (solid line). Extra peaks are due to substrate and buffer layers.

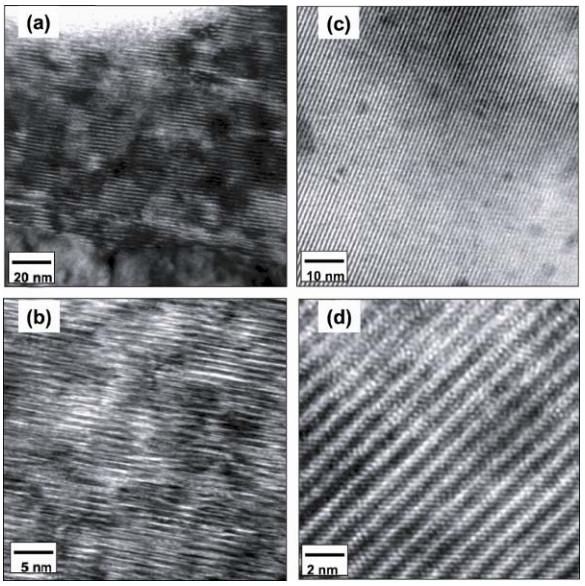

Fig. 2.69. TEM images. (a),(b) standard MOD processing of Y123, showing a high density of 124-type SF; no faulting is apparent (c) after high-temperature oxygen anneal or (d) with 50% excess Dy.

The addition of excess rare earth (RE) atoms into the Y123 films also reduces the I_c peak for fields oriented in the *ab*-plane. Fig. 2.67 (•) shows results for a sample containing a 50% Dy addition. This effect is similar to that resulting from the high-temperature oxygen anneal process; however, the addition of Dy also increases the pinning in perpendicular field orientations as indicated by the broad peak for H//*c* compared to the undoped Y123 sample. TEM confirms that RE doping, greatly reduces *n* as shown in Fig. 2.69(d) for a sample with 50% excess Dy doping.

XRD analysis of Dy-doped Y123 films in Fig. 2.70 shows the SF frequency decreases with increasing RE concentration, with the effect saturating at f_{124} = 0.03 (0.026 nm^{-1}) for doping beyond 30%. The Dy-free sample in Fig. 2.70 was prepared similarly to the sample used in Fig. 2.69, but has a slightly different *n*.

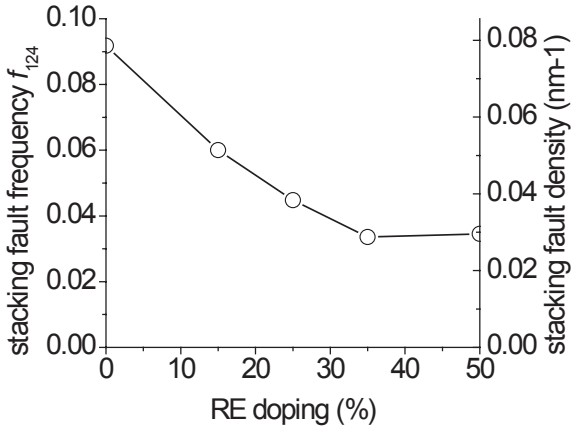

Fig. 2.70. SF probability and density for Y123 films doped with excess Dy.

The enhanced critical current observed for H//*ab* in the MOD-based Y123 films is associated with the presence and density of 124-type SF. Small changes in the processing parameters of the MOD-based Y123 films, such as insertion of the high-temperature oxygen anneal step or the addition of excess RE atoms, can drastically alter the Y124-type SF density and thus the critical current for H//*ab*. The development of a commercial process for preparing Y123 films for 2G HTS wire applications requires the ability to reproducibly control the density of SF in order to tune the performance of the Y123 films for optimized performance as a function of applied magnetic field and field orientation.

2.13.4 Conclusion

In order to facilitate the development of the optimum parameters and to assist in establishing the mechanism for the 124-type SF growth, a simple XRD analysis was developed to measure the 124-type SF density in Y123 films prepared by the MOD process. The identity of the defects is confirmed by characteristic asymmetries in peak broadening, which agree in both observed and calculated diffraction patterns as well as in the absence of broadening in the (006) reflection. This simple XRD technique provides a rapid means of optimizing processing parameters to adjust the 124 SF density in the Y124 films. The XRD and TEM characterizations are complementary: XRD is most sensitive to high densities of SFs, where TEM images become unclear, while SFs are best resolved using TEM at low SF densities, where XRD patterns become difficult to distinguish from those of unfaulted samples. Future work will address conditions under which SFs form and under which conditions they are removed.

The fitting of XRD data provides a rapid, nondestructive, quantitative measure of the 124-type SF density in Y123 films, which is correlated to the strong peak in the angular dependence of critical current at 77K for H//*ab*. The pattern of peak broadening observed in the XRD scans is specific to the crystallography of the 124-type SF. The 124-type SF densities can be measured down to a 1% frequency or a density of 0.009 nm^{-1}. The method described in this paper to estimate the SF density provides a convenient, expedient, and nondestructive way of determining the SF density and thus to enable optimization of transport properties of Y123 films in 2G HTS wires.

2.13.5 References

1. M. Tachiki and S. Takahashi, *Solid State Commun*. **72**, 1083 (1989).

2. M. Murakami et al., *Jpn J Appl Phys* 1 **28**, 1189 (1989).

3. P. H. Kes et al., *Cryogenics* **29**, 228 (1989).

4. L. Diaz et al., *Phys. Rev. Lett.* **80**, 3855 (1998).

5. J. Mannhart et al., *Z Phys B Con Mat* **86**, 177 (1992).

6. P. C. McIntyre and M. J. Cima, *J. Mater. Res.* **9**, 2778 (1994).

7. X. Li et al., *Physica C* **390**, 249 (2003).

8. T. Siegrist et al., *Phys. Rev. B* **35**, 7137 (1987).

9. P. Marsh et al., *Nature* **334**, 141 (1988).

10. J. Karpinski et al., *J Less-Common Met* **150**, 129 (1989).

11. H. W. Zandbergen et al., *Nature* **331**, 596 (1988).

12. J. A. Ourmazd et al., *Nature* **327**, 308 (1987).

13. C. Grigis, S. Schamm, and D. Dorignac, *J. Mater. Res.* **14**, 2732 (1999).

14. J. W. Seo et al., *Physica C* **225**, 158 (1994).

15. C. L. Jiaet al., *Physica C* **182**, 163 (1991).

16. A. Goyal et al., *Appl. Phys. Lett.* **69**, 1795 (1996).

17. A. Goyal, M. P. Paranthaman, and U. Schoop, *MRS Bull.* **29**, 552 (2004).

18. M. W. Rupich et al., *MRS Bull.* **29**, 572 (2004).

19. S. Hendricks and E. Teller, *J. Chem. Phys.* **10**, 147 (1942).

20. D. Cullity and S. R. Stock, p. 149 in *Elements of X-Ray Diffraction*, 3rd ed.. Prentice Hall, Upper Saddle River, N.J. (2001).

2.14 $YBa_2Cu_3O_{7-\delta}$ Formation by Processing of Fluorine-Free Precursor Films

K. Kim, Y. Zhang, R. Feenstra, D. K. Christen, H. M. Christen, S. Cook, F. A. List, J. Tao, S. J. Pennycook, and Y. Zuev

2.14.1 Introduction

One of the principal approaches to the formation of epitaxial HTS for coated conductors is the ex situ technique, whereby a precursor coating is converted to the superconductor in a separate processing step. This ex situ process can use different methods for growing precursor layers such as coevaporation, metal organic deposition [1] and sol gel processes [2]. BaF_2-containing precursor films are decomposed using water vapor, resulting in the formation of gaseous HF [3,4]. The reaction rate of BaF_2 decomposition and YBCO formation is determined by removal of HF by both gaseous convection and diffusion. The conversion to YBCO of fluorine-free, environmentally stable PVD-deposited precursors may be conducted without the need of water vapor or the undesirable buildup and necessary removal of HF. Elimination of the latter could significantly simplify the conversion process because high gas flow rates or low-pressure processing [5] would be unnecessary. Large YBCO growth rates with excellent epitaxy and superconducting properties may be possible if F-free precursors are used, based on the preliminary results of studies by Hammond et al., who used electron beam co-evaporated YBCO precursors [6]. An additional potential benefit is expanded compatibility with various classes of lattice-matched buffer layers, which encompass many single-layer perovskite-like materials. (To date, CeO_2 is the only buffer layer that has shown complete compatibility with the BaF_2 ex situ process.)

Here we report initial baseline studies on the formation of epitaxial YBCO on lanthanum aluminate (LAO) single-crystal substrates by converting fluorine-free, laser-ablated precursor films. In this study, the precursor film deposition and conversion processes were performed in the same chamber.

2.14.2 Experimental Procedure

The precursor films were formed by pulsed laser deposition (PLD) from a ceramic YBCO target onto single-crystal $LaAlO_3$ substrates at room temperature and in an oxygen ambient of 1.0×10^{-1} Torr. A KrF (248nm) excimer laser was used as the ablation source at an energy density of 2 J/cm^2 and at a repetition rate of 10 Hz. As-deposited precursor films with typical thickness of 0.2 μm were converted into crystallized $YBa_2Cu_3O_{7-\delta}$ by heat treatment in the same chamber, usually without breaking vacuum. A reducing gas mixture of Ar/4%H_2 at a pressure of 1 Torr was admitted during heat-up for processing. After the desired temperature was reached, oxygen was introduced rapidly as a processing gas. Guidance for the processing conditions of temperature and oxygen pressure was taken from the previous work of Hammond et al. [6,7]. After a few minutes of processing, the temperature was decreased while maintaining the oxygen pressure. The resulting YBCO film was then annealed at 450°C in atmospheric oxygen ambient for 18 h for further oxygenation.

X-ray diffraction θ-2θ scans were used to confirm the phase development in the films. Surface observation and the compositional analysis were conducted by SEM and energy-dispersive X-ray spectroscopy (EDS). The superconducting transition temperature and the critical current density were measured with a SQUID magnetometer; a standard four-point technique was used to evaluate the temperature-dependent resistivity. Atomic resolution Z-contrast imaging by scanning transmission electron microscope was used to analyze the YBCO crystal nanostructure.

2.14.3 Results and Discussion

The entire processing procedure (without breaking vacuum) consists of three major steps: precursor deposition; heat-up; and conversion. Figure 2.71 shows the schematic procedure of this processing related to the YBCO stability diagram. Heating the precursor film in the reducing ambient (1 Torr of Ar/4%H_2) is an important parameter in order to obtain *c*-axis perpendicular YBCO. The X-ray diffraction θ-2θ scans in Fig. 2.72 show that heating the precursor film in an oxygen ambient produces a polycrystalline YBCO

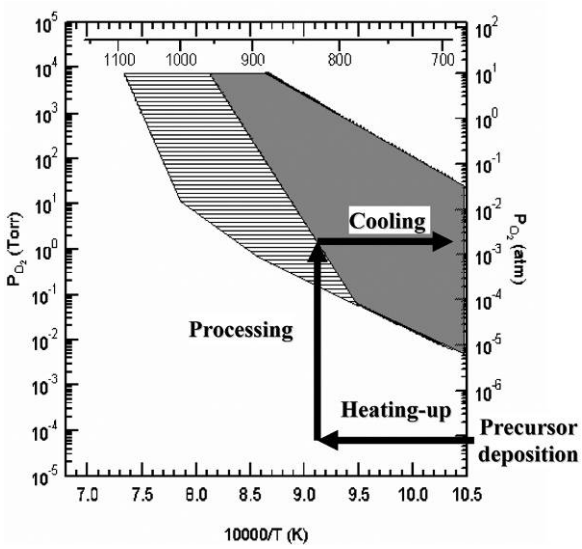

Fig. 2.71. The schematic procedure of in situ processing for laser-ablated, fluorine-free precursor film. This process consists of precursor deposition, heat-up, and conversion (processing).

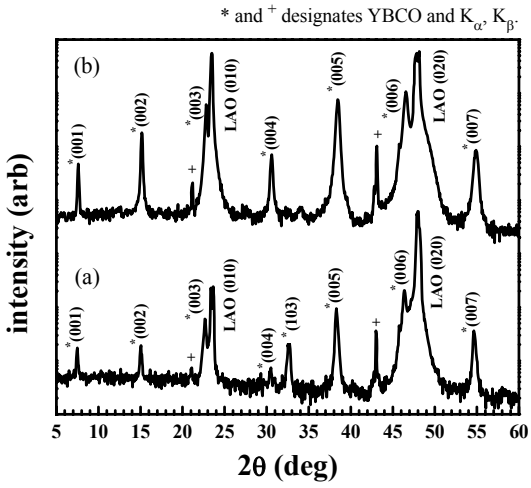

Fig. 2.72. X-ray diffraction θ-2θ scans of in situ processed $YBa_2Cu_3O_{7-\delta}$ films heated in (a) 3.0 × 10^{-1} Torr of oxygen and (b) 1 Torr of 4% Ar/H_2 mixture gas.

component. The as-deposited precursor film on $LaAlO_3$ showed a smooth surface with some particulates as shown in Fig. 2.73(a). Although the as-heated precursor film and in situ processed YBCO film showed different surface morphology in Fig. 2.73(b) and (c), the composition and the Y : Ba : Cu ratios from EDS analysis remained same after processing as indicated in Fig. 2.73(d)-(f).

Figure 2.74 is the x-ray diffraction θ-2θ scans of $YBa_2Cu_3O_{7-\delta}$ films processed in situ at the different processing temperatures of 780, 820, and 850°C. No significant phase differences were found in the X-ray pattern. The superconducting transition temperatures of the YBCO films measured magnetically at 4 Oe are indicated in Fig. 2.75. The offset temperatures are below 80 K in each case, and sharp transitions cannot be observed. However, long-term oxygen annealing at 450°C in 1 atm of oxygen for 18 h improved the transition temperature values.

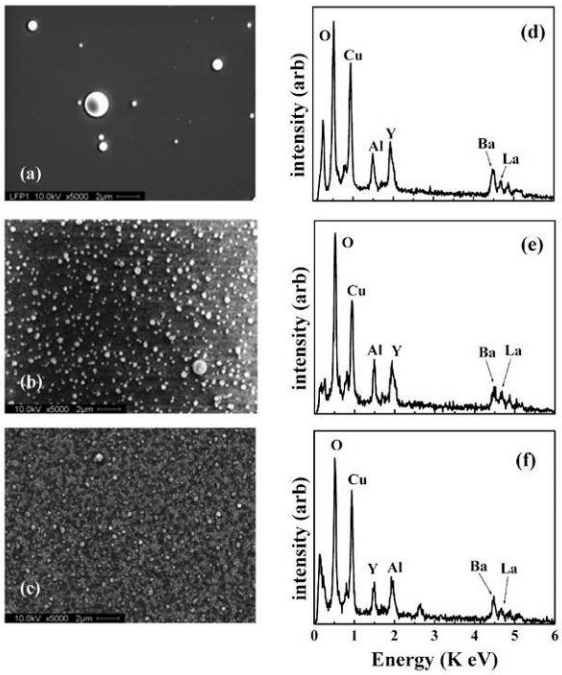

Fig. 2.73. The surface SEM pictures. (a) As-deposited precursor film, (b) as-heated precursor film in 4% Ar/H_2 gas, and (c) processed YBCO film. The EDS graphs are of (d) as-deposited precursor film, (e) as-heated precursor film, and (f) processed YBCO film. La and Al peaks come from the substrate.

In order to understand the need for the long oxygenation times, the YBCO nanostructure was observed by Z-contrast STEM. Figure 2.76(a) is a low resolution ZSTEM image showing both the LAO substrate and the processed YBCO film. Fig. 2.76(b), (c) and (d) are images taken near the interface between the LAO substrate and YBCO film, the middle part of YBCO film, and the upper part of YBCO film, respectively. The images taken at different scales show that the F-free in situ processed YBCO film is nearly defect free. Of the few

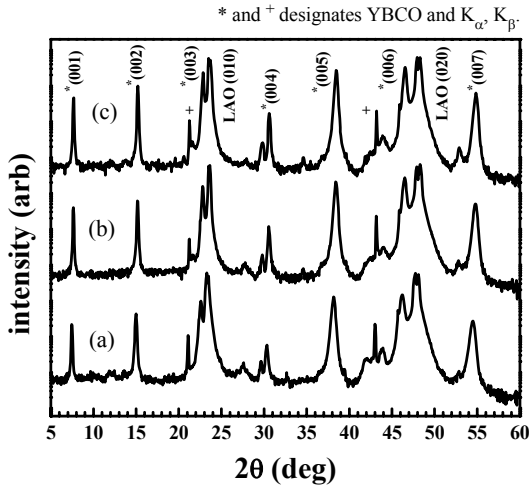

Fig. 2.74. The X-ray diffraction θ-2θ scans of in situ processed $YBa_2Cu_3O_{7-\delta}$ films at processing temperatures of (a) 780°C, (b) 820°C and (c) 850°C.

observable defects, most are planar intergrowths in the ~20 nm layer near the YBCO-substrate interface. There is improved perfection away from the interface, and virtually no threading defects through the film thickness can be observed. The lack of visible nanoscale defects is consistent with the difficulty in oxygen uptake. Oxygen tracer diffusion studies in single-crystal YBCO have shown that the diffusion coefficient of oxygen in *c*-direction is about 10^{-6} of that in the *a* or *b* direction [8]. As a result, lack of *c*-axis-oriented defects render it difficult to achieve complete oxygen uptake. Figure 2.77 is the resistivity versus temperature graph of a processed YBCO film on $SrTiO_3$ substrate, before and after a long-term oxygen anneal. In this case, the resistivity was not improved by the low-temperature soak. Figure 2.78 shows the magnetically determined critical current density values at 5 K and 77 K. The F-free processed YBCO film grown on LAO substrate showed a critical current density value of 1.06 MA/cm^2 at 77 K, which is lower than an ex situ YBCO from comparable PVD BaF_2-based precursors. The critical current density results shows relatively weak flux pinning which can also be explained by the lack of defects inside the YBCO film.

2.14.4 Conclusion

Epitaxial thin films of YBCO have been synthesized from F-free, laser ablated precursors. Processing for the best materials involves raising the oxygen pressure after heating in a reducing ambient such as 4% Ar/H_2 mixture gas. The superconducting transition temperature was measured to be 88 K, with resulting critical current density of about 1 MA/cm^2 at 77 K, as determined by magnetic hysteresis. Properties indicate that materials lack an appropriate level of defects needed both for oxygenation and flux pinning.

2.14.5 References

1. U. Schoop, et al., *IEEE Transactions on Applied Superconductivity* **15**, 261116 (2005).

2. M. Paranthaman, et al., *IEEE Transactions on Applied Superconductivity* **11**, 3146–49 (2001).

3. V. F. Solovyov, H. J. Wiesmann, and M. Suenaga, *Physica C* **353**, 14–22 (2001).

4. V. F. Solovyov, H. J. Wiesmann, and M. Suenaga, *Supercond. Sci. Technol.*, **16**, L37–L39 (2003).

5. Y. Zhang, et al., *Supercond. Sci. Technol*. **17**, 1154–59 (2004).

6. T. Ohnishi, J-U. Huh, and R. H. Hammond, *J. Mater. Res*. **19**, 977–81 (2004).

7. R. H. Hammond, J. Storer, and D. K. Christen, *2006 DOE Superconductivity Peer Review*, http://www.energetics.com/meetings/supercon06/agenda.html.

8. S. J. Rothman et al., *Physical Review B* **44**, 2326–33 (1991).

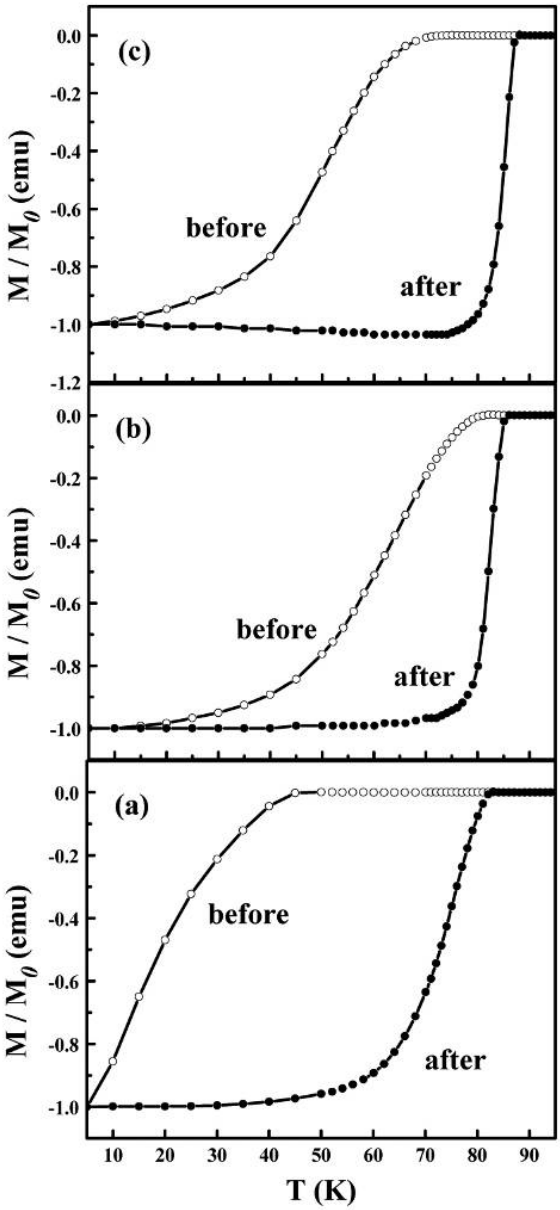

Fig. 2.75. The low-field magnetization vs temperature graphs of in situ processed $YBa_2Cu_3O_{7-\delta}$ films. Processing temperatures were (a) 780°C, (b) 820°C, and (c) 850°C. Samples are compared before and after oxygenation at 450°C in 1 atm of oxygen for 18 h.

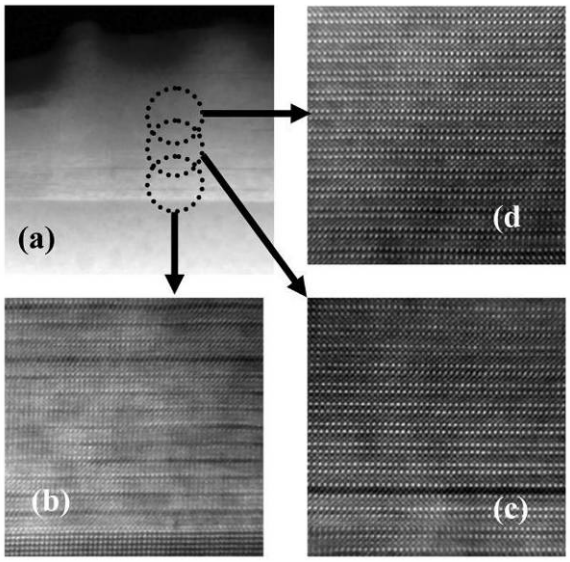

Fig. 2.76. The Z-contrast STEM images of (a) low resolution cross-section, (b) interface between LAO substrate and YBCO, (c) middle part of the YBCO film and (d) upper part of the YBCO film.

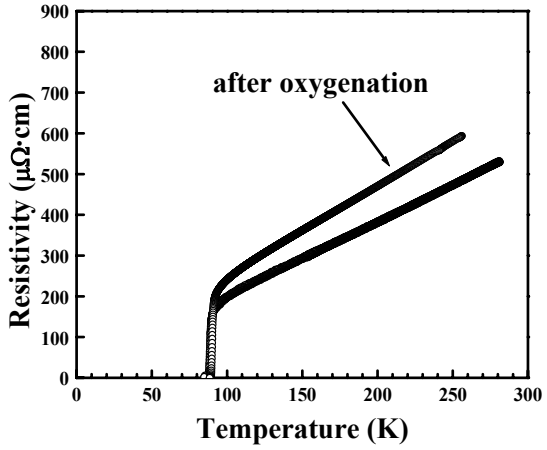

Fig. 2.77. The resistivity vs temperature graph of a YBCO film on $SrTiO_3$ substrate processed in situ at 820°C, before and after oxygenation at 450°C in 1 atm of oxygen for 24 h.

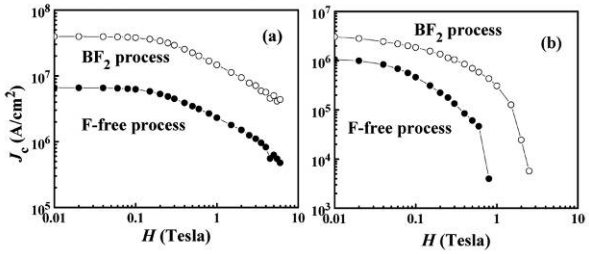

Fig. 2.78. The current density versus magnetic field graphs of YBCO precursors processed in situ on $LaAlO_3$ substrate compared with YBCO processed from a BaF_2 precursor at (a) 5 K and (b) 77 K.

2.15 Fabrication of Filamentary YBCO Coated Conductor by Inkjet Printing

F. A. List, T. Kodenkandath, and M. W. Rupich

2.15.1 Introduction

Applications of HTS coated conductors involving alternating electric and magnetic fields (ac applications) may require transposed filamentary HTS structures to reduce ac losses during device operation [1]. Several methods to fabricate filamentary 2G conductors have been recently considered. They include both subtractive methods (e.g., laser ablation [2,3], photolithography [4], and mechanical scribing [5]), wherein HTS is first applied to the entire conductor substrate and then selectively removed, and additive methods (e.g., ink transfer printing [6] and inkjet printing), wherein HTS is applied to only selected areas of the conductor substrate with no subsequent removal step. Among these methods, inkjet printing is particularly attractive because of its potential simplicity, flexibility, low cost, and high rate. A review of inkjet printing for materials and device fabrication is provided by Calvert [7].

Ideally, inkjet printing of HTS precursor solutions involves the controlled delivery of precursor "ink" droplets to a substrate. The droplets are spherical in shape and uniform in volume. They travel along a

straight line to the substrate and spread over the substrate in a manner to form precursor filaments of controlled thickness and width. These filaments are then decomposed and converted to filamentary HTS film.

Practically, many factors during inkjet printing and processing contribute to the quality of the final filamentary HTS conductor. Drying of the solution at the ink dispenser orifice, wetting failure of the solution on the substrate during printing, and cracking of the precursor during decomposition are a few factors that can degrade the final conductor quality. Cracking of HTS precursors deposited by dip coating has been reported by several authors [8,9] and has been associated with a reduction of critical current for the resulting HTS films [9]. The conversion of precursor to HTS conductor, although rather well understood for nonfilamentary conductors [10,11], depends on geometry (e.g., width, thickness, and spacing) for filamentary conductors. These factors collectively may present a challenge to the success of an inkjet printing route to filamentary HTS conductor fabrication. The purpose of this paper is to demonstrate, by example, capabilities of inkjet printing using high-performance HTS precursor ink and substrate.

2.15.2 Experimental

Both the RABiTS™ substrates and the metal-organic YBCO precursor solutions used for this work were prepared at American Superconductor Corporation (AMSC). The substrates consisted of deformation-textured 75-μm-thick Ni-5at%W, on which were sequentially grown 75-nm-thick epitaxial layers of Y_2O_3, YSZ, and CeO_2. Substrates were cut to 1.0 × 3.0 cm and were printed with filaments that were generally parallel to the long dimension. AMSC's standard metal-organic precursor solution was modified for compatibility with the inkjet printing process.

Inkjet printing of the YBCO precursor was accomplished by using ~50-μm-diam droplets from a single, stationary, piezoelectric nozzle (MicroFab Technologies, Plano, Texas) operated at 0.5 to 2.0 kHz. A substrate was attached to an *x-y* stage equipped with 0.1-μm optical encoders and was translated beneath the stationary nozzle. The substrate motion and droplet delivery were synchronized so that filamentary precursor patterns could be printed at lines speeds of 1 to 10 cm/s. Standard drafting software was used to control stage motion, thus facilitating filamentary pattern generation.

Following printing, the precursor deposit was decomposed to remove volatiles and organic residue. This was accomplished in wet flowing oxygen at temperatures of 400°C and below. A compact furnace fitted with a flat quartz window was used for real-time microscopic observation of the precursor during decomposition so that the microstructural evolution of the filamentary precursor films could be better understood.

Conversion of the decomposed precursor to YBCO was conducted at reduced pressure in a system with an in situ X-ray diffraction capability [11]. Substrates were heated resistively in a mixture of argon, oxygen, and water at a total pressure of several Torr while the crystalline phase development of YBCO was followed. The converted YBCO samples were then sputter coated with a layer of silver (~1 μm thick) and oxygenated at 500°C for 1 h. Transport critical current was measured in liquid nitrogen (~77 K) and self-field by the standard four-probe technique with a voltage probe spacing of 1.0 cm and a 1-μV/cm criterion. A Sloan Dektak IIA stylus profilometer was used to determine the thicknesses of the precursor and the YBCO.

2.15.3 Results and Discussion

A potential advantage of inkjet printing when compared with methods commonly used to continuously deposit HTS solution precursor (e.g., slot-die and dip coating) is its flexibility. In principle with inkjet printing, wide ranges of filament thickness and width are accessible with accurate and precise control. To examine these ranges, several test patterns were printed. Figure 2.79 shows the filament profiles, after decomposition, for a series of 1.0-mm-wide parallel filaments of different thickness. Each filament consists of a series of parallel lines, and each line consists of a series of equally spaced, overlapping ~50-μm-diam droplets. Filaments of different thicknesses are achieved in this case by using

different densities of lines. The thickness of the decomposed precursor film is reduced during conversion by a factor of approximately 2.2, which is reflected in the scaling of the ordinate axes. For thicknesses less than 2.5 μm (~1.1-μm YBCO), decomposed filaments are smooth, crack-free, and uniform along their lengths. For thicker filaments, cracking is observed during decomposition and is evident in Fig. 2.79 as high-frequency roughness. The systematic variation of thickness across each filament generally observed in Fig. 2.79 (i.e., the left side of each filament is thicker than the right side) is believed to be due to the sequence by which ink lines were printed (i.e., leftmost lines were printed first) and dried.

Figure 2.80 shows the thickness profiles after decomposition for a series of nominally 2.2-μm-thick (~1 μm YBCO) parallel filaments of different widths. Filaments of different widths are achieved by using a fixed line density and a different number of lines per filament—ranging in this case from one to twelve. The actual widths of the filaments vary from 170 to 830 μm. All filaments are smooth, crack-free, and uniform along their length. The decrease in average filament thickness observed in Fig. 2.80 for narrower filaments is a consequence of asymmetrical line broadening during printing of multiple-line filaments. The outward spreading of ink that occurs at the edges of each filament has a greater effect on filament thickness for narrower filaments. Compensation for this effect for narrow filaments can be accomplished by increasing the droplet density along lines and increasing the density of lines for multiple-line filaments.

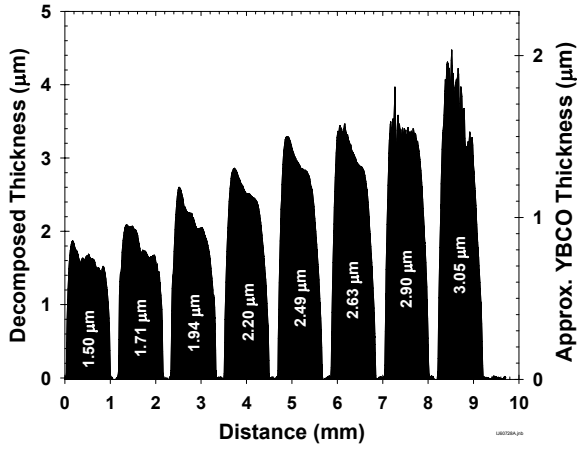

Fig. 2.79. Profilometer thickness after decomposition for eight precursor filaments of different thickness. The trace is perpendicular to the filament length. The average decomposed precursor filament thickness is listed for each filament. The high frequency roughness for the thickest three filaments is associated with microscopic precursor cracking.

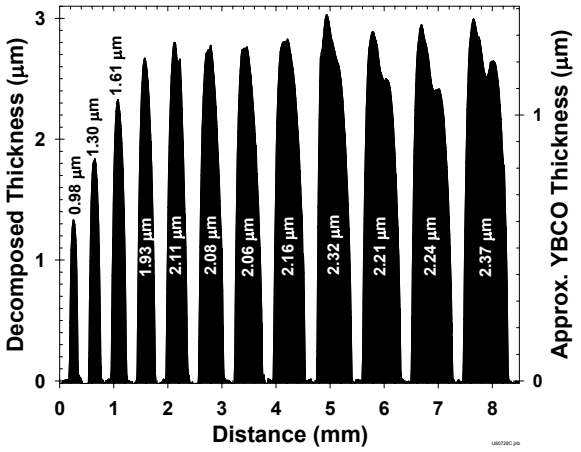

Fig. 2.80. Profilometer thickness after decomposition for twelve precursor filaments of different width. The trace is perpendicular to the filament length. The average decomposed precursor filament thickness is listed for each filament.

Following decomposition, the precursor is converted to YBCO. The conversion conditions for optimal YBCO performance depend on many factors, including precursor properties such as stoichiometry, thickness, and distribution. The use of inkjet printing facilitates systematic studies of the relationships between conversion conditions and precursor properties and offers an opportunity to better understand the mechanisms underlying conversion. Of particular interest in reducing ac losses in HTS coated conductors is the relationship between conversion and filament width because hysteretic ac losses scale linearly with filament width [1].

To examine the effects of filament widths on processing and properties, five filamentary precursor samples were prepared; the patterns used are shown in Fig. 2.81. Each sample consisted of an array of parallel filaments of equal width, thickness, and gap spacing between filaments. For all samples, the

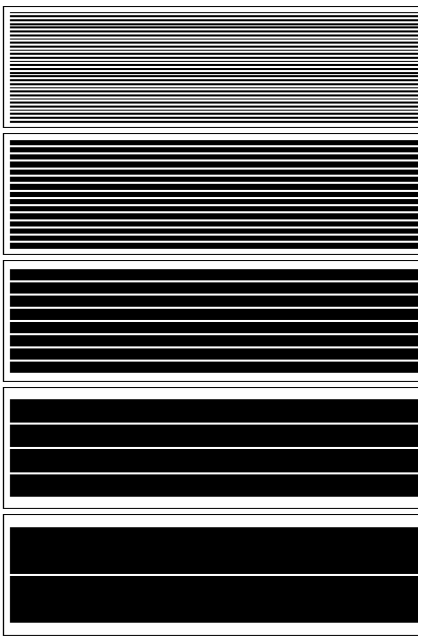

Fig. 2.81. Print patterns for five samples. The target YBCO thickness for all filaments is 1.0 μm and the target gap spacing is 100 μm. Top to bottom:

Filament width (mm)	Count
0.25	31
0.50	15
1.00	8
2.00	4
4.00	2

target YBCO filament thickness was 1.0 μm, and the target gap spacing was 100 μm. The target filament widths ranged from 250 μm to 4.0 mm. The actual average filament thicknesses and widths, determined with a profilometer after conversion, were within 10% of those targeted. Following printing and decomposition, all samples were individually converted in the in-situ X-ray diffraction system under conditions found suitable for 1-cm-wide, nonfilamentary, BaF_2-based evaporated precursor deposits [11]. No attempt was made to optimize the conversion conditions for the inkjet filamentary solution precursors.

The X-ray diffraction data collected during conversion are shown in Fig. 2.82. The intensities of the epitaxial YBCO(002) diffraction peaks are normalized to compensate for small differences in precursor print density for each sample. Several minutes after reaching the conversion temperature, the intensity of the YBCO(002) peak begins to develop for all samples and rises linearly with time until a knee is reached at 40 to 60 min, depending on the filament width. No X-ray intensity for randomly oriented YBCO(103) was detected in any of the five samples. The rate of intensity rise, expressed in angstroms per second, is shown in the inset of Fig. 2.82, where the maximum YBCO(002) intensity for a particular sample is assumed to be that for a fully converted 1-μm-thick YBCO film. Clearly, as seen from the data in the inset, the rate of precursor conversion depends on filament width; narrower filaments undergo more rapid conversion.

Following conversion, the critical current was measured for each of the five samples. Results are shown in Fig. 2.83. The widest filaments (4 mm) show a critical current of nearly 160 A/cm-width. As the filament width decreases, so does the critical current. Reduced critical current has been associated with the formation of microcracks for thick YBCO films prepared by solution precursor methods [9]. No evidence of such microcrack formation was observed for any of the five samples. Whether the trends observed in Figs. 2.82 and 2.83 hold generally for filamentary precursors or whether these trends apply only to a narrow set of processing conditions is the subject of further studies. Because of its high precision and accuracy, inkjet printing is well suited for studies of this type.

2.15.4 Conclusion

Inkjet printing of a standard HTS precursor solution has been demonstrated on a laboratory scale. Precursor filaments of technical interest for a range of widths and thicknesses have been deposited. Conditions for decomposition and conversion of precursor filaments have been identified that result in critical currents of nearly 160 A/cm-width. Based on this work, inkjet printing appears to be a powerful tool for both low-cost manufacturing of HTS coated conductors and fundamental studies of precursor processing.

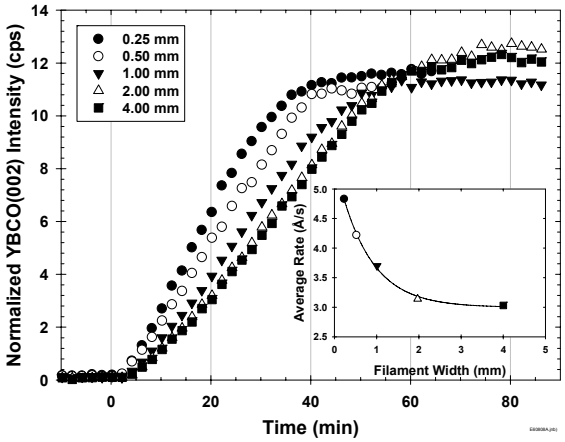

Fig. 2.82. YBCO(002) X-ray diffraction intensity during conversion for samples of different filament width. Inset: average YBCO conversion rate as a function of filament width. The line is a guide for the eye.

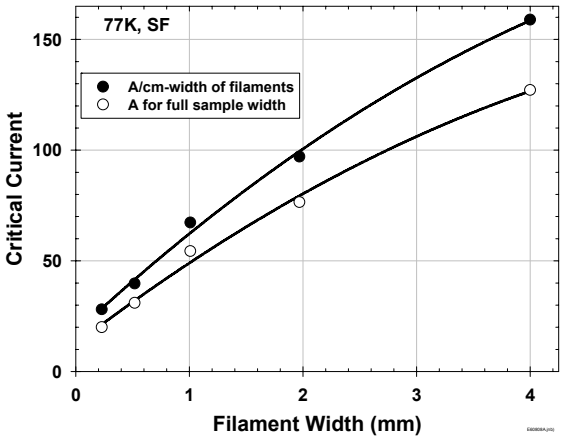

Fig. 2.83. Critical current as a function of filament width for the five converted samples (○). Data are also plotted normalized by the cumulative filament width (●). Lines are guides for the eye.

2.15.5 References

1. W. J. Carr, Jr., *AC Losses and Macroscopic Theory of Superconductors*, second ed., Taylor & Francis (2001).

2. M. D. Sumption, P. N. Barnes, and E. W. Collins, *IEEE Trans. Appl. Supercond.* **15** (2), 2815–18 (June 2005).

3. M. Majoros, et al., *IEEE Trans. Appl. Supercond.* **15** (2), 2819–22 (June 2005).

4. D. W. Hazelton, et al., pp. 859–68 in *Advances in Cryogenic Engineering—ICMC*, vol. 52, ed. U. Balachandra (2006).

5. S. P. Ashworth and F. Grilli, *Supercond. Sci. Technol.* **19**, 227–32 (2006).

6. P. Clem and J. Voigt, *Superconductivity for Electric Systems 2005 Annual Peer Review*. Online: http://www.energetics.com/supercon05.html.

7. P. Calvert, *Chem. Mater.* **13**, 3299–3305 (2001).

8. J. T. Dawley, et al., *IEEE Trans. Appl. Supercond.* **11** (1), 2873–76 (March 2001).

9. R. Teranishi, et al., *IEEE Trans. Appl. Supercond.* **15** (2), 2663–66 (June 2005).

10. V. F. Solovyov, H. J. Wiesmann, and M. Suenaga, *Supercond. Sci. Technol.* **18**, 239–48 (2005).

11. F. A. List, et al., *Physica C* **391**, 350–62 (2003).

2.16 High-Performance High-T_c Superconducting Wires via Incorporation of 1D Nanostructures

S. Kang, A. Goyal, J. Li, A. A. Gapud, P. M. Martin, L. Heatherly, J. R. Thompson, D. K. Christen, F. A. List, M. Paranthaman, and D. F. Lee

Second-generation high-temperature superconducting (2G HTS) wires based on $REBa_2Cu_3O_{7-\delta}$ (REBCO) films have significant potential for large-scale civilian and military applications. Many of these potential applications require large critical currents in high applied magnetic fields. For epitaxial HTS

films on textured substrates such as RABiTS™, the "inter-granular" critical current density is significantly improved due to the elimination of weakly linked, high-angle grain boundaries. However, for practical application of HTS materials, the in-field performance or the "intra-granular" critical current density also needs to be enhanced further. It is also essential to increase the overall current-carrying capacity of the coated conductors. The simplest approach is to increase the thickness of the superconductor. However, gradual deterioration of the critical current density occurs with increasing superconductor thickness. For films deposited by in situ techniques such as by pulsed laser deposition (PLD), as the superconducting layer becomes thicker, a "dead" layer (a layer that provides no contribution to the current-carrying ability) forms after a critical thickness of ~1.5 μm. Even when special techniques were used to eliminate the dead layer, the in-field current capacity of thick HTS films is still insufficient to meet the requirements of many applications. This problem can be resolved by improving the flux-pinning by introducing appropriate defects into the films.

It is known that defects within superconducting materials can pin the magnetic flux lines so that large currents can flow through the materials in the presence of high applied magnetic fields. However, in order for the defects to be effective in pinning the flux, their size, density, and geometry need to be appropriately controlled. To increase the density of defects for effective pinning, there have been extensive studies on introducing artificial pinning defects. Among these, linear defects have proved to be the most effective. We have previously reported on a promising approach that simulated the linear defect structures through the incorporation of periodic columnar defects composed of self-aligned nanodots and nanorods of $BaZrO_3$ (BZO) into the YBCO film, resulting in enhancement in the in-field transport critical current density. Similar in-field enhancements have also been partially reproduced in 0.25- to 0.3-μm-thick films on ion-beam-assisted-deposition (IBAD) substrates, indicating the general viability of this approach. However, in all of the previous studies, the films were relatively thin (0.2–0.3 μm), and it was not clear whether it would be possible to propagate such defects through the thickness of the significantly thicker films required to enable practical applications.

We report here large enhancements of critical currents and the engineering critical current density (J_E) in self-field as well as excellent retention of this current in high, applied magnetic fields by both increasing the thickness of the YBCO films and incorporating extended columnar defects composed of self-aligned nanodots of BZO during growth of PLD film on RABiTS™. Figure 2.84 shows field-dependent critical current vs applied field at 77 K with the magnetic field parallel to YBCO *c*-axis (*H*//*c*) for a 3.0-μm-thick YBCO + 2 vol. % BZO film on RABiTS™. The critical current decrease is only a factor of 4.3 at 1.5 tesla. The self-field critical current of this film was 389 A and the corresponding self-field critical current density was 1.3 MA/cm^2. The exponent α, in the relation $J_c \sim H^{-\alpha}$ was determined to be 0.34 for this sample; the typical value is 0.5 for pure YBCO films, indicating strong pinning for H//*c* for the BZO-doped film. The inset in Fig. 2.84 shows the angular dependence of critical current at 77 K and 1 tesla, with the field always in the maximum Lorentz force configuration. Part of the variation of critical current with field orientation or angle is expected due to the electronic mass anisotropy of YBCO. However, the dominant peak for *H*//*c* indicates that there is strong vortex pinning by defects correlated to the *c*-axis in this film.

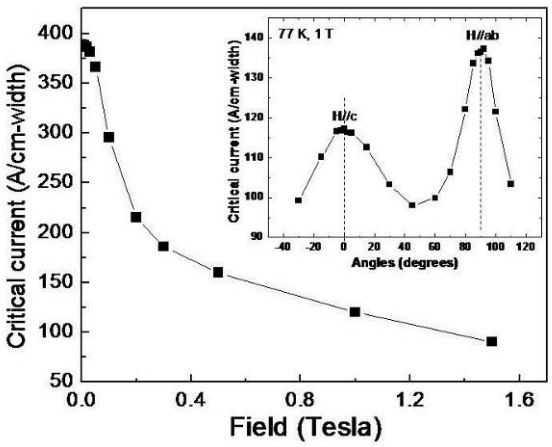

Fig. 2.84. Critical current vs applied magnetic field for a film of YBCO+2vol.%BZO grown epitaxially on RABiTS™. Inset shows the angular dependence of critical current at 77 K, 1 tesla.

In the cross-section TEM images (Fig. 2.85) of 3-μm-thick YBCO film grown epitaxially on RABiTS™ with the configuration Ni-3at%W (50 μm) / Y_2O_3 (65 nm) / YSZ (185 nm) / CeO_2 (30 nm),

extended columns of BZO nanodots can be seen aligned along the crystallographic *c*-axis of YBCO, the growth direction of the film. Similar to the 0.2-μm-thick YBCO films reported by us previously, self-aligned BZO nanodots were observed through the entire cross section of the 3-μm-thick YBCO film. Extended BZO nanodots were formed from the bottom of YBCO layer [Fig. 2.85(b)] to the top of the YBCO layer [Fig. 2.85(c)]. These self-aligned columns of BZO nanodots form to minimize energy or strain in the growing film stemming from the large lattice mismatch (~9%) between YBCO and BZO. Using high-resolution electron microscopy in plan view, we have previously shown that for 0.2-μm-thick films on RABiTS™, four misfit edge dislocations exist around each BZO nanodot. Subsequent nanodots align vertically, so that these misfit dislocations are also aligned, thereby minimizing the misfit strain in the film. These aligned misfit dislocations form ideal, extended flux-pinning centers. This periodic array of columnar defects is highly effective in pinning superconducting vortices or flux lines, thereby resulting in the significantly enhanced performance of the 2G wire in high applied magnetic fields, as shown in Figs. 2.86 and 2.87.

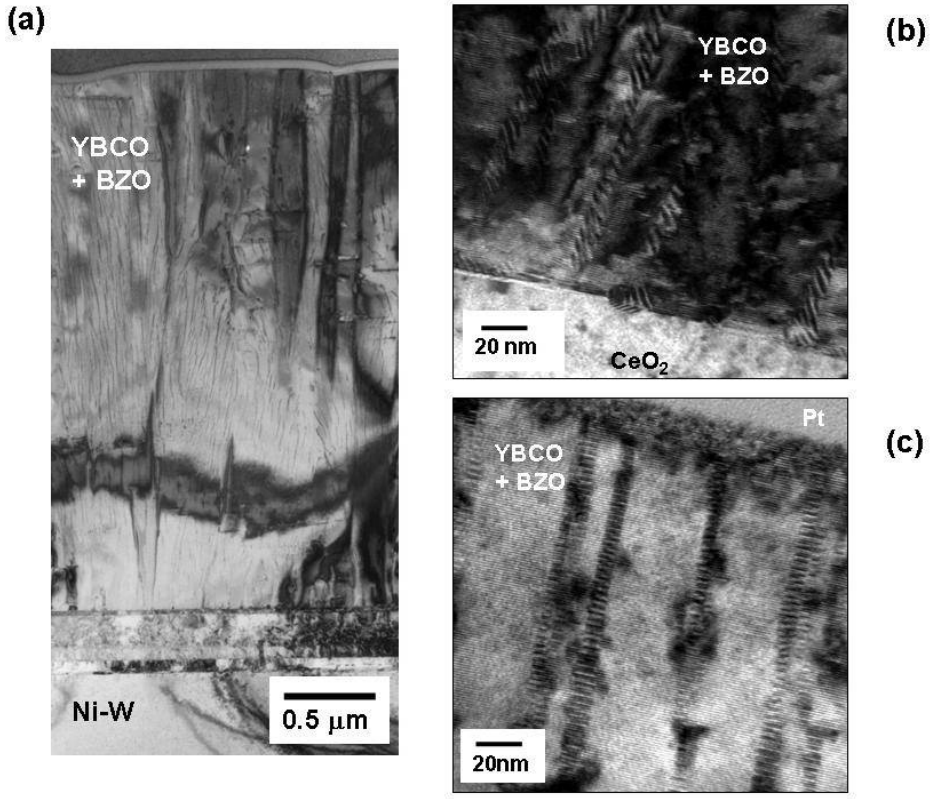

Fig. 2.85. Cross-section TEM micrographs for 3.0-μm-thick YBCO film with BZO nanodots grown epitaxially on RABiTS™. (a) An entire cross-section image shows that BZO nanodots aligned along the *c*-direction of YBCO. (b) Higher-magnification TEM image shows nucleation of BZO nanodots at the film/buffer interface. (c) Higher-magnification TEM image shows that the columns of self-aligned BZO nanodots extend to the top of the YBCO layer.

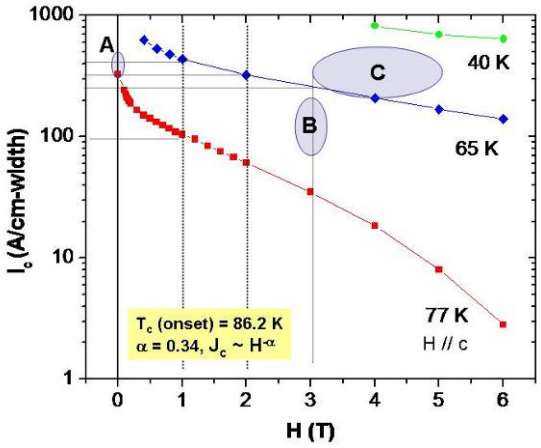

Fig. 2.86. Field-dependent critical currents at higher applied magnetic fields at three measurement temperatures (77, 65, and 40 K). Industry's minimum wire performance requirements for various applications are also shown.

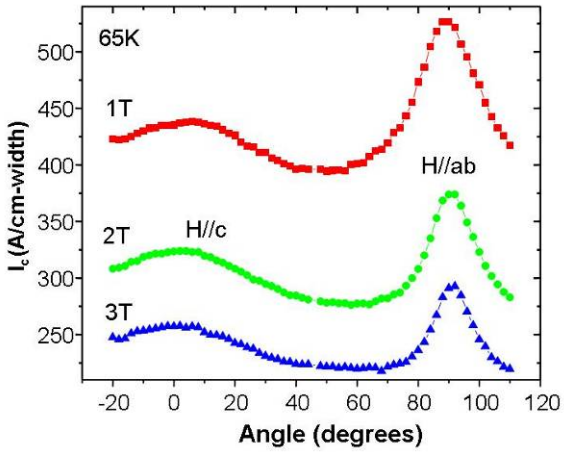

Fig. 2.87. Angular-dependent critical currents at 65 K with applied magnetic fields of 1, 2, and 3 tesla. At 65 K, 1 tesla, the current per unit width is ~400 A/cm for all angles or applied field orientation. At 65 K, 3 tesla, the current per unit width is greater than 200 A/cm for all angles or applied field orientation. At 65 K, 3 tesla, the calculated engineering current density is 40, 740 A/cm^2 without considering a stabilizer and 21, 154 A/cm^2 assuming a 50-µm-thick stabilizer at the angle corresponding to the lowest critical current.

Figure 2.86 shows I_c vs H for $H//c$, at higher fields and different temperatures (77, 65, and 40 K). The sample used for these measurements is the same BZO-doped sample for which data are shown in Fig. 2.84. Due to the limitations on the maximum measuring current, the 5-mm-wide sample was patterned into a 0.2-mm-wide bridge. The self-field critical current is somewhat reduced from that shown in Fig. 2.84 due to sample handling. Nevertheless, at 77 K and low field, the critical current is still over 300 A/cm-width, which is suitable for power cable applications. At 65 K and 3 tesla, the critical current is over ~250 A/cm-width, well above the threshold values of ~100 A/cm-width for military applications such as supermagnets for electric ship propulsion systems and magnetic energy storage. At 65 K and 3 tesla, the engineering current density for $H//c$ is 46 kA/cm^2. For practical applications, a stabilizer layer comprising a high electrical conductivity material such as Cu of about 50-µm thickness will be required to protect the superconductor in case of local loss of superconductivity. If one were to assume that a 50-µm-thick stabilizer layer will be deposited on top of the YBCO layer, the engineering current density for H//c is calculated to be 24.5 kA/cm^2, still well over the required 15 kA/cm^2. For large-scale rotating machinery such as motors and generators, an engineering current density of 20 to 30 kA/cm^2 in the operating temperature range of 55 to 65 K in applied fields of 3 to 5 tesla is required. The operating temperature range of 55 to 65 K is needed for widespread application as this is a temperature regime accessible by present cryocooler technology. Figure 2.86 shows that at 65 K, the engineering current density corresponds to 46, 37, and 33 kA/cm^2 without the stabilizer in applied fields of 3, 4, and 5 tesla, clearly above the range needed for application at 65 K. At lower temperatures, for example at 55 K, the engineering current density is expected to much higher than the values at 65 K. At 40 K, extrapolated critical current is over 1000 A/cm-width in applied fields of 3.5 tesla. Figure 2.87 shows the angular dependence of critical current at 65 K at applied magnetic fields of 1, 2, and 3 tesla. All the three angular-dependent critical current curves show similar features, indicating that similar pinning mechanisms are operational at these temperatures. At 65 K, 1 tesla, a critical current of ~ 400 A/cm-width for all field orientations was obtained. At 3 tesla, a critical current of ~200 A/cm-width for all field orientations was

obtained. The engineering current density at 65 K, 3 tesla, is calculated to be over ~40 kA/cm^2 at all applied field orientations without consideration of a stabilizer and 21 kA/cm^2, assuming a 50-μm-thick stabilizer, still well over the required 15 kA/cm^2 value.

In summary, we have successfully engineered defect structures within the HTS film and obtained transport properties exceeding the HTS industry's wire performance requirements for a range of applications: a critical current greater than 300 A/cm in self-field for underground transmission cables; a critical current greater than 100 A/cm and an engineering current density greater than 15,000 A/cm^2 at 65 K, 3 tesla, for military applications; and an engineering current density of 30 to 40 kA/cm^2 at 55 to 65 K, in operating fields of 3 to 5 tesla for rotating machinery such as motors and generators. This was made possible via incorporation of a periodic array of extended columnar defects, comprised of self-aligned nanodots of non-superconducting material, extending through the entire 3-μm thickness of the superconducting film. These columnar defects are highly effective in pinning the superconducting vortices or flux-lines, thereby resulting in the significantly enhanced properties. These results are of significant importance because they demonstrate the feasibility to fabricate HTS wires with adequate performance required to revolutionize the electric power industry as well as applications in the military, medicine, transportation, and high-energy physics.

2.17 High In-Field Critical Current Densities in Epitaxial $NdBa_2Cu_3O_{7-\delta}$ Films on RABiTS™ by Pulsed Laser Deposition

S. H. Wee, A. Goyal, P. M. Martin, and L. Heatherly

2.17.1 Introduction

Coated-conductor or second-generation HTS wires based on $REBa_2Cu_3O_{7-\delta}$ (RE = rare earth elements, REBCO) films grown on textured metallic substrates with oxide buffer layers are being considered for a number of electric power applications such as magnets, transmission cables, and motors. Compared with first-generation HTS wire (based on $Bi_2Sr_2Ca_2Cu_3O_{10+\delta}$), coated conductors based on REBCO-type materials have much better field dependence of critical current and critical current density [1]. However, further improvement of critical current and critical current density in high applied magnetic fields is still required for many large-scale practical HTS applications. Improving flux-pinning in REBCO films by increasing the density of defects is a preferred route for achieving this goal. Hence, there have been extensive studies on introducing artificial pinning defects such as columnar defects via heavy-ion irradiation [2], periodic array of submicron holes [3], substrate surface modification [4], and magnetic particles and/or nano-particles [5–7] in REBCO films. Recently, Kang et al. demonstrated fabrication of 3-μm-thick epitaxial $YBa_2Cu_3O_{7-\delta}$ (YBCO) films with columns of self-assembled nanodots of $BaZrO_3$ on RABiTS™ that meet or exceed performance requirements for most large-scale HTS applications [8].

Another mechanism for enhancement in pinning is via cation disorder. Research on melt-processed REBCO, in particular, with RE^{3+} ions of Nd, Eu, Sm, and Gd, has shown significant enhancements in flux-pinnng characteristics. Compared with bulk YBCO, such REBCO materials have exhibited higher critical current density in applied magnetic fields as well as higher superconducting transition temperatures (T_c = 92 ~ 96 K) [9]. These notable advantages in bulk, melt-processed REBCO have motivated efforts to grow high-quality REBCO films for use in coated conductors. Recently, Takahashi et al. reported that $GdBa_2Cu_3O_{7-\delta}$ (GdBCO) films grown on IBAD-$Gd_2Zr_2O_7$ buffer layered metallic substrates had better critical current density in magnetic field than YBCO films [10,11]. Similar enhancements of in-field critical current density have been also reported for $SmBa_2Cu_3O_{7-\delta}$, $(Dy,Ho)Ba_2Cu_3O_{7-\delta}$, and $(Nd,Eu,Gd)Ba_2Cu_3O_{7-\delta}$ films grown on various types of single-crystal substrates [12–14].

In this study, we have grown epitaxial $NdBa_2Cu_3O_{7-\delta}$ (NdBCO) films on RABiTS™ via pulsed laser deposition. Bulk NdBCO has higher transition temperature (T_c = 96 K) as well as higher in-field critical current density [9] and higher irreversibility fields (~13 tesla at 77 K) [15] than YBCO and other REBCO bulks. Hence, NdBCO films are also expected to have higher transition temperatures and critical current

densities in magnetic fields. However, there have been few reports on fabrication of high-critical-current-density NdBCO films with superior in-field properties. This paper demonstrates that, compared with YBCO films, epitaxial NdBCO films grown on RABiTS™ substrates have significantly improved in-field critical current density in high applied magnetic fields at all field orientations.

2.17.2 Experimental Procedure

Stoichiometric NdBCO powder was synthesized by using commercially available powders of Nd_2O_3, $BaCO_3$, and CuO with purities over 99.9 % via solid state synthesis at 880°C for 12 h in flowing air gas. The powders were then presintered at 1000°C for 12 h in flowing 1%O_2/Ar gas in order to prepare single phase NdBCO. The powder was then pressed and sintered at 1000°C for 6 h in flowing 1%O_2/Ar gas. NdBCO films were prepared on RABiTS™ with the configuration of Ni-3at.%W (50 μm)/Y_2O_3 (50 nm)/YSZ (200 nm)/CeO_2 (30 nm) via pulsed laser deposition using a XeCl laser (λ = 308 nm) at a repetition rate of 10 Hz. Laser energy density and substrate-to-target distance were 1.5 J/cm^2 and 6.5 cm, respectively. Films were grown at a substrate temperature, T_s, of 760°C in 1%O_2/Ar gas at a deposition pressure of 800 mTorr. After deposition, samples were annealed in situ at T_s = 500°C and P(O_2) = 500 Torr, and annealed ex situ at 450°C for 1 h in flowing O_2 gas after depositing sputtered Ag electrodes onto the films. Transport properties of the samples (0.5 cm × 2 cm) were measured using the standard four-probe method. Phase and textural analysis was done using X-ray diffraction. Film thickness was confirmed by cross-sectional transmission microscopy.

2.17.3 Results and Discussion

2.17.3.1 Expitaxial growth of high-critical-current-density NdBCO films on RABiTS™

Figure 2.88 shows θ-2θ X-ray diffraction patterns for NdBCO films grown on RABiTS™ at different substrate temperatures. All samples have a cube-on-cube, epitaxial relationship with the substrate and have strong out-of-plane *c*-axis orientation. While much of the film corresponds to NdBCO, small peaks related to phases of $NiWO_4$, NiO, and $BaCeO_3$ can also be seen. The secondary phases are attributed to oxidation of metal substrates and interface reaction between the CeO_2 layer and the NdBCO film during deposition. As the substrate temperature is increased from 740 to 820°C, the peaks for these secondary phases continue to be intensified linearly.

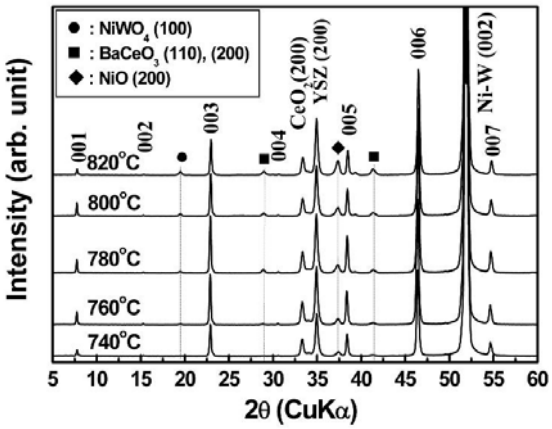

Fig. 2.88. The θ-2θ X-ray diffraction patterns for NdBCO films grown at various substrate temperatures.

Full-width-half-maximum (FWHM) of (113) φ-scan and (006) ω-scan, and the percentage cube texture in NdBCO films as a function of substrate temperature is shown in Fig. 2.89. Regardless of substrate temperature, FWHM of the (113) φ-scan and (006) ω-scan for all samples is more or less constant with values of ~ 7° and ~ 4°, respectively. Samples also have similar percentage cube texture of ~ 91 to 92%. Compared with values for epitaxial YBCO films grown on the same RABiTS™ [16], the values are similar and indicate that the films have good epitaxy.

Figure 2.90 shows the dependence of transport critical current density (at 77 K, self-field) for 0.13-μm-thick NdBCO films on the substrate temperature. With substrate temperatures increasing from 740 to 760°C, critical-current-density values increased from 2.4 to 3.4 MA/cm^2 and then decreased to 0.9 MA/cm^2 at 820°C. Thus, the highest critical current density (J_c = 3.4 MA/cm^2) is obtained from the sample deposited at 760°C, which is somewhat lower than the optimum substrate temperature for YBCO

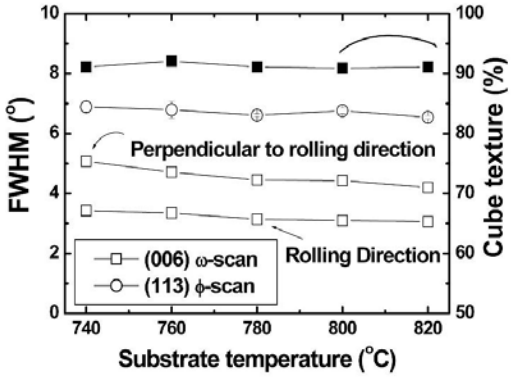

Fig. 2.89. FWHM of (113) φ-scan and (006) ω-can, the percentage of cube textures for NdBCO films grown at temperature range of 740 to ~ 820°C.

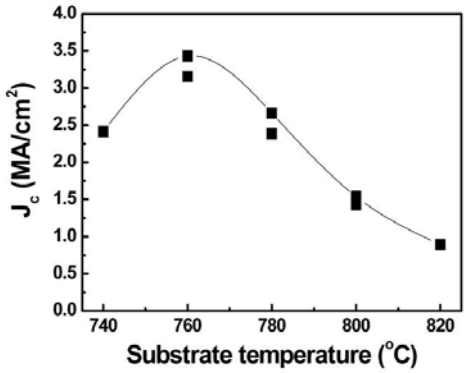

Fig. 2.90. A dependence of transport critical current density at 77 K and self-field for NdBCO films on substrate temperature.

films on same RABiTS™ (T_s = 790°C) [7,8,16]. As shown in Figs. 2.88 and 2.89, while the degree of texture does not correlate well with substrate temperature, the secondary phase content increases with rise in substrate temperature. Increased formation of reaction phases such as $BaCeO_3$ phase will lead to local decomposition of NdBCO and hence will reduce critical current density.

2.17.3.2 Critical current densities for NdBCO films in applied magnetic field

The dependence of critical current density on applied magnetic field (H) for NdBCO films with different thicknesses at 77 K and with the field applied parallel to c-axis ($H//c$) is shown in Fig. 2.91. For comparison, critical-current-density data for 0.2-μm-thick YBCO film grown on RABiTS™ is also shown. The critical current densities (77 K, self-field) for NdBCO films with thickness of 0.13 and 0.25 μm are 3.4, and 2.2 MA/cm^2, respectively. All the NdBCO samples, data for which is shown in Fig. 2.91, have much higher critical-current-density values in applied magnetic fields than those of 0.2-μm-thick YBCO film. The critical current densities for NdBCO samples with thicknesses from 0.13 to 0.25 μm at the specific field (1 tesla), are 0.46, 0.39, and 0.45 MA/cm^2, respectively, more than two times higher than the 0.19 MA/cm^2 for YBCO sample.

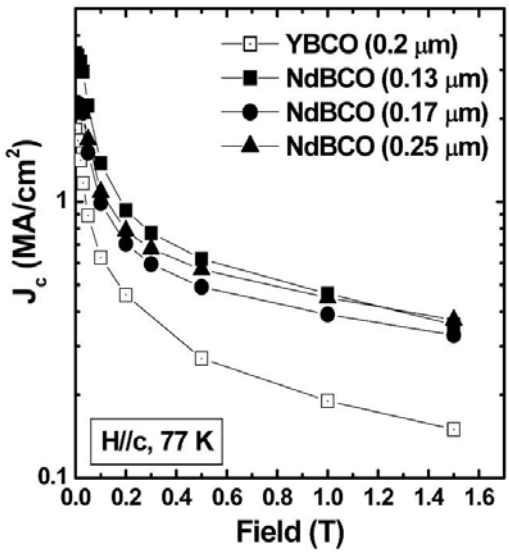

Fig. 2.91. Transport critical current density at 77 K for YBCO and NdBCO films in applied magnetic field parallel to the *c*-axis of the films.

Figure 2.92 shows a log-log plot of J_c/J_c(self-field) for YBCO and NdBCO films vs applied magnetic field. In all films, J_c vs H exhibits a plateau at the low magnetic fields followed by a power-law behavior of $J_c \sim H^{\alpha}$ at intermediate fields. Compared with 0.2-μm-thick YBCO film, NdBCO films with thicknesses from 0.13 to 0.25 μm have significantly weaker field dependence, suggesting the presence of the increased density of pinning centers. The exponent, α, for NdBCO films with thicknesses from 0.13 to 0.25 μm are ~ 0.49, ~ 0.43, and ~ 0.39, respectively, which are lower than α ~ 0.52 for 0.2-μm-thick YBCO film.

The angular dependence of critical current density for YBCO and NdBCO films at 77 K and 1 tesla is shown in Fig. 2.93. NdBCO films with thicknesses from 0.13 and 0.25 μm exhibit higher critical-current-density values for the entire angular range than a pure 0.2-μm-thick YBCO film with prominent peaks of critical current density at 0° (*H*//*c*), indicative of strong correlated pinning for *H*//*c*. Significant enhancements of the in-field critical current density for *H*//c have been observed in NdBCO single crystals wherein substitution of Nd^{3+} ions for Ba^{2+} sites, resulting in lower -transition-temperature regions thought to act as field-induced pinning centers [17].

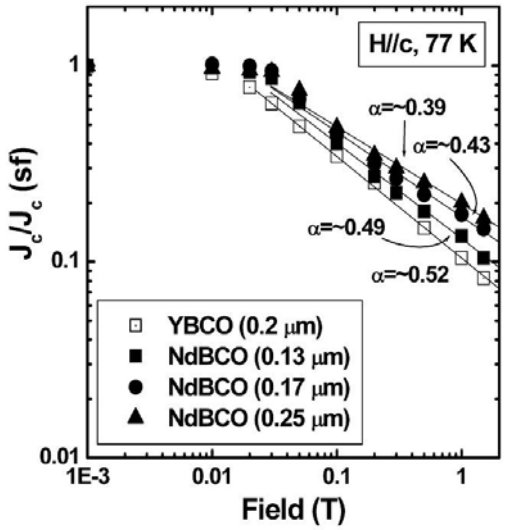

Fig. 2.92. Normalized critical current density, J_c/J_c (sf), at 77 K for YBCO and NdBCO films in applied magnetic field parallel to the *c*-axis of the films.

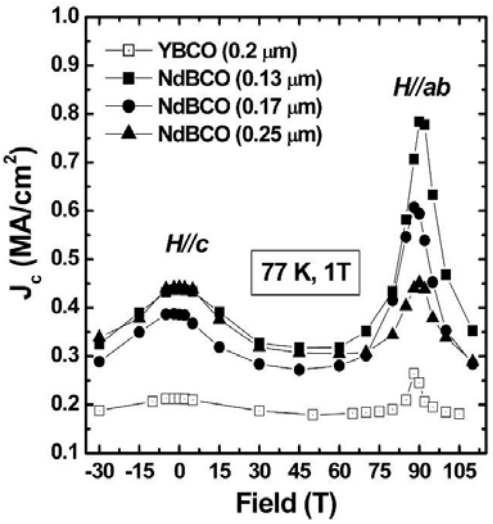

Fig. 2.93. The critical current density at 77 K and 1 tesla for YBCO and NdBCO films in a magnetic field applied from -30° to 110° to the *c*-axis of the films.

2.17.4 Conclusion

High-quality epitaxial NdBCO films were grown on RABiTS™ via pulsed laser deposition. All samples grown at deposition temperature between 740 to 820°C have good in-plane, out-of plane, and percentage cube texture, but widely different critical current densities at 77 K, self-field (ranging from 0.9 to 3.4 MA/cm^2). When the films were grown at optimum substrate temperature (760°C), the samples having different thicknesses of 0.13 to 0.25 μm exhibited high critical current densities at 77 K, self-field, of more than 2 MA/cm^2. Compared with YBCO film, the NdBCO films have higher in-field critical current density under applied field at all field directions and strong additional critical-current-density peaks along the field direction of *H*//*c*, which can be attributed to the presence of an increased density of *c*-axis–correlated pinning centers within NdBCO films.

2.17.5 References

1. J. L. MacManus-Driscoll, *Annu. Rev. Mater. Sci.* **28**, 421–462 (1998).

2. L. Civale, et al., *Phys. Rev. Lett.* **67**, 648 (1991).

3. A. Castellanos, R. Wördenweber, G. Ockenfuss, A. Hart, and K. Keck *Appl. Phys. Lett.* **71**, 962 (1997).

4. K. Matsumoto, et al., *Japan J. Appl. Phys.* **44**, L246 (2005).

5. T. Haugen, et al., *Nature* **430**, 867 (2004).

6. J. L. Macmanus- et al., *Nat. Mater.* **3**, 439 (2004).

7. A. Goyal et al., *Supercond. Sci. Technol.* **18**, 1533 (2005).

8. S. Kang et al., *Science* **311**, 1911 (2006).

9. M. Murakami, et al., *Supercond. Sci. Technol.* **9**, 1015 (1996).

10. K. Takahashi, et al., *Supercond. Sci. Technol.* **18**, 1118 (2005).

11. Y. Yamada, et al., *Appl. Phys. Lett.* **87**, 132502 (2005).

12. Y. Yoshida, et al., *IEEE Trans. Appl. Supercond.* **15**, 2727 (2005).

13. J. L. Macmanus-Driscoll et al., *Appl. Phys. Lett.* **84** 5329 (2004).

14. C. Cai, et al., *Appl. Phys. Lett.* **84**, 377 (2004).

15. T. Wolf, et al., *Phy. Rev. B* **56**, 6308 (1997).

16. S. Kang, et al., *J. Am. Ceram. Soc.* **88**, 2677 (2005).

17. T. Egi, et al., *Appl. Phys. Lett.* **67**, 2406 (1995).

2.18 Strong Flux-Pinning in Epitaxial $NdBa_2Cu_3O_{7-\delta}$ Films with Columnar Defects Composed of Self-Assembled Nanodots of $BaZrO_3$

S. H. Wee, A. Goyal, P. M. Martin, J. Li, M. Paranthaman, and L. Heatherly

$REBa_2Cu_3O_{7-\delta}$ (RE = rare earth elements, REBCO) melt-processed bulk materials have significantly higher critical current density in applied magnetic fields than bulk $YBa_2Cu_3O_{7-\delta}$ (YBCO) has, implying much improved flux-pinning [1]. REBCO materials also have a higher superconducting transition temperature (T_c = 92~96 K) [1]. Despite these apparent advantages, these compounds have not attracted much attention for use in coated conductors because of the difficulty in growing high-quality REBCO films. Recently, Takahashi et al. demonstrated that $GdBa_2Cu_3O_{7-\delta}$ (GdBCO) films grown on IBAD-$Gd_2Zr_2O_7$ buffer layered metallic substrates had better critical current densities in a magnetic field than YBCO films [2]. Similar enhancements of in-field critical current density was also reported for $SmBa_2Cu_3O_{7-\delta}$, $(Dy,Ho)Ba_2Cu_3O_{7-\delta}$, and $(Nd,Eu,Gd)Ba_2Cu_3O_{7-\delta}$ films grown on single crystal substrates [3–5].

To increase the density of defects for effective pinning, there have been extensive studies on introducing artificial pinning defects such as columnar defects via heavy-ion irradiation [6], periodic array of submicron holes [7], magnetic particles and/or nanoparticles [8,9] in YBCO. Among these, linear defects such as the columnar defects produced via heavy ion irradiation have proved to be the most effective. This approach, however, is not practical for scale-up as it is not only too expensive and because it can render the metallic substrate radioactive. A promising approach that simulated the defect structures formed by heavy-ion irradiation was the incorporation of periodic columnar defects composed of self-aligned nanodots and nanorods of $BaZrO_3$ (BZO) into the YBCO film [10,11], resulting in enhancement in the transport critical current density. Compared with YBCO films without the incorporation of self-assembled nanodots and nanorods, a factor of ~5 improvement in critical current density in the field range 0.4 to 1.5 tesla at 77 K and over a factor of 6 beyond 7 tesla were obtained. Similar results have also been attempted in 0.25- to 0.3-μm-thick films on ion-beam-assisted-deposition (IBAD) substrates [12], indicating the general viability of this approach. Yamada et al. incorporated self-assembled nanodots of BZO within GdBCO films. In contrast to the massive enhancements in flux-pinning observed for YBCO films with self-assembled nanodots of BZO, the enhancement observed by Yamada et al. was only in magnetic fields over 6 tesla [12].

In this paper, we have grown $NdBa_2Cu_3O_{7-\delta}$ (NdBCO) films with and without incorporation of self-assembled nanodots of BZO on Rolling-Assisted-Biaxially-Textured-Substrate (RABiTS™) samples.

Pure NdBCO films with a critical current density over 2 MA/cm^2 were grown on RABiTS™ by pulsed laser deposition. These NdBCO films were found to have improved critical current density in applied magnetic fields compared with YBCO films. Incorporation of columns of self-assembled nanodots of BZO within the NdBCO films was found to result in significantly improved critical current densities at all levels of applied field as well as in all field orientations. This study illustrates the combined effects of two different pinning mechanisms in enhancing the critical current density in applied magnetic fields.

Stochiometric NdBCO powder was synthesized by using commercially available powders of Nd_2O_3, $BaCO_3$ and CuO via solid-state synthesis at 880°C for 12 h in flowing air gas. The powders were then presintered at 1000°C for 12 h in flowing 1%O_2/Ar gas. NdBCO powder and 2 vol. % BZO nanopowder (commercially available from Sigma Aldrich Co.) plus NdBCO powder were pressed and sintered at 1000°C for 6 h in flowing 1%O_2/Ar gas. Both NdBCO films with and without incorporation of BZO nanoparticles were prepared on RABiTS™ with the configuration of Ni-3at.%W (50 μm) / Y_2O_3 (50 nm) / YSZ (200 nm) / CeO_2 (30 nm) via pulsed laser deposition with a XeCl laser (λ = 308 nm) at a repetition rate of 10 Hz. Laser energy density was 1.5 J/cm^2, and substrate-to-target distance was and 6.5 cm. Films were grown at a substrate temperature (T_s) of 760°C in 1%O_2/Ar gas at a deposition pressure of 800 mTorr. After deposition, samples were annealed in situ at T_s = 500°C and P(O_2) = 500 Torr, and annealed ex situ at 450°C for 1 h in flowing O_2 gas after depositing sputtered Ag electrodes onto the films. Transport properties of the samples (0.5 × 2 cm^2) were measured using the standard four-probe method. Phase and textural analysis was done using X-ray diffraction. Microstructural analysis was done by cross-section transmission electron microscopy (TEM).

Figure 2.94 shows θ-2θ X-ray diffraction patterns of NdBCO and BZO-doped NdBCO films. Both films have a cube-on-cube epitaxial relationship with the substrate and have strong out-of-plane *c*-axis orientation. While much of the film corresponds to NdBCO, small peaks related to phases of $NiWO_4$, NiO, and $BaCeO_3$ can also be seen. These secondary phases are caused by oxidation of metal substrates and interface reaction between CeO_2 layer and NdBCO film during the deposition at 760°C. Table 2.6 summarizes the transition temperature, the critical current density (at 77 K, self-filed), and the textures for 0.17-μm-thick NdBCO and BZO-added NdBCO films. The critical current densities at 77 K, self-field, for NdBCO and BZO-doped NdBCO films are 2.2 and 2.4 MA/cm^2, respectively. Both films also have a high transition temperature of 92 to ~ 93 K, measured in transport. Full-width-half-maximum (FWHM) of (113) φ-scan and (006) ω-scan for both samples are ~ 7° and ~ 5°, respectively. Compared with the textures of epitaxial YBCO films on the same RABiTS™ [13], these values are similar and indicate that both films have good in-plane and out-of plane textures.

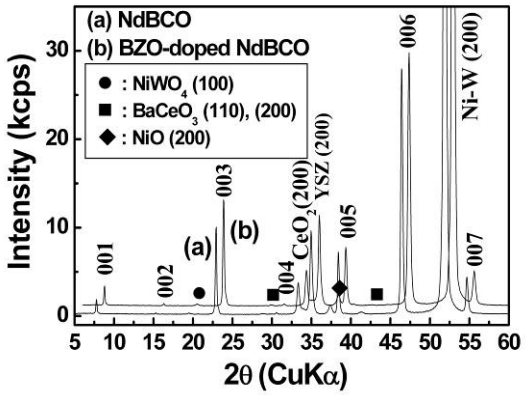

Fig. 2.94. The θ-2θ X-ray diffraction patterns for NdBCO and BZO-doped NdBCO films.

Table 2.6. Critical current density (77 K, self-field) and the textures for 0.17-μm-thick NdBCO and BZO-doped NdBCO films

	T_c (K)	J_c (MA/cm^2)	FWHM (°)		Percent cube (%)
			(006) ω-scan	(113) φ-scan	
NdBCO	93	2.2	3.91 (4.71)[a]	6.94	94.2
BZO-doped NdBCO	92	2.4	3.63 (4.88)[a]	7.2	94.3

[a]The scan direction is perpendicular to the rolling direction of RABiTS™. FWHM of ω-scan for this direction is usually larger than that for the rolling direction.

Superconducting transport properties of the 0.17-μm-thick NdBCO and BZO-doped NdBCO films in applied magnetic field are shown in Fig. 2.95. For comparison, critical current density data for 0.2-μm-thick YBCO film grown on RABiTS™ are also shown. Figure 2.95(a) shows the magnetic field (H) dependence of critical current density at 77 K with the field applied parallel to c-axis ($H//c$). The critical current densities for NdBCO and BZO-doped NdBCO films have significantly weaker field dependence than those of YBCO films. The BZO-doped NdBCO film exhibits lesser sensitivity to magnetic field than the NdBCO film, implying that incorporation of columns of self-aligned nanodots of BZO results in further improvement of flux pinning. When compared at the specific field of 1.5 tesla, the critical current densities for NdBCO and BZO-doped NdBCO samples are reduced by a factor of ~7 and 5, respectively; the critical current density dropped by a factor of ~12 for the YBCO sample. Figure 2.95(b) shows a log-log plot of J_c/J_c(sf), vs applied magnetic field. In all films, J_c vs H exhibits a plateau at the low magnetic fields followed by a power-law behavior of $J_c \sim H^{-\alpha}$ at intermediate fields. The values represented by the exponent α for NdBCO and BZO-doped NdBCO films are ~ 0.37 and ~ 0.43, respectively; both are lower than α ~ 0.52 for pure YBCO film.

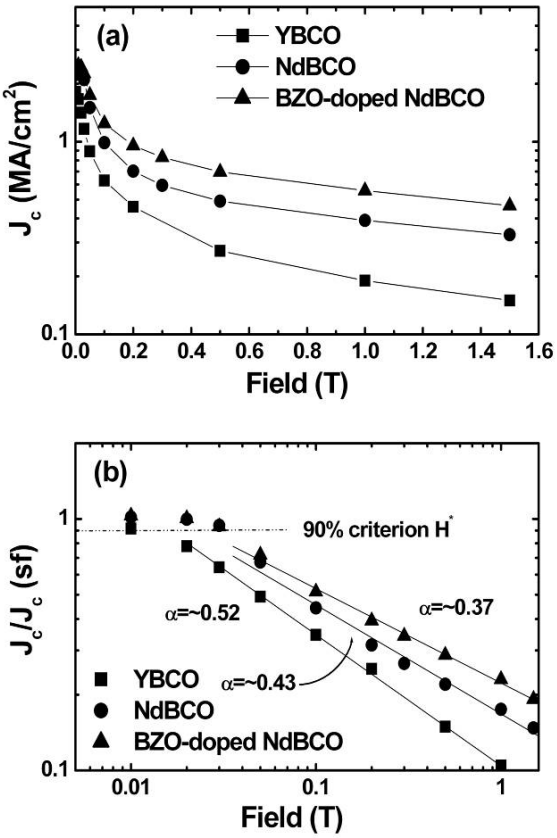

Fig. 2.95. Transport critical current density (a) and normalized critical current density (J_c/J_c, self-field), (b) at 77 K for YBCO, NdBCO, and BZO-doped NdBCO films, in an applied magnetic field parallel to the c-axis of the films.

Figure 2.96 shows the angular dependence of critical current density for YBCO, NdBCO, and BZO-doped NdBCO films at 77 K and 1 tesla. Both NdBCO films exhibit higher critical current density values at the whole angles than YBCO film with prominent peaks of critical current density at 0° ($H//c$), indicative of strong correlated pinning along the c-axis. Significant enhancements of the in-field critical current density for $H//c$ have been observed in NdBCO single crystals wherein Nd^{3+} ions substituted for Ba^{2+} sites, resulting in lower-transition temperature regions, have been speculated to act as field-induced pinning centers [14]. For BZO-doped NdBCO films, in addition, the peak of critical current density along the c-axis is observed to be much broader and higher than that for pure NdBCO film. Figure 2.97 is a cross-section TEM micrograph for 2 vol. % BZO-doped NdBCO film, showing columnar defects composed of self-assembled nanodots of BZO along the c-axis of the film, which have been previously observed in YBCO films, are resulting in the enhanced pinning over the pure NdBCO film.

In conclusion, high-critical-current-density NdBCO films were grown epitaxially on RABiTS™ with and without incorporation of columns of self-assembled nanodots of BZO. The results demonstrate that pure NdBCO film has significantly stronger pinning along both field directions of $H//c$ and $H//ab$ compared with YBCO film. Incorporation of columnar defects composed of self-assembled BZO nanodots into the NdBCO film further enhances flux pinning and results in additional gains in pinning in the entire angular range.

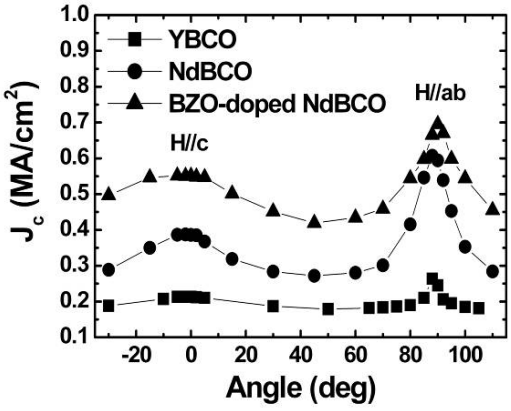

Fig. 2.96. Transport critical current density at 77 K and 1 tesla for YBCO, NdBCO, and BZO-doped NdBCO films, in a magnetic field applied from –30° to 110° to the *c*-axis of the films.

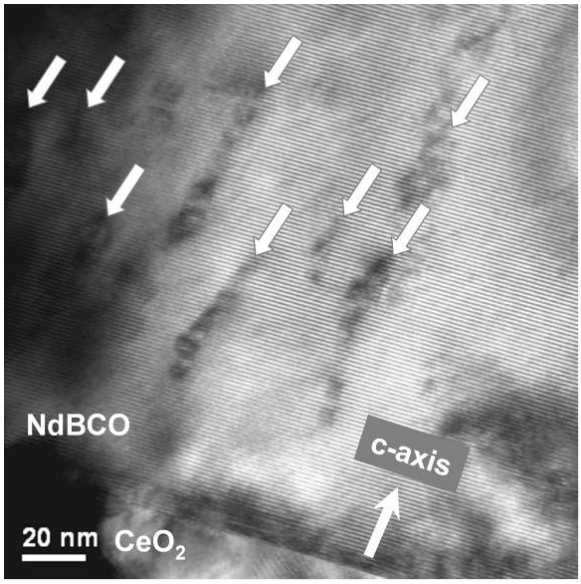

Fig. 2.97. Cross-section TEM image of a NdBCO film with self-aligned nanodots of BZO grown epitaxially on RABiTS™. Columns of BZO nanodots aligned along the [001] or the crystallographic *c*-axis of NdBCO are clearly seen in the films, as indicated by arrows.

2.18.1 References

1. M. Murakami, et al., *Supercond. Sci. Technol*. **9**, 1015 (1996)

2. K. Takahashi, et al., *Supercond. Sci. Technol.* **18** 1118 (2005).

3. Y. Yoshida, et al., *IEEE Trans. Appl. Supercond.* **15**, 2727 (2005).

4. J. L. Macmanus-Driscoll et al., *Appl. Phys. Lett.* **84**, 5329 (2004).

5. C. Cai, et al., *Appl. Phys. Lett.* **84**, 377 (2004).

6. L. Civale, et al., *Phys. Rev. Lett*. **67**, 648 (1991).

7. A. Castellanos, et al., *Appl. Phys. Lett.* **71**, 962 (1997).

8. T. Haugen, et al., *Nature* **430**, 867 (2004).

9. J. L. Macmanus-Driscoll, et al., *Nat. Mater.* **3**, 439 (2004).

10. A. Goyal et al., *Supercond. Sci. Technol.* **18**, 1533 (2005).

11. S. Kang et al., *Science* **311**, 1911 (2006).

12. Y. Yamada, et al., *Appl. Phys. Lett.* **87**, 132502 (2005).

13. S. Kang, et al., *J. Am. Ceram. Soc*. **88**, 2677 (2005).

14. T. Egi, et al., *Appl. Phys. Lett.* **67** 2406 (1995).

2.19 Enhancement of Flux Pinning in $YBa_2Cu_3O_{7-\delta}$ Thin Films Embedded with Epitaxially Grown Y_2O_3 Nanostructures using a Multilayering Process

A. A. Gapud (University of South Alabama); D. Kumar, S. K. V. Viswanathan, and J. Abiade (North Carolina A&T State University); C. Cantoni, M. Varela, S. J. Pennycook, and D. K. Christen (ORNL)

Previous methods that were used to controllably produce flux-pinning defects in HTS materials, such as heavy-ion irradiation, are not deemed viable for large-scale, long-length or "reel-to-reel" production of high-critical-current-density films. With the advent of nanostructure processing in recent years came more economical alternatives of modifying the film growth process to introduce nanostructures that perturb the crystal lattice. For films made by pulsed laser deposition (PLD), one may readily take advantage of island growth, which could be interrupted before a continuous layer is formed. Processing conditions can be fine-tuned to achieve the optimal level of nanoparticle density and size, analogous to optimizing irradiation-induced defects. One particular variant of this involves the deposition of alternating layers of YBCO and a nonreacting oxide that would grow epitaxially with it. This is done by switching targets periodically during the deposition, as demonstrated previously by Haugan and co-workers to introduce nano-disks of Y_2BaCuO_5 (211) into YBCO, which successfully enhanced critical current density over a wide range of field orientations.

Although nanodots of Y_2O_3 have been shown to induce additional pinning due to strain in the YBCO lattice, such strain could have detrimental effects on the YBCO; aside from the thickness dependence of critical current density, there is also a limitation placed on the thickness at which such films could be grown. In the study presented here we succeeded in producing more coherent growth between the two species so that any flux pinning would be induced only by the nanodots themselves. The result is an enhancement of the $J_c(B)$ by up to one order of magnitude in moderate magnetic fields B, and also in achieving a self-field J_c (10 K) > 80 MA/cm^2**.**

Laser ablation was done at the target of either YBCO or Y_2O_3, over a 1 × 4 mm^2 spot size from a 12 × 4 mm^2 aperture. For controlled studies, deposition was on single-crystal $SrTiO_3$ or $LaAlO_3$ substrates, which were heated in flowing O_2 gas and then cooled naturally in 500 Torr of O_2. The Y_2O_3 and YBCO targets were mounted on a carousel for switching, rastering, and rotating. Nominal film thicknesses used for the Y_2O_3 deposition were 0.5, 1, and 2 nm; each YBCO spacer layer was maintained at 10 nm. Electrical transport measurements of resistivity, critical temperature, T_c, and critical current density were conducted on two samples (samples III and IV), using a four-probe method in which pulsed currents were applied to minimize Joule heating from the contact resistance. The irreversibility line, H_{irr}, was determined as the field where the V(I) curve has a power of 2 in the vicinity of the 1-μV/cm criterion for critical current density; this corresponds to critical current density levels of ~ 10^3 A/cm^2. Magnetization measurements on samples I and II were conducted in a Quantum Design MPMS SQUID magnetometer, and the cross-section microstructure of sample II was analyzed using an aberration-corrected VG Microscopes HB501UX dedicated STEM. X-ray diffractometry was also performed on all four films to determine film crystallinity and to analyze the Y_2O_3 diffraction peaks.

STEM observations confirm that the Y_2O_3 has indeed grown in the form of nanodots. Figure 2.98(a) is a low-magnification image from sample II. The inset of Fig. 2.98(a) shows an electron diffraction pattern from that area. The YBCO (001) lattice vector has been highlighted with an arrow; the Y_2O_3 (002) reflection has been marked with a circle, showing that they are perfectly aligned with each other. Nanodots in the image have been indicated with arrows, and their size is variable, ranging between 3 and 10 nm.

Figure 2.98(b) shows a high-resolution Z-contrast STEM image of one such Y_2O_3 nanodot. The Y_2O_3 nanoparticles are crystalline and coherent with the YBCO matrix. Actually, the YBCO *c*-axis is parallel to the Y_2O_3 nanoparticle *c*-axis, while the (110) axis of Y_2O_3 lies parallel to the YBCO *a* or *b* directions. In Fig. 2.98(b), Y atomic planes in YBCO have been highlighted with white dotted lines, indicating that the interface runs parallel to the YBCO *ab*-plane and that it consists of a Y plane shared between both

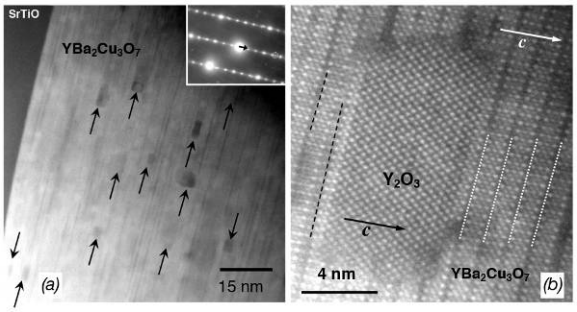

Fig. 2.98. Cross-section high-resolution STEM of multilayer film II. (a) Nanoparticles (indicated by arrows) are clearly discernible with sizes ranging from 3 to 10 nm and spaced about 5 to 20 nm apart. The dark fringes (marked by white lines) demarcate the YBCO unit cells (c = 11.7 Å); planar inclusions are marked by dashed black lines. Inset: Electron diffraction pattern of this area. The arrow shows the YBCO (001) reflection; the circle marks the (002) Y_2O_3 reflection. (b) High-resolution image of a Y_2O_3 nanoparticle coherent with the YBCO matrix.

materials. Furthermore, there is no discernible amorphization of either material; neither is there any obvious sign of strain fields in the YBCO lattice around the particles.

As independent confirmation and comparison with the unembedded nanodot dimensions, we calculated the particle size from X-ray diffraction (XRD) at wavelength λ using the Scherrer formula, $t = 0.9\lambda/(\Delta\theta\cos\theta_B)$, which relates $\Delta\theta$, the FWHM of the diffraction peak at $2\theta_B$, with the average size t of crystallites. To do this, we fabricated model systems comprising one layer of Y_2O_3 grown on a single YBCO layer that had been deposited on single crystal LAO. Such samples were grown with Y_2O_3 nominal thicknesses of 1 and 2 nm. We then measured the XRD intensity of the Y_2O_3 (200) peak. Applying the Scherrer equation yielded Y_2O_3 crystallite sizes of ~ 6 nm for both thicknesses. This result is consistent with the TEM results and strongly implies that Y_2O_3 content in this range makes little difference in the particle size, nor does the additional step of embedding the nanoparticles within the YBCO matrix.

Transport J_{cT} vs B at 77 K for samples III and IV, which had the thickest Y_2O_3 at 2 nm, are shown in Fig. 2.99. Also included are data for sample V, a pure YBCO film that was grown in the same chamber and under similar conditions. All samples had a slightly degraded critical temperature (T_c = 89 K), but no correlation with nominal Y_2O_3 thickness was found. The enhancement in $J_c(B)$ is quite significant, a factor of three for multilayers on LAO and a factor of five for multilayers on STO, at B = 5 tesla. Another clear indicator that flux pinning has been enhanced is the upward shift of the irreversibility field, H_{irr}, which increased from 5.6 to 6.8 and 7.4 tesla.

The dependence of J_{cT} on the orientation of the applied magnetic field gives additional insight as to the nature of the flux pinning. The lower inset of Fig. 2.99 shows the data for samples IV and V, at 77 K and 2 T. Both curves are very typical of random pinning; specifically, the absence of any "peak" for orientations about the direction of the *c*-axis clearly shows that there is no correlation or preferential direction for the pinning or, therefore, of the pinning defects themselves. This would be consistent with a homogeneous distribution of Y_2O_3 nanoinclusions. Therefore improvement in pinning is fairly isotropic and enhancement in J_{cT} occurs over a wide range of field orientations. (The result is similar for sample III.) One additional feature of note is that for both samples III and IV, the "peak" in the vicinity of the *a/b* axis orientation is significantly higher: J_{cT} (90°)/J_{cT} (0°) is about 3.0 for the multilayered sample; for the control sample this ratio is closer to 2.5. This would be consistent with the presence of planar defects, as marked in Fig. 2.98, most likely intergrowths of copper-rich Y-248 phase. An excess level of yttrium and/or yttrium oxide could have such an effect.

Another indicator of the flux pinning mechanism is in the power-law exponent α for the low-field regime (usually ~ 0.1 to 1 tesla at 77 K), where $J_c(B) \sim B^{-\alpha}$. For the pure YBCO film, α is about ½, which is typically observed for PLD growth. According to a model by Nelson and Vinokur, for fields above some "matching" field, α = 1/2 is consistent with flux lines shearing past pinned bundles, implying a relatively dilute distribution of extended pinning defects. This is consistent with the expected growth of linear defects as a consequence of island growth for films grown by laser ablation. (Note: while this may seem inconsistent with the results of field-orientation dependence of critical current density in the lower inset in Fig. 2.99, it should be pointed out that the latter was measured at 2 tesla, well above the power-law regime.) With the introduction of Y_2O_3 layers, the field sensitivity of J_{cT} is decreased noticeably: α is reduced to 0.30, which would be consistent with more efficient pinning. While there is a model by

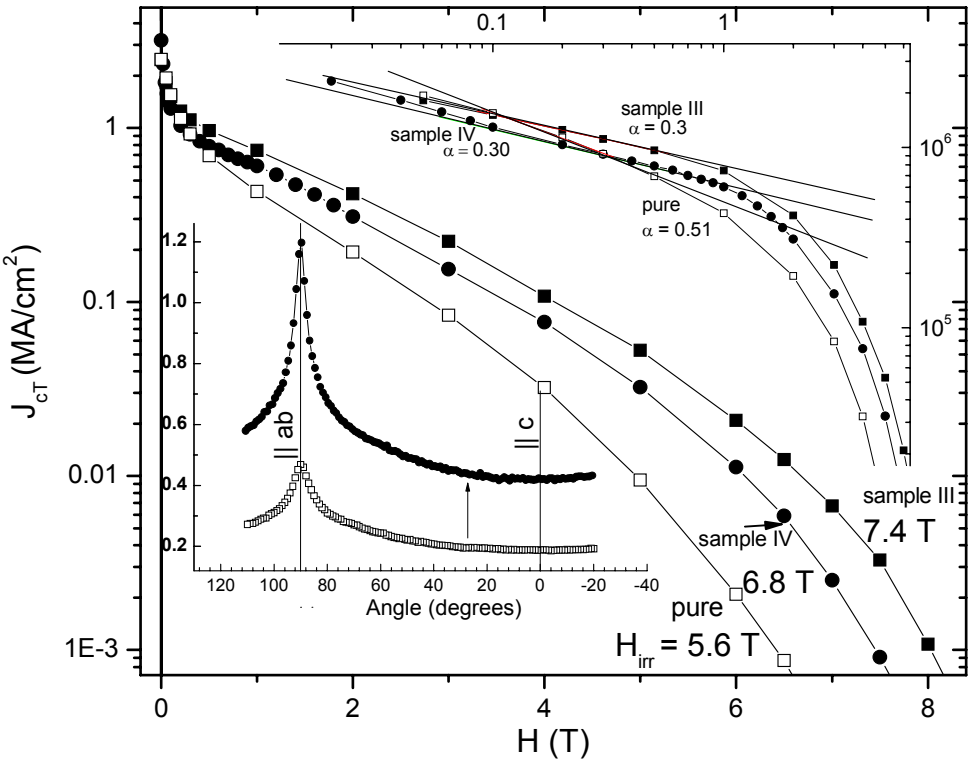

Fig. 2.99. Magnetic field dependence of transport critical current density, J_{cT}, at 77 K for *B* || c of multilayered film, YBCO/(Y2O3/YBCO) × 9. At B = 5 tesla, for sample IV and sample III, the critical current density is enhanced by a factor of at least three and five, respectively. For sample III, the irreversibility field increases by 32% from 5.6 to 7.4 tesla. Lower inset: dependence of J_{cT} on orientation angle of the field relative to the *c* direction (maximum Lorentz configuration) for sample IV, showing a uniform increase in J_{cT} over all angles measured. Upper inset: For the field regime where $J_c(B) \sim B^{-\alpha}$, in both cases α decreases 33%.

Ovchinnikov and Ivlev predicting α ~ 0.6 for the case of uncorrelated, strong but dilute pinning sites (and which was observed in a recent study involving nano-inclusions in ex situ grown YBCO film) there is as yet no reported model for α ~ 0.3, as far as we know. However, this low value of power-law exponent has been observed in other very strong-pinning systems comprising nanoprecipitates in YBCO.

There is even improvement at self-field, where the critical current density of sample III is increased from 2.5 to 3.4 MA/cm^2 for sample V. For sample IV on STO there is no enhancement, but the fact that the self-field critical current density was not degraded is noteworthy, considering that impurities had been added to the YBCO. Although at such very low flux densities in self-field the pinning may be sufficient to make any dissipative flux flow highly unlikely, the defects could also impede the percolative flow of supercurrent.

The transport current results are consistent with the magnetization critical current density, $J_{c,M}(B)$, measured at lower fields for samples I and II, which had the nominally thinner Y_2O_3 layers at 0.5 and 1 nm, respectively. The latter is clearly superior, as shown in Fig. 2.100. Included in Fig. 2.100 are data for a high-quality, pure sample (open circles). At temperatures down to 10 K, the multilayer samples have

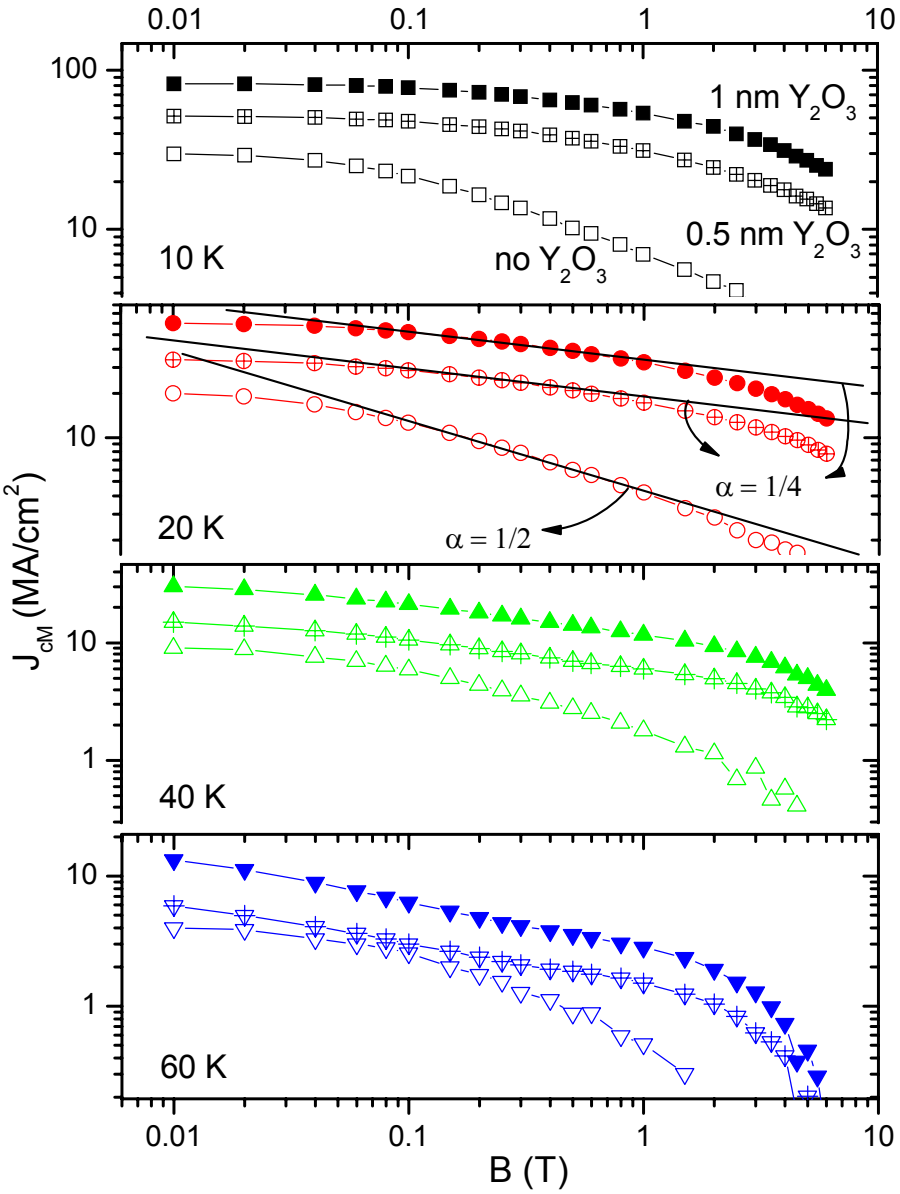

Fig. 2.100. Enhancement of magnetization $J_c(B)$ in multilayer films at four different temperatures. The addition of nominally 0.5-nm Y_2O_3 layers increases critical current density in moderate fields, *B,* by at least a factor of two, with greater improvement at lower temperatures. For the 1-nm Y_2O_3 layers, the enhancement is by at least another factor of two over the 0.5-nm case and as much as an order of magnitude over the pure films. Both multilayer films have a smaller linear-regime exponent α relative to the control sample, indicating a change in pinning mechanism. Between the two multilayer films, α is the same, implying no change in the pinning mechanism when the Y_2O_3 layer nominal thickness is doubled.

significantly higher J_{cM} in field, increasing by an order of magnitude for the sample with 1-nm Y_2O_3 layers at fields close to 1 tesla. At 10 K, the critical current density reaches a maximum of more than 80 MA/cm^2. Interestingly, the improvement is greater towards lower temperatures. In addition, when the Y_2O_3 nominal thickness is increased twofold in this case, the critical current density also increases about twofold, almost uniformly over the entire range of fields B. This result might be consistent if there were a twofold increase in the density of nanodots as result of twofold increase in the number of laser ablation pulses (all other parameters unchanged). The alternative possibility of an enhancement of pinning strength of each nanodot is less likely; the Scherrer equation showed little change in nanodot size with respect to number of laser shots of Y_2O_3.

As with the transport critical-current-density data of Fig. 2.99, the magnetization critical-current-density data are plotted on a log-log scale in order to visually analyze the regime where $J_c \sim B^{-\alpha}$, and the α values are consistent. The pure YBCO shows the value α ~ ½; for the multilayer films, α varies from 1/4 to 1/3 with temperature.

To summarize, using pulsed laser deposition in a multilayering scheme, we have inserted coherent crystallite Y_2O_3 nanodots within well-formed and nonstrained YBCO thin films on single-crystal substrates, resulting in as much as a tenfold increase in critical current density in applied magnetic fields, as well as in self-field, reaching a very high value of 81 MA/cm^2 at 10 K.

2.20 Substrate Surface Decoration with CeO_2 Nanoparticles: an Effective Method for Improving Flux Pinning in $YBa_2Cu_3O_{7-\delta}$ Films

T. Aytug, M. Paranthaman, A. A. Gapud, S. Kang, M. Varela, P. M. Martin, J. M. Raitano, S.-W. Chan, J. R. Thompson and D. K. Christen

2.20.1 Introduction

In response to progress in applying high-temperature superconductors (HTSs) to technological applications (i.e. motors, generators, transmission lines) there is a significant interest in reducing the falloff of intragrain critical current density with respect to magnetic field strength. Concurrently decreasing the anisotropic dependence of critical current density on the orientation of field is crucial because HTS wires (coated conductors) in power systems experience magnetic fields varying over a distribution of angles [1]. To solve these issues, introduction of strong flux pinning defects in HTS materials is important. Recent advances in nanostructure engineering have stimulated efforts to artificially introduce nanostructures as flux pinning defects in the crystal matrix of the HTS film. Among the approaches being used are multilayering of YBCO with second-phase materials [2–4], mixed rare-earth doping [5,6], compositional modifications, either by second phase $BaZrO_3$ (BZO) inclusions [7] or by addition of BZO and yttrium-stabilized zirconium particles [8,9], process-induced modifications with excess yttrium [10], and decoration of substrate surfaces by nano-scaled particles [11–15]. The decoration of the substrate surfaces presents several advantages over other methods. It is a simple technique for induced growth defects in HTS that is applicable to any substrate template, and it allows control of the geometry and number density of the nanoparticles prior to HTS film growth. Various nanoparticle species can be applied by virtually any deposition technique, including scalable physical vapor deposition (PVD) [14], a cost-effective wet chemical solution approach [15], and its derivative of suspension-based techniques.

In this paper, we demonstrate enhanced in-field critical current density performance and provide evidence of *c*-axis-correlated vortex pinning in YBCO films deposited on modified $SrTiO_3$ (STO) [100] substrates via preformed nanoparticles of CeO_2 [16].

2.20.2 Experimental

As an alternative to PVD and chemical solution routes [14,15], the substrate surfaces can also be decorated by preformed nanoparticles suspended in an organic solution. In this approach, CeO_2 nanoparticles were first coated with oleic acid and then dispersed in methanol and/or in an *n*-hexane

solution. Oleic acid serves as a surfactant to prevent agglomeration when the particles are suspended in an aqueous environment. The particles were then spin-coated onto the substrates followed by annealing at temperatures ranging from 600 to 700°C in order to burn out the organic compounds. Figure 2.101 shows a typical contact-mode atomic force microscopy (AFM) height image of CeO_2 nanoparticles prepared on STO substrates using the suspension-based approach. Particles of average diameter ~90 nm are observed to be randomly distributed over the substrate surface. To avoid the possible complication of "matching field, B_Φ" effects, we have used a low density of nanoparticles, similar to that in Fig. 2.101 (B_Φ = 0.017 tesla), for all of our studies. Despite the use of a surfactant, some level of agglomeration is evident from Fig. 2.101; the average size of the CeO_2 particles was 4 nm prior to dispersion into organic solution.

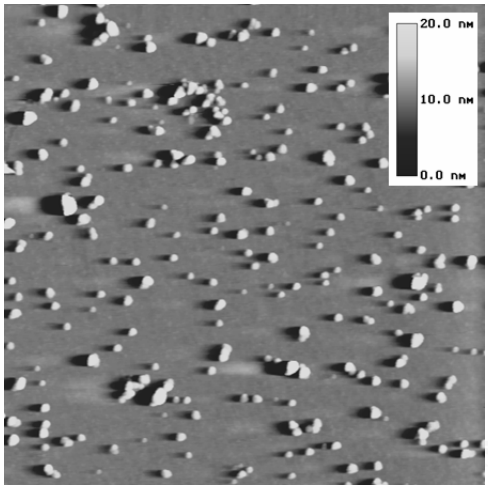

Fig. 2.101. AFM image of a $SrTiO_3$ substrate decorated with CeO_2 nanoparticles.

Subsequently, *c*-axis-oriented YBCO films of thickness 200 to 300 nm were grown on both modified and untreated control substrate surfaces by pulsed laser deposition, using a KrF excimer laser system operated at an energy density of ~ 4 J/cm^2. During deposition, the substrates were maintained at 780°C in 120 to 200 mTorr of O_2. After YBCO deposition, the samples were first cooled to 500°C at a rate of 5°C/min; then the O_2 pressure was increased to 550 Torr, and the samples cooled to room temperature at the same rate.

Microstructural examination of the samples was conducted using scanning transmission electron microscopy (STEM) in an dedicated, aberration-corrected STEM (VG Microscopes HB501UX). Both conventional TEM and high-resolution STEM imaging have been used for analysis of studied films. Transport superconducting property measurements at fields of up to 14 tesla were conducted using a conventional four-probe technique. A voltage criterion of 1 μV/cm was used to define critical current density. Angular dependence measurements were made at 77 K for fields up to 3 tesla, in the maximum Lorentz force configuration.

2.20.3 Results And Discussion

In this work, we show that decoration of STO surfaces with preformed CeO_2 nanoparticles qualitatively changed the YBCO flux pinning, compared with the control samples. This is unlike our previous studies of STO substrates decorated with PVD and/or solution-processed nanoparticles [14,15], where qualitative features were little changed. Here, our main goal is to present a comparative analysis of some key flux-pinning features in the samples. Figure 2.102 shows the angular dependence of critical current density at several fields for a typical YBCO film grown on CeO_2 treated substrate (PLD,

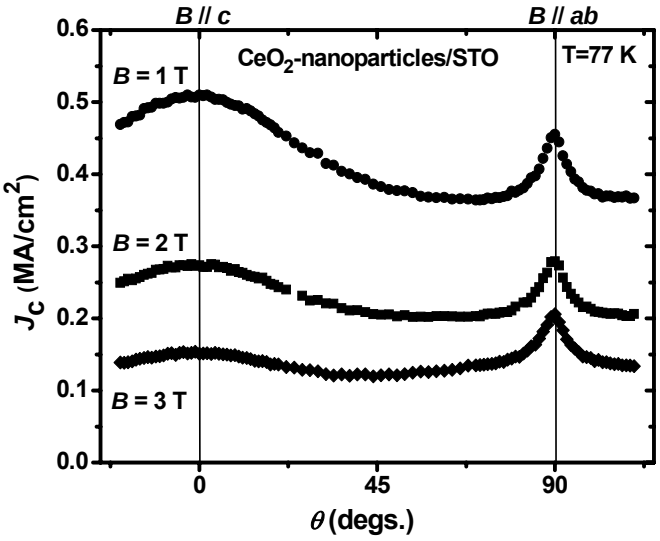

Fig. 2.102. Angular dependence of critical current density at several fields for a 0.3-μm-thick YBCO film on a CeO_2-modified $SrTiO_3$ substrate.

0.2 μm). Previous results obtained on Ir(PVD)- and MgO(solution)-modified STO had shown an improvement in isotropic pinning, along with enhancement of critical current density over wide range of field orientations. Here, at a given field, the critical current density exhibits a broad peak about the *c*-axis, indicative of correlated strong pinning defects aligned near that direction as well as a possible distribution of these defects over a wide angular range. Unlike the observations on PVD and solution treatments, in this case the anisotropic scaling approach [17] fails to fit the data. This is not surprising because the mass anisotropy model alone applies only to pinning from isotropic defects. Moreover, the relative shift in the magnitudes of critical current density for $B||c$ or $B||a$-b with increasing magnetic field is understandable, considering the direct dependence of pinning on the anisotropy of B/B_{irr}, where B_{irr} is the irreversibility field. That is, as B is increased toward B_{irr}, the decrease in the factor $J_c \propto (1-B/B_{irr})^2$ [18–21] is much more sensitive for $B||c$.

The enhanced *c*-axis pinning also implies an improved in-field critical current density performance. The transport J_c-B characteristics of the same sample is compared with that of a control YBCO film in Fig. 2.103 for $B||c$-axis, where the critical current density is normalized by the self-field $J_c(sf)$. Both samples have similar superconducting transition temperatures ($T_c \sim 88$ K).

In HTS materials, at intermediate fields, the critical current density falls off with commonly observed characteristics of a power-law behavior, $J_c(B) \propto B^{-\alpha}$. With the introduction of CeO_2 particles, YBCO film shows significant reduction in power-law exponent $\alpha \sim 0.3$ (compared with $\alpha \sim 0.5$ for control sample), indicating a weakened field dependence that is consistent with more effective *c*-axis correlated vortex pinning. Specifically, a factor of ~ 3 improvement in critical current density is achieved at $B = 1$ tesla at 77 K, and over a factor of five beyond 1.5 tesla. To date, there has been no proposed model mechanism to predict $\alpha = 0.3$. However, recently this low power-law exponent was observed in other nano-engineered superconductive systems with strong pinning [4,6–8].

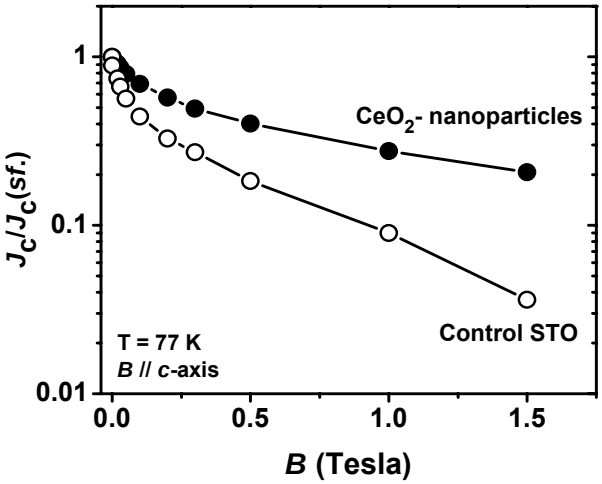

Fig. 2.103. Transport $J_c/J_c(sf)$, where $J_c(sf)$ is the critical current density at self-field, vs magnetic field for the same YBCO film presented in Fig. 2.102. The data are compared with a pure YBCO film on an as-received $SrTiO_3$ substrate. The self-field J_c (77K, $B||c$) values of the YBCO films on reference and CeO_2 modified substrates are 1.1 and 1.9 MA/cm^2; and at 1 tesla 0.1 and 0.52 MA/cm^2, respectively.

The STEM observation of the CeO_2-modified sample provides support for the presence of *c*-axis-aligned defect structures (correlated disorder) within the YBCO film (Fig. 2.104). While we have observed continuing presence of PVD and solution-processed nanoparticles at the YBCO/STO interface [14,15], in this case we could not identify CeO_2 nanoparticles on the substrate surface. Nevertheless, a large number of brighter contrast regions that originate from the interface can be identified as extended defects, possibly induced by the CeO_2 nanoparticles.

These defects are most likely extended strain fields from low-angle grain boundaries or threading dislocations. The formation of additional crystalline defects such as *a*-axis oriented grains in the YBCO can also give rise to the observed enhancement in critical current density for $B||c$-axis (see Fig. 2.103, inset). No *a*-axis growth is observed for films deposited on control samples. The results reported here are similar to the observations of Matsumoto et al. [12] and Nie et al [22], where no Y_2O_3 or CeO_2 nanoparticles were visible at the film-substrate interface after the YBCO deposition, but strongly enhanced pinning along the *c*-axis was obtained. Particularly, in the latter work, the absence of CeO_2 nanoparticles is attributed to reconstruction of YBCO-CeO_2 interface during the YBCO growth, which

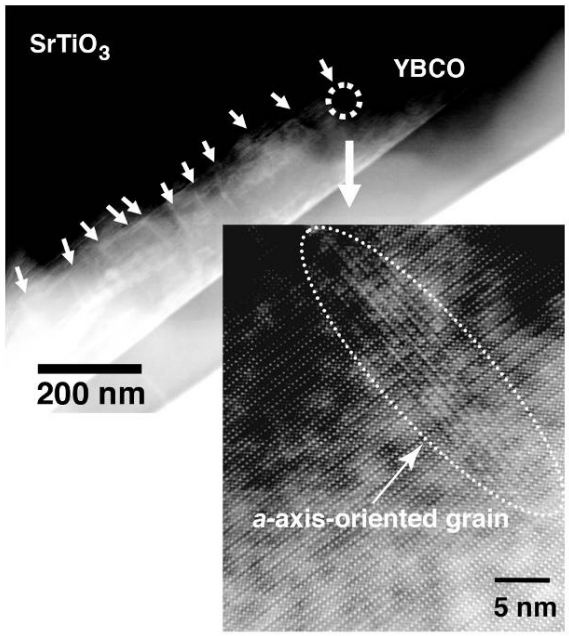

Fig. 2.104. Cross-sectional low-magnification Z-STEM image of YBCO/CeO_2 nanoparticles/$SrTiO_3$. Arrows indicate *c*-axis-aligned defects originating from the interface, possibly induced by the CeO_2 nanoparticles. Inset: High-resolution close-up view of the circled region, displaying growth of *a*-axis-oriented grains within the YBCO matrix.

resulted in a flatter interface. We believe that the main differences between the resulting flux pinning mechanisms reported here and in the case of PVD and solution-based processed nanoparticles arise from different growth mechanisms of YBCO. That is, in the latter two cases nanoparticles are grown epitaxial with respect to the substrate surface, whereas preformed particles could assume a variety of orientations. This suggests that while coherent growth of YBCO is possible over the nanoparticles processed with PVD and solution approaches, the crystal nucleation and the growth continuity of YBCO is expected to be disrupted on or about the random CeO_2 particle surface, leading to possible *c*-axis-aligned growth defects. Recently we have obtained similar results when this approach was extended to disperse nanoparticles on biaxially textured substrates. The data are not presented here; our aim is to minimize other contributions (e.g., substrate surface roughness, grain boundaries) and to assess the effects and understanding of flux pinning in YBCO films with preformed nanoparticle decorations on single crystal substrates.

The present results on single-crystal substrates point to the effectiveness of using suspended preformed nanoparticles to produce correlated defect structures. Yet, it would be very interesting to combine other pinning improvement techniques with surface nanoengineering to assess the possibility to further enhance the flux pinning in HTS films.

2.20.4 Summary

In summary, using nano-structure engineering we have demonstrated significant enhancement of flux pinning in YBCO films via pretreatment of substrate surfaces. A scalable and inexpensive technique of suspension-based preformed CeO_2 nanoparticles was applied on single-crystal (001) $SrTiO_3$ substrates prior to YBCO deposition. On modified substrates, YBCO films showed weaker field dependence than those deposited on untreated control samples. In addition, enhanced critical current density performance in magnetic fields oriented near the *c*-axis is another highlight of the present study.

2.20.5 References

1. M. W. Rupich, et al., *MRS Bulletin* **29** (8), 572 (2004).

2. T. Haugan, et al., *Nature* **430**, 867 (2004).

3. J. Hänisch, et al., *Appl. Phys. Lett*. **86**, 122508 (2005).

4. A. A. Gapud, et al., *Supercond. Sci. Technol*. **18**, 1502 (2005).

5. J. L. MacManus-Driscoll, et al., *Appl. Phys. Lett*. **84**, 5329 (2004).

6. C. Cai, B. Holzapfel, et al., *Appl. Phys. Lett*. **84**, 377 (2004).

7. J. L. MacManus-Driscoll, et al., *Nature* **3**, 439 (2004).

8. A. Goyal, et al., *Supercond. Sci. Technol*. **18**, 1533 (2005).

9. Y. Yamada, K. et al., *Appl. Phys. Lett*. **87**, 132502 (2005).

10. A. A. Gapud, et al., *IEEE Trans. Appl. Supercond*. **15**, 2578 (2005).

11. J. M. Huijbregtse, et al., *Phys. Rev. B* **62**, 1338 (2000).

12. K. Matsumoto, et al., *Jpn. J. Appl. Phys*. **44**, L246 (2005).

13. A. Crisan, et al., *Appl. Phys. Lett*. **79**, 4547 (2001).

14. T. Aytug, et al., *J. Appl. Phys*. **98** (11), 114309-114309-5 (2005).

15. T. Aytug, et al., "Analysis of flux pinning in $YBa_2Cu_3O_{7-\delta}$ films by nanoparticle-modified substrate surfaces," *Phys. Rev. B*, in press.

16. F. Zhang, et al., *J. Appl. Phys*. **95**, 4319 (2004).

17. G. Blatter, et al., *Rev. Mod. Phys*. **66**, 1125 (1994).

18. L. Civale, et al., *Phys Rev. B* **43**, 13732 (1991).

19. J. D. Hettinger, et al., *Phys. Rev. Lett*. **62**, 2044 (1989).

20. P. Fabbricatore, et al., *Phys Rev. B* **54**, 12543 (1996).

21. M. R. Koblischka and J. Sosnowski, et al., *Eur. Phys. J. B* **44**, 277 (2005).

22. J. C. Nie, et al., *Supercond. Sci. Technol.* **17**, 845 (2004).

3. Summary of Technology Partnership Activities

3.1 Background

ORNL is a key participant in DOE's national effort on HTS electric power applications. ORNL has formed effective teams that combine the resources of the Laboratory with the entrepreneurial drive of private companies. New technology partnership mechanisms, a feature of the ORNL Superconducting Technology Program for Electric Power Systems since its inception in 1988, have resulted in 42 superconductivity "pilot center" cooperative agreements and 17 cooperative research and development agreements (CRADAs). Ten cooperative agreements and two interagency agreements were active during FY 2006. In addition, licensing agreements, joint inventions, and joint publications with the private industry partners have ensured that there *is* technology transfer throughout the program.

Technology partnering on Laboratory-industry teams can occur in several ways. In the ORNL program, the cooperative development level of technology partnering is emphasized: joint Laboratory-industry teams work on problems that (1) require combined resources and expertise and (2) have a clear objective of precompetitive research and technology development. For the project to succeed, each partner depends on the success of the other. Most of the cooperative projects with private industry and the Laboratory precompetitive R&D projects involve developing key technology in which commercialization of the results is expected to occur after a minimum of 3 to 5 years.

3.2 Relationship to the DOE Mission

The ORNL program mission is that of its program sponsor, DOE's Office of Electricity Delivery and Energy Reliability Superconductivity Program: to develop the technology base necessary for industry to proceed to commercialization of electric energy applications of HTS. HTS will enable new energy-efficient motors, transformers, and transmission lines and will also provide electric power equipment manufacturers with strategic technology for global competitiveness. Electric utilities can defer acquisition of new transmission rights-of-way with successful introduction of superconducting cables. System stability and protection will be enhanced with the introduction of fault-current limiters. Distributed utility systems in the future, which will include distributed generation systems, will benefit from the small size and light weight of the next generation of electric power equipment. In addition, oil-free power transformers and cables will provide a cost-effective, more environmentally friendly option for the utility sector.

3.3 Funding

DOE funding for the ORNL program and a summary of funds-out cooperative agreements in FY 2006 are shown in Table 3.1. Funds-out to industry, universities, and other federal agencies (e.g., the National Institute of Standards and Technology) was more than $3 million in FY 2006.

3.4 Technology Partnership Approach

An interdisciplinary approach uses many of the resources available at ORNL to meet the program goals for joint Laboratory-industry development of HTS technology for electric power applications. The superconductivity agreement mechanism interlinks R&D projects with industry and universities that optimize utilization of facilities, expertise, and program resources for the benefit of all participants. This program also coordinates the ORNL activities with the other national laboratories, government agencies, university centers, and industry groups.

Cooperative agreements ensure that technology development is industry-driven. The ORNL Office of Technology Transfer and Economic Development and patent counsel work together to place these agreements. Where appropriate, these efforts are coordinated with projects within ORNL that are funded by the DOE Office of Science as well as Work for Others and ORNL Laboratory Director's R&D Fund projects.

Effective funds-out to industry is used to supplement industry cost share. In FY 2006, $3 million in funds-out to industry and universities was provided through cooperative agreements and subcontracts. To keep industry involved from the start of the program and to ensure commercialization potential, all of these technology-partnering mechanisms are augmented by CRADAs, user agreements, and licensing activities.

Responsiveness to American industry has high priority in this program. An ORNL ad hoc technical review committee, consisting of a project manager, a scientific coordinator, a manager for conductor development, and a manager for applications development, reviews all inquiries from industry and recommends projects for possible funding. This review ensures that (1) the proposed work fits the program mission, (2) the work is collaborative, (3) there is legitimate commercial interest, and (4) the work is feasible. Substantial private-sector cost share is required on cooperative agreements.

ORNL provides support to the DOE Headquarters (DOE-HQ) Superconductivity Program for Electric Power Systems by identifying, guiding, and monitoring R&D at ORNL and ORNL subcontractor sites and by performing coordination, analysis, and planning of activities related to the national program.

ORNL works with the other program laboratories to address such issues as communication among program participants, workshop and meeting implementation, planned competitive solicitations and superconductivity agreements, and coordination of technical and economic assessments. ORNL leads the Superconductivity Partnerships with Industry Technical Review Committee and manages the Cryogenics Initiative subcontracts on behalf of all the program stakeholders.

3.5 Program Inventions

A summary of the new invention disclosures for FY 2006 is shown in Table 3.2. Patents issued in FY 2006 are shown in Table 3.3, and all patents issued since 1995 are shown in Table 3.4.

Table 3.1. Superconductivity program summary of cooperative agreements as of September 30, 2006

Participant	Approved term	Type[a]	Total agreement cost share ($K)			Technology area
			By DOE		By industry	
			To ORNL	To industry		
American Superconductor	4/5/01–4/4/08	C	2,400	0	2,400	HTS conductors for electric power applications; Wire Development Group; and YBCO wires
American Superconductor	8/29/05–12/17/07	C(FI)	0	0	99	Low-cost fabrication of 2G wire for ac applications
General Electric Company	8/2/02–7/08	C	1,050	0	1,050	Design and development of a 100-MVA HTS generator
Metal Oxide Technologies	7/5/05–7/4/07	C	370	0	425	Develop HTS research targeted to power intensive commercial applications
NIST-Gaithersburg	12/1/00–12/31/07	IAG	0	1,290	1,290	YBCO phase diagram support
NIST-Boulder	3/98–2/29/07	IAG	0	1,747	1,747	Electromechanical properties for superconductor applications
Oxford Instruments	1/94–12/31/06	C	1,450	0	1,675	Develop technology for dip-coated BSCCO-2212 wire and RABiTS™
Reliance Electric Company	8/12/05–3/12/07	C	75	0	75	HTS Motor Coil Quench Model
Southwire Company	2/1/97–9/30/07	FO	12,066	500	12,631	Develop HTS cable technology
SuperPower, Inc.	10/8/02–9/30/08	C	870	0	500	Produce high current density YBCO coated conductors
SuperPower, Inc.	7/01/04–2/28/07	C	850	0	850	Matrix fault current limiter SPI
Waukesha Electric Systems	6/15/97–9/30/07	FO	3,197	250	2,556.4	HTS transformer
Total active agreements			22,328	3,787	25,668	
Total completed agreements			16,104	5,785.6	20,746.7	
Totals			38,432	9,573	46,415	

[a]FO = funds-out; FI = funds-in; IAG = interagency agreement; and C = CRADA.

Table 3.2. Invention disclosures during FY 2006

I.D. No.	Title	Inventor
1643	Methods to improve the texture of the buffer layers for YBCO coated conductors (CRADA)	M. Paranthaman, A. Goyal, M. W. Rupich, S. Sathyamurthy, T. Kodenkandath, X. Li
1669	New innovative oxide buffer with much improved texture	M. Paranthaman, M. S. Shuiyan
1689	High throughput buffer layers for IBAD-MgO templates without the homoepi MgO layers (CRADA)	M. Paranthaman, A. Goyal, T. Aytug, V. Selvamanickam, X. Xiong
1694	HTS conductor with controlled grain boundaries	A. Goyal
1695	Epitaxial devices on structural ceramic fibers	A. Goyal
1711	Nonmagnetic and mechanically strong, cube textured Ni-alloy for a range of applications	A. Goyal
1713	Novel multi-functional buffer for YBCO coated conductors	M. Paranthaman, T. Aytug

Table 3.3. Patents issued in FY 2006

Patent No. (ID No.)	Date issued	Title
6,956,012 B2 (889.1)	October 18, 2005	Method of Depositing an Electrically Conductive Oxide Buffer Layer on a Textured Substrate and Articles Formed Therefrom
0830218 European (1640-X)	May 24, 2006	Structures Having Enhanced Biaxial Texture and Method of Fabricating Same
7,087,113 (0963)	August 8, 2006	Textured Substrate Tape and Devices Thereof

Table 3.4. Cumulative listing of patents

Patent No. (ID No.)	Date issued	Title
		FY 1995
5,357,756 (1185-X)	October 25, 1994	Bipolar Pulse Field for Magnetic Refrigeration
5,395,821 (1039-X)	March 7, 1995	Method of Producing Pb-Stabilized Superconductor Precursors and Method of Producing Superconductor Articles Therefrom
		FY 1996
5,525,583 (1471-X) (with AMSC)	June 11, 1996	Superconducting Magnetic Coil
5,546,261	August 13, 1996	Hermetically Sealed Superconducting Magnet Motor
		FY 1997
5,646,097	July 8, 1997	Method of Fabricating a (1223) Tl-Ba-Ca-Cu-O Superconductor
		FY 1998
5,739,086 (1640-X)	April 14, 1998	Structures Having Enhanced Biaxial Texture and Method of Fabricating Same
5,741,377 (1640-X)	April 21, 1998	Structures Having Enhanced Biaxial Texture and Method of Fabricating Same
		FY 1999
5,830,828 (1193-X)	November 3, 1998	Process for Fabricating Continuous Lengths of Superconductor
5,846,912 (1512-X)	December 8, 1998	Method for Preparation of Textured $YBa_2Cu_3O_x$ Superconductor
5,898,020 (1640-X)	April 27, 1999	Structures having Enhanced Biaxial Texture and Method of Fabricating Same
5,958,599 (1640-X)	September 28, 1999	Structures Having Enhanced Biaxial Texture
		FY 2000
5,964,966	October 12, 1999	Method of Forming Biaxially Textured Alloy Substrates and Devices Thereon
5,968,877 (18-19)	October 19, 1999	High Tc YBCO Superconductor Deposited on Biaxially Textured Ni Substrate
5,972,847 (458)	October 26, 1999	Method for Making High-Critical-Current-Density $YBa_2Cu_3O_7$ Superconducting Layers on Metallic Substrates.
713892 Australia (1640-X)	March 30, 2000	Structures Having Enhanced Biaxial Texture and Method of Fabricating Same
6,055,446 (1193)	April 25, 2000	Continuous Lengths of Oxide Superconductors
6,077,344 (223)	June 20, 2000	Sol-Gel Deposition of Buffer Layers on Biaxially Textured Metal Substances
6,106,615 (368)	August 22, 2000	Method of Forming Biaxially Textured Alloy Substrates and Devices Thereon
6,114,287 (534) (HTSPC-023)	September 5, 2000	Method of Deforming a Biaxially Textured Buffer Layer on a Textured Metallic Substrate and Articles Therefrom

Table 3.4 (continued)

Patent No. (ID No.)	Date issued	Title
		FY 2001
6,150,034 (467)	November 21, 2000	Buffer Layers on Rolled Nickel, or Copper as Superconductor Substrates
6,156,376 (467)	December 5, 2000	Buffer Layers on Metal Surfaces having Biaxial Texture as Superconductor Substrates
6,159,610 (467)	December 12, 2000	Buffer Layers on Metal Surfaces having Biaxial Texture as Superconductor Substrates
6,180,570 B1 (312)	January 30, 2001	Biaxially Textured Articles Formed by Plastic Deformation
6,256,521 B1 (1784, new 148)	July 3, 2001	Preferentially Oriented, High Temperature Superconductors by Seeding and a Method for their Preparation
6,261,704 B1 (218)	July 17, 2001	MGO Buffer Layers on Rolled Nickel or Copper as Superconductor Substrates
6,270,908 B1 (734)	August 7, 2001	Rare Earth Zirconium Oxide Buffer Layers on Metal Substrates
6,286,194 B (1193)	September 11, 2001	Apparatus for Fabricating Continuous Lengths of Superconductor
		FY 2002
6,296,701 B1 (296)	October 2, 2001	Method of Depositing an Electrically Conductive Oxide Film on a Textured Metallic Substrate and Articles Formed Therefrom
6,331,199 B1	December 18, 2001	Biaxially Textured Articles Formed by Powder Metallurgy
6,375,768 B1 (312)	April 23, 2002	Method for Making Biaxially Textured Articles by Plastic Deformation
6,385,835 B1	May 14, 2002	Apparatus for Fabricating Continuous Lengths of Superconductor
6,399,154 B1 (734)	June 4, 2002	Laminate Article
6,440,211 B1 (649)	August 27, 2002	Method of Depositing Buffer Layers on Biaxially Textured Metal Substrates
6,447,714 B1 (316)	September 10, 2002	Method for Forming Biaxially Textured Articles by Powder Metallurgy
6,451,450 B1 (749)	September 17, 2002	Method of Depositing a Protective Layer over a Biaxially Textured Alloy Substrate and Composition Therefrom
		FY 2003
6,468,591 (218)	October 22, 2002	Method for making MgO buffer layers on rolled nickel or copper as superconductor substrates
6,486,100 B1	November 26, 2002	Method for Preparing Preferentially Oriented, High Temperature Superconductors Using Solution Reagents
6,555,256 B1	April 29, 2003	Method of Depositing an Electrically Conductive Oxide Film on a Textured Metallic Substrate and Articles Formed Therefrom
6,599,346 B2 (316.3)	July 29, 2003	Biaxially Textured Articles Formed by Powder Metallurgy
6,602,313 B2 (316.2)	August 5, 2003	Biaxially Textured Articles Formed by Powder Metallurgy
6,607,839 B2 (316.9)	August 19, 2003	Biaxially Textured Articles Formed by Powder Metallurgy
6,610,413 (316.5)	August 26, 2003	Biaxially Textured Articles Formed by Powder Metallurgy

Table 3.4 (continued)

Patent No. (ID No.)	Date issued	Title
6,610,414 (316.11)	August 26, 2003	Biaxially Textured Articles Formed by Powder Metallurgy
6,617,283 B2 (889)	September 9, 2003	Method of Depositing an Electrically Conductive Oxide Buffer Layer on a Textured Substrate and Articles Formed Therefrom
		FY 2004
6,635,097 B2 (316.4)	October 21, 2003	Biaxially Textured Articles Formed by Powder Metallurgy
6,645,313 B2 (1697-X)	November 11, 2003	Powder-in-Tube and Thick-Film Methods of Fabricating High Temperature Superconductors having Enhanced Biaxial Texture
6,663,976 B2 (649.2)	December 16, 2003	Laminate Articles on Biaxially Textured Metal Substrates
418279 Korea (1640-X)	January 30, 2004	Structures Having Enhanced Biaxial Texture and Method of Fabricating Same
6,700,297 B2	March 2, 2004	Superconducting PM Undiffused Machines with Stationary Superconducting Coils
6,716,795 B2 (726.2)	Apr. 6, 2004	Buffer Architecture for Biaxially Textured Structures and Method of Fabricating Same
6,740,421 B1 (1205)	May 25, 2004	Rolling Process for Producing Biaxially Textured Substrates
6,764,770 B2 (1047)	July 20, 2004	Buffer Layers and Articles for Electronic Devices
6,784,139 B1 (375)	August 31, 2004	Conductive and Robust Nitride Buffer Layers on Biaxially Textured Substrates
6,790,253 B2 (316.13)	September 14, 2004	Biaxially Textured Articles Formed by Powder Metallurgy
6,797,030 (316.12)	September 28, 2004	Biaxially Textured Articles Formed by Powder Metallurgy
		FY 2005
2 217 822 Canadian (1640-X)	November 23, 2004	Structures Having Enhanced Biaxial Texture and Method of Fabricating Same
6,846,344 B2 (316.07)	January 25, 2005	Biaxially Textured Articles Formed by Powder Metallurgy
03601830 Japan (1640-X)	October 1, 2004	Structures Having Enhanced Biaxial Texture and Method of Fabricating Same
6,890,369 B2 (316.6)	May 10, 2005	Biaxially Textured Articles Formed by Powder Metallurgy
6,902,600 B2	June 7, 2005	Biaxially Textured Articles Formed by Powder Metallurgy
		FY 2006
6,956,012 B2 (889.1)	October 18, 2005	Method of Depositing an Electrically Conductive Oxide Buffer Layer on a Textured Substrate and Articles Formed Therefrom
0830218 European (1640-X)	May 24, 2006	Structures Having Enhanced Biaxial Texture and Method of Fabricating Same
7,087113 (0963)	August 8, 2006	Textured Substrate Tape and Devices Thereof

4. Events, Honors, and Awards

4.1 ORNL Superconductivity Researcher Elected to the Board of Applied Superconductivity Conference, Inc.

Dr. David K. Christen, leader of the Superconductive and Energy Efficient Materials Group in the Materials Science and Technology Division (Fig. 4.1), has been elected to the Applied Superconductivity Conference Inc. Board—Materials section. Dr. Christen has been performing research on superconductivity for the past 32 years. His current interests include high-temperature superconductivity, epitaxial growth of films and coatings, flux-pinning mechanisms, and vortex dynamics as well as coated conductor development and technology

The Applied Superconductivity Conference (ASC) is one of the major superconductivity meetings in the world and has traditionally been attended by many researchers from academia, industry, and private and government research institutions. ASC is organized by the IEEE Council on Superconductivity, which promotes programs and activities that cover the science and technology of superconductivity and their applications. Peer-reviewed papers submitted to the conference are published in the *IEEE Transactions on Applied Superconductivity*.

Fig. 4.1. David K. Christen.

4.2 Two ORNL Superconductivity Researchers Elected as Directors of the Cryogenic Society of America

Dr. Michael J. Gouge and Dr. Jonathan A. Demko, of the Fusion Energy Division (Fig. 4.2), were elected to the board of directors of the Cryogenic Society of America on Aug. 30, 2006. Dr. Gouge will serve as a two-year director; Dr. Demko will serve as a four-year director. Dr. Gouge is leader of the Applied Superconductivity Group, where Dr. Demko is a group member. The Applied Superconductivity Group is presently involved with HTS cables, transformers, motors, and generators as well as quench and stability, ac loss, and other studies of HTS conductors and coils.

Fig. 4.2. Michael J. Gouge (left) and Jonathan A. Demko.

4.3 Superconducting Technology Wins First Nano 50 Award for ORNL

Nanotech Briefs® Nano50™

AWARDING THE BEST IN SMALL TECH

The innovative HTS wire technology entitled “HTS Wires Enabled via 3D Self-Assembly of Insulating Nanodots,” developed at ORNL, has been named a winner in the second annual *Nanotech Briefs*®’ Nano 50™ Awards in the “Technology” category.

Presented by *Nanotech Briefs* magazine, the monthly digital publication from the publishers of *NASA Tech Briefs*, the Nano 50 Award recognizes the top 50 technologies, products, and innovators that have significantly impacted, or are expected to impact, the state of the art in nanotechnology. The winners of the Nano 50 awards are the "best of the best"—the innovative people and designs that will move nanotechnology to key mainstream markets (Fig. 4.3).

The technology developed by ORNL researchers demonstrates a route to sustaining high supercurrents in wires in the presence of a large applied magnetic field, a step that could greatly expand practical applications of superconductors. An obstacle to many superconductor applications that operate in the presence of a magnetic field is the insufficient ability to "pin" the penetrating magnetic flux lines. A consequence of this lack of pinning is flux line motion, which dissipates energy and negates superconductivity. ORNL researchers have succeeded in incorporating a 3D array of self-assembled nanodots of insulating material through the entire thickness of the thick-film superconductor. These nanoscale defects effectively pin the flux lines and prevent their movement, enabling high supercurrents, even in the presence of high applied magnetic fields. In research sponsored by the DOE Office of Electricity Delivery and Energy Reliability, ORNL researchers are working with U.S. HTS wire manufacturers to introduce effective pinning nanodefects into their respective fabrication processes.

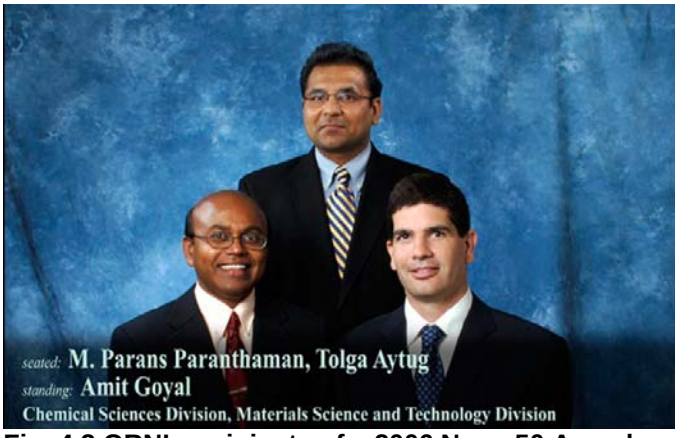

Fig. 4.3.ORNL recipients of a 2006 Nano 50 Award.

Nano 50 Awards are considered to be one of the most prestigious awards in the "nanoworld." The nominations were judged by a panel of nanotechnology and Micro-Electro-Mechanical Systems (MEMS) experts. The technologies, products, and innovators receiving the 50 highest scores were named Nano 50 Award winners. This is the first Nano 50 Award won by ORNL and is also the first awarded for a superconductor technology. The Nano 50 Awards will be presented at a special awards dinner to be held during the NASA Tech Briefs National Nano Engineering Conference in Boston, November 9 and 10, 2006.

4.4 Micrograph of Novel Nano-Dielectric Material Featured on Cover of *Nanotechnology*

An investigation on the dielectric properties and influence of particle size on breakdown strength of nanocomposite dielectrics was recently published in *Nanotechnology* (Enis Tuncer et al., *Nanotechnology* **18** (2), 2007, doi:10.1088/ 0957-4484/18/2/025703). Figure 4(c) in the paper was selected for the cover for *Nanotechnology* and the article will be featured in this issue (Fig. 4.4).

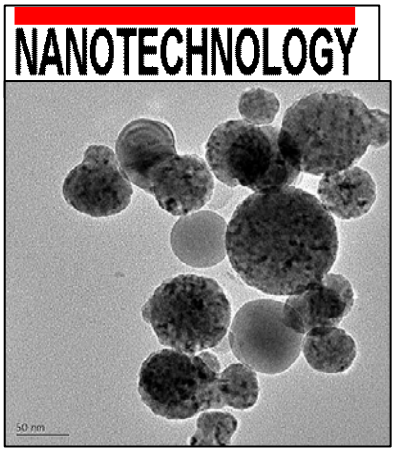

Fig. 4.4. ORNL image selected for the cover of *Nanotechnology*.

4.5 HTS Program Members Are Recipients of UT-Battelle/ORNL Awards Night Recognition

Parans Paranthaman, Amit Goyal, and Tolga Aytug were acknowledged at the 2006 Awards Night ceremony as recipients of the Science and Technology award for "Excellence in Technology Transfer." The award recognized their contributions for the development, patenting, and transfer of the high-throughput buffer layer technology being commercialized by SuperPower, Inc., that enabled the achievement of world record performance in SuperPower's long-length, second-generation superconducting wires.

Alvin R. Ellis, Isidor Sauers, Mark Roden, Jonathan A. Demko, Robert Duckworth, Christopher M. Rey, D. Randy James, and Michael J. Gouge, along with three employees of Southwire Company, were honored for accomplishments in "Engineering Research and Development" (see Fig. 4.5). The team was acknowledged for its achievements in the invention, development, design, fabrication, and successful testing of the world's most compact superconducting power cable.

Fig. 4.5. Superconductivity researchers recognized at the 2006 Awards Night for engineering R&D.

4.6 Amit Goyal, Distinguished Scientist in the Materials Science and Technology Division, Recognized for His Work

Rochester Distinguished Scholar Medal

In May 2006, Amit Goyal (Fig. 4.6) received the 2006 Rochester Distinguished Scholar Medal from the University of Rochester. Given by the university to graduates who have had distinguished careers, most often in academia, industry, or government. Over the years, fewer than 25 have been named Rochester Distinguished Scholars. This honor was bestowed upon Dr. Goyal at the 2006 annual commencement at the University of Rochester. The recipient addressed the graduating doctoral class during the annual commencement ceremony.

Fig. 4.6. Dr. Amit Goyal.

The University of Rochester (located in Rochester, N.Y.) is one of the nation's leading private universities. Founded in 1850, it consistently ranks among the top colleges and universities nationwide in federally financed science, engineering, medical, and other research. In the area of research productivity, the University ranks twelfth among leading private universities nationwide. Rochester faculty and alumni have included 8 Nobel Prize winners and 12 Pulitzer Prize winners. Rochester is a leading user and charter member in the University Research Association, which manages Fermilab, the world's highest-energy accelerator, in Batavia, Illinois.

Global Indus Technovator and ASM-IIM Lectureship Awards

Amit Goyal is one of ten recipients of the Global Indus Technovator Award for 2005. The Global Indus Technovator Awards were instituted to recognize and felicitate distinguished innovators of Indus origin (countries in southeast Asia) working at the cutting-edge of technology that may be harnessed for

far-reaching applications. The goals of the award are to recognize and encourage the innovative and creative spirit of people of Indus origin worldwide and to identify role models for South Asian youth around the world. The award ceremony was held in January 2006 at the Massachusetts Institute of Technology in Boston. The award recipients were selected by a panel of distinguished judges from more than 100 nominations from around the world for innovative work at the forefront of biotechnology, healthcare, materials and devices, information technology, and grassroots technology.

Goyal also won a2006 ASM-IIM Lectureship Award. ASM-IIM (American Society of Metals - Indian Institute of Metals) Visiting Lecturers are ambassadors-at-large for ASM International to the materials community in India. The ASM-IIM visiting lectureship program, established in 1979, is intended to promote international cooperation between ASM International and the materials community in India.

Inventor-of-the-Year Recognition and Battelle Stars Award

Amit Goyal received the Inventor-of-the-Year Award at the UT-Battelle Awards Night, held on December 9, 2005. The citation for his award reads "For establishing an intellectual property portfolio that has resulted in ORNL's world-wide dominance in high temperature superconducting wire fabrication." Amit recently became the first inventor at ORNL to receive 50 patents (46 U.S. patents and 4 European patents), surpassing all past and present employees of ORNL in the number of issued patents.

Dr. Goyal also received the 2006 Battelle Stars Award from Battelle Memorial Institute, Columbus, Ohio, for his prolific number of inventions. He was recognized as the ORNL inventor of the year on April 28, 2006, at the 2006 Battelle Annual Recognition and Reward Banquet in Columbus, Ohio.

4.7 Mariappan Parans Paranthaman, Senior Scientist in the Chemical Sciences Division, Receives "Outstanding Mentor" Award

Parans Paranthaman was named "Outstanding Mentor" for 2006 (Fig. 4.7). His involvement with interns was perhaps be best summed up by the recollection of one of his protégés: "As most people can gather after meeting him or seeing his face on the outstanding inventor's wall, he is one of the nicest and most dedicated people I have met. What makes him even more 'outstanding' was the way he approached my internship. He gave me my own personal and tailored research project on the forefront of his own research, so by the end I was not coming up to other people with my samples and asking them what to do next. I made my own decisions and received positive results. I was working on samples and procedures that no one in the world had done before. He gave me responsibility, knowledge, and a helping hand this summer. These three things aided in the overall transition I made from a student researcher to something close to a scientist."

Fig. 4.7. The Outstanding Mentor Award.

4.8 Parans Paranthaman Publishes "Superconductor Wires" Article in the 2006 *McGraw-Hill Yearbook of Science & Technology*

Parans Paranthaman (Fig. 4.8) was invited by McGraw-Hill to write an article on Superconductor Wires. It was published in the *McGraw-Hill 2006 Yearbook of Science and Technology* (pages 319–22). The article provides the present status of second-generation superconductor wire research and applications. The yearbook provides a broad overview of important recent developments in science, technology, and engineering as selected by a board of distinguished consulting editors. Each contribution is a concise article by one or more authorities in the field. Librarians, students, teachers, the scientific community, journalists and writers, and the general reader continue to find in the *McGraw-Hill Yearbook of Science and Technology* the information they need to follow the rapid pace of advances in science and technology and to understand the developments in these fields that will shape the world of the twenty-first century.

Fig. 4.8. Parans Paranthaman.

4.9 2006 Summer Intern Program

The ORNL Superconductivity Program hosted six summer interns in FY 2006 (see Table 4.1 and Figs. 4.9–4.13).

Table 4.1. Superconductivity program 2006 summer interns

Name/school	Program	Mentor
James Robert Davis Tuscola High School Waynesville, N.C.	Laboratory Science Teacher Professional Development	M. Paranthaman
Albert A. Gapud University of South Alabama	Faculty and Student Teams Program	D. K. Christen
Jonathan Daniel Hebert University of South Alabama	Faculty and Student Teams Program	D. K. Christen
Ali Moradmand University of South Alabama	Faculty and Student Teams Program	D. K. Christen
Megan Nicole Mallette Valparaiso University	Science Undergraduate Laboratory Internship	C. M. Rey
Benjamin James Taylor Tennessee Technological University	Science Undergraduate Laboratory Internship	M. Paranthaman

Fig. 4.9. James R. Davis (Teacher, Tuscola High School, Waynesville, N.C.)

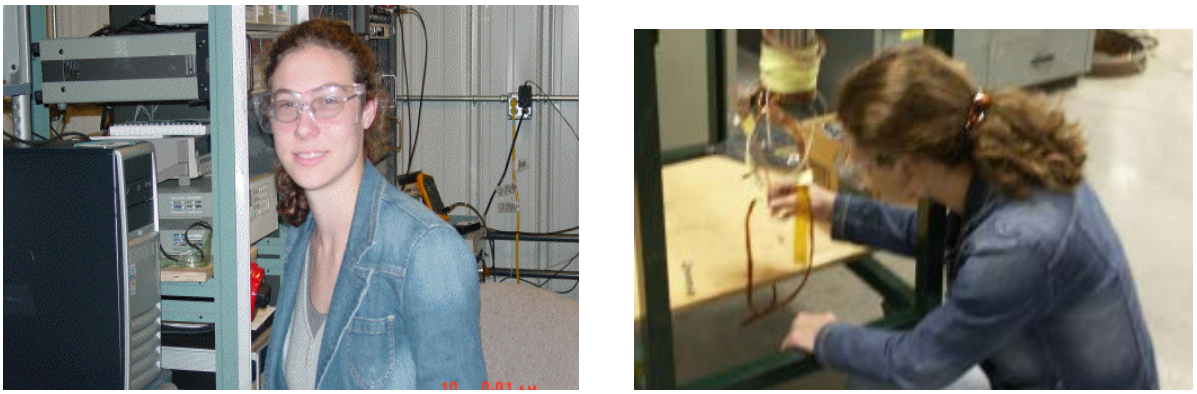

Fig. 4.10. Megan Nicole Mallette (Valparaiso University).

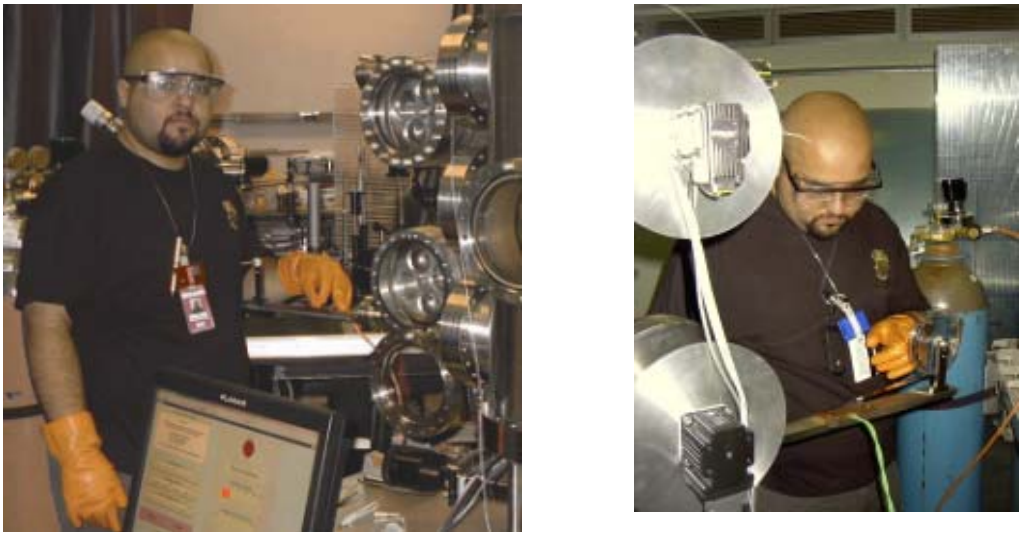

Fig. 4.11. Ali Moradmand (University of South Alabama).

Fig. 4.12. Jonathan D. Hebert (University of South Alabama).

Fig. 4.13. Benjamin J. Taylor (Tennessee Tech University).

5. FY 2006 Presentations/Publications

Published

Aytug, T., M. Paranthaman, A. A. Gapud, S. Kang, H. M. Christen, K. J. Leonard, P. M. Martin, J. R. Thompson, and D. K. Christen (ORNL), R. Meng, I. Rusakova, and C. W. Chu (Univ. of Houston), "Enhancement of flux pinning and critical currents in $YBa_2Cu_3O_{7-\delta}$ films by nano-scale Iridium pre-treatment of substrate surfaces," *J. Appl. Physics* **98**, 114309 (2005).

Aytug, T., M. Paranthaman, K. J. Leonard, H. Y. Zhai, M. S. Bhuiyan, E. A. Payzant, A. Goyal, S. Sathyamurthy, D. B. Beach, P. M. Martin, and D. K. Christen (ORNL), X. Li, T. Kodenkandath, U. Schoop, and M. W. Rupich (AMSC), and H. E. Smith (AFRL), "Assessment of chemical solution synthesis and properties of $Gd_2Zr_2O_7$ thin films as buffer layers for second generation high-temperature superconductor wires," *J. Mater. Res*. **20** (11), 2988 (November 2005).

Bhattacharya, R., P. Spagnol, D. F. Lee, and D. K. Christen, "Epitaxial Growth of Metal and Superconductor Oxide Films," p. 409 in *Epitaxial Growth of Functional Oxides*, ed. A. Goyal, Y. Kuo, O. Leonte, and W. Wong-Ng, The Electrochemical Society, Inc., Pennington, New Jersey (2005).

Bhuiyan, M. S., M. Paranthaman, A. Goyal, L. Heatherly, and D. B. Beach, "Deposition of rare earth tantalate buffers on textured Ni-W substrates for YBCO coated conductor using chemical solution deposition approach," *J. Mater. Res.* **21** (3), 767–73 (Mar. 2006).

Bhuiyan, M. S., M. Paranthaman, and K. Salama, "Topical Review: Solution-derived textured oxide thin films—a review," *Supercond. Sci. Technol.* **19**, R1–R21 (2006).

Cantoni, C., D. K. Christen, A. Goyal, L. Heatherly, F. A. List, E. D. Specht, M. Varela, and S. J. Pennycook, "Metal-oxide interfaces in 2nd generation HTS wires: Mechanism of epitaxial growth of oxide films mediated by a sulfur superstructure," p. 53 in *Interfaces in Electronic Materials,* ed. L. Cook, D. Misra, S. Mukhopadhyay, W. Wong-Ng, O. Leonte, and K. Sundaram, The Electrochemical Society, Inc., Pennington, New Jersey (2006).

Cheggour, N., and J. W. Ekin (NIST), C. L. H. Thieme (AMSC), Y.-Y. Xie and V. Selvamanickam (SuperPower), and R. Feenstra (ORNL), "Reversible axial-strain effect in Y-Ba-Cu-O coated conductors," *Supercond. Sci. Technol.* **18**, S319–S324 (December 2005).

Cheggour, N., and J. W. Ekin (NIST), Y.-Y. Xie and V. Selvamanickam (SuperPower), C. L. H. Thieme and D. T. Verebelyi (AMSC), "Enhancement of the irreversible axial-strain limit of Y-Ba-Cu-O-coated conductors with the addition of a Cu layer, *Appl. Phys. Lett.* **87**, 212505 (2005).

Chowdhuri, P., and C. Pallem (Tennessee Technological Univ.), J. A. Demko and M. J. Gouge (ORNL), "Feasibility of electric power transmission by DC superconducting cables, *IEEE Transactions on Applied Superconductivity* **14** (4), 3917–26 (December 2005).

Feldmann, D. M., T. G. Holesinger, C. Cantoni, R. Feenstra, N. A. Nelson, D. C. Larbalestier, D. T. Verebelyi, X. Li, and M. Rupich, "Grain orientations and grain boundary networks of $YBa_2Cu_3O_{7-}$ films deposited by metalorganic and pulsed laser deposition on biaxially textured Ni-W substrates," *J. Mater. Res.* **21**, (4) 923–34 (April 2006).

Gapud, A. A., D. Kumar, S. K. Viswanathan, C. Cantoni, M. Varela, J. Abiade, S. J. Pennycook, and D. K. Christen, "Enhancement of flux pinning in $YBa_2Cu_3O_{7-\delta}$ thin films embedded with epitaxially grown Y_2O_3 nanostructures using a multi-layering process," *Supercond. Sci. Technol.* **18**, 1502–1505 (2005).

Goyal, A., N. Rutter, C. Cantoni, and D. F. Lee, "Long-range current flow and percolation in RABiTS-type conductors and the relative importance of out-of-plane and in-plane misorientations in determining J_c," *Physica C* **426-431**, 1083–90 (October 2005).

Haugan, T., P. Barnes, R. Nekkanti, J. M. Evans, L. Brunke, I. Maartense, J. P. Murphy, A. Goyal A. Gapud, and L. Heatherly, "Deposition of $(211_{\sim 1.0nm}/123_{\sim 10nm})$xN multilayer coated conductors on Ni-based textured substrates," p. 359 in *Epitaxial Growth of Functional Oxides*, ed. A. Goyal, Y. Kuo, O. Leonte, and W. Wong-Ng, The Electrochemical Society, Inc., Pennington, New Jersey (2005).

Hawsey, R. A., and D. K. Christen, "Progress in research, development, and pre-commercial deployment of second generation HTS wires in the USA," *Physica C* **445-448**, pp, 488–95 (2006).

Holesinger, T. G., B. J. Gibbons, S. R. Foltyn, P. N. Arendt, V. Matias, Q. X. Jia, L. Stan, S. Kreiskott, J. Y. Coulter, R. F. DePaula, R. Feenstra, A. A. Gapud, E. D. Specht, T. Kodendandath, W. Zhang, X. Li, D. T. Verebelyi, U. Schoop, and M. W. Rupich, "TEM studies of interfacial microstructures in $YBa_2Cu_3O_7$ coated conductors," p. 111 in *Interfaces in Electronic Materials,* ed. L. Cook, D. Misra, S. Mukhopadhyay, W. Wong-Ng, O. Leonte, and K. Sundaram, The Electrochemical Society, Inc., Pennington, New Jersey (2006).

Holesinger, T. G., P. N. Arendt, J. R. Groves, L. Stan, J. A. Kennison, R. F. DePaula, R. Feenstra, A. A. Gapud, E. D. Specht, D. M. Feldmann, S. I. Kim, D. C. Larbalestier, W. Zhang, T. Kodendandath, X. Li, E. Thompson, D. T. Verebelyi, C. Thieme, U. Schoop, and M. W. Rupich, "Microstructural development in $YBa_2Cu_3O_7$ coated conductors based on ex situ YBCO conversion processes," p. 346 in *Epitaxial Growth of Functional Oxides*, ed. A. Goyal, Y. Kuo, O. Leonte, and W. Wong-Ng, The Electrochemical Society, Inc., Pennington, New Jersey (2005).

Ijaduola, A. O., J. R. Thompson, R. Feenstra, D. K. Christen, A. A. Gapud, and X. Song, "Critical currents of ex-situ $YBa_2Cu_3O_{7-}$ thin films on rolling assisted biaxially textured substrates: Thickness, field, and temperature dependencies," *Phys. Rev. B* **73**, 134502 (2006).

Kang, S., A. Goyal, J. Li, A. A. Gapud, P. M. Martin, L. Heatherly, J. R. Thompson, D. K. Christen, F. A. List, M. Paranthaman, and D. F. Lee (ORNL), "High-performance high-T_c superconducting wires," *Science* **311**, 1911–14 (March 31, 2006).

Kim, K., M. Paranthaman, D. P. Norton, T. Aytug, C. Cantoni, A. A. Gapud, A. Goyal, and D. K. Christen, "A perspective on conducting oxide buffers for Cu-based YBCO-coated conductors," *Supercond. Sci. Technol.* **19,** R23–R29 (2006).

Lee, D. F., H. M. Christen, F. A. List, L. Heatherly, K. J. Leonard, C. M. Rouleau, S. W. Cook, P. M. Martin, M. Paranthaman, and A. Goyal (ORNL), "R&D of RABiTS-based coated conductors: Conversion of ex situ YBCO superconductor using a novel pulsed electron-beam deposited precursor," *Physica C* **426-431**, 878–86 (October 2005).

List, F. A., P. G. Clem, L. Heatherly, J. T. Dawley, K. J. Leonard, D. F. Lee, and A. Goyal, "Low-pressure conversion studies for YBCO precursors derived by PVD and MOD methods," *IEEE Transactions on Applied Superconductivity* **15** (2) 2656–58 (June 2005).

Palau, A, T. Puig, and X. Obradors (Institut de Ciencia de Materials de Barcelona), and R. Feenstra and A. A. Gapud (ORNL), "Correlation between grain and grain-boundary critical current densities in *ex situ* coated conductors with variable $YBa_2Cu_3O_{7-\delta}$ layer thickness," *Appl. Phys. Lett*. **88**, 122502 (2006).

Palau, A, T. Puig, and X. Obradors (Institut de Ciencia de Materials de Barcelona), and R. Feenstra, A. A. Gapud, and E. D. Specht (ORNL), D. M. Feldmann (University of Wisconsin-Madison), and T. G. Holesinger (LANL), "Grain and grain-boundary critical currents in coated conductors with noncorrelating $YBa_2Cu_3O_7$ and substrate grain-boundary networks," *Appl. Phys. Lett.* **88**, 132508 (2006).

Paranthaman, M. P., "Superconductor Wires," pp. 319–22 in *McGraw-Hill Yearbook of Science & Technology 2006*, McGraw-Hill Professional, Columbus, Ohio.

Paranthaman, M. P., S. Sathyamurty, L. Heatherly, P. M. Martin, and A. Goyal (ORNL), T. Kodenkandath, X. Li, C. L. H. Thieme, and M. W. Rupich (AMSC), "All MOD buffer/YBCO approach to coated conductors," *Physica C* **445-448**, 529–32 (2006).

Polyanskii, A., R. L. S. Emergo, J. Z. Wu, T. Aytug, D. K. Christen, G. K. Perkins, and D. Larbalestier, "Magneto-optical imaging and electromagnetic study of $YBa_2Cu_3O_7$ vicinal films of variable thickness," *Phys. Rev. B* **72** (17), 174509 (November 2005).

Sathyamurthy, S., M. Paranthaman, L. Heatherly, P. M. Martin, E. D. Specht, and A. Goyal, "Solution-processed lanthanum zirconium oxide as a barrier layer for high I_c-coated conductors," *J. Mater. Res.* **21**, (4) 910–14 (April 2006).

Specht, E. D., A. Goyal, J. Li, and P. M. Martin (ORNL), X. Li and M. W. Rupich (AMSC), "Stacking faults in $YBa_3Cu_3O_{7-x}$: Measurement using X-ray diffraction and effects on critical current,"*Appl. Phys. Lett.* **89**, 162510 (2006).

Stewart, E., M. S. Bhuiyan, S. Sathyamurthy, M. Paranthaman, "Studies of solution deposited cerium oxide thin films on textured Ni-alloy substrates for YBCO superconductor," *Materials Research Bulletin* **41**, 1063–68 (2006).

Wee, S. H., A. Goyal, P. M. Martin, J. Li, M. Paranthaman, and L. Heatherly, "Strong flux-pinning in epitaxial $NdBa_2Cu_3O_{7-\delta}$ films with columnar defects comprised of self-assembled nanodots of $BaZrO_3$," *Supercond. Sci. Technol.* **19** (10), L42–L45 (2006).

Wee, S. H., A. Goyal, P. M. Martin, and L. Heatherly, "High in-field critical current densities in epitaxial $NdBa_2Cu_3O_{7-\delta}$ films on RABiTS by pulsed laser deposition," *Supercond. Sci. Technol*. **19 (**8), 865–68 (August 2006)**.**

Wong-Ng, W., I. Levin, R. Feenstra, M. Vaudin, and L. P. Cook, "Phase evolution and texture of $Ba_2YCu_3O_{6+x}$ films using the 'BaF_2 conversion process," p. 382 in *Epitaxial Growth of Functional Oxides*, ed. A. Goyal, Y. Kuo, O. Leonte, and W. Wong-Ng, The Electrochemical Society, Inc., Pennington, New Jersey (2005).

Wong-Ng, W., I. Levin, L. P. Cook, and R. Feenstra, "Nature of the transient BaF_2-related phases in the 'BaF_2' processing of $Ba_2YCu_3O_{7-x}$ superconductors," *Appl. Phys. Lett.* **88**, 102507 (2006).

Wu, J. Z., R. Emergo, X. Wang, D. Christen, T. Aytug, and M. Paranthaman, "J_cs in HTS thick films: Influence of out-of plane misorientation," p. 313 in *Epitaxial Growth of Functional Oxides*, ed. A. Goyal, Y. Kuo, O. Leonte, and W. Wong-Ng, The Electrochemical Society, Inc., Pennington, New Jersey (2005).

Xu, Y., A. Goyal, K. J. Leonard, M. Paranthaman, and E. D. Specht (ORNL), and D. Shi (University of Cincinnati), "Processing dependence of texture, and critical properties of $YBa_2Cu_3O_{7-\delta}$ films on RABiTS substrates by a non-fluorine MOD method," *J. Am. Ceram. Soc.* **89** (3), 914–20 (2006).

Submitted

Aytug, T., M. Paranthaman, A. A. Gapud, S. Kang, M. Varela, P. M. Martin, J. M. Raitano, S.-W. Chan, J. R. Thompson, and D. K. Christen, "Decoration of substrate surfaces: an effective method for improving flux pinning in $YBa_2Cu_3O_{7-}$," submitted to *IEEE Trans. Appl. Supercond*.

Aytug, T., D. K. Christen, M. Paranthaman, A. A. Gapud, H. M. Christen, S. Kang, M. Varela, K. J. Leonard, A. Goyal, P. M. Martin, J. R. Thompson, and A. O. Ijaduola, (ORNL), R. Meng, I. Rusakova, and C. W. Chu (University of Houston), T. H. Johansen (University Of Oslo), and S. W. Chan (Columbia University), "Enhancement of flux pinning in $YBa_2Cu_3O_{7-\delta}$ films via nanoscale modifications of substrate surfaces," book chapter submitted to *Flux Pinning and AC Loss Studies on YBCO Coated Conductors*, Nova Scientific Publishers.

Aytug, T., M. Paranthaman, K. J. Leonard, S. Kang, P. M. Martin, L. Heatherly, A. Goyal, A. O. Ijaduola, J. R. Thompson, D. K. Christen, R. Megn, I. Rusakova, and C. W. Chu, "Analysis of flux pinning in $YBa_2Cu_3O_{7-}$ films by nanoparticle-modified substrate surfaces," submitted to *Phys. Rev. B*.

Bhuiyan, M. S., S. Sathyamurthy, and M. Paranthaman (ORNL), "Development of modified MOD-TFA approach for thick YBCO film growth," submitted to *IEEE Trans. Appl. Supercond*.

Demko, J. A., I. Sauers, D. R. James, and M. J. Gouge (ORNL), D. Lindsay, M. Roden, and J. Tolbert (Southwire), and D. Willén and C. Træholt (NKT cables), "Triaxial HTS cable for the AEP Bixby project," submitted to *IEEE Trans. Appl. Supercond*

Duckworth, R. C., M. Paranthaman, F. A. List, and M.J. Gouge (ORNL), "AC losses in YBCO coated conductors with inkjet filaments," submitted to *IEEE Trans. Appl. Supercond*.

Feenstra, R., F. A. List, Y. Zhang, D. K. Christen, V. A. Maroni, D. J. Miller, and D. M. Feldmann, "Characterization of phase evolution in YBCO coated conductors produced by the ex situ BaF_2 process," submitted to *IEEE Trans. Appl. Supercond*.

Goyal, A., P. M. Martin, J. Li, A. A. Gapud, E. D. Specht, and M. Paranthaman (ORNL), W. Zhang, Y. Huang, X. Li, and M. Rupich (AMSC), "Enhanced flux-pinning in 4-cm wide, RE-doped, MOD YBCO conductors on RABiTS," submitted to *IEEE Trans. Appl. Supercond*.

Hawsey, R. A., and D. K. Christen (ORNL), "progress in research, development, and pre-commercial deployment of second generation HTS wires in the USA," submitted to proceedings of the 18th International Symposium on Superconductivity, 2005, to be published in *Physica C*.

Heatherly, L., H. Hsu, S. Sathyamurthy, M. Paranthaman, J. Li, and A. Goyal (ORNL), X. Li and M. W. Rupich (AMSC), "Slot die coating and conversion of LZO on rolling assisted biaxially textured NiW substrates with and without a very thin seed layer," submitted to *IEEE Trans. Appl. Supercond*.

James, D. R., I. Sauers, and A. R. Ellis (ORNL), K. Tekletsadik (SuperPower consultant), and D. W. Hazelton (SuperPower), "Breakdown and partial discharge measurements of some commonly used dielectric materials in liquid nitrogen for HTS applications," submitted to *IEEE Trans. Appl. Supercond*.

Kim, K., Y. Zhang, R. Feenstra, D. K. Christen, H. M. Christen, S. Cook, F. A. List, J. Tao, S. J. Pennycook, and Y. Zuev, "$YBa_2Cu_3O_{7-}$ formation by processing of laser-ablated, fluorine-free precursor films," submitted to *IEEE Trans. Appl. Supercond*.

List, F. A., T. Kodenkandath and M.W. Rupich (AMSC), "Fabrication of filamentary YBCO coated conductor by MOD inkjet printing," submitted to *IEEE Trans. Appl. Supercond*.

Ozer, M. M., J. R. Thompson, and H. H. Weitering, "Robust superconductivity in quantum-confined Pb," submitted to *Physical Review B*.

Paranthaman, M. P., "MOD buffer/YBCO approach to fabricate low-cost second generation hts wires," submitted to *IEEE Trans. Appl. Supercond*.

Rey, C. M., and R. C. Duckworth, "Current-voltage measurements in a 2G YBCO coil," submitted to *IEEE Trans. Appl. Supercond*.

Sathyamurthy, S., K. J. Leonard, M. S. Bhuiyan, T. Aytug, amd M. Paranthaman (ORNL), "Low-cost approaches for flux-pinning enhancements in YBCO films using solution processing," submitted to *IEEE Trans. Appl. Supercond*.

Sauers, I., D. R. James, A. R. Ellis, and M. O. Pace, "High voltage testing of a 5-m triaxial HTS Cable," submitted to *IEEE Trans. Appl. Supercond*.

Specht, E. D., A. Goyal, and W. Liu, "Local epitaxy of $YBa_2Cu_3O_x$ on polycrystalline Ni measured by X-ray microdiffraction," submitted to *Journal of Mtls. Res.*

Tuncer, E., I. Sauers, and D. R. James (ORNL), "Electrical properties of semiconducting tapes used in HTS power cables," submitted to *IEEE Trans. Appl. Supercond*.

Wee, S. H., A. Goyal, P. M. Martin, and L. Heatherly (ORNL), "Fabrication of high-*J*c $NdBa_2Cu_3O_{7-\delta}$ and $BaZrO_3$-doped $NdBa_2Cu_3O_{7-\delta}$ films on RABiTS**,**" submitted to *IEEE Trans. Appl. Supercond*.

Xiong, X., K. Lenseth, J. Reeves, Y. Qiao, R. Schmidt, Y. Chen, Y. Li, Y. Xie, P. Arendt, R. DePaula, L. Stan, S. Foltyn, M. Paranthaman, T. Aytug, A. Goyal, and V. Selvamanickam, "High throughput processing of long-length IBAD MgO & Buffer templates at SuperPower," submitted to *IEEE Trans. Appl. Supercond*.

Zhang, Y., R. Feenstra, and D. K. Christen, "X-ray photoelectron spectroscopy study on E-beam co-evaporated YBCO precursors and their post-deposition conversion,"submitted to proceedings for the 2005 MRS Spring Meeting, San Francisco, California, March 28–April 4, 2005.

Zhang, W., Y. Huang, X. Li, T. Kodenkandath, M. Rupich, U. Schoop, D. T. Verebelyi, C. L. H. Thieme, and E. Siegal (AMSC), T. G. Holesinger (LANL), D. J. Miller and V. A. Maroni (ANL), A. Goyal and M.P. Paranthaman (ORNL), "Control of flux pinning in MOD YBCO coated conductors," submitted to *IEEE Trans. Appl. Supercond*.

Abstracts Submitted in Preparation for Talks

Aytug, T., M. Paranthaman, H. M. Christen, S. Kang, K. J. Leonard, A. A. Gapud, P. M. Martin, A. Goyal, A. O. Ijaduola, J. R. Thompson, and D. K. Christen (ORNL), R. Meng, I. Rusakova, C. W. Wu (Univeristy of Houston), T. H. Johansen (University of Oslo), "Enhancement of flux pinning in $YBa_2Cu_3O_{7-\delta}$ films via nanoscale modifications of substrate surface," submitted to ASC 2006 Applied Superconductivity Conference, Seattle, Washington, August 27–September 1, 2006.

Aytug, T., M. Paranthaman, D. K. Christen, "A new conductive buffer layer architecture for electrical self-stabilization of YBCO coated conductors," abstract submitted to the Materials Science & Technology 2006 Conference, Oct. 15–19, 2006, Cincinnati Ohio.

Bhuiyan, M. S., S. Sathyamurthy, and M. Paranthaman (ORNL), "Development of modified MOD-TFA approach for thick YBCO film growth," submitted to ASC 2006 Applied Superconductivity Conference, Seattle, Washington, August 27–September 1, 2006.

Bhuiyan, M. S., M. Paranthaman, and S. Sathyamurthy, "A modified MOD-TFA approach for thick REBCO film growth," abstract submitted to the Materials Science & Technology 2006 Conference, Oct. 15–19, 2006, Cincinnati Ohio.

Christen, D. K., "High-temperature superconducting wires: How basic research has contributed to development progress," Colloquim given at University of South Alabama, Mobile, Alabama, December 1, 2005.

Demko, J. A., I. Sauers, D. R. James, and M. J. Gouge (ORNL), D. Lindsay, M. Roden, and J. Tolbert (Southwire), D. Willen and C. Traeholt (NKT Research & Innovation A/S), "Triaxial HTS cable system design for the AEP Bixby project," submitted to ASC 2006 Applied Superconductivity Conference, Seattle, Washington, August 27–September 1, 2006.

Duckworth, R. C., M. Paranthaman, F. A. List, and M. J. Gouge (ORNL), "AC losses in YBCO coated conductors with inkjet filaments," submitted to ASC 2006 Applied Superconductivity Conference, Seattle, Washington, August 27–September 1, 2006.

Feenstra, R., A. A. Gapud, E. D. Specht, A. Ijaduola, J. R. Thompson, D. K. Christen, D. M. Feldmann, X. Song, D. C. Larbalestier, T. G. Holesinger, A. Palau, T. Puig, and X. Obradors, "Meandering grain boundaries in ex situ YBCO coated conductors," MRS Spring Meeting, San Francisco, California, April 17–21, 2006.

Feenstra, R., "Changing perspectives on the thickness dependence of J_c in YBCO coated conductors," Stanford-Wisconsin Workshop on Coated Conductors, Palo Alto, California, April 23–26, 2006 (**INVITED**).

Feenstra, R., Y. Zhang, and D. K. Christen (ORNL), V. A. Maroni and D. J. Miller (ANL), D. M. Feldmann (Univ. of Wisconsin), and T. G. Holesinger (LANL), "Characterization of phase evolution in YBCO coated conductor produced by the ex situ BaF_2 process," submitted to ASC 2006 Applied Superconductivity Conference, Seattle, Washington, August 27–September 1, 2006.

Feenstra, R,. "Grain boundary issues and thickness dependence of J_c in coated conductors," Department of Energy Basic Energy Sciences Workshop on Basic Research Needs for Superconductivity, Arlington, Virginia, May 8–10, 2006 (**INVITED**).

Goyal, A., P. M. Martin, J. Li, A. A. Gapud, E. D. Specht, and M. Paranthaman (ORNL), W. Zhang, Y. Huang, X. Li, and M. Rupich (AMSC), "Enhanced flux-pinning in 4-cm wide, RE-doped, MOD YBCO conductors on RABiTS," submitted to ASC 2006 Applied Superconductivity Conference, Seattle, Washington, August 27–September 1, 2006.

Goyal, A., S. Kang, J. Li, P. M. Martin, L. Heatherly, J. R. Thompson, D. K. Christen, F. A. List, M. Paranthaman, D. F. Lee (ORNL), A. A. Gapud (University of S. Alabama), "Ultra-high performance HTS conductors," submitted to ASC 2006 Applied Superconductivity Conference, Seattle, Washington, August 27–September 1, 2006.

Goyal, A., "Mechanism of current-flow in high-performance, epitaxial YBCO films on RABiTS," submitted to ASC 2006 Applied Superconductivity Conference, Seattle, Washington, August 27–September 1, 2006.

Heatherly, L., H. Hsu, S. Sathyamurthy, M. Paranthaman, J. Li, and A. Goyal (ORNL), X. Li and M. W. Rupich (AMSC), "Slot die coating and conversion of LZO on rolling assisted biaxially textured NiW substrates with and without a very thin seed layer," submitted to ASC 2006 Applied Superconductivity Conference, Seattle, Washington, August 27–September 1, 2006.

James, D. R., I. Sauers, and A. R. Ellis (ORNL), K. Tekletsadik (SuperPower consultant), and D. W. Hazelton (SuperPower), "Breakdown and partial discharge measurements of some commonly used dielectric materials in liquid nitrogen for HTS applications," submitted to ASC 2006 Applied Superconductivity Conference, Seattle, Washington, August 27–September 1, 2006.

Kim, K., Y. Zhang, R. Feenstra, C. Cantoni, D. K. Christen and H. M. Christen, "$YBa_2Cu_3O_{7-x}$ formation by in situ processing of laser-ablated, fluorine-free precursor films," MRS Spring Meeting, San Francisco, California, April 17–21, 2006.

List, F. A., T. Kodenkandath and M. W. Rupich (AMSC), "Fabrication of filamentary YBCO coated conductor by MOD inkjet printing," submitted to ASC 2006 Applied Superconductivity Conference, Seattle, Washington, August 27–September 1, 2006.

Paranthaman, M. P., S. Sathyamurthy, T. Aytug, M. S. Bhuiyan, and A. Goyal (ORNL), T. Kodenkandath, X. Li, and M.W. Rupich (AMSC), "MOD buffer/YBCO approach to fabricate low-cost second generation HTS wires" submitted to ASC 2006 Applied Superconductivity Conference, Seattle, Washington, August 27-September 1, 2006.

Paranthaman, M. P., S. Sathyamurthy, T. Aytug, M. S. Bhuiyan, L. Heatherly, H. Hsu, and A. Goyal (ORNL), T. Kodenkandath, X. Li, W. Zhang, C. L. H. Thieme, and M. W. Rupich (AMSC), and X. Xiong, Y. Chen, J. Reeves, and V. Selvamanickam, "Strategic buffer layer development for high performance 2G wires," abstract submitted to the Materials Science & Technology 2006 Conference, Oct. 15-19, 2006, Cincinnati Ohio.

Rey, C. M., "Critical current measurements of a 2G YBCO coil," submitted to ASC 2006 Applied Superconductivity Conference, Seattle, Washington, August 27–September 1, 2006.

Sathyamurthy, S., K. J. Leonard, M. S. Bhuiyan, T. Aytug, amd M. Paranthaman (ORNL), "Low-cost approaches for flux-pinning enhancements in YBCO films using solution processing," submitted to ASC 2006 Applied Superconductivity Conference, Seattle, Washington, August 27–September 1, 2006.

Sathyamurthy, S., and M. Paranthaman, "Influence of ambient relative humidity on the crystallization characteristics of sol-gel processed lanthanum zirconium oxide epitaxial thin films," abstract submitted to the Materials Science & Technology 2006 Conference, October 15–19, 2006, Cincinnati Ohio.

Sauers, I., D. R. James, A. R. Ellis, and M. O. Pace, "High-voltage testing of a 5-m triaxial HTS cable," submitted to ASC 2006 Applied Superconductivity Conference, Seattle, Washington, August 27–September 1, 2006.

Thompson, J. R., A. Goyal, S. Kang, K. J. Leonard, P. M. Martin, A. A. Gapud, M. Varela, M. Paranthaman, A. O. Ijaduola, E. D. Specht, D. K. Christen, S. J. Pennycook, F. A. List, R. Feenstra, and X. Song, "Vortex pins—BZO columnar defects or non-aligned inclusions—in YBCO coated conductors," MRS Spring Meeting, San Francisco, California, April 17–21, 2006.

Tuncer, E., I. Sauers, and D. R. James (ORNL), "Electrical properties of semiconducting tapes used in HTS power cables," submitted to ASC 2006 Applied Superconductivity Conference, Seattle, Washington, August 27–September 1, 2006.

Wee, S. H., A. Goyal, P. M. Martin, and L. Heatherly (ORNL), "Fabrication of high-*J*c $NdBa_2Cu_3O_{7-\delta}$ and $BaZrO_3$-doped $NdBa_2Cu_3O_{7-\delta}$ films on RABiTS," submitted to ASC 2006 Applied Superconductivity Conference, Seattle, Washington, August 27–September 1, 2006**.**

Xiong, X., K. Lenseth, J. Reeves, Y. Qiao, R. Schmidt, Y. Chen, Y. Li, Y. Xie, P. Arendt, R. DePaula, L. Stan, S. Foltyn, M. Paranthaman, T. Aytug, A. Goyal, and V. Selvamanickam, "High throughput processing of long-length IBAD MgO and buffer templates at SuperPower," submitted to ASC 2006 Applied Superconductivity Conference, Seattle, Washington, August 27–September 1, 2006.

Zhang, W., Y. Huang, X. Li, T. Kodenkandath, M. Rupich, U. Schoop, D. T. Verebelyi, C. L. H. Thieme, and E. Siegal (AMSC), T. G. Holesinger (LANL), D. J. Miller and V. A. Maroni (ANL), A. Goyal and M. P. Paranthaman (ORNL), "Control of flux pinning in MOD YBCO coated conductors," submitted to ASC 2006 Applied Superconductivity Conference, Seattle, Washington, August 27–September 1, 2006.

Zhang, Y., R. Feenstra, and D. K. Christen, "Effects of pre-annealing on the epitaxial conversion of $YBa_2Cu_3O_{7-x}$ precursor films made by E-beam co-evaporation," MRS Spring Meeting, San Francisco, California, April 17–21, 2006.

INTERNAL DISTRIBUTION

1. C. A. Blue
2. P. F. Britt
3. M. V. Buchanan
4. D. K. Christen
5. D. C. Christensen
6. F. V. Damiano
7. M. J. Gouge
8. A. Goyal
9. G. R. Gruzalski
10. R. A. Hawsey
11. L. L. Horton
12. J. Johnson, OTIC
13. T. J. King, Jr.
14. W. Koncinski
15–24. D. F. Lee
25. S. L. Milora
26. M. Paranthaman
27. M. Reeves
28. S. J. Zinkle

EXTERNAL DISTRIBUTION

29. N. Aversa, Consultant, Waukesha Electric Systems, 400 S. Prairie Ave., Waukesha, WI 53186-5937
30. B. Marchionini, Energetics, Inc., 901D Street, SW, Washington, DC 20004
31. P. N. Barnes, Air Force Research Laboratory, AFRL/PRPG, 2645 Fifth Street, WPAFB, OH 45433-7919
32. R. Bhattacharya, National Renewable Energy Laboratory, 1617 Cole Blvd., Golden, CO 80401
33. J. W. Bray, Physicist/Program Manager, General Electric Corporate Research and Development, P.O. Box 8, Schenectady, NY 12301
34. S. W. Butler, Texas Center for Superconductivity at the University of Houston, Houston Science Center 206, Houston TX 77204-5002
35. L. Castellani, Metal Oxide Technologies Inc., 8807 Emmott Rd., Suite 100, Houston, TX 77040
36. H. S. Chhabra,OE-10, U.S. Department of Energy, 6H-034/FORS, 1000 Independence Ave., S.W., Washington, DC 20585
37. P. G. Clem, Sandia National Laboratories, MS 1411, P.O. Box 5800, Albuquerque, NM 87185-1405
38. G. Crabtree, Argonne National Laboratory, ET/212, 9700 South Cass Ave., Argonne, IL 60439-4838
39. S. J. Dale, Florida Adv. Power Lab, Florida State University, 2000 Levy Ave., Bldg. A, Tallahassee, FL 32310
40. P. Hoffman, OE-10, U.S. Department of Energy, 6H-034/FORS, 1000 Independence Ave., S.W., Washington, DC 20585
41. N. Cheggour, National Institute of Standards and Technology, 325 Broadway, Boulder, CO 80303
42. H. Harshavardhan, Neocera, 10000 Virginia Manor Rd., Beltsville, MD 20705
43. D. Haught, OE-10, U.S. Department of Energy, 1000 Independence Ave., S.W., Washington, DC 20585
44. X. Huang, General Electric Corporate Research and Development, EP-113, P.O. Box 8, Schenectady, NY 12301
45. K. Kolevar, OE-1, U.S. Department of Energy, 1000 Independence Ave., S.W., Washington, DC 20085

46. V. Kruse, Southwire Company, P.O. Box 1000, Carrollton, GA 30119
47. D. C. Larbalestier, Applied Superconductivity Center, Department of Mechanical Engineering, Florida State University, 253 Shaw Building, 2031 East Paul Dirac Drive, Tallahassee, FL 32310-
48. W. C. Lin, U.S. Department of Energy, Office of Assistant Manager for Energy Research and Development, Oak Ridge Field Office, P.O. Box 2008, Oak Ridge, TN 37831-6269
49. D. Lindsay, Ultera-Southwire Company, P.O. Box 1000, Carrollton, GA 30119
50. A. P. Malozemoff, American Superconductor Corporation, Two Technology Dr., Westborough MA 01581
51. K. R. Marken, Jr., Los Alamos National Laboratory, Superconductivity Technology Center, P.O. Box 1663, MS K763, Los Alamos, NM
52. V. Maroni, Argonne National Laboratory, Chemical Technology, 9700 South Cass Ave., Bldg. 205, Argonne IL 60439
53. S. P. Mehta, Waukesha Electric Systems, 400 S. Prairie Ave., Waukesha, WI 53186-5937
54. P. Pellegrino, SuperPower, Inc., 450 Duane Avenue, Schenectady, NY 12305
55. D. E. Peterson, Los Alamos National Laboratory, Superconductivity Technology Center, P.O. Box 1663, MS K763, Los Alamos, NM 87545
56. E. Pleva, Waukesha Electric Systems, 400 S. Prairie Ave., Waukesha, WI 53186-5937
57. M. W. Rupich, American Superconductor Corporation, Two Technology Drive, Westborough, MA 01581
58. R. F. Schiferl, Rockwell Automation Power Systems, 26391 Curtiss Wright Pkwy, Suite 102, Richmond Heights, OH 44143
59. V. Selvamanickam, SuperPower, Inc., 450 Duane Avenue, Schenectady, NY 12305
60. V. F. Solovyov, Brookhaven National Laboratory, Materials Science Dept., Bldg. 480, P.O. Box 5000, Upton, NY 11973-5000
61. H. Weinstock, Physics and Electronics, Air Force Office of Scientific Research, AFOSR/NE, 4015 Wilson Blvd., Room 713, Arlington VA22203-1954
62. W. Wong-Ng, National Institute of Standards and Technology, Ceramics Division, Building 223, A-256 Materials, Gaithersburg, MD 20899
63. G. Yurek, American Superconductor Corporation, Two Technology Drive, Westborough, MA 01581